Synthesis of Novel Iron-based Nanomaterials for the Removal of the Antibiotic Ciprofloxacin from Water

オマル エイ エム ファリオウナ

Ph.D. Thesis on

Synthesis of Novel Iron-based Nanomaterials for the Removal of the Antibiotic Ciprofloxacin from Water

by

OMAR A. M. FALYOUNA

Supervised by

Assoc. Prof. Osama Eljamal

Water and Environmental Engineering Laboratory (WEEL)
Department of Earth System Science and Technology (ESST)
Interdisciplinary Graduate School of Engineering Sciences (IGSES)
Kyushu University

Japan

March 2023

Abstract

The persisting occurrence of ciprofloxacin (CIP) and other antibiotics in our limited water resources has fatal health and environmental consequences. This research adopts zerovalent iron nanoparticles (Fe^0) as an excellent remedial agent to propose novel iron-based nanomaterials with unique properties to efficiently remove CIP from water. **The first project** focused on coating Fe^0 nanoparticles with a shell of magnesium hydroxide [$Mg(OH)_2$] to overcome the shortcomings of Fe^0 nanoparticles and promote the remediation of CIP from aquatic environments. The outcomes of the batch experiments demonstrated that encapsulating Fe^0 nanoparticles by $Mg(OH)_2$ layer with a [$Mg(OH)_2/Fe^0$] mass ratio of 5% boosted the removal efficiency of CIP from 41.76% to 96.31%. Moreover, the optimization process for the treatment parameters revealed that CIP-polluted water was optimally treated by Mg/Fe^0 nanoparticles under the following conditions: [Mg/Fe^0] = 0.5 g L^{-1}, [CIP] = 100 mg L^{-1}, initial pH = 3 – 11, temperature = 25 °C, and treatment time = 60 min. Also, the desorption experiments confirmed that the removal of CIP by Mg/Fe^0 nanoparticles was completely governed by chemical and physical adsorption. Furthermore, the proposed regeneration protocol succeeded in recycling Mg/Fe^0 nanoparticles for five consecutive treatment cycles with removal efficiencies higher than 95%. **The second project** aimed to enhance the reactivity of Fe^0 nanoparticles in eliminating CIP from aqueous solutions by adding the organic ligand oxalate. The outcomes of the batch experiments showed that adding 0.3 mM of oxalate to Fe^0 nanoparticles increased the adsorption of CIP from 45.05% to 95.74%. Moreover, the optimal removal of CIP by (Fe^0/oxalate) nanoparticles was attained under the following circumstances: [Fe^0] = 0.3 g L^{-1}, [Oxalate] = 0.3 mM, initial pH = 7, temperature = 25 °C, and treatment time = 30 min. Similar to Mg/Fe^0 nanoparticles, the desorption experiments emphasized that the remediation of CIP by (Fe^0/oxalate) nanoparticles was fully controlled by adsorption instead of oxidation. In addition, the results proved that adding oxalate is a cost-effective approach to improve the reactivity of Fe^0 nanoparticles as the treatment cost of 1 L of CIP-polluted water notably declined from ¥65.716 (Fe^0 alone) to ¥29.124 (Fe^0/oxalate). It is important to highlight that the performance of Mg/Fe^0 and (Fe^0/oxalate) nanoparticles in remediating CIP-polluted water are reported for the first time in this study. Also, their outstanding competence is promising and has great potential in tackling CIP contamination in actual polluted waters.

Acknowledgments

The whole praise, prostrations, and supplications are to Allah, who aided me in every moment of this project and helped me finish this work. I would like to express my sincere gratitude to my supervisor, Assoc. Prof. Osama ELJAMAL for his remarkable guidance, support, and constant encouragement throughout my doctoral study at Kyushu University. Also, I am incredibly thankful to Prof. Yuji SUGIHARA and Assoc. Prof. Hooman Farzaneh for their valuable comments and suggestions on the presented work. I would also like to thank all the Water and Environmental Engineering Laboratory (WEEL) members and my colleagues in the Department of Earth System Science and Technology (ESST) for their prompt and professional assistance whenever needed. Additionally, I must thank the Japanese Ministry of Education, Culture, Sports, Science, and Technology (MEXT) for their financial support during my postgraduate studies. Finally, my whole gratitude to my family; my beloved parents, my wife, my son and unborn baby, my sister, and my brothers for their encouragement and love and for believing in me, to whom I am dedicating this work.

Omar Falyouna

March 2023

Journal Publications

1. "Magnetic Zeolite Synthesis for Efficient Removal of Cesium in a Lab-scale Continuous Treatment System", **Omar Falyouna**, Osama Eljamal, Ibrahim Maamoun, Atsushi Tahara and Yuji Sugihara, Journal of Colloid and Interface Science, vol.571, pp.66–79, July 2020.

2. "Chemical Deposition of Iron Nanoparticles (Fe^0) on Titanium Nanowires for Efficient Adsorption of Ciprofloxacin from Water", **Omar Falyouna**, Ibrahim Maamoun, Khaoula Bensaida, Atsushi Tahara, Yuji Sugihara and Osama Eljamal, Water Practice and Technology, vol.17 (1), pp.75–83, September 2021.

3. "Encapsulation of Iron Nanoparticles with Magnesium Hydroxide Shell for Remarkable Removal of Ciprofloxacin from Contaminated Water", **Omar Falyouna**, Ibrahim Maamoun, Khaoula Bensaida, Atsushi Tahara, Yuji Sugihara and Osama Eljamal, Journal of Colloid and Interface Science, vol.605, pp.813–827, January 2022.

4. "Synthesis of Hybrid Magnesium Hydroxide/Magnesium Oxide Nanorods [$Mg(OH)_2$/MgO] for Prompt and Efficient Adsorption of Ciprofloxacin From Aqueous Solutions", **Omar Falyouna**, Khaoula Bensaida, Ibrahim Maamoun, U.P.M. Ashik, Atsushi Tahara, Kazuya Tanaka, Noboru Aoyagi, Yuji Sugihara and Osama Eljamal, Journal of Cleaner Production, vol.342, 130949, March 2022.

5. "Promotion of Ciprofloxacin Adsorption from Contaminated Solutions by Oxalate Modified Nanoscale Zerovalent Iron Particles", **Omar Falyouna**, Mohd Faizul Idham, Ibrahim Maamoun, Khaoula Bensaida, UPM Ashik, Yuji Sugihara and Osama Eljamal, Journal of Molecular Liquids, vol.359, 119323, August 2022.

Conference Proceedings

1. "Behavior of Dental Composite Materials in Sterilized and Non-sterilized Landfill Leachate", **Omar Falyouna**, Gabriella Kakonyi, Steven Mulligan, Andrew Fairburn, Keyvan Moharamzadeh, Nicholas Martin and Steven Thornton, Proceedings of 4th International Exchange and Innovation Conference on Engineering & Sciences (IEICES), Fukuoka (Japan), pp.72–76, October 2018.
2. "Removal of Cesium from Contaminated Waters by Employing Iron-based Nanoparticles and Nanocomposites", **Omar Falyouna**, Osama Eljamal and Ibrahim Maamoun, Proceedings of 5th International Exchange and Innovation Conference on Engineering & Sciences (IEICES), Fukuoka (Japan), pp.26–27, October 2019.
3. "Removal of Ciprofloxacin from Aqueous Solutions by Nanoscale Zerovalent Iron-based Materials: A Mini Review", **Omar Falyouna**, Ibrahim Maamoun, Khaoula Bensaida, Yuji Sugihara and Osama Eljamal, Proceedings of 6th International Exchange and Innovation Conference on Engineering & Sciences (IEICES), pp.179–185, Fukuoka (Japan), October 2020.
4. "Chemical Deposition of Iron Nanoparticles (Fe^0) on Titanium Nanowires for Efficient Adsorption of Ciprofloxacin from Water", **Omar Falyouna**, Ibrahim Maamoun, Khaoula Bensaida, Atsushi Tahara, Yuji Sugihara, and Osama Eljamal, Proceedings of 12th Eastern European Young Water Professionals Conference, Riga (Latvia), pp.128–135, April 2021.
5. "Mini Review on Recent Applications of Nanotechnology in Nutrient and Heavy Metals Removal from Contaminated Water", **Omar Falyouna**, Ibrahim Maamoun, Khaoula Bensaida, Mohd Faizul Idham, Yuji Sugihara and Osama Eljamal, Proceedings of 7th International Exchange and Innovation Conference on Engineering & Sciences (IEICES), Fukuoka (Japan), pp.161–169, October 2021.
6. "Effect of Water Matrix on Ligand-assisted Adsorption of Ciprofloxacin from Aqueous Solutions by Zerovalent Iron Nanoparticles", **Omar Falyouna**, Ibrahim Maamoun, Mohd Idham, and Osama Eljamal, Proceedings of 8th International Exchange and Innovation Conference on Engineering & Sciences (IEICES), Fukuoka (Japan), October 2022.

Poster Presentations

1. “Enlargement of the oxidative capacity of iron nanoparticles by the addition of oxalate to efficiently remove ciprofloxacin from water”, **Omar Falyouna**, Khaoula Bensaida, Ibrahim Maamoun, Ashik, Atsushi, Yuji Sugihara and Osama Eljamal, 5th IWA Specialized International Conference ‘Ecotechnologies for Wastewater Treatment (EcoSTP), Milan (Italy), June 2021.

Table of Contents

List of Figures

List of Tables

Chapter 1

Introduction

1.1. Background

All creatures on earth need three primary resources to survive water, soil, and air. Water is considered the most crucial element for the sustenance of life on this plant [1–3]. Szent-Gyorgyi described the significance of water in life: “That water functions in a variety of ways within a cell can not be disputed. Life originated in water, is thriving in water, water being its solvent and medium. It is the matrix of life.” [4]. Water is widespread in the environment and forms the lakes, rivers, seas, oceans, and groundwater. Figure 1.1 demonstrates that 97.5% of the hydrosphere is saline water, leaving only 2.5% of the total water on this plant as fresh waters [5,6].

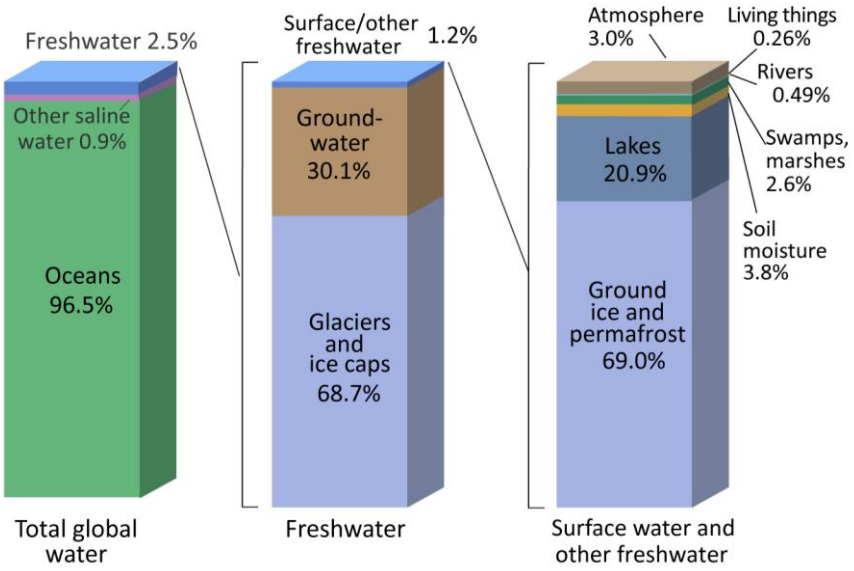

Figure 1.1 Water distribution on earth (Credit: U.S. Geological Survey, Water Science School. https://www.usgs.gov/special-topic/water-science-school, Data source: Igor Shiklomanov's chapter "World freshwater resources" in Peter H. Gleick (editor), 1993, Water in Crisis: A Guide to the World's Fresh Water Resources)

Although it is a small fraction, not all fresh waters are available to be utilized because, as shown in Figure 1.1, most of the fresh waters, i.e., 68.7%, are stored in the form of ice caps and glaciers, and it is difficult to be recovered and used for our diverse needs [1,7]. While groundwater, the renewable water resource, is the second largest portion of fresh water (30.1%) (Figure 1.1) [6,7]. The smallest part of fresh water, e.g., 1.2%, is concentrated in rivers, lakes, and reservoirs (Figure 1.1) [6]. Man has extensively utilized groundwater, surface water, and rainwater, as accessible and available sources of fresh water, for household, recreational, agricultural, and industrial purposes [8,9]. However,

most countries nowadays, especially in arid and semi-arid regions, suffer from a severe shortage of fresh water due to many causes, for instance, climate change, population increase, unwise water consumption, and water pollution [10,11]. The World Health Organization (WHO) recently reported that more than 50% of the world's population will live in water-stressed areas by 2025 [12].

1.2. Water Pollution

1.2.1. Definition

Water pollution occurs when the quality and composition of water are changed by introducing foreign and hazardous substances, making it no longer suitable for any application [13]. Water pollution is a global threat as it intensifies the scarcity of fresh water and spreads many acute waterborne diseases, such as dysentery, giardiasis, typhoid, hepatitis, cholera, diarrhea, cryptosporidiosis, and so forth [14]. According to WHO, 80% of the diseases are transmitted by water, and more than 2 billion people use drinking water sources contaminated with feces [9]. Furthermore, it is reported that more than 14000 are dying daily because of various waterborne diseases [15]. In addition, The Joint Monitoring Programme (JMP) report declared that at least 2.1 billion people are lake of safe drinking water in their homes [16].

1.2.2. Types of water pollutants

A water pollutant is any chemical, physical, or biological matter that deteriorates water quality or causes detrimental impacts on the aquatic environment and those who consume the water [1,15]. Chemical water pollutants can be classified into two groups: macropollutants and micropollutants. Macropollutants are detected in water at mg L^{-1} concentrations, such as nitrate (NO_3^-) and phosphorous (P) [10,17]. On the other hand, micropollutants occur in water and exert lethal effects at very low concentrations (i.e., μg L^{-1} and ng L^{-1}) [10,18]. Some of the micropollutants are agrochemicals [e.g., pesticides, insecticides, herbicides, etc.], pharmaceuticals and personal care products (PPCPs) [e.g., antibiotics, hormones, antiepileptic drugs, β-blockers, blood lipid regulators, soaps, sunscreens, lotions, fragrances, and so on], endocrine disrupting chemicals (EDCs) [e.g., diethylstilbesterol (DES), mycotoxins, bisphenol A, phytoestrogens, estrone, etc.], perfluorinated compounds (PFCs), surfactants, plasticizers, flame retardants, dyes, synthetic fragrances, detergents, radioactive elements [e.g., cesium (Cs^+), strontium (Sr),

uranium (U), and so on.], heavy metals [e.g., Arsenic (As), chromium (Cr), mercury (Hg), lead (Pb), etc.] and so forth [10,19–21]. Physical pollutants include plastics, suspended sediments, floating debris, heat, radiation, etc. [1,22,23]. Whereas biological pollutants include protozoans, pathogens, viruses, worms, and so on [1,23].

1.2.3. Sources of water pollution

Anthropogenic activities such as sewage and wastewater, industrial activities, agricultural practices, nuclear energy and weapons, mining, oil spills, and so on, are the main causes of water pollution [23,24]. There are two different sources for water pollution: point source pollution and non-point source pollution [15]. Point source pollution can be easily handled as the source of pollution is known, such as sewer pipes, septic tanks, wastewater treatment plants, industrial drainage pipes, etc. [25]. In contrast, non-point source pollution is more challenging to be tackled as the source of pollution is unknown, or the pollutants invade the water from multiple points [15,26]. Agriculture is a good example of non-point source pollution where agrochemicals can easily infiltrate groundwater or any adjacent water body from infinite locations [27].

1.3. Pharmaceuticals and personal care products (PPCPs)

Pharmaceuticals and personal care products (PPCPs) are groups of organic compounds with distinctive chemical and physical characteristics that are originated to protect human lives, improve the daily life of individuals, and help farmers to maintain and enhance their agricultural production [28]. Pharmaceuticals are categorized into many classes in accordance with their applications such as antibiotics, hormones, antihypertensives, lipid regulators, antidepressants, anticonvulsants, and anti-inflammatory drugs [29]. While personal care products can be classified into various groups namely: preservatives, fragrances, disinfectants, toothpastes, and sunscreens [30].

1.3.1. Antibiotics

Antibiotics are organic chemicals designed to target harmful bacteria without negatively affecting the cells and tissues of the host (e.g., humans, animals, fish, etc.) [31]. Numerous types of antibiotics were developed, after the discovery of penicillin by Fleming in 1929, to prevent and treat several bacterial infections among humans, animals, and plants [32,33]. Antibiotics can be classified according to their route of administration, chemical structure, action mechanism, and action spectrum [34]. However, they are commonly

categorized based on their action mechanism into various classes: aminoglycosides, fluoroquinolones, macrolides, β-lactams, glycopeptides, rifamycin, monobactams, chloramphenicol, carbapenems, lincomycin, sulfonamides, polypeptides, polyenes, tetracyclines, and so forth. [34,35]. Some of these antibiotics are naturally produced in the environment, such as tetracyclines and chloramphenicol, whereas some of them are chemically synthesized, such as sulfonamides and fluoroquinolones [36–38].

1.3.2. The fluoroquinolone antibiotic ciprofloxacin

Fluoroquinolone antibiotics are synthetic chemotherapeutic agents specifically designed to halt the growth of harmful bacteria via inhibiting the main bacterial enzymes such as topoisomerase IV and DNA gyrase [39,40]. Ciprofloxacin (CIP) is a second-generation fluoroquinolone antibiotic. It is extensively prescribed in both human and veterinary medicine to prevent the propagation of most gram-negative bacterial infections and some gram-positive bacterial infections [41–44]. CIP is approved by US Food and Drug Administration (FDA) to treat various bacterial infections such as pneumonia, typhoid fever, prostatitis, anthrax, salmonellosis, urinary tract infections, joint, bone, skin, gastrointestinal infections, lower respiratory tract infections, as well as sexually transmitted infections (i.e., chancroid and gonorrhea) [45,46].

1.3.3. Occurrence and possible routes for ciprofloxacin to enter the environment

Figure 1.2 summarizes the possible pathways for CIP to enter the environment. Effluents of domestic wastewater treatment plants (WWTPs) are the main anthropogenic source for CIP to enter many aquatic environments [47,48]. After being administrated, CIP is partially metabolized in the human body, while the rest of CIP will be excreted, as parent compounds, with its metabolites through feces and urine to the sewer networks and eventually reach WWTPs [49]. Throughout the treatment stages in WWTPs, 80-90% of CIP will be removed via adsorption on the sludge [41,50]. However, the complete elimination of CIP by WWTPs is complex and challenging because CIP is stable and highly resistant to degradation [42]. Consequently, residues of CIP and its metabolites will be discharged with the treated effluents to the nearby water bodies, for instance, rivers, lakes, bonds, sea, ocean, and so on [46,51]. Also, if the treated effluents and the sludge of WWTPs are used in agriculture, wide agricultural lands, groundwater, and adjacent water bodies will be heavily polluted by CIP [52,53]. Usually, the detected concentrations of CIP in the effluents of WWTPs, groundwater, or surface water range

from ng L^{-1} to µg L^{-1} [54]. In contrast, according to the statistics presented by the worldwide health communities, the level of CIP pollution in hospital and pharmaceutical wastewater is much higher than that in municipal wastewater, reaching around 150 µg/L and 50 mg/L released from hospital and pharmaceutical factories, respectively [55,56]. Moreover, CIP and other pharmaceuticals might leak from poorly designed pharmaceutical landfill sites to pollute the surrounding soil and groundwater [44,57,58]. Furthermore, when it is used as food additives in food-producing animals, unmetabolized CIP will be discharged with feces and urine to pollute the soil of livestock and poultry farms [58]. If these animal manures are used as fertilizers, the agricultural land and the underground water will be polluted by CIP [51,59].

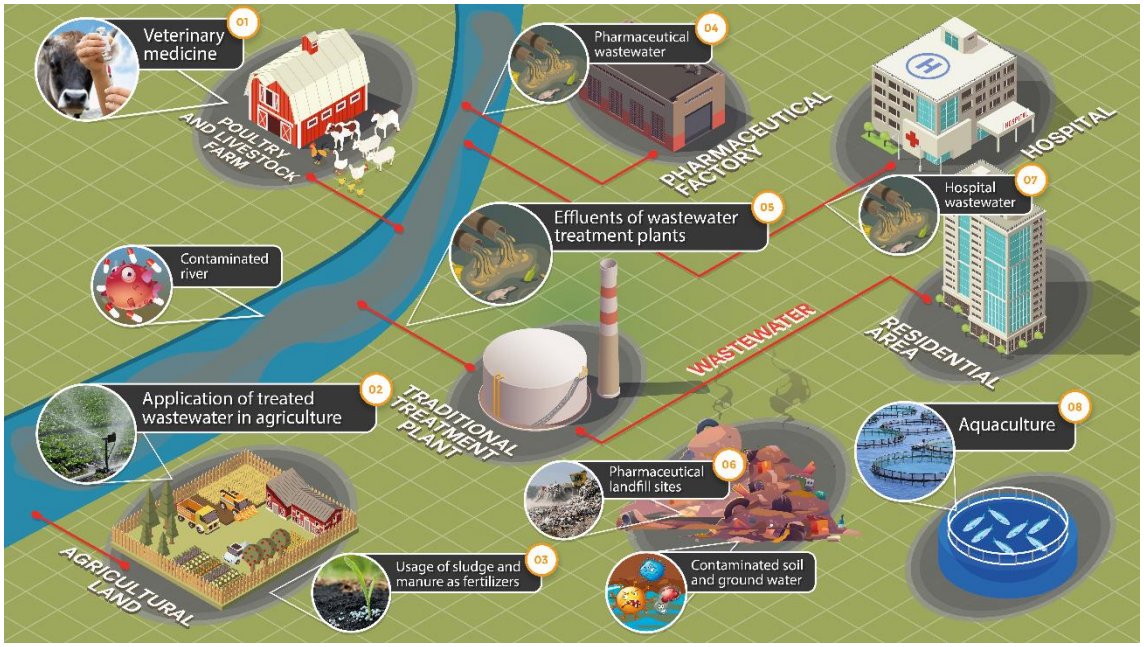

Figure 1.2 Possible pathways for ciprofloxacin to enter the environment.

Moreover, CIP is still extensively used in aquaculture, where the water of pools will be enormously loaded with huge amounts of unconsumed CIP [60]. These waters will be responsible for the pollution of water resources by CIP if they are not adequately treated before being discharged into the environment [61,62].

1.3.4. Heath threats and ecotoxicity of ciprofloxacin

CIP consumption in medicine is essential to protect humans, animals, and plants from bacterial infections. However, the frequent occurrence of CIP in water induces the growth of antimicrobial resistance genes (ARGs) as well as antimicrobial resistance bacteria (ARB) [63,64]. These genes and bacteria are evolved enough to tolerate most developed antibiotics and can cause incurable infections [65]. The global fatalities of ARGs and

ARBs are currently more than 700,000 people annually [66]. This figure is expected to dramatically increase to 10 million by 2050 if no urgent and serious actions are being made to decrease the concentrations of CIP and other antibiotics in the limited water resources [66]. Furthermore, The Centers for Disease Control and Prevention predicted that more than 2 million people in the United States of America (USA) would be infected by ARGs and ARBs every year, and at least 23,000 of them are expected to die annually because of antimicrobial infections [67]. The widespread and persistent pollution of water resources by CIP is a worldwide health and ecological threat, and it is considered by many international organizations, for example, the Global Water Research Coalition (GWRC), as one of the top priority contaminants among pharmaceuticals [33,68].

1.3.5. State-of-the-art treatment technologies for ciprofloxacin pollution

Several treatment technologies were developed over the years to efficiently remove CIP from aqueous solutions under different circumstances and conditions [69,70]. Some of these techniques are adsorption by various adsorbents [e.g., activated carbon (AC), biochar, clay minerals, multiwall carbon nanotubes (MWCNT), graphene oxides, metal-organic frameworks (MOFs), etc.] [71], bioremediation [44,72–74], ozonation [75,76], chlorination [54,77], advanced oxidation processes (AOPs) [78–80], photodegradation [81,82], electrocoagulation [56,83], membrane technology (e.g., reverse osmosis (RO) [84], ultrafiltration [85], and nanofiltration [86]), ionic exchange [87], and so forth.

Some of these methods have many disadvantages when it comes to the removal of CIP from aquatic environments. For instance, chlorination generates highly toxic byproducts during the treatment process, requiring further treatment steps for these compounds [88]. Also, one of the drawbacks of ozonation is the production of very toxic byproducts during the treatment process, in addition to the high cost and energy of producing the highly poisonous ozone [88]. Biodegradation is not efficient and time-consuming technology to remove CIP because CIP is recalcitrant to biodegradation. Pan *et al.* demonstrated that less than 57% of CIP was degraded by *Thermus sp. Strain* (C419), a thermophilic bacterium isolated from sludge, after five days of incubation at a temperature of 70 °C and initial pH of 6.5 with the addition of sodium acetate [74]. Moreover, biodegradation is not a favorable option when the background concentration of organic matter is high compared to the concentration of CIP where the microorganisms prefer to consume the available organic matter rather than CIP [89]. Membrane technologies have many

downsides, such as being very expensive, especially in a large-scale application, high energy consumption, fouling, clogging, and demand for remineralization of the treated water [71,88].

1.4. Zerovalent iron nanoparticles (Fe^0)

1.4.1. Background

Nanotechnology is the science of producing materials in a nanometer scale with particle sizes ranging from 1 to 100 nm. In the early 20th century, Richard Zsigmondy was the first to observe nanomaterials by employing an ultramicroscope [90]. In addition, he was the first to describe the particle size with the term 'nanometer'. Nanotechnology is a promising approach that is getting the attention of many researchers in the field of water and wastewater technologies because it has the potential to overcome the limitations of traditional treatment technologies and can meet the strict water regulations. It provides an efficient, cost-effective, and environmentally friendly solution to treat different wastewater streams such as domestic, agriculture, industrial, hospital, and radioactive wastewaters. Zerovalent iron nanoparticles (Fe^0) are well-known and excellent remedial nanomaterials for a broad spectrum of organic and inorganic contaminants and pollutants in water, such as nutrients, radionuclides, heavy metals, pharmaceuticals, and personal care products (PPCPs), agrochemicals, chlorinates solvents, halogenated organic compounds (HOCs), etc. [91–93]. It is distinguished by its core-shell structure, remarkable adsorption capacity, high surface area and surface reactivity, and strong redox potential (Figure 1.3) [94,95].

1.4.2. Removal mechanisms of organic pollutants by Fe^0 nanoparticles

Fe^0 nanoparticles can remove organic pollutants, like CIP, through two different mechanisms: adsorption and oxidation [91]. Adsorption happens on the surface of Fe^0 nanoparticles. In contrast, oxidation occurs by reactive oxygen species (ROS), which are produced during the corrosion of Fe^0 nanoparticles in aqueous solutions.

Several reactions will happen when Fe^0 nanoparticles get in contact with water and/or oxygen. These reactions are highly pH-dependent, and they can be summarized as follows [69,96,97]:

$$Fe^{0}_{(s)} + O_2 \rightarrow H_2O_2 + Fe^{2+} \quad (1.1)$$

$$Fe^{0}_{(s)} + H_2O_2 \rightarrow Fe^{2+} + H_2O \quad (1.2)$$

$$Fe^{2+} + O_2 \rightarrow Fe^{3+} + O_2^{\cdot -} \quad (1.3)$$

$$Fe^{2+} + O_2^{\cdot -} \rightarrow H_2O_2 + Fe^{3+} \quad (1.4)$$

$$Fe^{2+} + H_2O_2 \rightarrow OH^{\cdot} \; and/or \; Fe(IV) \quad (1.5)$$

$$Fe^{3+} \rightarrow Fe^{3+}_{(s)} \quad (1.6)$$

Fe^0 nanoparticles will react with oxygen to release ferrous ions (Fe^{2+}) and formulate hydrogen peroxide (H_2O_2) [Equation (1.1)]. If the circumstances of the aqueous solution are ideal, Fe^{2+} ions will be oxidized by oxygen to ferric ions (Fe^{3+}) and generate extra H_2O_2 [Equations (1.3) and (1.4)]. Finally, the produced Fe^{2+} ions and H_2O_2 will react with each other to produce reactive oxygen species (ROS), for instance, hydroxyl radicals ($OH^{\bullet}$) or/and ferryl ions (Fe[IV]) [Equation (1.5)]. This reaction is called the Fenton reaction, and the generated ROS will be responsible for the degradation of organic pollutants in water.

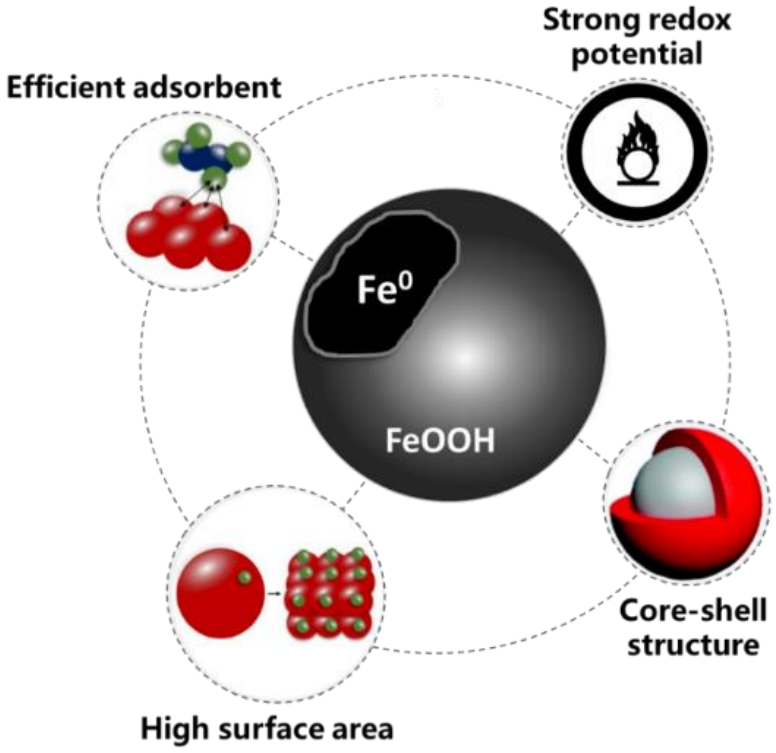

Figure 1.3 Features of zerovalent iron nanoparticles in the removal of pollutants from water.

1.4.3. Defects and improvement techniques of iron nanoparticles

Despite the superb characteristics of Fe^0 nanoparticles, several pitfalls limit, hinder or impair the decontamination competence of Fe^0 nanoparticles in environmental applications (Figure 1.4). Out of these defects, particle agglomeration, fast surface oxidation and passivation, low oxidants yield [Equation (1.5)], and poor transportability in porous mediums [98,99]. Various improvement and modification techniques were employed to overcome these weaknesses and improve the reactivity of Fe^0 nanoparticles, such as **(I)** noble metal deposition on the surface of Fe^0 nanoparticles (e.g., Cu, Ni, Ag, Au, and Pd) [100–102], **(II)** immobilization and deposition of Fe^0 nanoparticles on various supporting materials; for example, activated carbon, biochar, graphene oxide, carbon nanotubes, etc. [103–105], **(III)** stabilization of Fe^0 nanoparticles with different types of polymers and surfactants [i.e., polyacrylamide (PAM), polyvinylpyrrolidone (PVP), starch, carboxymethyl cellulose (CMC), guar gum, etc.] [106–108], **(IV)** encapsulation of Fe^0 nanoparticles with a shell layer of different materials, for example, bismuth, magnesium hydroxide, sulfide, and so on [63,109,110], and **(V)** addition of oxidants such as hydrogen peroxide (H_2O_2), peroxymonosulfate, persulfate ($S_2O_8^{2-}$), etc. [111–113].

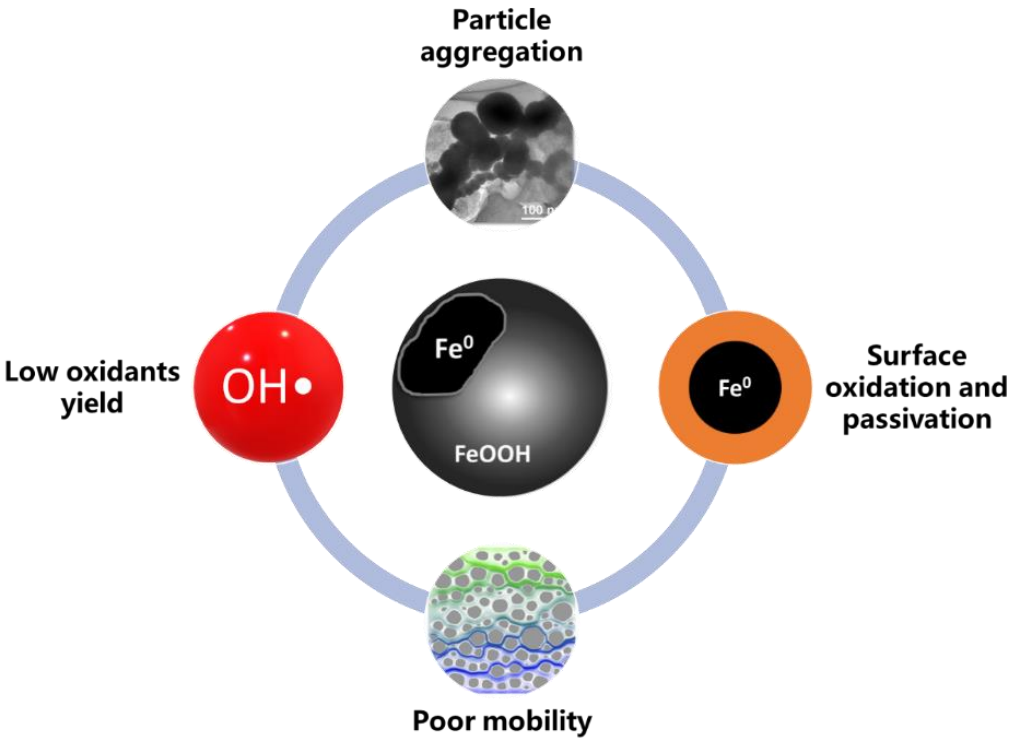

Figure 1.4 Defects of zerovalent iron nanoparticles in environmental applications.

1.4.4. Previous application of iron-based nanomaterials for ciprofloxacin removal

Several iron-based nanomaterials and nanocomposites were previously used for eliminating CIP from aqueous solutions [69]. Table 1.1 epitomizes the latest application of different iron-based nanomaterials in remediating CIP from aquatic mediums under various conditions such as CIP initial concentration (mg L^{-1}), nanomaterial dosage (g L^{-1}), initial pH of the solution, oxidant concentration (mM), and contact time (min). Each iron-based nanomaterial or treatment system was compared based on the final removal efficiency under the optimized treatment parameters.

Table 1.1 Previous application of iron-based nanomaterials for CIP removal from polluted waters.

Nanomaterial	Treatment conditions						Ref.
	[CIP] (mg L^{-1})	Nanomaterial dosage (g L^{-1})	Initial pH	Oxidant con. (mM)	Contact time (min)	Removal efficiency (%)	
Microscale zero-valent iron (ZVI)	21.54	2.5	6.5	-	120	85%	[114]
Persulfate activation by microscale zerovalent iron (PS/ZVI)	9.94	0.126	3	2.25	60	84.5%	[115]
Wheat straw-supported Fe^0 nanoparticles (WS-Fe^0)	50	1	6	-	240	97%	[116]
Fe^0 nanoparticles encapsulated in carbon dots	-	-	-	-	-	51%	[117]
Hydrogen peroxide activation by Fe^0 nanoparticles (H_2O_2/Fe^0)	10	0.16754	7	100	50	100%	[79]
Hydrogen peroxide activation by biochar-supported Fe^0 nanoparticles (H_2O_2/BC-Fe^0)	100	0.4	3~4	20	60	70%	[119]

Table 1.1 Previous application of iron-based nanomaterials for CIP removal from polluted waters (cont.).

Nanomaterial	Treatment conditions						Ref.
	[CIP] (mg L^{-1})	Nanomaterial dosage (g L^{-1})	Initial pH	Oxidant con. (mM)	Contact time (min)	Removal efficiency (%)	
Persulfate activation by sulfide-coated Fe^0 nanoparticles supported by biochar (PS/S-Fe^0/BC)	50	0.4	5	1	60	89.78%	[120]
Persulfate activation by granular adsorbent-supported Fe/Ni nanoparticle (PS/Ni@PGA)	100	0.1	3	10	720	93.24%	[121]
(1) Ultrasonic enhanced hydrogen peroxide activation by Fe^0 nanoparticles (H_2O_2/Fe^0/aeration/US)	100	0.117	7	3	60	94%	[122]
Ultrasonic enhanced persulfate activation by Fe^0 nanoparticles (US/PS/Fe^0)	50	0.12	4.5	6.25	60	57%	[123]
(2) Hydrogen peroxide activation by Fe^0 nanoparticles with aeration and weak magnetic field (Fe^0/H_2O_2/aeration/WMF)	100	0.6	7	-	10	97%	[124]
(3)Polyvinylpyrrolidone stabilized Fe^0/Cu bimetallic particles (PVP-Fe^0/Cu)	100	0.5	6	-	120	98.4%	[106]

Table 1.1 Previous application of iron-based nanomaterials for CIP removal from polluted waters (cont.).

Nanomaterial	Treatment conditions						Ref.
	[CIP] (mg L^{-1})	Nanomaterial dosage (g L^{-1})	Initial pH	Oxidant con. (mM)	Contact time (min)	Removal efficiency (%)	
[4] Green synthesized bimetallic nanoparticles (GT-Fe^0/Cu)	9.94	0.5	6	-	90	100%	[125]

[1] Aeration flow rate = 1.61 L min^{-1}
[2] Weak magnetic field intensity = 40 mT
[3] Weak magnetic field intensity = 2 mT and Fe^0/Cu = 1:0.04
[4] Weak magnetic field intensity = 5 mT and GT-Fe^0/Cu = 1/0.08

de Lima Perini *et al.* were the first to use the microscale zerovalent iron particles (ZVI) to remove CIP from water [114]. They demonstrated that 85% of 21.58 mg L^{-1} of CIP was removed by 2.5 g L^{-1} of ZVI after 120 min. The unsatisfied performance of ZVI in the previous study encouraged Hoa *et al.* to enhance the competence of ZVI towards the elimination of CIP by adding persulfate (PS) as a strong oxidant [Equations (1.7)-(1.9)] [115]. Their outcomes illustrated that 84.5% of 9.96 mg L^{-1} of CIP was removed within 60 min by only 0.126 g L^{-1} of ZVI after adding 2.25 mM of PS. The efficacy of (PS/ZVI) is clearly better than the bare ZVI as the required mass of ZVI to treat CIP-polluted water was significantly reduced from 2500 mg L^{-1} to 126 mg L^{-1}. This improvement is attributed to the massive production of the reactive oxygen species [e.g., sulfate ($SO_4^{\bullet-}$) and hydroxyl radicals ($OH^{\bullet}$)] in the aqueous medium after the successful activation of PS by ZVI as shown in the following equations:

$$Fe^0 + 2H^+ \rightarrow Fe^{2+} + H_2 \quad \textbf{(1.7)}$$

$$Fe^{2+} + S_2O_8^{2-} \rightarrow Fe^{3+} + SO_4^{\bullet-} + SO_4^{2-} \quad \textbf{(1.8)}$$

$$SO_4^{\bullet-} + H_2O \rightarrow SO_4^{2-} + OH^{\bullet} + H^+ \quad \textbf{(1.9)}$$

In water and wastewater remediation, zerovalent iron nanoparticles (Fe^0) are more reactive and efficient than the micro-sized iron particles (ZVI). Shao *et al.* supported the bare Fe^0 nanoparticles with wheat straw (WS-Fe^0) to overcome the agglomeration of Fe^0 nanoparticles and promote the removal of CIP from polluted water [116]. They found that

approximately 85% of 50 mg L^{-1} of CIP was eliminated by 1 g L^{-1} of Fe^0 nanoparticles. On the other hand, the efficiency of Fe^0 nanoparticles improved from 85% to around 97% after supporting Fe^0 nanoparticles by wheat straw (WS-Fe^0). The presence of wheat straw during the formation of Fe^0 nanoparticles allowed them to be fully distributed on the surface of the wheat straw, which helped in decreasing the degree of agglomeration and enhanced the competence of Fe^0 nanoparticles in removing CIP over a wide range of pH (i.e., 4–10). Pirsaheb *et al.* tried to utilize carbon dots as supporting material for Fe^0 nanoparticles [117]. However, the modification process couldn't enhance the reactivity of Fe^0 nanoparticles as less than 51% of CIP was removed by Fe^0 nanoparticles encapsulated in carbon dots.

Table 1.1 shows that many researchers chose to improve the reactivity of Fe^0 nanoparticles in treating CIP-polluted water by adding strong oxidants to promote the generation of reactive oxygen species (ROS) and effectively oxidize and decontaminate CIP from aqueous solutions. For example, Mondal *et al.* added 100 mM of hydrogen peroxide (H_2O_2) to 167.54 mg/L of Fe^0 nanoparticle and accomplished 100% removal efficiency of 10 mg L^{-1} of CIP at pH ranges between 6.2-7.3 [79]. As previously explained in section 1.4.2, the corrosion of Fe^0 nanoparticles in water produces H_2O_2 [Equation (1.2)]. However, the concentration of the produced H_2O_2 is insufficient to generate enough reactive oxygen species (ROS) to degrade and oxidize organic pollutants in water. Thus, the addition of a sufficient amount of H_2O_2 (e.g., 100 mM) to Fe^0 nanoparticles in aqueous mediums will generate vast amounts of strong hydroxyl radicals ($OH^{\bullet}$) according to the following reactions [118]:

$$\boldsymbol{Fe^0 + H_2O_2 \rightarrow Fe^{2+} + 2OH^-} \quad \textbf{(1.10)}$$

$$\boldsymbol{Fe^{2+} + H_2O_2 \rightarrow Fe^{3+} + OH^{\bullet}} \quad \textbf{(1.11)}$$

These radicals are strong enough to degrade and decontaminate CIP in polluted waters. This explains the remarkable performance of H_2O_2/Fe^0 in removing CIP from water. Mao *et al.* employed two modification techniques to boost the efficiency of Fe^0 nanoparticles, namely, support of Fe^0 nanoparticles with biochar (BC-Fe^0) and add the strong oxidant hydrogen peroxide (H_2O_2) [119]. Despite using various modification techniques, less than 70% of 100 mg L^{-1} of CIP was removed after the activation of 20 mM of H_2O_2 by 0.4 g L^{-1} of (BC-Fe^0) nanocomposite under acidic pH (i.e., 3~4). Also, Gao *et al.* prepared sulfide-coated iron nanoparticles supported by biochar (PS/S-Fe^0/BC) to activate PS and

oxidize CIP in water [120]. Like Mao *et al.*, the complicated treatment system of Gao *et al.* failed to completely eliminate 50 mg L^{-1} of CIP with a removal efficiency of less than 89.78%. Liu *et al.* explored the possibility of activating persulfate by stabilized bimetallic Fe/Ni@PGA to produce strong oxidants, for example, sulfate radicals ($SO_4^{\bullet-}$) and efficiently degrade CIP in aquatic environments [121]. Fe/Ni@PGA succeeded in activating persulfate under acidic solution (pH = 3) and degraded around 93.24% of 100 mg L^{-1} of CIP. Conversely, as most of the advanced oxidation processes (AOPs), Fe/Ni@PGA failed to activate persulfate at neutral pH (pH = 5-7), and approximately 40% and 20 % of 100 mg L^{-1} of CIP were eliminated at an initial pH of 5 and 7, respectively. Pirsaheb *et al.* [122] and Rahmani *et al.* [123] combined Fe^0 nanoparticles with ultrasonication (US) and the addition of hydrogen peroxide and persulfate, respectively, to efficiently remediate CIP-polluted waters. The suggested treatment system by Pirsaheb *et al.* [e.g., (H_2O_2/Fe^0/aeration/US)] treated 94% of 100 mg L^{-1} of CIP [122]. Whilst the advanced oxidation process proposed by Rahmani *et al.* [e.g., (US/PS/Fe^0)] barely removed 57% of 50 mg L^{-1} of CIP [123]. On another occasion, Pirsaheb *et al.* proposed another advanced oxidation process to remediate CIP from aquatic mediums based on the activation of hydrogen peroxide by Fe^0 nanoparticles with the aid of aeration and weak magnetic field (Fe^0/H_2O_2/aeration/MF) [124]. 97% of 100 mg L^{-1} of CIP was promptly eliminated within 10 min by activating hydrogen peroxide by 600 mg L^{-1} of Fe^0 nanoparticles at neutral pH (i.e., pH = 7) under the influence of 40 mT of weak magnetic field (WMF). Th presence of WMF improved the efficacy of the treatment system via several methods [124]. During the treatment process, the WMF will increase the dissolution of iron to ferrous ions (Fe^{2+}) [Equation (1.1)] and hydrogen peroxide, which will allow more radicals to be produced in the system [Equation (1.5)]. In addition, the WMF improves oxygen solubility and promotes the release of electrons in the system. These electrons will be available to directly react with water and oxygen and produce more radicals in water. Moreover, the utilization of WMF throughout the treatment process extend the lifespan of the generated radicals in the system.

Chen *et al.* adopted another approach to modify Fe^0 nanoparticles by stabilizing Fe^0/Cu bimetallic nanoparticles using the soluble polymer polyvinylpyrrolidone (PVP) [106]. The competence of polyvinylpyrrolidone stabilized Fe^0/Cu bimetallic particles (PVP-Fe^0/Cu) was further reinforced by the presence of WMF. PVP-Fe^0/Cu nanoparticles remediated 98.4% of 100 mg L^{-1} of CIP within 120 min under the effect of a magnetic

flux density of 2 mT. In another research article, Chen *et al.* utilized the extracts of green tea instead of sodium borohydride as a green reducing agent to synthesize bimetallic GT-Fe^0/Cu nanoparticles [125]. The green-synthesized bimetallic nanoparticles (GT-Fe^0/Cu) exhibited a better performance in treating CIP-polluted waters (Removal efficiency = 80%) than the traditionally synthesized bimetallic nanoparticles (Fe^0/Cu) (Removal efficiency = 55%). It is important to mention that Chen *et al.* also applied GT-Fe^0/Cu under the influence of a weak magnetic field with a flux density of 5 mT to promote the complete removal of CIP from polluted water.

1.4.5. The adopted modification technologies for Fe^0 nanoparticles in this study

The previous articles in the literature have confirmed that bare Fe^0 nanoparticles can't effectively eliminate CIP from polluted water due to the complexity of CIP, in addition, to the recalcitrance of CIP to degradation. Thus, it can be observed from Table 1.1 that all the previous researchers modified Fe^0 nanoparticles with one or more of the improvement techniques to develop effective iron-based nanomaterials or iron-based treatment systems for CIP pollution. Table 1.1 demonstrates that some of the developed iron-based nanomaterials didn't accomplish the complete removal of CIP from polluted water despite using single or multiple enhancement methods, for example, ZVI [114], PS/ZVI [115], Fe^0 nanoparticles encapsulated in carbon dots [117], H_2O_2/BC-Fe^0 [119], PS/S-Fe^0/BC [120], and US/PS/Fe^0 [123]. Another group of the proposed iron-based treatment systems succeeded in remediating CIP-polluted water, with removal efficiencies of more than 90%, by adding highly toxic oxidants such as hydrogen peroxide [79,124] and persulfate [121]. The employment of such systems in water and wastewater treatment applications is unfavorable because these systems could only operate under strongly acidic conditions (pH < 3). Furthermore, the residues of the utilized oxidants after the treatment process will cause secondary pollution, which may require further treatment steps before final discharge to the environment. It is worth noting that Chen *et al.*, in both studies [106,125], improved the oxidative capacity of polyvinylpyrrolidone stabilized Fe^0/Cu bimetallic particles (PVP-Fe^0/Cu) and green synthesized bimetallic nanoparticles (GT-Fe^0/Cu) via using weak magnetic fields instead of using toxic oxidants. However, the application of weak magnetic field increases the required energy for the treatment process, and consequently increases the overall treatment cost. Moreover, the utilization of magnetic field in open water bodies such as river, lake, bond, etc., is challenging, impractical, or in some situations impossible. Also, the use of copper as a

doping metal in PVP-Fe^0/Cu and GT-Fe^0/Cu nanoparticles could cause a secondary pollution when these nanomaterials are applied in huge quantities in real contaminated sites.

In the light of the previous research articles, more efficient, feasible, simple, environmentally friendly, cost-effective, and energy-saving techniques to enhance the reactivity of Fe^0 nanoparticles and efficiently treat CIP-polluted waters in real contaminated sites are needed. Hence, this study adopts more environmentally friendly approaches to improve the competence and reactivity of Fe^0 nanoparticles in remediating CIP-polluted waters, namely coating Fe^0 nanoparticles with magnesium hydroxide shell and addition of the organic ligand oxalate to Fe^0 nanoparticles.

1.4.5.1. Coating Fe^0 nanoparticles with magnesium hydroxide shell

Magnesium hydroxide [Mg $(OH)_2$] is a non-poisonous and environmentally friendly substance used in many industrial fields such as the manufacture of flam-retardant, food processing, heritage preservation, paper production, and so forth [126]. Furthermore, it is widely utilized to remove various types of pollutants from drinking water, surface water, groundwater, and wastewater [127–130]. During the past years, more than 48,000 tons of $Mg(OH)_2$ have been used annually in wastewater treatment applications [131]. $Mg(OH)_2$ has several unique characteristics, for instance, nontoxicity, non-magnetization, cost-effectiveness, high surface area, high stability, low solubility index, and so on. These features make $Mg(OH)_2$ an excellent coating material for Fe^0 nanoparticles [132]. Recently, Maamoun *et al.* demonstrated that coating Fe^0 nanoparticles with a shell of $Mg(OH)_2$ remarkably improved the physiochemical properties of Fe^0 nanoparticles, such as reactivity, dispersity, and mobility [109]. Also, Chen *et al.* illustrated that the aggregation and oxidation of Fe^0 nanoparticles were minimized by coating Fe^0 nanoparticles with $Mg(OH)_2$ layer [129].

$Mg(OH)_2$-coating iron nanoparticles (Mg/Fe^0) were applied to remove a limited number of pollutants, for example, chromium [133], lead(II) [134], and uranium(VI) [129]. However, the removal of organic pollutants from water, particularly CIP, by Mg/Fe^0 nanoparticles has not been reported yet. Therefore, this study is the first in the literature that examines the competence of Mg/Fe^0 nanoparticles in treating CIP-polluted water.

1.4.5.2. Addition of the organic ligand oxalate

The production of ROS by Fe^0 nanoparticles is faint and inadequate to target complex organic pollutants like CIP, as only less than 7% of the applied Fe^0 nanoparticles can be converted to ROS [135]. The deficiency of the oxidative capacity of Fe^0 nanoparticles may result from various factors as follows [97]:

1. The high surface energy of Fe^0 nanoparticles favors the formulation of water via a four-electron transfer reaction [Equation (1.2)] rather than the generation of H_2O_2 through a two-electron transfer reaction [Equation (1.1)] [136].
2. The activation rate of O_2 by Fe^{2+} [Equations (1.3) and (1.4)] under acidic pH is negligible and weak at pH below 5, which reduces the production of H_2O_2 and superoxide radicals ($O_2^{\bullet-}$) in the aqueous solution [137].
3. The reaction of Fe^0 with H_2O will increase the pH of the aqueous medium and thus promote the precipitation of Fe^{3+} [Equation (1.6)] and formulation of a passivation layer of iron oxide and hydroxides on the surface of Fe^0 nanoparticles. This layer will preserve the core of Fe^0 nanoparticles from corrosion and restrain the interaction with pollutants in water [135].

It is also important to note that the corrosion of Fe^0 nanoparticles [Equation (1.1)] controls the kinetics of the subsequent reactions [Equations (1.2)-(1.5)]. In other words, besides the low generation of ROS, the oxidation of Fe^0 nanoparticles require acidification which limits the application of Fe^0 nanoparticles to treat organic pollutants in water [135].

The addition of oxidants to Fe^0 nanoparticles, such as hydrogen peroxide (H_2O_2) [138], persulfate ($S_2O_8^{2-}$) [120], peracetic acid [139], hypochlorous acid (HClO) [140], etc., was previously employed to enhance the production of ROS by Fe^0 nanoparticles. However, these chemicals are poisonous, unstable, corrosive, and explosive, which makes their application, transportation, and storage in contaminated locations challenging and dangerous [141,142]. Organic ligands or chelating compounds are considered more environmentally friendly alternatives to the toxic oxidants because they can improve ROS generation by Fe^0 nanoparticles and promote the oxidation of organic pollutants in water [137]. Oxalic acid (OA) is a low molecular weight organic acid (LMWOA). It is released to the soil by plants as one of the components of roots exudates to enhance the mobilization of nutrients, e.g., iron (Fe), phosphorous (P), zinc (Zn), cadmium (Cd), etc.

[143,144]. Several articles declared that adding the organic ligand oxalate ($C_2O_4^{2-}$), the salt form of oxalic acid, to Fe^0 nanoparticles significantly enhanced the oxidation of some organic compounds and improved the removal of certain heavy metals [135,137,145,146].

The detailed literature review revealed that most of the previous researchers investigated the enhanced oxidation of simple organic compounds by (Fe^0/oxalate) system, for example, phenol (C_6H_6O) [146], methanol (CH_3OH) [135], nitrobenzene ($C_6H_5NO_2$) [122], and 4-chlorophenol (C_6H_5ClO) [145]. On the contrary, the role and the enhancement mechanism of oxalate to promote the removal of antibiotics from aqueous solutions, particularly CIP, by Fe^0 nanoparticles haven't been reported yet.

1.5. Research aim and objectives

This study aims to develop and synthesize innovative iron-based nanomaterials for efficient and effective remediation of the micropollutant CIP from polluted waters.

The current study consists of two main research projects. The first project focuses on the remediation of CIP-polluted waters by Mg/Fe^0 nanoparticles. The objectives of the first project were as follows:

- Synthesis of Fe^0 and Mg/Fe^0 nanoparticles in the laboratory through a chemical reduction process.
- Characterization of Fe^0 and Mg/Fe^0 nanoparticles via several characterization instruments to reveal their physiochemical features and confirm the success of the coating protocol.
- Evaluate the performance of Mg/Fe^0 nanoparticles in treating CIP-polluted water under the influence of various parameters such as [$Mg(OH)_2$/Fe^0] mass ratio, the dosage of Mg/Fe^0 nanoparticles (g L^{-1}), initial pH of the polluted water, initial CIP concentration (mg L^{-1}), and treatment temperature (°C).
- Conduct desorption experiments to distinguish the contribution of adsorption and oxidation in removing CIP by Mg/Fe^0 nanoparticles.
- Perform kinetics, isotherm, and thermodynamic analysis for the experimental data to disclose the nature of the interaction between CIP and Mg/Fe^0 nanoparticles in aqueous solutions.

- Design a regeneration protocol for Mg/Fe^0 nanoparticles in order to be recycled for many treatment processes.
- Carry out longevity tests on Mg/Fe^0 nanoparticles to identify the proper conditions for their transportation and storage in contaminated sites.
- Propose, for the first time, a prototype treatment system based on Mg/Fe^0 nanoparticles to remediate continuous streams of CIP-polluted waters.

On the other hand, the second project concentrates on evaluating the competence of (Fe^0/oxalate) nanoparticles in eliminating CIP from polluted waters. Several objectives for the second project had been set as follows:

- Identify the physicochemical changes of Fe^0 nanoparticles before and after the reaction with oxalate in water.
- Determine the improvement mechanism of adding the organic ligand oxalate to Fe^0 nanoparticles towards the removal of CIP from polluted water.
- Carry out laboratory-scall experiments to systematically optimize the treatment parameters of CIP-polluted waters by (Fe^0/oxalate) nanoparticles, namely oxalate concentration (mM), Fe^0 nanoparticles dosage (g L^{-1}), the concentration of dissolved oxygen, initial pH of the aqueous medium, initial CIP concentration (mg L^{-1}), and reaction temperature (°C).
- Implement kinetics, isotherm, and thermodynamic analysis for the elimination of CIP from polluted water by (Fe^0/oxalate) nanoparticles.
- Examine the impact of natural organic matters (i.e., humic acid), ionic strength of polluted water, and coexisting ions (e.g., anions and cations) on the competence of (Fe^0/oxalate) nanoparticles in treating CIP-polluted water.
- Inspect the reusability of (Fe^0/oxalate) nanoparticles for many treatment cycles.
- Prepare cost analysis for the treatment of CIP-polluted water by (Fe^0/oxalate) nanoparticles.

1.6. Thesis Outline

The framework of the Ph.D. thesis consists of five main chapters as follows:

Chapter 1 provides background information about water pollution by antibiotics, particularly the recalcitrant ciprofloxacin. In addition, it discusses the occurrence and fate of ciprofloxacin in the environment and its health threats and ecotoxicity. Moreover,

chapter 1 covers the state-of-the-art treatment technologies for CIP pollution. Also, it includes an overview about zerovalent iron nanoparticles, their features and defects, their modification techniques, and their applications in CIP remediation from polluted waters. Finally, chapter 1 summarizes the aim and objectives of the Ph.D. research projects.

Chapter 2 summarizes the list of chemicals utilized in all experiments. Moreover, it describes the procedures to synthesize various kinds of iron-based nanomaterials in detail. Also, it explains the concepts of the characterization techniques employed to reveal the physicochemical properties of the iron-based nanomaterials. In addition, chapter 2 clarifies the specifications of each component of the prototype lab-scale treatment system. Furthermore, it epitomizes the experimental plan for the research work, the procedures for conducting the batch experiments, and the analytical instruments used in the laboratory. In addition, it clarifies the concept of kinetics, isotherm, and thermodynamic modeling for the adsorption of CIP by iron-based nanomaterials.

Chapter 3 covers the outcomes of remediating CIP-polluted water by Mg/Fe^0 nanoparticles. In detail, chapter 3 reveals the physicochemical properties of Mg/Fe^0 nanoparticles, such as external morphology, surface elemental composition, crystallinity, etc. It also discusses the effectiveness of Mg/Fe^0 nanoparticles in eliminating CIP from water under different treatment conditions, for example, Mg/Fe^0 dosage (g L^{-1}), initial pH of the polluted solution, reaction temperature (°C), and initial CIP concentration (mg L^{-1}). Moreover, the removal mechanism of CIP by Mg/Fe^0 nanoparticles was illustrated in this chapter. In addition, chapter 3 provides a regeneration and recycling protocol for Mg/Fe^0 nanoparticles. Moreover, chapter 3 demonstrates the adequacy of utilizing Mg/Fe^0 nanoparticles in a prototype treatment system to remediate large volumes of CIP-polluted water. Also, chapter 3 illustrates the appropriate storage option for Mg/Fe^0 nanoparticles for one month. Finally, chapter 3 includes an economic assessment of using Mg/Fe^0 nanoparticles for environmental and remediation applications.

Chapter 4 presents the results of removing CIP from aqueous solutions by (Fe^0/oxalate) nanoparticles. In detail, it elucidates physiochemical changes of Fe^0 nanoparticles before and after the reaction with different concentrations of oxalate in water. Also, it explains the impact of various parameters, for instance, oxalate concentration (mM), Fe^0 nanoparticle's dosage (g L^{-1}), initial pH of polluted water, reaction temperature (°C), and initial concentration of CIP in water (mg L^{-1}), on the competence of (Fe^0/oxalate) nanoparticles to clean up CIP-polluted solutions. Moreover, it discloses the enhancement mechanism of adding oxalate to Fe^0 nanoparticles toward

removing CIP from water. Furthermore, chapter 4 investigates the influence of water matrix, such as ionic strength, dissolved organic matters, and coexisting ions (e.g., cations and anions), on the remediation efficiency of (Fe^0/oxalate) nanoparticles. Similar to Mg/Fe^0 nanoparticles, chapter 4 suggests regeneration and recycling procedures for reusing (Fe^0/oxalate) nanoparticles for multiple treatment processes. Finally, chapter 4 provides a cost estimation for the treatment of CIP-polluted water by (Fe^0/oxalate) nanoparticles.

Finally, **Chapter 5** highlights each research project's significant findings and conclusions. In addition, it summarizes the recommendations for prospective researchers. Finally, chapter 5 includes possible research ideas for future work.

Chapter 2

Materials & Methods

2.1. Chemicals

Table 2.1 summarizes the specifications, supplying company, and applications of all used chemicals in this research. In addition, all chemicals were analytical of grade and directly utilized in the experiments with no prior treatment. Also, all chemical solutions were prepared using deionized water (18.2 Ω.cm @ 25 ℃, Direct-Q water purification system, Merck KGaA, Germany).

Table 2.1 List of utilized chemicals in the experiments.

Chemical Name	Specifications	Company	Application
Ciprofloxacin hydrochloride monohydrate	$C_{17}H_{18}FN_3O_3.HCl.H_2O$, MW = 367.81, purity > 98%.	Tokyo Chemical Industry CO., LTD, Japan	Preparation of CIP stock solution
Ferric chloride hexahydrate	$FeCl_3.6H_2O$, MW = 270.30, purity = 99.0%, CAS No.: 10025-77-1	JUNSEI, Japan	Fe^0 nanoparticles synthesis
Sodium borohydride	H_4BNa, MW = 37.83, purity ≥ 98%, CAS No.: 16940-66-2	Sigma Aldrich, USA	Fe^0 nanoparticles synthesis
Magnesium chloride hexahydrate	$MgCl_2.6H_2O$, MW = 203.30, purity = 97%, CAS No.: 7791-18-6	FUJIFILM Wako Pure Chemicals, Japan	Mg/Fe^0 synthesis and effect of coexisting cations
Sodium hydroxide	NaOH, MW = 40, purity = 97%, CAS No.: 1310-73-2	JUNSEI, Japan	Mg/Fe^0 synthesis and pH adjustment
Ethanol	C_2H_5OH, MW = 46.07, purity = 99.5%, CAS No.: 64-17-5	FUJIFILM Wako Pure Chemicals, Japan	Preparation of magnesium chloride and sodium hydroxide solutions
Hydrochloric acid	HCl, MW = 36.46, standard content = 35 ~ 37%.	FUJIFILM Wako Pure Chemicals, Japan	pH adjustment for zero point of charge [$pH_{(ZPC)}$] experiments

Table 2.1 List of utilized chemicals in the research projects (cont.).

Chemical Name	Specifications	Company	Application
Nitric acid	HNO_3, MW = 63.01, standard content = 69 ~ 70%, CAS No.: 7697-37-2	FUJIFILM Wako Pure Chemicals, Japan	pH adjustment for batch experiments
Sodium oxalate	$Na_2C_2O_4$, MW = 134, purity ≥ 99.5%, CAS RN: 62-76-0	FUJIFILM Wako Pure Chemicals, Japan	Removal of CIP in batch experiments
Potassium chloride	KCl, MW = 74.55, purity = 99.0%	FUJIFILM Wako Pure Chemicals, Japan	Measurement of $pH_{(ZPC)}$ and effect of coexisting cations
Calcium chloride dihydrate	$CaCl_2.2H_2O$, MW = 147.01, purity = 70.0~78.0%	JUNSEI, Japan	Effect of coexisting cations
Sodium nitrate	$NaNO_3$, MW = 84.99, purity = 99.0%	JUNSEI, Japan	Effect of coexisting anions
Sodium carbonate	Na_2CO_3, MW = 105.99, purity = 99.8%.	FUJIFILM Wako Pure Chemicals, Japan	Effect of coexisting anions
Sodium sulfate	Na_2SO_4, MW = 142.04, purity = 99.0%.	FUJIFILM Wako Pure Chemicals, Japan	Effect of coexisting anions
Sodium chloride	NaCl, MW = 58.44, purity = 99.5%.	FUJIFILM Wako Pure Chemicals, Japan	Effect of ionic strength
Humic acid	Not available	Sigma-Aldrich	Effect of natural organic matters
2-Propanol	$(CH_3)_2CHOH$, MW = 60.10, CAS No.: 67-63-0	FUJIFILM Wako Pure Chemicals, Japan	Radical inhibitor

2.2. Synthesis of zerovalent iron nanoparticles (Fe^0)

Fe^0 nanoparticles were synthesized in the laboratory using the chemical reduction technique [63,147,148]. The concept of this method is based on the chemical reduction of dissolved ferric ions (Fe^{3+}) to zerovalent iron (Fe^0) via potent reducing agents such as sodium borohydride ($NaBH_4$). Figure 2.1 shows a schematic diagram for the synthesis of Fe^0 nanoparticles in the laboratory. In detail, one gram of Fe^0 nanoparticles was produced as follows: 5 grams of ferric chloride hexahydrate ($FeCl_3.6H_2O$) were added to 200 ml of deoxygenated deionized water (DDIW) to prepare the ferric solution (Fe^{3+}). The term deoxygenated deionized water indicates that deionized water was purged by pure nitrogen gas (N_2) for 10 min until the oxygen level was lower than one ppm. This step was essential to protect the produced nanoparticles from oxidation. Subsequently, 2.2 grams of sodium borohydride ($NaBH_4$) was dissolved in 100 ml of DDIW to obtain the borohydride solution ($[BH_4]^-$). The two solutions were magnetically mixed for 15 min before the reduction process to ensure the complete dissolution of solid substances. Afterwards, as demonstrated in Figure 2.1, a four-neck flask was installed inside a water bath to control the reduction temperature at 30 °C. In addition, a mechanical mixer was mounted in the central neck of the flask to vigorously mix the solutions during the reduction process at a speed of 400 rpm. Under the continuous purging of pure nitrogen gas (N_2), the ferric solution was poured into the flask; then, the borohydride solution was drop wisely added to the ferric solution through a peristaltic pump (NRP-3000, Tokyo Rika Kikai Co., Ltd., Japan) at a flow rate of 20 ml min^{-1}. The brownish orange color of the ferric solution gradually disappeared and turned to black after introducing the borohydride solution because of the chemical reduction of ferric ions (Fe^{3+}) to zerovalent iron (Fe^0) as illustrated in equation (2.1) [109,149]:

$$\boldsymbol{2FeCl_3 \cdot 6H_2O + 6NaBH_4 + 18H_2O \rightarrow 2Fe^0 \downarrow + 21H_2 \uparrow + 6B(OH)_3 + 6NaCl} \qquad \textbf{(2.1)}$$

After adding the borohydride solution, the black mixture was stirred for 5 min as an aging time to guarantee the complete formation of zerovalent iron nanoparticles (Fe^0). After that, a vacuum filtration system (Φ47mm SPC glass filtration system, SIBATA Scientific Technology LTD., Japan) was used to collect the black precipitates under the nitrogen atmosphere (N_2) to prevent the passivation of Fe^0 nanoparticles. It is important to mention that, during the filtration process, the acquired black powder was washed with 300 mL of DDIW to remove any chemical residues. The freshly obtained Fe^0 nanoparticles were directly used in the batch experiments.

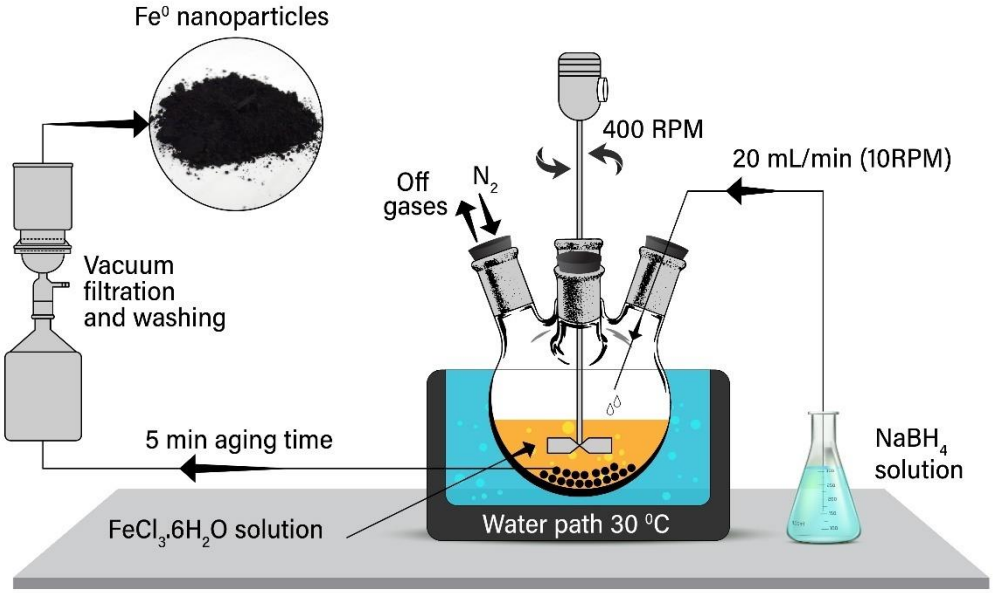

Figure 2.1. Schematic diagram for the synthesis of Fe^0 nanoparticles via the chemical reduction method.

2.3. Synthesis of $Mg(OH)_2$-encapsulated Fe^0 nanoparticles (Mg/Fe^0)

Fe^0 nanoparticles were encapsulated with a superfine layer of magnesium hydroxide (Mg/Fe^0) using the modified thermal precipitation method as manifested in **Error! Reference source not found.** [133,149]. Thoroughly, 0.5 g of Fe^0 nanoparticles were encapsulated with a magnesium hydroxide shell (Mg/Fe^0) as follows: 0.5 g of newly synthesized Fe^0 nanoparticles were mixed with 300 mL of ethanol under a continuous flow of pure nitrogen gas (N_2). Then, the admixture of (Fe^0/ethanol) was treated by ultrasonication (38 kHz, 100 W, ASU-10, AS ONE Corporation, Japan) for 30 min to make sure that Fe^0 nanoparticles were fully dispersed in ethanol before the beginning of the precipitation step. Moreover, the temperature of the ultrasonication bath was controlled at 50 °C to successfully coat Fe^0 nanoparticles with $Mg(OH)_2$ layer. Thereafter, to guarantee the constant molarity ratio between magnesium (Mg^{2+}) and hydroxide ions (OH^-) as displayed in equation (2.2) and to attain various mass ratios between $Mg(OH)_2$ and Fe^0, specific volumes of 2 g L^{-1} of (Mg^{2+}/ethanol) solution and 6 g L^{-1} of (NaOH/ethanol) solution were sequentially added to the mixture of (Fe^0/ethanol) by a peristaltic pump (SMP-23AS, AS ONE Corporation, Japan) at a flow rate of 2 ml min^{-1}.

$$Mg^{2+} + 2OH^- \rightarrow Mg(OH)_2 \downarrow \qquad (OH^-/Mg^{2+}: 2) \qquad \textbf{(2.2)}$$

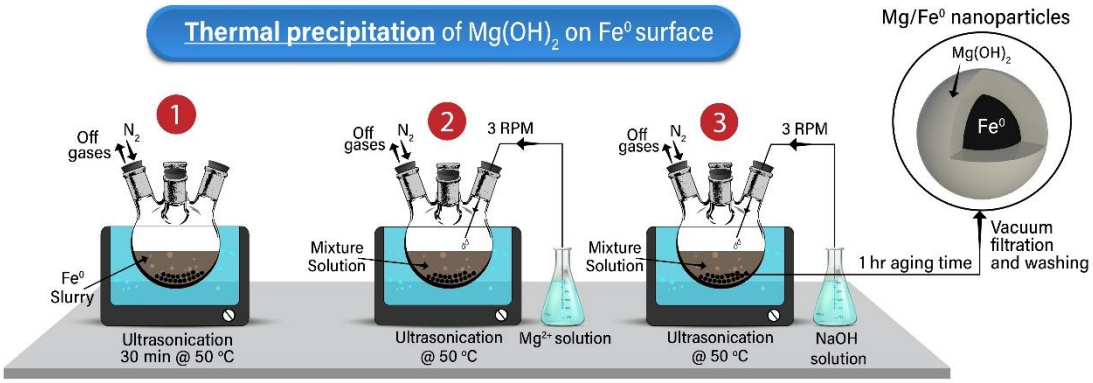

Figure 2.2 Schematic diagram for coating Fe^0 nanoparticles with $Mg(OH)_2$ shell throughout a modified thermal precipitation technique.

For example, to produce 0.5 g of Mg/Fe^0 nanoparticles with a 5% [$Mg(OH)_2/Fe^0$] mass ratio, 12.5 ml of (Mg^{2+}/ethanol) solution and 13.75 ml of (NaOH/ethanol) solution were drop-wisely introduced to the (Fe^0/ethanol) mixture. After adding (Mg^{2+}/ethanol) and (NaOH/ethanol) solutions, one hour aging time was adjusted in the ultrasonicator. Moreover, it is essential to point out that pure nitrogen gas (N_2) was constantly purged throughout the coating stage to protect Mg/Fe^0 nanoparticles from oxidation. Finally, Mg/Fe^0 nanoparticles were rinsed with 200 mL of ethanol and acquired by a vacuum filtration system (Φ90mm SPC glass filtration system, SIBATA Scientific Technology LTD., Japan).

2.4. Characterization of nanomaterials

The physicochemical characteristics of the synthesized nanomaterials, e.g., Fe^0 nanoparticles, Mg/Fe^0 nanoparticles, and (Fe^0/oxalate) nanoparticles, were revealed using several techniques such as transmission electron microscopy (TEM), scanning electron microscopy (SEM), energy dispersive x-ray spectroscopy (EDS), x-ray diffraction (XRD), Fourier transform infrared spectroscopy (FTIR), Brunauer–Emmett–Teller specific surface area analyzer (SSA_{BET}), and laser diffraction particle size analyzer. Furthermore, the point of zero charge of the nanomaterials was determined using the salt addition method. Details of each technique are provided in the following subsections.

2.4.1. Transmission electron microscopy (TEM)

Transmission electron microscopy (TEM) is a technology used to visualize the morphological properties of nanomaterials, such as shape, particle size, and distribution [150,151]. TEM specimens of Fe^0 and Mg/Fe^0 nanoparticles before and after the reaction

with CIP were prepared as follows [63,152–154]: a small portion of each nanomaterial was dispersed in 10 mL of ethanol under ultrasonication (38 kHz, 100 W, ASU-10, AS ONE Corporation, Japan) for 10 min to ensure that the nanomaterials were not agglomerated or aggregated. Afterwards, two to three droplets of the dispersed nanomaterials were deposited onto nitorocellulose film (30-40nm thickness) supported by a carbon layer (10-15nm thickness) (COL-C10, Okenshoji Co., Ltd., Japan). The samples were kept in a vacuum dryer for 5 min to allow the vaporization of ethanol before TEM analysis. The morphology of nanomaterials was then acquired by JEM-ARM 200F (JEOL Co., Japan) at an acceleration voltage of 200 kV.

2.4.2. Scanning electron microscopy (SEM)

Scanning electron microscopy (SEM) is a tool utilized to get information about the surface topography of nanomaterials by scanning their surfaces with a concentrated beam of electrons [46,155]. TEM analysis provides higher-resolution morphological images than SEM analysis [150]. However, sample preparation and analysis procedures of TEM are more complicated and time-consuming than SEM analysis [156]. For SEM analysis, the specimens of Fe^0 and (Fe^0/oxalate) nanoparticles, before and after the interaction with CIP, were prepared as follows [46,157]: two-sided carbon tape was placed on the SEM sample stub. Hereafter, the powder form of Fe^0 and (Fe^0/oxalate) was sprinkled on the surface of the carbon tape. Then, SEM images of Fe^0 and (Fe^0/oxalate) nanoparticles were obtained by JSM-IT700HR (JEOL Ltd., Japan) at an operating voltage of 15 kV.

2.4.3. Energy dispersive x-ray spectroscopy (EDS)

Energy dispersive x-ray spectroscopy (EDS) is an analytical method employed to identify and quantify the surface elemental composition of nanomaterials [158,159]. Usually, EDS systems are attached to an electron microscopy device, for instance, TEM or SEM [160,161]. EDS analysis for the synthesized nanomaterials, before and after the removal of CIP, was performed in conjunction with TEM (JEM-ARM 200F, JEOL Co., Japan) and SEM (JSM-IT700HR, JEOL Ltd., Japan) analysis.

2.4.4. X-ray diffraction (XRD)

X-ray diffraction (XRD) analysis is an accreditable method to define nanomaterials' chemical composition, crystal structure, and crystallite size [147,162]. XRD analysis for the fabricated nanomaterials, before and after the elimination of CIP, was conducted by

TTR Rigaku diffractometer (Rigaku, Tokyo, Japan), which employs Cu k_α radiation to generate X-rays with a wavelength of 1.5418Å. The diffractometer was operating at 50 kV and 300 mA while the range of scanning angle (2θ) was set to be from 3° to 90° at a scanning rate of 2°/min.

The crystallite size of freshly synthesized nanomaterials was determined using Scherrer's equation [46,149,153,163]:

$$\boldsymbol{D = \frac{K\lambda}{\beta\, cos\theta_B}} \qquad \textbf{(2.3)}$$

Where D, K, λ, β, and θ_B denote for crystallite size of nanomaterial (nm), shape constant (K = 0.89 or 0.9), wavelength of applied x-ray (λ = 0.154 nm), peak width at half maximum height (radians), and reflection angle (radians), respectively.

2.4.5. Fourier Transform Infrared spectroscopy (FTIR)

Fourier Transform Infrared spectroscopy (FTIR) is an instrument used to define the functional groups of nanomaterials [153,164]. In addition, FTIR can also be employed to determine the chemical compositions of nanomaterials [160,165]. Moreover, the reactive sites on the surface of nanomaterials can be recognized by FTIR [160]. Surface functional groups and chemical composition of freshly prepared nanomaterials, as well as the nature of the interaction between the nanomaterials and CIP, were obtained by FT/IR-4200 (JASCO, Japan) within an infrared absorption frequency of 500 to 4000 cm^{-1}.

2.4.6. Brunauer–Emmett–Teller specific surface area (SSA_{BET}) analysis

Brunauer–Emmett–Teller specific surface area (SSA_{BET}) analysis is a method used to measure the surface area per mass of nanomaterials ($m^2\ g^{-1}$) through gas absorption such as nitrogen, argon, or krypton [166]. N_2 adsorption-desorption isotherms and specific surface area of Fe^0 nanoparticles were acquired by 3Flex surface characterization (Micromeritics, USA) at 77.15K [46]. Before SSA_{BET} analysis, Fe^0 nanoparticles were preheated at 423.15K and degassed at 623.15K for 2 h under a continuous flow of N_2 gas to ensure that the surface of Fe^0 nanoparticles was clean from any impurities.

2.4.7. Particle size & size distribution

Laser diffraction particle size analysis is a technique used to measure particle size and particle size distribution (PSD) of nanomaterials within a range of 20 nm to 2000 µm [46,167]. The particle size distribution of Fe^0 nanoparticles was measured by a SALD-2300 laser diffraction analyzer (SHIMADZU, Japan).

2.4.8. Point of zero charge of nanomaterials [$pH_{(PZC)}$]

The zero point of charge [$pH_{(ZPC)}$] of Fe^0 nanoparticles, Mg/Fe^0 nanoparticles, and (Fe^0/oxalate) nanoparticles was defined using the salt addition method [46,133,168,169]. Five glass vials were filled with 50 mL of 0.1 M of potassium chloride (KCl), and the pH of each vial was modified to a particular value (e.g., 2, 5, 7, 9, and 11) using sodium hydroxide (NaOH) and hydrochloric acid (HCl). After the pH adjustment, 0.1 g of a nanomaterial was added to each vial and kept at room temperature for 24 h. At the end of the experiment, the final pH of the solution was recorded by a portable pH meter (D-210P-S, LAQUA, HORIBA). Then, the plot of pH_{Final} (Y-axis) verse $pH_{Initial}$ (X-axis) was constructed where the intersection point between this plot and bisector represents the zero point of charge [$pH_{(ZPC)}$] of the nanomaterial of interest.

2.5. Experimental procedures

2.5.1. Reactivity experiments

The reactivity of the synthesized nanomaterials [e.g., Fe^0, Mg/Fe^0, and (Fe^0/oxalate)] and their competence in removing CIP from aqueous solutions were evaluated through various batch experiments. The batch experiments were conducted in a 200 ml Erlenmeyer flask under multiple conditions, for instance, nanomaterial dosage (g L^{-1}), CIP initial concentrations (mg L^{-1}), initial pH, reaction temperature (°C), and contact time (min). Initially, the performance of the nanomaterials was examined under primary conditions, as illustrated in Table 2.2 and Table 2.3. Then, based on the outcomes of the preliminary experiments, an experimental plan was set up to systematically optimize the treatment conditions of CIP by the proposed nanomaterials by varying the numerical value of each parameter within a specific range, as shown in Table 2.2 and Table 2.3. The optimization process aimed to define the optimum treatment conditions that achieve the best removal efficiency of CIP by the suggested nanomaterials within a reasonable treatment cost.

Table 2.2 Design of batch experiments for Mg/Fe^0 nanoparticles.

Targeted parameter	[CIP] (mg L^{-1})	[$Mg(OH)_2/Fe^0$] mass ratio	Nanomaterial dosage (g L^{-1})	Initial pH	Temperature (°C)
Primary conditions	100	0.05	0.5	5	25
Optimization of [$Mg(OH)_2/Fe^0$] mass ratio	100	0.05–02	0.5	5	25
Optimization of Mg/Fe^0 dosage	100	0.05	0.2–1.5	5	25
Optimization of initial pH	100	0.05	0.5	3–11	25
Optimization of temperature	100	0.05	0.5	5	25–55
Effect of CIP concentration	50–200	0.05	0.5	5	25

*Note: In all experiments, the volume of CIP solution and the contact time were 200 ml and (5–240) min, respectively.

Table 2.3 Design of batch experiments for (Fe^0/oxalate) nanoparticles.

Targeted parameter	[CIP] (mg L^{-1})	(Fe^0/oxalate) dosage (g L^{-1})	[Oxalate] (mM)	Initial pH	Temperature (°C)
Primary conditions	100	0.3	0.3	7	25
Optimization of Fe^0 dosage for Fe^0 nanoparticles	100	0.1–1.1	0	7	25
Optimization of Fe^0 dosage for (Fe^0/oxalate) nanoparticles	100	0.1–1.1	0.5	7	25
Optimization of oxalate concentration for (Fe^0/oxalate) nanoparticles	100	0.1–0.5	0.1–0.9	7	25
Effect of dissolved oxygen content	100	0.3	0.3	7	25
Optimization of initial pH	100	0.3	0.3	3–11	25
Optimization of temperature	100	0.3	0.3	7	25–65
Effect of CIP concentration	10–100	0.3–0.7	0.3	7	25

*Note: In all experiments, the volume of CIP solution and the contact time were 200 ml and (5–30) min, respectively.

2.5.2. Effect of water matrix on the competence of nanomaterials

Domestic, hospital, industrial, and pharmaceutical wastewater are complex mediums and contain a variety of foreign ions and natural organic matters (NOM) with high concentrations [170,171]. These substances can negatively affect nanomaterials' effectiveness in removing CIP from these types of wastewater [172,173]. Hence, it was crucial to study the influence of ionic strength (IS) (i.e., NaCl), natural organic matters (e.g., humic acid), and coexisting ions (i.e., cations and anions) on the efficacy of (Fe^0/oxalate) nanoparticles, as displayed in Table 2.4, to ensure their competence in field-scale applications.

Table 2.4 Experimental plan for the influence of water matrix on the competence of (Fe^0/oxalate) nanoparticles.

No.	Parameter	Parameter value
1	Ionic Strength (IS) [NaCl]	0 –100 (mM)
2	Humic acid (HA)	5–40 (mg L^{-1})
3	Potassium (K^+)	10–50 (mM)
4	Calcium (Ca^{2+})	5–30 (mM)
5	Magnesium (Mg^{2+})	5–10 (mM)
6	Nitrate (NO_3^-)	5–30 (mM)
7	Sulfate (SO_4^{2-})	5–10 (mM)
8	Carbonate (CO_3^{2-})	5–10 (mM)

2.5.3. Desorption experiments

Identifying the responsible removal mechanisms of pollutants by nanomaterials is vital to understand and predict the behavior of these materials under different treatment circumstances. As mentioned in section 1.4.2, Fe^0 nanoparticles and other iron-based

nanoparticles can eliminate organic pollution through adsorption and oxidation. Therefore, desorption experiments were performed to determine the contribution of adsorption and oxidation in removing CIP by Mg/Fe^0 and (Fe^0/oxalate) nanoparticles. Desorption experiments were designed in accordance with the features of each nanomaterial as follows:

2.5.3.1. Mg/Fe^0 nanoparticles

After treating CIP-polluted solutions, the exhausted Mg/Fe^0 nanoparticles were collected via a vacuum filtration system (Φ90mm SPC glass filtration system, SIBATA Scientific Technology LTD., Japan). The acquired Mg/Fe^0 nanoparticles were then immersed in 0.2 L of 1 M NaOH solution and stirred via a magnetic stirrer at 1000 rpm for three hours at 25 ℃ to desorb the adsorbed molecules of CIP [174,175].

2.5.3.2. (Fe^0/oxalate) nanoparticles

(Fe^0/oxalate) nanoparticles were employed to treat CIP-polluted water at various initial pH (e.g., 5, 7, 9, and 11). Afterwards, the utilized (Fe^0/oxalate) nanoparticles were acquired by a vacuum filtration system (Φ90mm SPC glass filtration system, SIBATA Scientific Technology LTD., Japan). Hereafter, the exhausted (Fe^0/oxalate) nanoparticles were submerged in 0.2 L of deionized water with an initial pH of 3 at 25 ℃ for one day [63]. This procedure was repeated using deionized water with an initial pH of 5 and 12 to define the optimum pH for attaining the maximum desorption percentage.

For both iron-based nanomaterials [e.g., Mg/Fe^0 and (Fe^0/oxalate)], the released concentration of CIP in the desorption solution represents the percentage of CIP adsorption. In contrast, the difference between the total removal efficiency and the percentage of adsorption represents the proportion of oxidation.

2.5.4. Regeneration and recyclability of iron-based nanomaterials

Regeneration and reusing the spent nanomaterials for several treatment cycles are extremely important to decrease the cost of nanomaterial synthesis and the treatment process. Moreover, recycling the used nanomaterials significantly minimizes the generation of sludge after the completion of the treatment process. Hence, it is crucial to evaluate the recyclability and reusability of Mg/Fe^0 and (Fe^0/oxalate) nanoparticles to ensure their adequacy in field-scale applications. A regeneration and recycling protocol

for each iron-based nanomaterial was proposed based on the outcomes of the desorption experiments.

2.5.4.1. Mg/Fe^0 nanoparticles

The recyclability of Mg/Fe^0 nanoparticles for many adsorption cycles was examined as follows: 500 mg of Mg/Fe^0 nanoparticles were employed in five consecutive treatment cycles to remediate five liters of 100 mg L^{-1} of CIP-polluted water. At the end of each treatment process, the used Mg/Fe^0 nanoparticles were collected by a vacuum filtration system and regenerated by submerging them in 0.2 L of 1 mol L^{-1} NaOH solution for 1 h. Then, a new $Mg(OH)_2$ shell was provided to the exhausted Mg/Fe^0 nanoparticles, as elaborated in section 2.3, before starting the next treatment cycle.

2.5.4.2. (Fe^0/oxalate) nanoparticles

After the completion of the treatment stage, the used (Fe^0/oxalate) nanoparticles were collected via a vacuum filtration system. Then, the utilized (Fe^0/oxalate) nanoparticles were immersed in 0.2 L of deionized water with an initial pH of 5. Afterwards, the mixture was magnetically stirred for 1 h. Subsequently, the regenerated (Fe^0/oxalate) nanoparticles were collected by a vacuum filtration system and used again to treat CIP-polluted water.

2.5.5. Longevity and storage experiments for Mg/Fe^0 nanoparticles

Continuous exposure of Fe^0 nanoparticles to air will promptly oxidize them and diminish their decontamination reactivity towards water pollutants due to forming a passivation layer of iron oxides and hydroxides [Equation (1.6)]. Although the formation of a passivation layer of iron oxides and hydroxides on the surface of Fe^0 nanoparticles is beneficial for the adsorption of certain types of pollutants such as phosphorus, the presence of such a layer prevents the interaction between the reactive sites on the surface of Fe^0 nanoparticles and the organic pollutants, such as CIP, and reduces their removal from polluted waters. Coating Fe^0 nanoparticles with a shell of magnesium hydroxide should protect the core of Fe^0 nanoparticles from oxidation by minimizing the formulation of the passivation layer over time which allows the easy handling of Mg/Fe^0 nanoparticles during the transportation from the synthesis facilities to the contaminated locations in addition to the simple storage requirement in the site.

Longevity experiments were conducted to confirm the possibility of storing and conveying Mg/Fe^0 nanoparticles from manufacturing facilities to the contaminated sites without significant deterioration in their efficacy. Three empty plastic containers (10 ml) were prepared by adding 100 mg of Mg/Fe^0 nanoparticles to each container, sealed, and stored at room temperature. After storage for different periods, for instance, 5, 10, and 30 days, CIP-polluted solutions were treated, in batch experiments, by using the stored materials. Furthermore, to elucidate the effect of storage solution, three samples of Mg/Fe^0 nanoparticles (100 mg) were stored in 5 ml of different solutions, for example, deionized water, ethanol, and a mix of ethanol and deionized water with a volume ratio of 1:1. After one month of storage, batch experiments were executed using the stored materials to select the best storage solution for Mg/Fe^0 nanoparticles.

2.5.6. Sampling procedures and evaluation criteria

The treatment process of CIP-polluted solutions started after adding a specific dosage of the iron-based nanomaterials to the CIP solution and placing the Erlenmeyer flask on a magnetic stirrer (REXIM, AS ONE Corporation, Japan) at 500 rpm. At specific time intervals [e.g., 0, 5, 10, 30, 60, 90, 120, 180, and 240 min for Mg/Fe^0 nanoparticles and 5, 10, 20, and 30 min for (Fe^0/oxalate) nanoparticles], 2 ml liquid sample was taken from the flask by a 10 ml syringe (Terumo Corporation, Japan), immediately filtered by using a syringe filter (0.45 µm, Advantec Co., Ltd. Corporation, Japan), and stored in microtube (2 ml, BIO-BIK, Ina-optika corporation, Japan) for further analysis. The competence of Fe^0, Mg/Fe^0, and (Fe^0/oxalate) nanoparticles in eliminating CIP from polluted water was assessed by the calculation of removal efficiency (%) and removal capacity (mg g^{-1}) using the following equations:

$$\boldsymbol{Removal\ Efficiancy}\ (\%) = \frac{(\boldsymbol{C_i} - \boldsymbol{C_t})}{\boldsymbol{C_i}} \times \mathbf{100}\% \qquad \textbf{(2.4)}$$

$$\boldsymbol{Removal\ Capacity}\ (\boldsymbol{mg/g}) = \frac{(\boldsymbol{C_i} - \boldsymbol{C_t}) \times \boldsymbol{V}}{\boldsymbol{m}} \qquad \textbf{(2.5)}$$

Where C_i, C_t, V, and m symbolize CIP initial concentration (mg L^{-1}), CIP concentration (mg L^{-1}) at a particular time t (min), volume of CIP solution (L), and weight of the iron-based nanomaterial (g), respectively.

2.6. Prototype lab-scale treatment system (PLSTS)

A prototype lab-scale treatment system (PLSTS) was proposed as a suitable tool to remediate streams of CIP-polluted waters in real contaminated sites. The system was fabricated following the design consideration of our previous study [147]. Figure 2.3 demonstrates a schematic diagram for the proposed PLSTS. The treatment system consisted of five units: feeding tank, reactor, separation unit, aeration tank, and sand filtration column. The specifications and function of each unit are summarized in the following subsections.

2.6.1. Feeding tank

The feeding tank is a plastic container filled with 10 L of 100 mg L^{-1} of CIP-polluted solution. A peristaltic pump (EYELA RP-1100, Tokyo Rika Kikai Co., Ltd., Japan) was used to feed the system with the polluted water at different flow rates (Table 2.5).

2.6.2. Reactor

It is a 2 L four-neck flask, and it is the place where Mg/Fe^0 nanoparticles can interact with the polluted water and adsorb the molecules of CIP. A mechanical stirrer occupied the central neck of the four-neck flask to mix the solution at 250 rpm. On the other hand, the other three inlets were occupied by the feeding tube, the recycling tube, and the connecting tube between the reactor and separation unit. Also, the reactor was placed in a water bath to control the temperature at 25 °C (Figure 2.3).

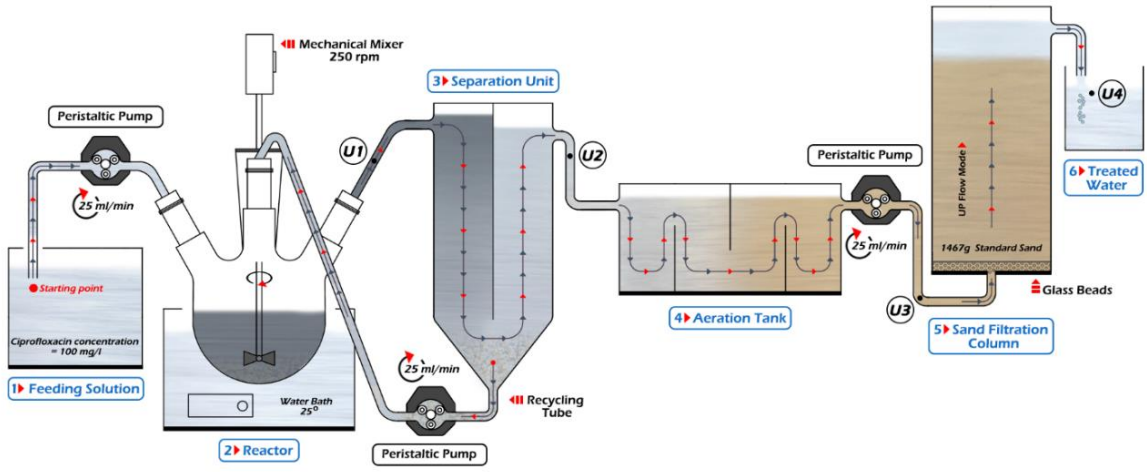

Figure 2.3 Schematic diagram for the prototype lab-scale treatment system.

2.6.3. Separation unit

It is a plexiglass unit with a specific structure designed to produce clean effluents by facilitating the settlement and the separation of Mg/Fe^0 nanoparticles from the solution. The separation unit consists of a straight cylindrical part with a height of 20 cm and an interior diameter of 11 cm with an effective volume of 1.9 L. Moreover, the straight cylindrical portion is divided by a plexiglass plate along its height to force the water to move in a U shape, as shown in Figure 2.3, which enhances the settlement process of Mg/Fe^0 nanoparticles. In addition, the bottom of the cylinder is attached to a plastic cone with a height of 7 cm to collect and recycle the settled Mg/Fe^0 nanoparticles in the reactor. The total effective volume of the separation unit is approximately 2 L (Figure 2.3).

2.6.4. Aeration tank

It is a plastic box with a 20.5 cm length, 14 cm width, 10 cm height, and an approximate volume of 2.87 L. This unit aimed to precipitate any Mg/Fe^0 nanoparticles discharged from the separation unit. Furthermore, as illustrated in Figure 2.3, the aeration tank was designed with a unique structure to increase the water flow pathway, expose it to air and oxidize any residue of Mg/Fe^0 nanoparticles.

2.6.5. Sand filtration column

It is a plexiglass cylindrical column with a height of 20 cm and an internal diameter of 11 cm. The filtration column was filled with 1467g of standard sand (JIS standard sand No.5, S-208, AS ONE cooperation, Japan) to remove any Mg/Fe^0 nanoparticles left from the separation unit and the aeration tank (Figure 2.3). Moreover, it was used to remove the color of the oxidized water in the aeration tank and produce clean effluents. The treated water from the aeration tank was pumped into the sand column by an up-flow mood to ensure that the water flowed within the whole section of the sand column. The pumping rate was adjusted to be 25 ml min^{-1}.

2.6.6. Recycling system

A recycling tube was established between the separation unit and the reactor to return the collected Mg/Fe^0 nanoparticles to the reactor (Figure 2.3). This process may enhance the efficiency of Mg/Fe^0 nanoparticles by increasing the interaction time between Mg/Fe^0 nanoparticles and CIP-polluted water. The recycling rate was controlled by a peristaltic

pump (EYELA RP-1100, Tokyo Rika Kikai Co., Ltd., Japan) at a flow rate of 25 ml min^{-1}.

2.6.7. Experimental design for PLSTS

The conditions of treating CIP-polluted solutions by Mg/Fe^0 nanoparticles, for example, Mg/Fe^0 dosage (g L^{-1}), initial pH, temperature (°C), and initial CIP concentration (mg L^{-1}), were optimized in the batch experiments. Thus, three treatment cycles were operated under the previously optimized treatment conditions, as presented in Table 2.5, to treat 10 liters of 100 mg L^{-1} CIP-polluted water. It can be seen from Table 2.5 that the only difference between each treatment cycle was the feeding flow rate, as it was changed from 25 to 75 ml min^{-1} to determine the optimum flow rate of the polluted water.

Table 2.5 Operational paramters of PLSTS**.**

Cycle No.	Flow rate (ml min^{-1})	Mg/Fe^0 dosage (g L^{-1})	Temperature (°C)	Initial pH	Recycling system
1	25	0.5	25 °C	6	Yes
2	50	0.5	25 °C	6	Yes
3	75	0.5	25 °C	6	Yes

2.7. Analytical instruments

CIP concentration in aqueous solutions was measured by UV-vis spectrophotometry at a wavelength of 275 nm (UV-1280, SHIMADZU, Japan). UV-1280 spectrophotometer was calibrated to determine CIP concentration in water. The calibration process was as follows: eight CIP standard solutions with concentrations of 0.25, 0.5, 0.75, 1, 2, 3, 4, and 5 mg L^{-1} were prepared. Then, 8 UV quartz cells were filled with 5 ml of each standard solution. After that, the cells were consecutively inserted in the UV-1280 to acquire the absorbance value at 275 nm. A calibration curve was developed by plotting the absorbance value (X-axis) against CIP concentration (Y-axis) as manifested in Figure 2.4. The equation of the calibration curve was as follows:

$$\mathbf{Y = 8.911X} \qquad \mathbf{(2.6)}$$

Where Y and X represent CIP concentration (mg L^{-1}) and the absorbance that was acquired from the UV-1280 spectrophotometer at 275 nm.

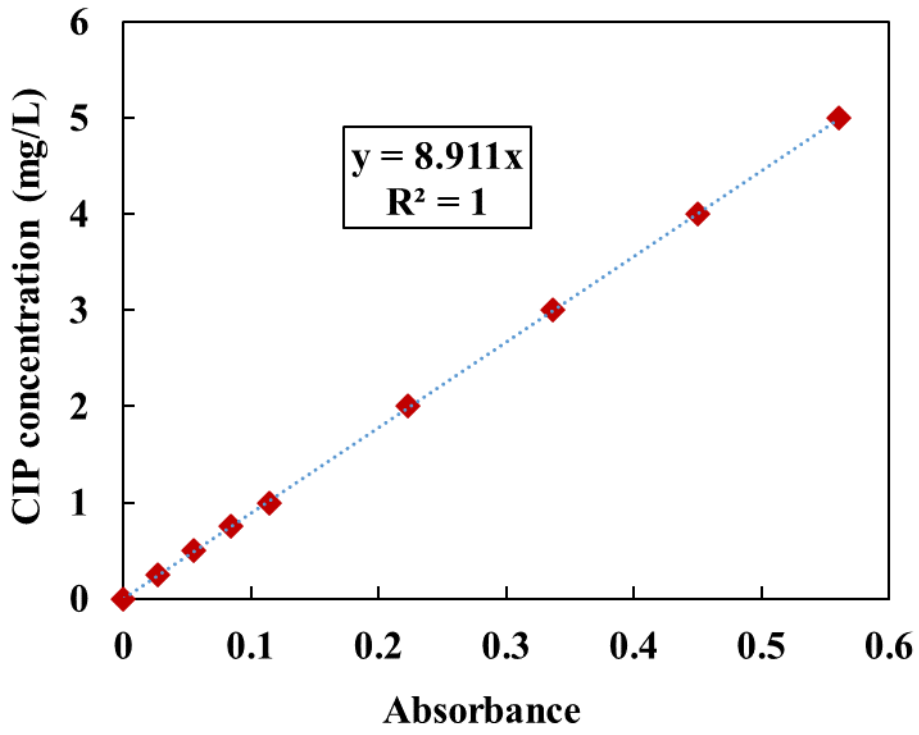

Figure 2.4. Calibration curve of UV-1280 spectrophotometer.

Figure 2.4 shows that the determination coefficient (R^2) of the obtained calibration curve was exactly 1, confirming the successful calibration of the UV-1280 spectrophotometer. It is important to mention that the collected samples were diluted using deionized water with the proper dilution factor to fit the calibration curve range (0 – 5 mg L^{-1}).

The concentrations of total dissolved iron [Fe] and ferrous ions [Fe^{2+}] were determined by UV–Vis spectrophotometer (DR3900, HACH Co., USA) following the USEPA FerroVer iron and 1,10-phenanthroline protocols, respectively. Then, the concentration of ferric ions [Fe^{3+}] was mathematically calculated using the following equation:

$$[Fe^{3+}]\ (mg\ L^{-1}) = [Fe]\ (mg\ L^{-1}) - [Fe^{2+}]\ (mg\ L^{-1}) \quad \textbf{(2.7)}$$

In addition, the concentration of magnesium ions (Mg^{2+}) was measured by DR3900 spectrophotometer (HACH, USA) following the Metal Phthalein Colorimetric Method (0.5 to 10 mg L^{-1}). Furthermore, pH, redox potential (E_h), and solution temperature were recorded using LAQUA pH meter (HORIBA Advanced Techno, Co., Ltd., Japan).

2.8. Modeling of ciprofloxacin adsorption

Kinetics, isotherm, and thermodynamic analysis for the adsorption of CIP by Mg/Fe^0 and (Fe^0/oxalate) nanoparticles were performed using various models to get more insights into

the nature of the reaction between CIP and the iron-based nanomaterials in aqueous solutions [63,176]. In addition, they provide numerical outcomes that help in defining the type (e.g., physisorption and chemosorption) and mechanism of CIP adsorption from polluted waters [46].

2.8.1. Nomenclature of kinetics, isotherm, and thermodynamic modeling.

Terminologies of kinetics, isotherm, and thermodynamic modeling are summarized in Table 2.6.

Table 2.6 Nomenclature of kinetics, isotherm, and thermodynamic modeling.

Abbreviation	Nomenclature	Unit
q_t	The adsorption capacity at a given time t.	mg g^{-1}
q_e	The adsorption capacity at equilibrium.	mg g^{-1}
t	Time.	min
k_1	Pseudo-first-order rate constant.	min^{-1}
k_2	Pseudo-second-order rate constant.	g mg^{-1} min^{-1}
k_{intra}	Intraparticle diffusion rate constant.	mg g^{-1} × $min^{1/2}$
C	A constant in the Intraparticle diffusion model depends on the nature of the adsorption.	mg g^{-1}
α	The initial adsorption rate constant of Elovich model.	mg g^{-1} min^{-1}
β	Desorption constant	mg g^{-1}
K_L	Langmuir isotherm constant.	L mg^{-1}
C_e	The equilibrium concentration of a contaminant.	mg L^{-1}
Q^0	The maximum adsorption capacity that is obtained from Langmuir isotherm model.	mg g^{-1}
C_0	The initial concentration of contaminant.	mg L^{-1}
K_f	Freundlich isotherm constant.	(mg g^{-1}) (L mg^{-1})$^{1/n}$
n	Adsorption intensity.	N/A
R	Universal gas constant.	8.314 J mol^{-1} K^{-1}
T	Absolute temperature	K
b_T	Temkin isotherm constant.	N/A
A_T	Temkin isotherm equilibrium binding constant.	L g^{-1}

Table 2.6 Nomenclature of kinetics, isotherm, and thermodynamic modeling (cont.).

Abbreviation	Nomenclature	Unit
q_s	Theoretical isotherm saturation capacity.	mg g^{-1}
K_{ad}	Dubinin–Radushkevich isotherm constant.	mol^2 J^{-2}
ε	Dubinin–Radushkevich isotherm constant.	N/A
E	Mean adsorption energy.	J mol^{-1}
K_S	Sips isotherm constant.	L mg^{-1}
n_S	Dimensionless constant for Sips model.	N/A
ΔG^0	Gibbs free energy change	J mol^{-1}
ΔGH^0	Enthalpy change	J mol^{-1}
ΔS^0	Entropy change	J mol^{-1} K^{-1}

2.8.2. Kinetic modeling

Kinetics analysis describes the rate of CIP adsorption under certain conditions and predicts how fast the adsorption process will be under these circumstances [177]. The kinetics of CIP adsorption by iron-based nanomaterials was analyzed by four kinetic models: Pseudo first-order, Pseudo second-order, Elovich, and intraparticle diffusion. The concept of each model as well as their theoretical assumptions are described in the following sections.

2.8.2.1. Pseudo-first-order model:

Lagergren proposed pseudo-first-order model (PFO) to depict the adsorption kinetics of ocalic and malonic acids onto charcoal [178,179]. The following equation represents the differential equation of PFO:

$$\frac{dq_t}{dt} = k_1(q_e - q_t) \quad \textbf{(2.8)}$$

Equation (2.8) can be integrated (Boundary conditions are as follows: t = 0 to t = t and q = 0 to q > 0) to give the following form of the PFO model:

$$\ln(q_e - q_t) = \ln(q_e) - k_1 t \quad \textbf{(2.9)}$$

2.8.2.2. Pseudo-second-order model:

Blanchard et al. suggested the Pseudo second-order model (PSO) to describe the kinetics of removing heavy metals by natural zeolites [180]. The differential equation of PSO can be written, based on the reported form by Ho in 1995, as follows [181]:

$$\frac{dq_t}{dt} = k_2(q_e - q_t)^2 \quad \textbf{(2.10)}$$

After the integration of equation (2.10) (Boundary conditions are as follows: t = 0 to t = t and q = 0 to q > 0), the formula of PSO model can be rearranged as follows:

$$\frac{t}{q_t} = \frac{1}{k_2 q_e^2} + \frac{t}{q_e} \quad \textbf{(2.11)}$$

2.8.2.3. Elovich model

Roginsky and Zeldovich developed the Elovich model in 1934 to characterize the chemisorption of carbon monoxide on manganese dioxide [182]. The basic equation of the Elovich model is expressed as follows:

$$\frac{dq_t}{dt} = \alpha \exp(-\beta q) \quad \textbf{(2.12)}$$

After integrating equation (2.12), the Elovich equation can be written as follows:

$$q_t = \frac{1}{\beta} \ln(1 + \alpha\beta t) \quad \textbf{(2.13)}$$

2.8.2.4. Intraparticle diffusion model

In 1962, Weber and Morris proposed the intraparticle diffusion model [183]. The equation of the intraparticle diffusion model is expressed in equation (2.14):

$$q_t = k_{intra} \times t^{0.5} + C \quad \textbf{(2.14)}$$

2.8.3. Isotherm Modeling

Isotherm modeling characterizes the interaction of pollutants with adsorbents in aqueous mediums [184]. Moreover, it speculates adsorbents' surface properties and estimates their maximum adsorption capacities toward water pollutants. Five isotherm models were used to represent the equilibrium data of CIP adsorption by Mg/Fe^0 and (Fe^0/oxalate)

nanoparticles. These models are Langmuir, Freundlich, Temkin, Dubinin–Radushkevich, and Sips isotherm models.

2.8.3.1. Langmuir isotherm model

Langmuir isotherm model represents the monolayer adsorption of a pollutant on the surface of an adsorbent [185]. It assumes that the surface of an adsorbent has a limited number of identical adsorption sites, where each site can only adsorb a single molecule of a pollutant with no possible interaction between the neighboring sites. The equation of Langmuir can be written as follows:

$$\mathbf{q_e = \frac{Q_0\, K_L\, C_e}{1 + K_L\, C_e}} \qquad \textbf{(2.15)}$$

R_L is a dimensionless parameter called separation factor which was developed by Weber and Chakravorti to describe the adsorption nature of a pollutant by an adsorbent [186]. The separation factor (R_L) can be defined as follows:

$$\mathbf{R_L = \frac{1}{1 + K_L C_0}} \qquad \textbf{(2.16)}$$

The adsorption nature can be interpreted from the value of R_L as follows:

- The adsorption is unfavorable if $R_L>1$.
- The adsorption is favorable if $1 > R_L> 0$.
- The adsorption is irreversible if $R_L = 0$.
- The adsorption is linear if $R_L=1$.

It is important to mention that if the equilibrium data of an experiment is well fitted with the Langmuir isotherm model, this suggests that the adsorption type is chemisorption [185].

2.8.3.2. Freundlich isotherm model

Freundlich isotherm model was designed for the sorption of animal charcoal. It represents the multilayer adsorption of a pollutant on a heterogenous surface of an adsorbent. Freundlich's model supposes that heat and adsorption affinity are not uniformly

distributed over the surface of an adsorbent [185]. The equation of Freundlich is shown in the following equation:

$$q_e = K_f C_e^{\frac{1}{n}} \quad \textbf{(2.17)}$$

Similar to R_L in the Langmuir isotherm model, the inverse value of n can be used to demonstrate the nature of the adsorption as follows:

- If the value of (1/n) lies between 0 and 1, the adsorption is favorable.
- If the value of (1/n) is greater than 1, the adsorption is unfavorable.
- If the value of (1/n) equals 1, the adsorption is irreversible.

2.8.3.3. Temkin isotherm model

The original application of the Temkin isotherm model was to illustrate the chemisorption of hydrogen on platinum electrodes in an acid medium [185]. This model presumes that the heat of the adsorption for all molecules on the surface of the adsorbent is linearly decreasing as the adsorption is completed. The non-linear form of Temkin is displayed in the following equation:

$$q_e = \frac{R \times T}{b_T} \ln (A_T C_e) \quad \textbf{(2.18)}$$

2.8.3.4. Dubinin–Radushkevich isotherm model

Dubinin–Radushkevich was developed to describe the adsorption of vapors and gases on microporous materials such as activated carbon [185,187]. The non-linear formula of Dubinin–Radushkevich is illustrated in equation (2.19):

$$q_e = q_s \times e^{-(K_{ad} \times \varepsilon^2)} \quad \textbf{(2.19)}$$

The parameter (ε) can be calculated from the following equation:

$$\varepsilon = R \times T \times \left[1 + \frac{1}{C_e}\right] \quad \textbf{(2.20)}$$

Dubinin–Radushkevich model is also designed to differentiate between the chemical and physical adsorption of metals by calculating the required adsorption energy (E) to remove one molecule from the solution to the sorption site of an adsorbent [188]. For instance, if

the value of E is less than 8 kJ mol^{-1}, the adsorption is physisorption [189]. However, if the value of E lies between 8 and 16 kJ mol^{-1}, the adsorption is chemosorption [189]. The mean adsorption energy (E) (J mol^{-1}) can be calculated using the following formula:

$$\boldsymbol{E = \left[\frac{1}{\sqrt{2K_{ad}}}\right]} \qquad \textbf{(2.21)}$$

2.8.3.5. Sips isotherm model

Sips isotherm model is a three-parameter isotherm model [190]. It was developed as a combination of the Langmuir and Freundlich isotherm model to improve the prediction of adsorption on heterogeneous surfaces [191]. The equation of the Sips model is as follows [192,193]:

$$\boldsymbol{q_e = \frac{q_s \times (K_s C_e)^{n_s}}{1 + (K_s C_e)^{n_s}}} \qquad \textbf{(2.22)}$$

Sips isotherm equation can be reduced to the Freundlich isotherm formula when CIP concentration is very low. On the other hand, at high CIP concentrations, the Sips model is closer to represent the Langmuir isotherm equation.

2.8.4. Nonlinear regression analysis and Akaike's Information Criterion

Non-linear regression was employed to carefully fit the experimental outcomes with the kinetics and isotherm models and avoid any mistakes resulting from the linearization process. The non-linear regression was implemented using Microsoft Excel.

Akaike's Information Criterion (AIC) is a statistical method developed to choose the best model that describes the experimental data [194]. The model with the lowest AIC indicates that this model is the best to describe the experimental data.

The value of AIC value for each model can be determined using the following equation:

$$\boldsymbol{AIC = N \ln\left(\frac{SSE}{N}\right) + 2N_p + \frac{2N_p(N_p + 1)}{N - N_p - 1}} \qquad \textbf{(2.23)}$$

Where SSE, N, and N_p stand for the sum of square error, number of experimental data, and number of parameters in the model, respectively.

The Sum of square error (SEE) can be calculated using the following formula:

$$\boldsymbol{SSE = \sum_{t=0}^{t} \left(q_{t,experiment} - q_{t,model}\right)^2} \quad \textbf{(2.24)}$$

Where $q_{t,experiment}$ and $q_{t,\ model}$ stand for the experimental removal capacity (mg g^{-1}) and modeled removal capacity (mg g^{-1}), respectively, at a particular time t (min).

2.8.5. Thermodynamic modeling

Thermodynamic modeling was carried out to elucidate the influence of temperature on the treatment of CIP-polluted waters by Mg/Fe^0 and (Fe^0/oxalate) nanoparticles. Moreover, the analysis of thermodynamics is used to elaborate on the type of CIP adsorption by the proposed iron-based nanomaterials [195]. There are three important parameters for thermodynamic modeling, namely, Gibbs free energy change (ΔG^0), entropy change (ΔS^0), and enthalpy change (ΔH^0) [196]. ΔG^0 can be determined using Van't Hoff equation:

$$\boldsymbol{\Delta G^0 = -RT\, ln(K_d)} \quad \textbf{(2.25)}$$

The distribution coefficient (K_d) was calculated using the following formula [175]:

$$\boldsymbol{K_d = \frac{q_e}{C_e}} \quad \textbf{(2.26)}$$

The 3rd principle of thermodynamics describes the relationship between ΔG^0 and the other parameters of thermodynamics as follows:

$$\boldsymbol{\Delta G^0 = \Delta H^0 - T\Delta S^0} \quad \textbf{(2.27)}$$

After merging equation (2.25) and equation (2.27), the equation of Van't Hoff equation will be as follows:

$$\boldsymbol{ln(K_d) = -\frac{\Delta H^0}{R}\frac{1}{T} + \frac{\Delta S^0}{R}} \quad \textbf{(2.28)}$$

Based on equation (2.28), a plot of ln(K_d) versus 1/T was constructed where the slope and intercept of the plot were used to calculate ΔH^0 and ΔS^0, respectively. Then, equation (2.27) was used to calculate the value of ΔG^0.

Sign and magnitude of thermodynamics parameters provide valuable insights into the nature and type of CIP adsorption by the proposed iron-based nanomaterials. Table 2.7 and Table 2.8 clarify the meaning of both the sign and magnitude of thermodynamics parameters.

Table 2.7 Interpretation of the sign of thermodynamic parameters.

Thermodynamic parameter	Interpretation
$-\Delta H^0$	Exothermic and spontaneous reaction
$+\Delta H^0$	Endothermic and non-spontaneous reaction
$-\Delta S^0$	Lower disorder (less randomness)
$+\Delta S^0$	Higher disorder (more randomness)
$-\Delta G^0$	Spontaneous reaction
$+\Delta G^0$	Non-spontaneous reaction

Table 2.8 Interpretation of the magnitude of thermodynamic parameters.

The magnitude of the thermodynamic parameter	Nature of the reaction
$\Delta H^0 < 20\ kJ/mol$	Physisorption
$80\ kJ/mol < \Delta H^0 < 200\ kJ/mol$	Chemisorption
$2\ kJ/mol < \Delta G^0 < 20\ kJ/mol$	Physisorption
$80\ kJ/mol < \Delta G^0 < 400\ kJ/mol$	Chemisorption

The activation energy (E_a) of CIP adsorption by Mg/Fe^0 and (Fe^0/oxalate) nanoparticles was calculated using the Arrhenius equation as follows [197,198]:

$$\boldsymbol{ln(k_2) = ln(k_0) - \frac{E_a}{R}\frac{1}{T}} \qquad \textbf{(2.29)}$$

Where k_2, k_0, and E_a designate for Pseudo second-order rate constant (g mol^{-1} min^{-1}), adsorption rate constant (g mol^{-1} min^{-1}), and activation energy of adsorption (J mol^{-1}), respectively.

The activation energy of CIP adsorption by iron-based nanomaterials was calculated from the slope of the plot of $\ln(k_2)$ versus the reciprocal of temperature (T^{-1}). The magnitude of the activation energy (E_a) can elaborate on the nature of the adsorption, either physisorption (5–50 kJ mol^{-1}) or chemosorption (60–800 kJ mol^{-1}) [197].

Chapter 3

Encapsulation of iron nanoparticles with magnesium hydroxide shell for remarkable removal of ciprofloxacin from polluted waters

Graphical Abstract:

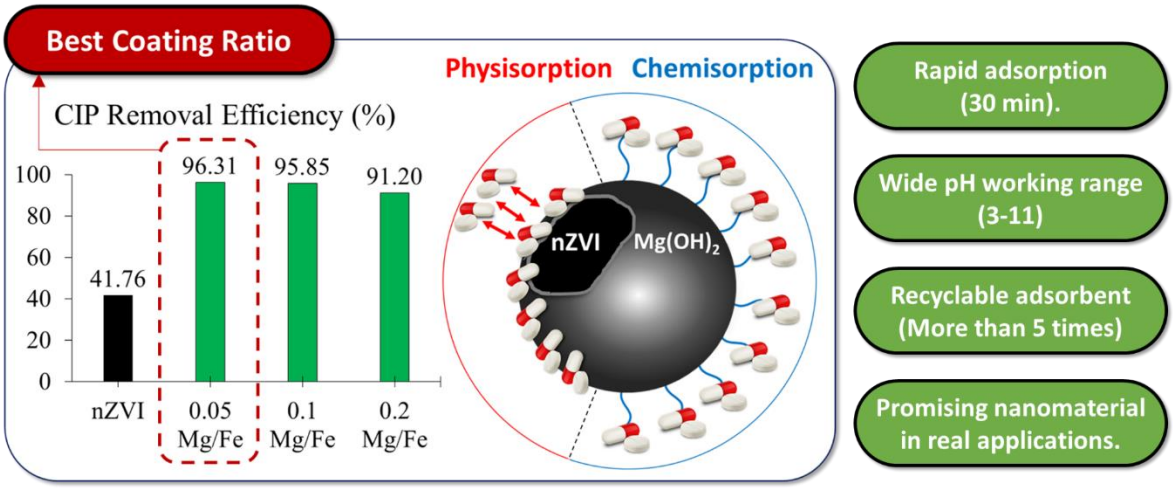

3.1. Characterization of nanomaterials

3.1.1. Transmission electron microscopy-energy-dispersive x-ray spectroscopy (TEM-EDS)

Figure 3.1 summarizes the results of TEM analysis for freshly synthesized Fe^0, Mg/Fe^0 ($[Mg(OH)_2/Fe^0]$ weight ratio = 0.05), and $Mg(OH)_2$ nano-powder at various resolutions (e.g. 20 and 100 nm). Figure 3.1.a & Figure 3.1.b illustrate that Fe^0 nanoparticles had a spherical shape with an approximate particle size of 70 nm. Moreover, Fe^0 nanoparticles preferred the formulation of a chain-like structure due to magnetic and electrostatic attractions between the neighboring Fe^0 nanoparticles [94]. In addition, Figure 3.1.c demonstrates that the low coating percentage of $[Mg(OH)_2/Fe^0]$ (i.e., 0.05) couldn't inhibit the aggregation of Mg/Fe^0 nanoparticles. Furthermore, Figure 3.1.d proves the emergence of the $Mg(OH)_2$ shell around Fe^0 nanoparticles and the formation of $Mg(OH)_2$ clouds that surround Mg/Fe^0 nanoparticles, which may reinforce them with additional adsorption locations for CIP. These clouds were more pronounced in the TEM pictures of Mg/Fe^0 nanoparticles with higher $[Mg(OH)_2/Fe^0]$ coating percentages, as illustrated in Figure 3.2. Interestingly, the production of $Mg(OH)_2$ nano-powder via a simple precipitation technique resulted in the development of two shapes of $Mg(OH)_2$: cubic and needles, as manifested in Figure 3.1.e & Figure 3.1.f . Figure 3.3 displays the EDS spectrum and elemental mapping of Mg/Fe^0 nanoparticles. It illustrates that the Mg/Fe^0 nanoparticles were mainly composed of iron (Fe), oxygen (O), and magnesium (Mg), with mass ratios of 78.13%, 21.76%, and 0.11%, respectively. The difficult detection of magnesium on the surface of Mg/Fe^0 nanoparticles by EDS was because of the low deposition ratio of $Mg(OH)_2$ (e.g., 5%).

3.1.2. X-ray diffraction analysis (XRD)

Crystalline structure and composition of iron-based nanoparticles were acquired by carrying out x-ray diffraction analysis (XRD, TTR, Rigaku Ltd., Japan). Figure 3.4 summarizes the XRD patterns for Fe^0 and Mg/Fe^0 ($[Mg(OH)_2/Fe^0]$ weight ratio = 0.05) nanoparticles before and after the elimination of CIP from aqueous solutions. Figure 3.4 illustrates that the strong distinctive peaks of Fe^0 appeared in XRD pattern of Fe^0 at 2θ = 44.86° and 2θ = 82.2° [133]. On the contrary, the XRD pattern of fresh Mg/Fe^0 nanoparticles (Figure 3.4) showed no major changes compared with the XRD pattern of

Fe^0 nanoparticles except for the weak detection of brucite [$Mg(OH)_2$] at two different locations (2θ = 19.75° and 38.87°). The trivial detection of brucite in the XRD pattern of Mg/Fe^0 nanoparticles can be elucidated by the low deposition ratio of $Mg(OH)_2$ (i.e., 5%) throughout the coating process.

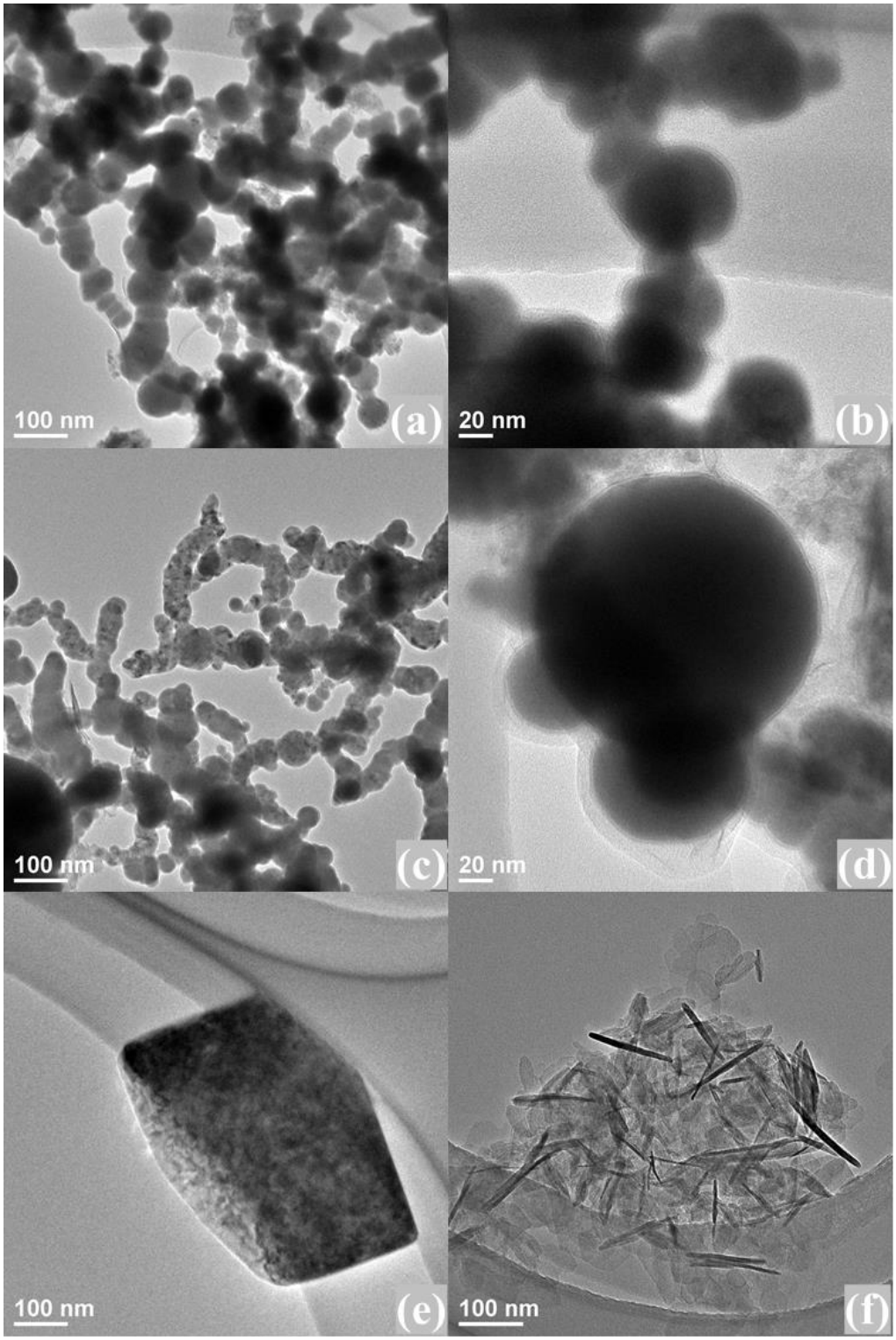

Figure 3.1 TEM pictures for newly produced nanomaterials: (a) & (b) for Fe^0 nanoparticles, (c) & (d) for Mg/Fe^0 nanoparticles ([$Mg(OH)_2/Fe^0$] weight ratio = 0.05), and (e) & (f) for $Mg(OH)_2$ nano-powder.

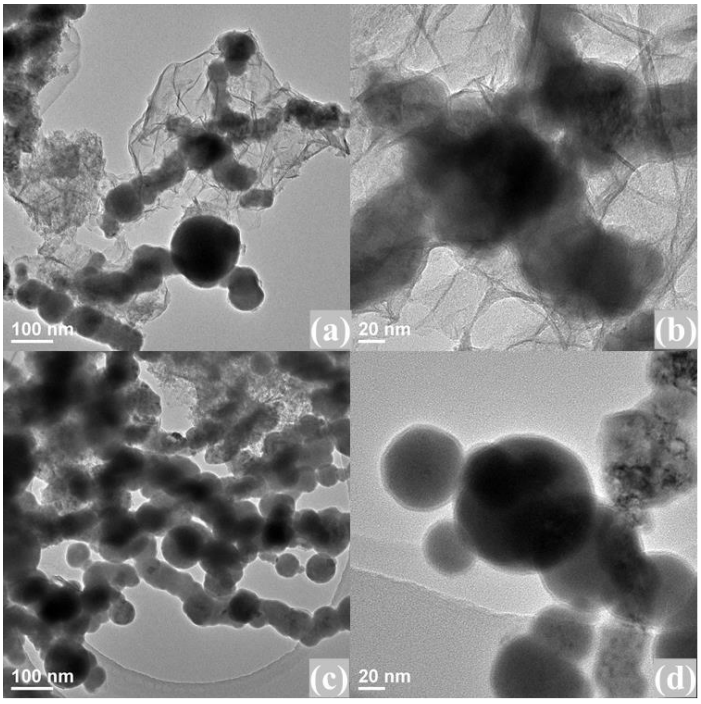

Figure 3.2 TEM pictures for newly produced Mg/Fe^0 nanoparticles with different coating ratios: **(a)** & **(b)** coating ratio = 0.1, and **(c)** & **(d)** coating ratio = 0.2.

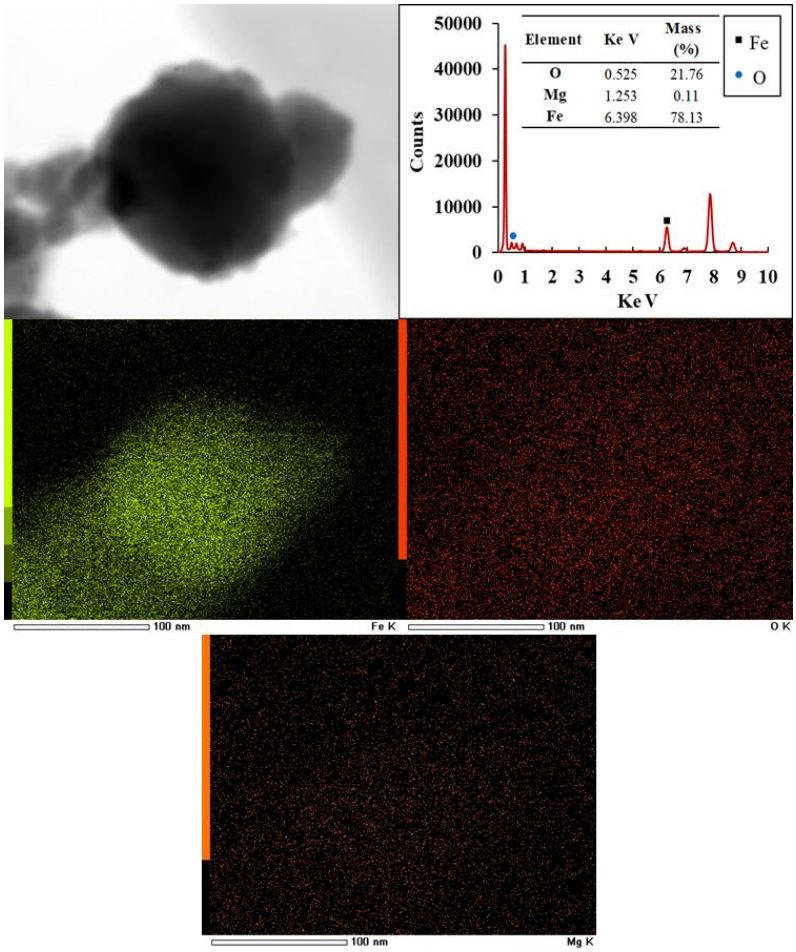

Figure 3.3 Outcomes of EDS analysis for newly synthesized Mg/Fe^0 nanoparticles with 5% coating ratio.

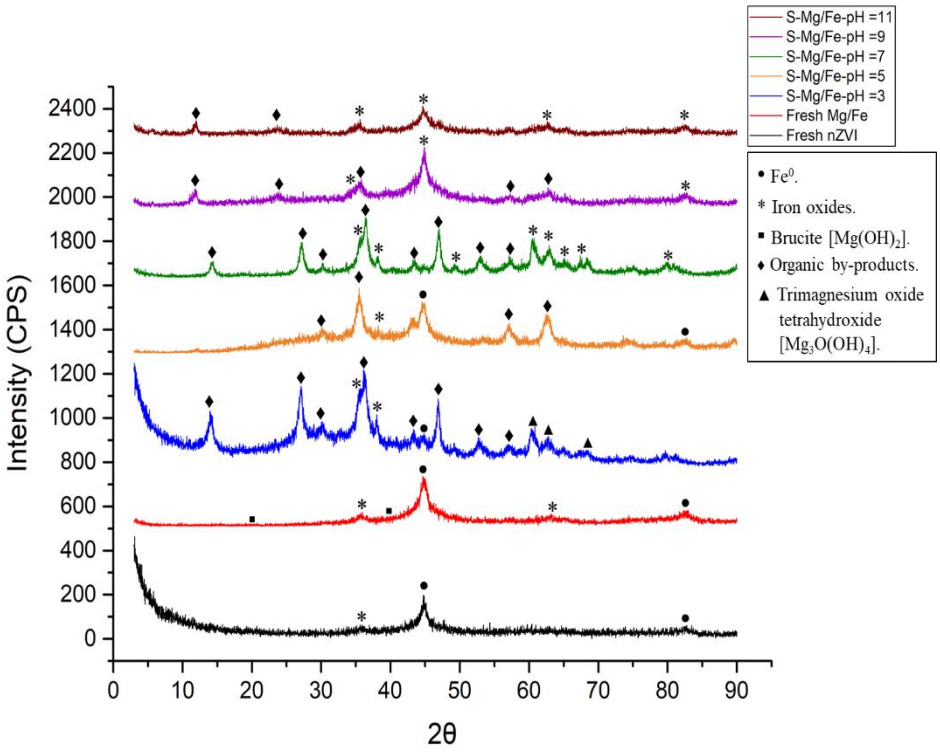

Figure 3.4 XRD analysis for Mg/Fe^0 nanoparticles ([$Mg(OH)_2/Fe^0$] weight ratio = 0.05) before and after the reaction with CIP at different initial pH.

3.2. Effect of [$Mg(OH)_2/Fe^0$] weight ratio

The influence of the coating percentage of Fe^0 nanoparticles by a thin layer of $Mg(OH)_2$ on the competence of Mg/Fe^0 nanoparticles toward remediating CIP-polluted waters was examined by chancing the [$Mg(OH)_2/Fe^0$] weight ratio from 0.05 (i.e., 5%) to 0.2 (i.e., 20%) during the coating process. Figure 3.5.a reveals the effect of [$Mg(OH)_2/Fe^0$] weight ratio on the removal of CIP by Mg/Fe^0 nanoparticles. In the early stage of reaction, 0.5 g L^{-1} of Fe^0 nanoparticles showed 88.20% removal percentage of CIP within the first 10 min of reaction. However, this trend did not continue later because Fe^0 nanoparticles gradually lost their adsorptive capacity by desorbing CIP molecules back to the solution to achieve 41.76% removal efficiency at the end of the reaction (i.e., 180 min) (Figure 3.5.a). This percentage was confirmed to be permanent even after 24 hr. of reaction (data are not shown). It is worth noting that, in this study, the behavior of Fe^0 nanoparticles in removing CIP from water is quite different from the previous reports [106,119,125]. For example, Chen *et al.* demonstrated that Fe^0 nanoparticles didn't show a desorption trend; on the other hand, Fe^0 nanoparticles could progressively remove CIP to reach a constant removal efficiency of 35% after 120 min of reaction [106].

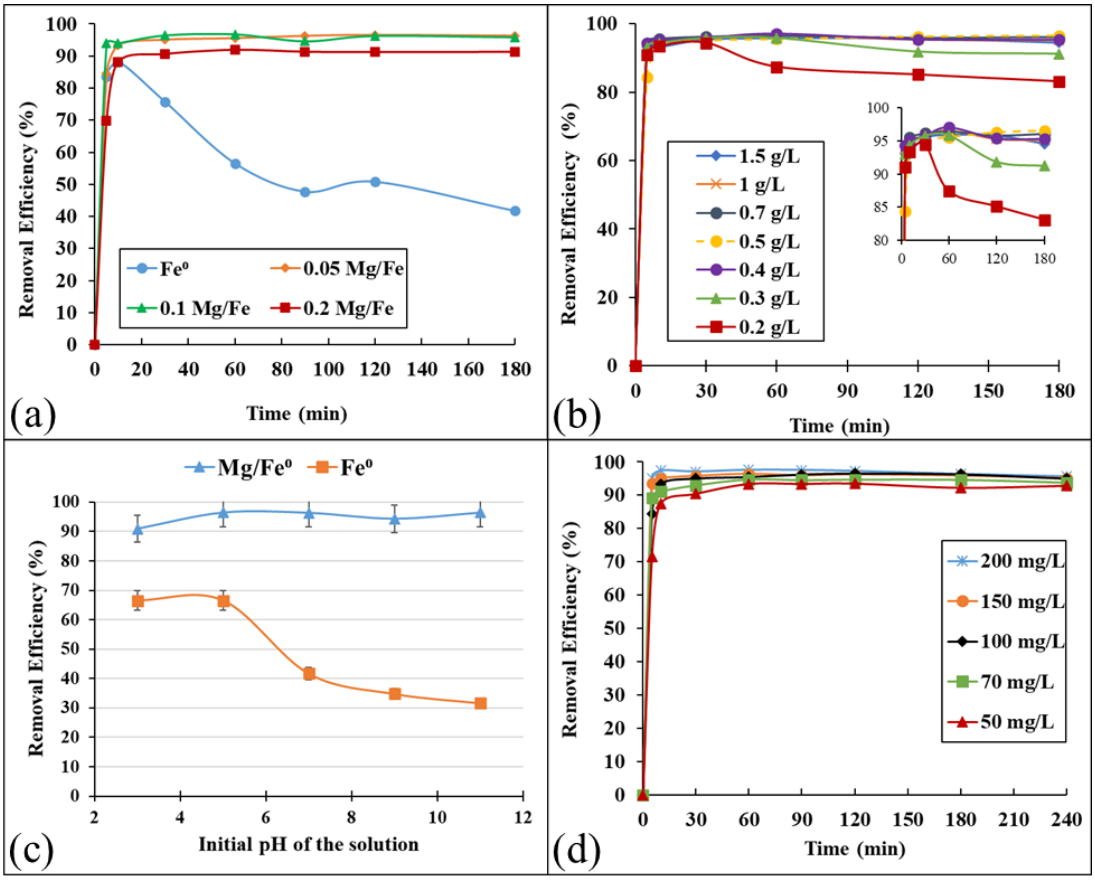

Figure 3.5 Effect of **(a)** [$Mg(HO)_2/Fe^0$] weight percentage and **(b)** dosage of Mg/Fe^0 nanoparticles,**(c)** initial pH of polluted water, and **(d)** initial CIP concentration.

This contradiction could be explained by the difference in the synthesis procedures of Fe^0 nanoparticles in this study and the previous studies. On the contrary, Figure 3.5.a illustrates that encapsulating Fe^0 nanoparticles by $Mg(OH)_2$ layer with a [$Mg(OH)_2/Fe^0$] weight ratio of 0.05 was enough to sharply enhance the removal of CIP, compared to Fe^0 nanoparticles, from 41.76% to 96.31%. Two hypotheses could explain this outstanding performance. The first hypothesis suggests that coating the surface of the highly reactive Fe^0 nanoparticles prevents the four electron-transfer reactions [Equations (3.1) and (3.2)] that hinder the Fenton reaction [Equation (3.3)] inside the Fe^0 environment by consuming the produced hydrogen peroxide [Equation (3.2)], which in turn deteriorates the oxidation of CIP by Fenton reaction [Equation (3.3)] [136]. However, the second hypothesis assumes that the presence of $Mg(OH)_2$ shell on the surface of Fe^0 nanoparticles strengthens the adsorption proportion by providing additional adsorption locations [199]. Both hypotheses will be tested in section 3.6, where the removal mechanism of CIP by Mg/Fe^0 nanoparticles will be clarified.

$$Fe_{(s)}^{0} + O_2 \rightarrow H_2O_2 + Fe^{2+} \text{ (Two electron-transfer reaction)} \quad \textbf{(3.1)}$$

$$Fe_{(s)}^{0} + H_2O_2 \rightarrow Fe^{2+} + H_2O \text{ (Two electron-transfer reaction)} \quad \textbf{(3.2)}$$

$$Fe^{2+} + H_2O_2 \rightarrow OH^{\cdot} \text{ and/or Fe(IV) (Fenton reaction)} \quad \textbf{(3.3)}$$

In the scope of determining the optimum [$Mg(OH)_2/Fe^0$] weight ratio that corresponds to the highest removal efficiency of CIP, the [$Mg(OH)_2$/ Fe^0] weight ratio further increased to 0.1 and 0.2. As shown in Figure 3.5.a, increasing the coating ratio of Fe^0 nanoparticles by $Mg(OH)_2$ from 0.05 to 0.1 and 0.2 slightly decreased the removal of CIP from 96.31% to 95.85% and 91.20%, respectively. The excessive precipitation of $Mg(OH)_2$ on the surface of Fe^0 nanoparticles may hide some reactive sites and prevent the dissolution of iron species as well as the electron transfer from the core of Fe^0 nanoparticles which may impact both the adsorption and oxidation of CIP by [0.1-Mg/Fe^0] and [0.2-Mg/Fe^0] nanoparticles [200]. According to Figure 3.5.a, the optimum weight ratio of [$Mg(OH)_2/Fe^0$] was 0.05. This ratio was used in the following experiments, and the nanomaterial with this ratio was named Mg/Fe^0 nanoparticles. According to our recent review, this study reported the remarkable removal of CIP by Mg/Fe^0 nanoparticles for the first time in the literature [69].

3.3. Effect of Mg/Fe^0 dosage and initial pH

The effect of Mg/Fe^0 dosage and initial pH on the uptake of CIP by Mg/Fe^0 nanoparticles from the water was investigated by alerting the value of each parameter as shown in Table 2.2, Figure 3.5.b, and Figure 3.5.c.

The weight of Mg/Fe^0 nanoparticles that should be added to a particular volume of CIP-polluted water must be controlled and optimized to minimize the treatment cost and facilitate the management of nanoparticles after the completion of the treatment process. Figure 3.5.b discloses the effect of increasing the dosage of Mg/Fe^0 nanoparticles from 0.2 to 1.5 g L^{-1} on removing 100 mg L^{-1} of CIP solution. Figure 3.5.b illustrated that 0.2 g L^{-1} of Mg/Fe^0 nanoparticles removed 83.12% of CIP after 180 min of reaction. However, increasing the dosage to 0.3, 0.4, and 0.5 g L^{-1} remarkably improved the removal efficiency to achieve 91.23%, 95.35%, and 96.54%, respectively. In contrast, increasing the dosage of Mg/Fe^0 nanoparticles from 0.5 to 0.7, 1, and 1.5 g L^{-1} slightly decreased the uptake percentage of CIP from 96.54% to 96.10%, 95.15%, and 94.56%,

respectively. This behavior might be attributed to the fact that increasing the dosage of Mg/Fe^0 nanoparticles will increase the aggregation between the particles, which may occupy or cover some of the reactive locations [201]. In conclusion, the optimum dosage of Mg/Fe^0 nanoparticles was selected to be 0.5 g L^{-1}, and this value was generalized in the subsequent experiments.

It is reported that the charge of the CIP molecule changes under different pH values [199]. For example, CIP becomes cationic molecule under pH < 6.1, zwitterionic molecule under 6.1 < pH < 8.1 and anionic molecule under pH > 8.6 [116]. Moreover, the influence of the pH is extended to alert the surface charge of the Mg/Fe^0 nanoparticles and promote or halt the release of iron ions which will affect the possible removal mechanisms such as adsorption and oxidation [202]. Thus, understanding the influence of initial pH on the removal of CIP by Mg/Fe^0 nanoparticles is important. Figure 3.5.c highlights the influence of initial pH on the efficacy of Fe^0 and Mg/Fe^0 nanoparticles in removing CIP from aqueous solutions. Figure 3.5.c emphasizes that removing CIP by Fe^0 nanoparticles was promoted under pH = 3, where the removal efficiency hit its maximum value of 66.56%. Comparable competence was also recorded at pH = 5. Conversely, the removal efficiency of CIP by Fe^0 nanoparticles pointedly deteriorated to 31.7% when the initial pH of the solution increased from 5 to 11. The acidic pH favors the corrosion and release of iron ions (e.g., Fe^{2+} and Fe^{3+}) form the core of Fe^0 nanoparticles which stimulate the oxidation of CIP by improving the generation of radicals inside the system [115]. These findings are consistent with the findings of Liu *at el.* as they remediated the antibiotic chloramphenicol from aquatic solutions at pH = 3 [203]. In contrast, the alkaline pH is not appropriate for the removal of CIP by Fe^0 nanoparticles as it encourages the formation of a passivation layer on the surface of Fe^0 nanoparticles which hides the reactive sites as well as hinders the dissolution of iron ions from the core of Fe^0 nanoparticles [120].

Surprisingly, encapsulating Fe^0 nanoparticles with a thin layer of $Mg(OH)_2$ neutralized the effect of pH on removing CIP from water by Mg/Fe^0 nanoparticles, as shown in Figure 3.5.c. In other words, more than 95% of 100 mg L^{-1} of CIP was removed by 0.5 g L^{-1} of Mg/Fe^0 nanoparticles when the initial pH changed from 5 to 11. However, the removal efficiency slightly declined to 90% under the strongly acidic pH (e.g., pH = 3). This drop might be due to the evolution of hydrogen gas inside the system, which prevents the adsorption of CIP on the surface of Mg/Fe^0 nanoparticles [203,204]. Since the pH of real

wastewater ranges from 6.5 to 8.5, it can be predicted that Mg/Fe^0 nanoparticles can be used to treat actual CIP-polluted waters with removal efficiencies exceeding 90% [205]. pH = 5 was selected as the optimum value and applied in the following experiments. Most of the proposed Fe^0-based nanomaterials in the literature prefer the acidic pH to remove CIP [119–121]. This behavior limits their application in real polluted sites. Moreover, Chen *et al.*, in both articles, tried to expand the pH working range of polyvinylpyrrolidone stabilized Fe^0/Cu bimetallic particles and green synthesized bimetallic Fe^0/Cu from (4-6) to (4-8) by applying a weak magnetic field during the treatment process [106,125]. Hence, this paper is the first to propose a nanomaterial with a wide working range of pH for eliminating CIP from polluted water.

The final pH of water at the end of the treatment process was also monitored to ensure the adequacy of discharging the treated water to nearby surface water bodies. Figure 3.6 illustrates that the final pH of the treated water notably increased from 3, 5, 7, 9, and 11 (Initial pH) to 8.6, 9.7, 10.23, 9.62, and 9.9 (Final pH). Partial dissolution of $Mg(OH)_2$ shell and corrosion of the core of Fe^0 nanoparticles will release hydroxide ions (OH^-) which in turn will increase the final pH of the treated water [206]. Based on Figure 3.6, the treated water by Mg/Fe^0 nanoparticles might need slight titration to neutral pH before discharging it to surface water bodies.

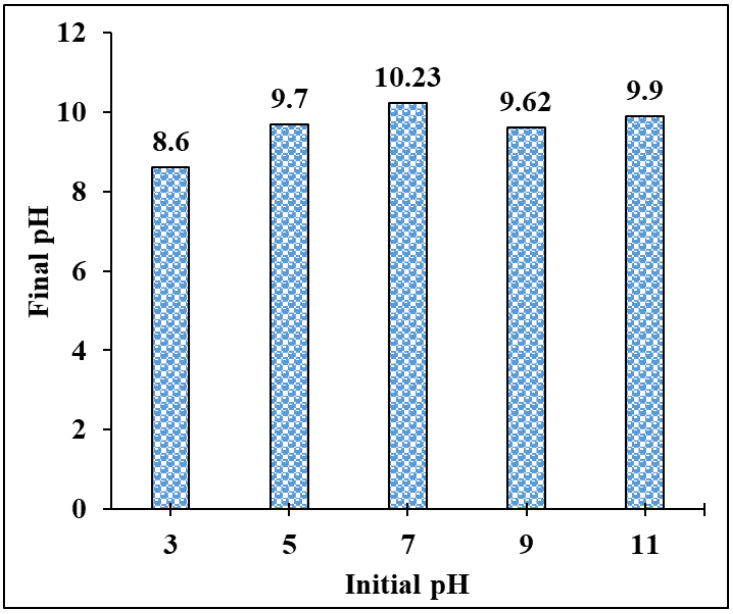

Figure 3.6 Monitoring the pH of the treated water at the end of the reaction. Treatment conditions were as follows: [Mg/Fe^0] = 0.5 g L^{-1}, [CIP] = 100 mg L^{-1}, temperature = 25 °C, and contact time = 180 min.

3.4. Effect of initial ciprofloxacin concentration

The effect of CIP initial concentration on the competence of Mg/Fe^0 nanoparticles was explored by increasing CIP initial concentration from 50 to 200 mg L^{-1}. Figure 3.5.d represents the efficiency of Mg/Fe^0 nanoparticles in treating CIP-polluted water with various initial concentrations (e.g., 50, 100, 150, and 200 mg L^{-1}). The effect of CIP initial concentration was notably minimized due to the extraordinary performance of Mg/Fe^0 nanoparticles to remove more than 93% of CIP over the studied range of concentrations, as demonstrated in Figure 3.5.d. Most of the previous research articles stated that the increasing the initial concentration of an antibiotic significantly deteriorate the uptake efficiency of the proposed nanomaterial [106,120,125,207,208]. For example, Demirezen *et al.* indicated that the removal rate of the antibiotic amoxicillin by iron oxide nanoparticles dimensioned from approximately 100% to less than 30% when the initial concentration of amoxicillin increased from 5 to 15 mg L^{-1} [209]. For the first time, this study offers a novel nanomaterial with outstanding performance in removing CIP regardless of CIP initial concentration in water.

3.5. Removal mechanism of ciprofloxacin by Mg/Fe^0 nanoparticles

Many sets of batch experiments were carried out with various objectives to experimentally identify the possible removal mechanisms of CIP by Mg/Fe^0 nanoparticles. Desorption tests were performed at different initial pH (e.g., 5, 7, 9, and 11) as depicted in section 2.5.3.1 to distinguish the contribution of adsorption and oxidation in the removal of CIP by Mg/Fe^0 nanoparticles. Figure 3.7 illustrates that after 180 min of CIP removal, the molecules of CIP started to desorb from the surface of the reacted Mg/Fe^0 nanoparticles after moving them to the desorbing solution (1 M NaOH) at 25 °C. The equilibrium of the desorption was quickly attained after approximately 30 min. Moreover, it can be noticed from Figure 3.7 that the initial pH of the solution during the adsorption can slightly affect the desorption of CIP from the surface of Mg/Fe^0 nanoparticles. For instance, 32.63% (39.2084 mg L^{-1}) of the total adsorbed molecules of CIP (94.813 mg L^{-1}) at pH = 5 were desorbed back to the aqueous solution. In contrast, the desorption percentage increased to 43.92%, 38.62%, and 43.92% when the initial pH elevated to 7, 9, and 11, respectively. Since the molecules of CIP were easily desorbed from the surface of Mg/Fe^0 nanoparticles, the percentages mentioned above could represent the proportion of the weak physisorption from the total removal efficiency,

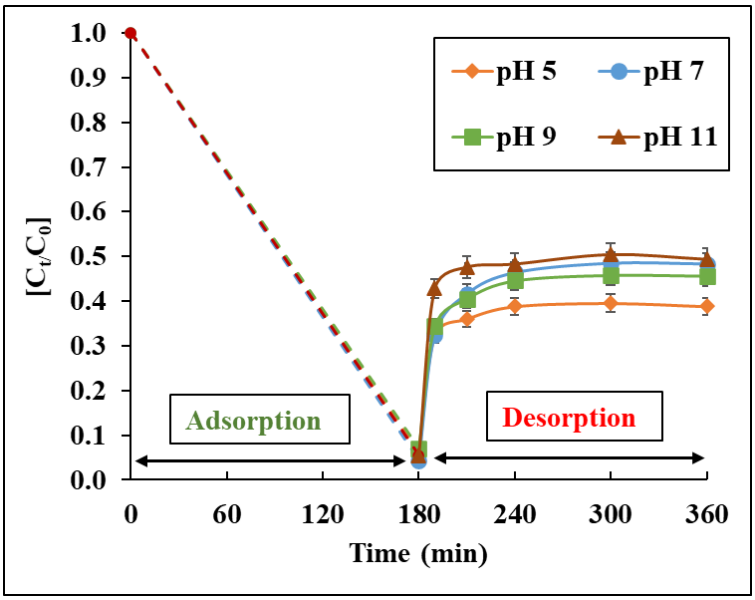

Figure 3.7 Desorption of CIP molecules after the adsorption by Mg/Fe^0 nanoparticles under different initial pH. The adsorption parameters were as follows: [Mg/Fe^0] = 0.5 g L^{-1}, [CIP] = 100 mg L^{-1}, temperature = 25 °C, and contact time = 180 min.

as displayed in Figure 3.8.a [210,211]. The neutral and alkaline pH promoted the development of iron oxides on the surface of Mg/Fe^0 nanoparticles, as displayed in the XRD patterns of the spent Mg/Fe^0 nanoparticles (Figure 3.4). Gu and Karthikeyan stated that the antibiotic CIP could be removed by aluminum and iron hydrous oxides [212]. Hence, the presence of iron oxides under neutral and alkaline conditions might be the reason behind the increase in physisorption proportion under these conditions.

The unknown part of the total removal efficiency could be either oxidation or chemical adsorption. The contribution of oxidation in the removal of CIP was defined by conducting batch experiments with the addition of 20 ml of 2-propanol to inhibit the possible generation of any oxidizing radicals (i.e., hydroxyl radicals) in the system. Figure 3.8.b indicates that adding 2-propanol didn't impede the exceptional performance of Mg/Fe^0 nanoparticles in removing CIP under different initial pH. These results confirm that the oxidation of CIP by Mg/Fe^0 nanoparticles is impossible, and chemisorption is the alternative mechanism. XRD analysis for Mg/Fe^0 nanoparticles after the reaction with CIP at different initial pH was conducted to support the experimental results. Figure 3.4 manifests that the XRD patterns of the spent Mg/Fe^0 nanoparticles over the studied pH range had several peaks identified as organic by-products related to CIP.

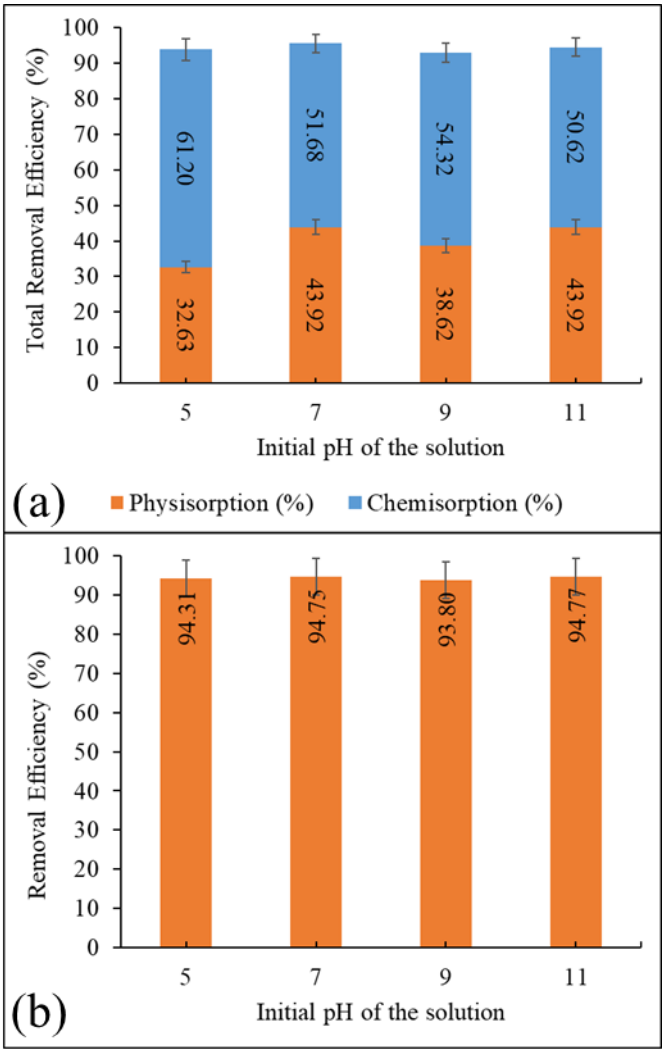

Figure 3.8 : (a) Contribution of physisorption and chemisorption in the adsorption of CIP at different initial pH and **(b)** removal of CIP with the addition of 2-propanol under different initial pH.

However, it is not appropriate to rely on these results to prove the occurrence of CIP oxidation because these by-products could be generated from the high temperature inside the XRD instrument during the analysis. Therefore, based on the results of the batch experiments, it can be said that the removal of CIP by Mg/Fe^0 nanoparticles was governed by both the physisorption and chemisorption processes. In addition, it is evident from these findings that CIP oxidation by Mg/Fe^0 nanoparticles didn't occur. It is worth mentioning that physisorption of CIP occurs on the high surface area of Mg/Fe^0 nanoparticles due to van der Waals forces or due to the electrostatic attraction between the opposite charges of CIP and Mg/Fe^0 nanoparticles [211]. On the other hand, chemisorption happens when iron species form a bidentate complex with the oxygen atoms of the carboxylic and keto groups in the structure of CIP [213,214].

3.6. Kinetics and isotherm analysis

Section 3.5 proved experimentally that the elimination of CIP by Mg/Fe^0 nanoparticles was completely controlled by adsorption. Hence, it is essential to perform kinetics and isotherm modeling for the adsorption of CIP by Mg/Fe^0 nanoparticles, as their findings could help to elaborate on the nature of the adsorption.

Four kinetic models, namely, Pseudo first-order, Pseudo second-order, intraparticle diffusion, and Elovich models, were used to represent the kinetics data. The outcomes of kinetics analysis and Akaike's Information Criterion (AIC) are epitomized in Table 3.1 and Figure 3.9. Figure 3.9 articulates that the reaction between Mg/Fe^0 nanoparticles and CIP in water was fast where the equilibrium was reached only after 10 min of starting the reaction despite changing the initial concentration from 50 to 200 mg L^{-1}. In addition, Table 3.1 indicates strong competition between Pseudo-first-order and Pseudo-second-order models to describe the kinetics of CIP adsorption by Mg/Fe^0 nanoparticles because of the high convergence between the experimental and the obtained data as well as the high R^2 for both models. Although Akaike's Information Criterion (AIC) was applied to select the best fitted kinetic model, the displayed AIC values in Table 3.1 for the two models are also close to each other. This conclusion recommends that the adsorption of CIP by Mg/Fe^0 nanoparticles was possibly controlled by both physisorption and chemisorption processes [179,180]. This suggestion agrees with the outcomes of the desorption experiments (Figure 3.7 and Figure 3.8). In contrast, intraparticle diffusion and Elovich models were excluded from the kinetic analysis due to the high values of AIC, low values of $R^{2,}$ and misrepresentation of the experimental data, as stated in Figure 3.9 and Table 3.1.

Langmuir, Freundlich, Temkin, and Dubinin-Radushkevich isotherm models were utilized to describe the equilibrium data, as manifested in Figure 3.10 and Table 3.2. From Table 3.2, the Freundlich isotherm model owns the lowest AIC value (57.05), which suggests the occurrence of multilayer adsorption of CIP on the heterogeneous surface of Mg/Fe^0 nanoparticles [185]. Since the value of (1/n) is greater than unity (i.e., 1.426), it indicates that the elimination of CIP by Mg/Fe^0 nanoparticles was govern by a cooperative adsorption process [184]. The results of isotherm analysis are consistent with the conclusions of kinetics analysis.

Table 3.1 Experimental data and kinetic parameters for Pseudo first-order, second-order, intraparticle diffusion, and Elovich models.

Experimental data		**Pseudo-first-order model**			
[CIP] (mg L^{-1})	**Adsorption capacity (mg g^{-1}), q_e**	**$q_{e,model}$ (mg g^{-1})**	**K_1 (min^{-1})**	**R^2**	**AIC**
50	99.27	99.03	0.30	0.99	9.74
70	140.19	140.30	0.59	0.99	18.57
100	178.27	179.46	0.42	0.99	12.54
150	305.04	307.07	0.74	0.99	15.18
200	408.14	413.94	0.80	0.99	27.72
Experimental data		**Pseudo-second-order model**			
[CIP] (mg L^{-1})	**Adsorption capacity (mg g^{-1}), q_e**	**$q_{e,model}$ (mg g^{-1})**	**K_2 (g mg^{-1} min^{-1})**	**R^2**	**AIC**
50	99.27	101.11	0.0073	0.99	23.05
70	140.19	141.40	0.022	0.99	3.65
100	178.27	181.51	0.0086	0.99	23.43
150	305.04	307.95	0.026	0.99	13.67
200	408.14	414.29	0.036	0.99	30.94
Experimental data		**Intraparticle diffusion model**				
[CIP] (mg L^{-1})	**Adsorption capacity (mg g^{-1}), q_e**	**$q_{e,model}$ (mg g^{-1})**	**K_{intra} (mg g^{-1} $min^{1/2}$)**	**C_{intra} (mg g^{-1})**	**R^2**	**AIC**
50	99.27	117.20	4.06	54.28	0.43	67.51
70	140.19	164.32	5.10	85.31	0.33	75.22
100	178.27	210.34	6.74	105.96	0.36	79.21
150	305.04	356.63	10.65	191.71	0.30	89.78
200	408.14	478.32	14.01	261.26	0.29	95.35

Table 3.1 Experimental data and kinetic parameters for Pseudo first-order, second-order, intraparticle diffusion, and Elovich models (cont.).

Experimental data		Elovich model				
[CIP] (mg L^{-1})	**Adsorption capacity (mg g^{-1}), q_e**	**$q_{e,\ model}$ (mg g^{-1})**	**α (mg g^{-1} min^{-1})**	**β (mg g^{-1})**	**R^2**	**AIC**
50	99.27	124.93	53.03	0.052	0.78	62.67
70	140.19	171.02	370.50	0.049	0.80	66.78
100	178.27	214.40	667.77	0.041	0.85	68.58
150	305.04	345.11	103024.93	0.04	0.92	71.27
200	408.14	467.15	5504.65	0.022	0.84	83.67

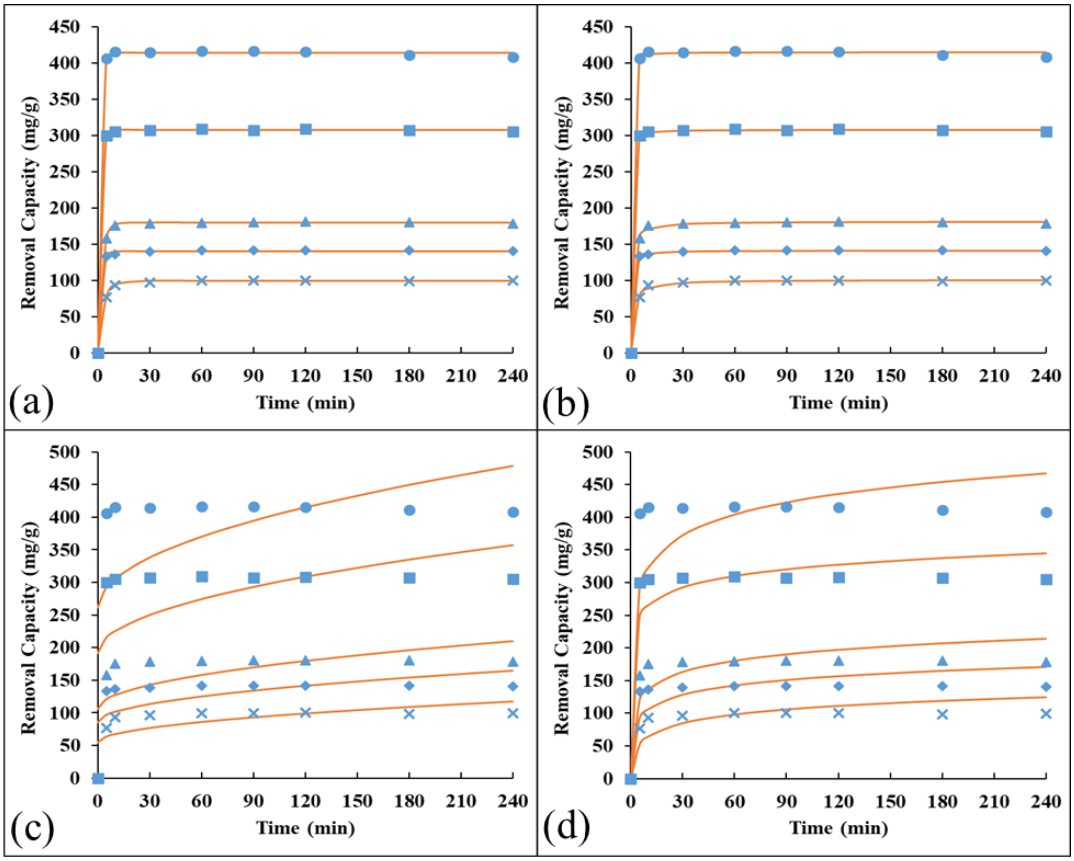

Figure 3.9 Kinetics analysis for CIP adsorption by Mg/Fe^0 nanoparticles. Adsorption conditions were as follows: $[Mg/Fe^0]$ = 0.5 g L^{-1}, initial pH = 5, temperature = 25 °C, [CIP] = 50 [×], 70[♦], 100[▲], 150[■], and 200[●] mg L^{-1}, and contact time = 240 min. The orang line represents the following kinetic models: **(a)** Pseudo first-order, **(b)** Pseudo second-order, **(c)** Intraparticle diffusion, and **(d)** Elovich.

Table 3.2 Isotherm analysis for CIP adsorption by Mg/Fe^0 nanoparticles.

Experimental data		**Freundlich Isotherm**				
Initial CIP con., C_i (mg L^{-1})	Adsorption capacity (mg g^{-1})	Freundlich adsorption capacity (mg g^{-1})	Freundlich isotherm constant, K_f [(mg/g)(mg/L)$^{1/n}$]	Adsorption intensity (n)	R^2	AIC
50	99.27	114.43	16.84	0.70	0.98	57.05
70	140.19	149.96				
100	178.27	150.72				
150	305.04	310.54				
200	408.14	406.28				
Experimental data		**Langmuir Isotherm**				
Initial CIP con., C_i (mg L^{-1})	Adsorption capacity (mg g^{-1})	Langmuir adsorption capacity (mg g^{-1})	Maximum adsorption capacity, q_e (mg g^{-1})	Langmuir constant (K_{ads}) (L mg $^{-1}$)	R^2	AIC
50	99.27	150.54	372415.75	0.00011	0.98	65.61
70	140.19	181.95				
100	178.27	182.595				
150	305.04	303.015				
200	408.14	365.78				
Experimental data		**Temkin Isotherm**				
Initial CIP con., C_i (mg L^{-1})	Adsorption capacity (mg g^{-1})	Temkin adsorption capacity (mg g^{-1})	Temkin isotherm equilibrium binding constant, A_T (L g^{-1})	Temkin isotherm constant, b_T	R^2	AIC
50	99.27	95.13	0.35	7.46	0.976	58.62
70	140.19	158.15				
100	178.27	159.33				
150	305.04	327.83				
200	408.14	390.47				

Table 3.2 Isotherm analysis for CIP adsorption by Mg/Fe^0 nanoparticles (cont.).

Experimental data			Dubinin-Radushkevich Isotherm			
Initial CIP con., C_i (mg L^{-1})	Adsorption capacity (mg g^{-1})	Dubinin-Radushkevich adsorption capacity (mg g^{-1})	Theoretical isotherm saturation capacity, q_s (mg g^{-1})	Dubinin–Radushkevich isotherm constant, K_{ad} (mol^2 J^{-2})	R^2	AIC
50	99.27	98.90	512.46	4.981E-06	0.967	60.74
70	140.19	159.17				
100	178.27	160.37				
150	305.04	325.34				
200	408.14	372.84				

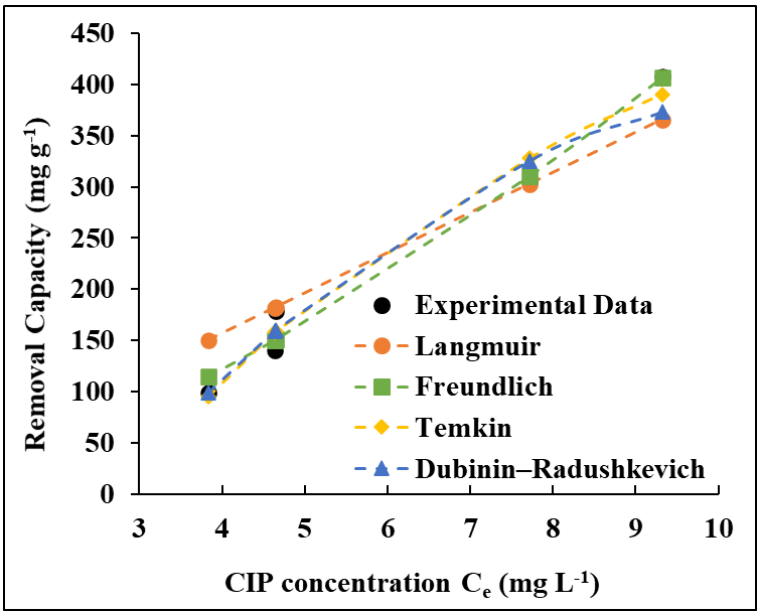

Figure 3.10 Isotherm analysis for CIP adsorption by Mg/Fe^0 nanoparticles. Adsorption conditions were as follows: [Mg/Fe^0] = 0.5 g L^{-1}, initial pH = 5, temperature = 25 °C, [CIP] = (50–200) mg L^{-1}, and contact time = 240 min.

3.7. Effect of temperature and thermodynamic analysis

The impact of temperature on the performance of Mg/Fe^0 nanoparticles in removing different concentrations of CIP was studied by gradually increasing the temperature of reaction from 25 to 55 °C, as exhibited in Table 2.2 and Figure 3.11. Figure 3.11 reveals that the progressive rise of temperature from 25 to 55 °C negatively affected the adsorption of 100 mg L^{-1} of CIP by Mg/Fe^0 nanoparticles because the removal efficiency decreased from 95.04% to 72.87%. This confirms that the reaction between CIP and Mg/Fe^0 nanoparticles was exothermic.

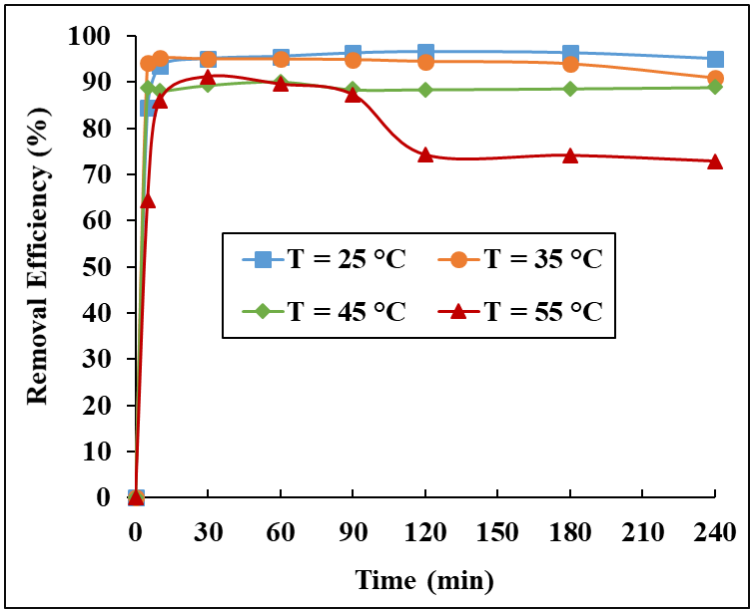

Figure 3.11 Impact of temperature on the adsorption of CIP by Mg/Fe^0 nanoparticles. Adsorption conditions were as follows: [Mg/Fe^0] = 0.5 g L^{-1}, initial pH = 5, [CIP] = 100 mg L^{-1}, and contact time = 240 min.

Thermodynamic analysis was performed as described in section 2.8.5 to give more insights into the reaction nature between CIP and Mg/Fe^0 nanoparticles. Figure 3.12 displays the application of Van't Hoff equation [Equation (2.28)] to obtain the values of ΔH^0 and ΔS^0. The coefficient of determination (R^2) after the application of Van't Hoff equation was 0.9996, as demonstrated in Figure 3.12. However, it is essential to point out that the experimental data of CIP adsorption at 45 °C were excluded from the thermodynamic analysis because it significantly decreased the value of R^2. Afterwards, the 3rd principle of thermodynamics [Equation (2.27)] was employed to determine the magnitudes of ΔG^0 at different reaction temperatures. The magnitudes of thermodynamic parameters were summarized in Table 3.3. The negative value of ΔH^0 suggests that the reaction between CIP and Mg/Fe^0 nanoparticles was exothermic [195]. Moreover, since the magnitude of ΔH^0 (i.e. -172.994) is between 80 and 200 KJ mol^{-1}, it elucidates that the adsorption of CIP was controlled by a chemical adsorption process [196]. Furthermore, Table 3.3 illustrates that the sign of ΔG^0 in all temperatures is negative which proves the spontaneity of the reaction between CIP and Mg/Fe^0 nanoparticles [215]. On the other hand, the negative sign of ΔS^0 tells that the randomness at the solid-liquid interface and the degree of freedom of the adsorbed molecules of CIP were decreasing during the adsorption process [199]. Similar findings were reported by Wang *et al.* when they attempted to remediate CIP from polluted waters using $Mg(OH)_2$ powder [199].

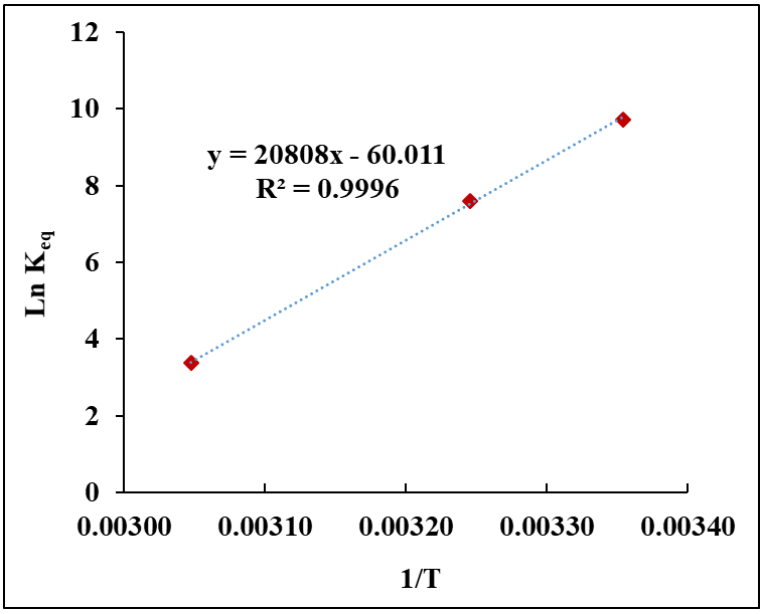

Figure 3.12 Thermodynamics analysis for the adsorption of CIP by Mg/Fe^0 nanoparticles.

Table 3.3 Thermodynamic parameters for the adsorption of CIP by Mg/Fe^0 nanoparticles.

T	K_d	ΔG^0 (kJ mol^{-1})	ΔH^0 (kJ mol^{-1})	ΔS^0 (kJ mol^{-1} K^{-1})
25	16841.52	-24.24	-172.99	-0.49
35	1969.52	-19.25		
55	29.15	-9.27		

3.8. Reusability of Mg/Fe^0 nanoparticles for many adsorption cycles

One of the biggest challenges for adsorption technology in wastewater treatment applications is sludge generation after treatment. However, recycling of adsorbents for several adsorption processes reduces the volume of the generated sludge after the treatment. Therefore, Mg/Fe^0 nanoparticles were reused for five successive adsorption processes. It is important to highlight that the time for CIP adsorption and desorption was considerably decreased from 240 min (Adsorption) and 180 min (Desorption) to only 60 min as the results of the adsorption and desorption kinetics (Sections 3.5 and 3.6) demonstrated that the equilibrium time for these processes was one hour. Figure 3.13 manifests the successful recycling of Mg/Fe^0 nanoparticles for five sequent adsorption cycles with no deterioration in the removal efficiency.

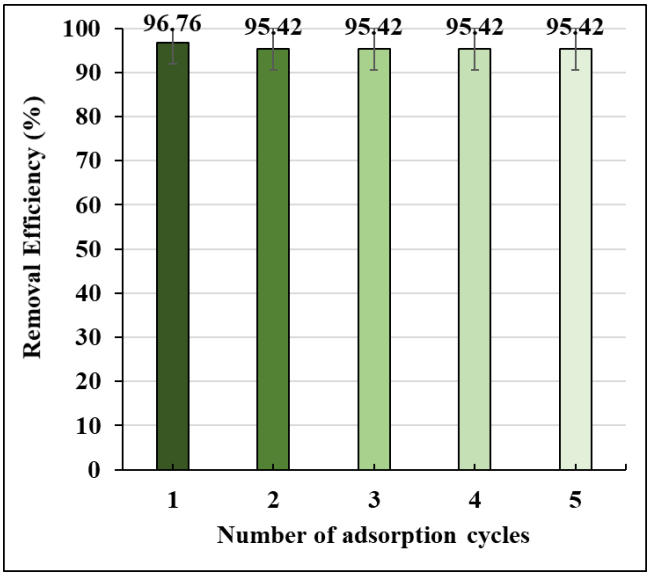

Figure 3.13 Reusability of Mg/Fe^0 nanoparticles for several treatment cycles. Adsorption conditions were as follows: $[Mg/Fe^0]$ = 0.5 g L^{-1}, [CIP] = 100 mg L^{-1}, volume of solution: 1L, temperature = 25 °C, and contact time = 60 min. Desorption conditions were as follows: desorption medium: 1M NaOH, volume of solution: 200 ml, temperature: 25°C, mixing speed = 1000 rpm, and desorption time = 60 min.

In other words, Mg/Fe^0 nanoparticles exhibited an excellent performance in eliminating CIP with removal efficiencies higher than 95% during the five treatment cycles where 0.5 g of Mg/Fe^0 nanoparticles were able to treat 5 L of 100 mg L^{-1} of CIP-polluted water. It also can be anticipated from Figure 3.13 that Mg/Fe^0 nanoparticles can endure more than five adsorption cycles. This reflects the suitability of Mg/Fe^0 nanoparticles in field-scale applications as they can significantly reduce the volume of the generated sludge and most importantly the treatment cost.

3.9.Performance of Mg/Fe^0 in a prototype treatment system

At this stage of the research, the outcomes of the optimization process were applied to design and fabricate, for the first time, a prototype lab-scale treatment system to treat large volumes of CIP-polluted water. Figure 2.3 shows the schematic diagram of the proposed treatment system. In addition, Table 3.4 illustrates that three treatment cycles were operated under the optimal conditions, but with changing the flow rate from 25 to 75 ml min^{-1} to investigate the flow rate's effect on the competence of treatment system.

Table 3.4 Operational paramters of the prototype treatment system.

Cycle No.	Flow rate (mL min^{-1})	Mg/Fe^0 dosage (g L^{-1})	Temperature (°C)	Initial pH	Mixing speed (rpm)	Recycling system
1	25	0.5	25 °C	6	250	Yes
2	50	0.5	25 °C	6	250	Yes
3	75	0.5	25 °C	6	250	Yes

Figure 2.3 also demonstrates that the chemical characteristics of water that flows out from the reactor, separation unit, aeration tank, and sand filtration column are noted as U1, U2, U3 and U4, respectively. Figure 3.14 summarizes the results of the treatment process in the three cycles. In the first cycle, the reactor (U1) showed a remarkable performance in removing more than 94% of CIP in the first hour of operation (Figure 3.14.a). However, the efficiency of the reactor started to deteriorate with time due to the continuous flow of the polluted water until it reached approximately 30% at the end of the treatment process. This trend indicates that the adsorption sites of Mg/Fe^0 nanoparticles were fully occupied with the molecules of CIP, and no extra molecules can be adsorbed on the surface of Mg/Fe^0 nanoparticles. On the other hand, the separation unit (U2) and aeration tank (U3) did not contribute to the removal process because they were only designed to separate the solid particles from the water and produce clean effluents. In contrast, the sand filtration column (U4) exhibited an unexpected and extraordinary performance in removing the residues of CIP from water, although it was only designed to remove the discharged particles from the separation unit and the aeration tank. Figure 3.14.a indicates that the sand filtration unit removed more than 50% of CIP in the fifth hour of operation. This percentage gradually increased to approximately 65% at the end of the treatment process due to the exhaustion of Mg/Fe^0 nanoparticles in the reactor (U1). Our previous article proved that the utilized sand in the filtration column had some zeolite impurities [147]. In addition, several researchers reported that CIP could be adsorbed by zeolitic materials [216,217]. Thus, the presence of zeolite impurities in the sand is responsible for the exceptional capability of the sand filtration column in removing the rest of CIP concentration. Figure 3.14.b and Figure 3.14.c demonstrate that increasing the flow rate from 25 to 50 and 75 mL min^{-1} accelerated the depletion of the reactivity of Mg/Fe^0

nanoparticles in the reactor (U1), where the removal efficiency of CIP decreased from 94.25% to 56.94% and 42%, respectively, within the first hour of the treatment process.

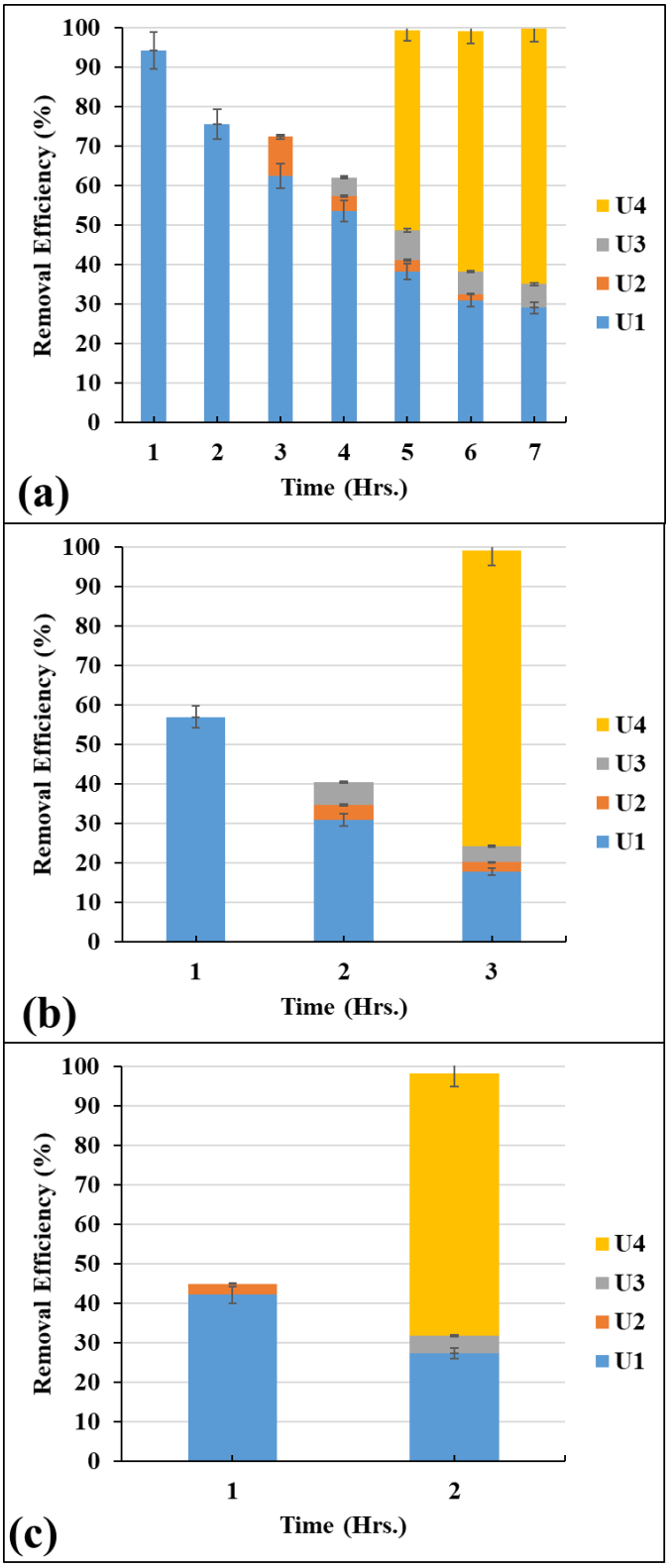

Figure 3.14 Competence of the prototype treatment system in the elimination of CIP by Mg/Fe^0 nanoparticles. The treatment parameters were as follows: flow rate: **(a)** 25, **(b)** 50 and **(c)** 75 mL min^{-1}, [CIP]: 100 mg L^{-1}, volume of CIP-polluted water = 10 L, [Mg/Fe^0]: 0.5 g L^{-1}, temperature: 25 °C and mixing speed: 250 rpm.

Similar to the first cycle, a further decline in the reactor's efficiency (U1) was noticed in the later stages due to the continual inflow of CIP-polluted water. Despite the poor performance of the reactor (U1), the sand filtration column (U4) succeeded in rejecting the residual concentrations of CIP and generating pure water, which can be directedly released to any surface water bodies without any further treatment. In summary, the optimum flow rate of the prototype treatment system is 25 ml min^{-1} to extend the life span of Mg/Fe^0 nanoparticles in the reactor. Furthermore, this flow rate will elongate the lifetime of the sand column and reduce the required times for cleaning or changing the sand inside the column. In the end, it is evident from Figure 3.14 that the components of the proposed treatment system could achieve 100% overall removal efficiency of CIP and generate clean water with no residues of CIP. These results are promising; however, it is vital to investigate the performance of the prototype treatment system in removing CIP from pharmaceutical wastewater, hospital wastewater as well as the effluents of traditional wastewater treatment plants as they contain many other contaminants which may decrease the efficiency of Mg/Fe^0 nanoparticles in removing CIP [218]. Also, it is crucial to estimate the cost of using Mg/Fe^0 nanoparticles and the prototype treatment system in real-scale applications. However, it is difficult to assess the cost of the treatment process at this stage because many factors will affect the overall cost, such as the volume of polluted water, required amounts of Mg/Fe^0 nanoparticles, and location of the contaminated sites (i.e., Transportation cost of equipment and materials) [218].

3.10. Storage and transportation of Mg/Fe^0 nanoparticles

It is essential to study the effect of storage time and storage conditions on the adsorption of CIP by Mg/Fe^0 nanoparticles to reveal the applicability of employing Mg/Fe^0 nanoparticles in remediating real contaminated sites. Figure 3.15.a elucidates that storing Mg/Fe^0 nanoparticles in empty containers at room temperature for 10 and 30 days insignificantly decreased the removal of CIP from 94.39% to 92.48% and 90.99%, respectively. The prolongated reactivity of Mg/Fe^0 nanoparticles is attributed to the presence of a magnesium hydroxide shell on the surface of Fe^0 nanoparticles as it preserves the core of Fe^0 nanoparticles from the fast oxidation over time [200,219]. Hu *et al.* declared that encapsulating Fe^0 nanoparticles with a magnesium hydroxide shell would decrease the corrosion of Fe^0 nanoparticles to less than 3% [220].

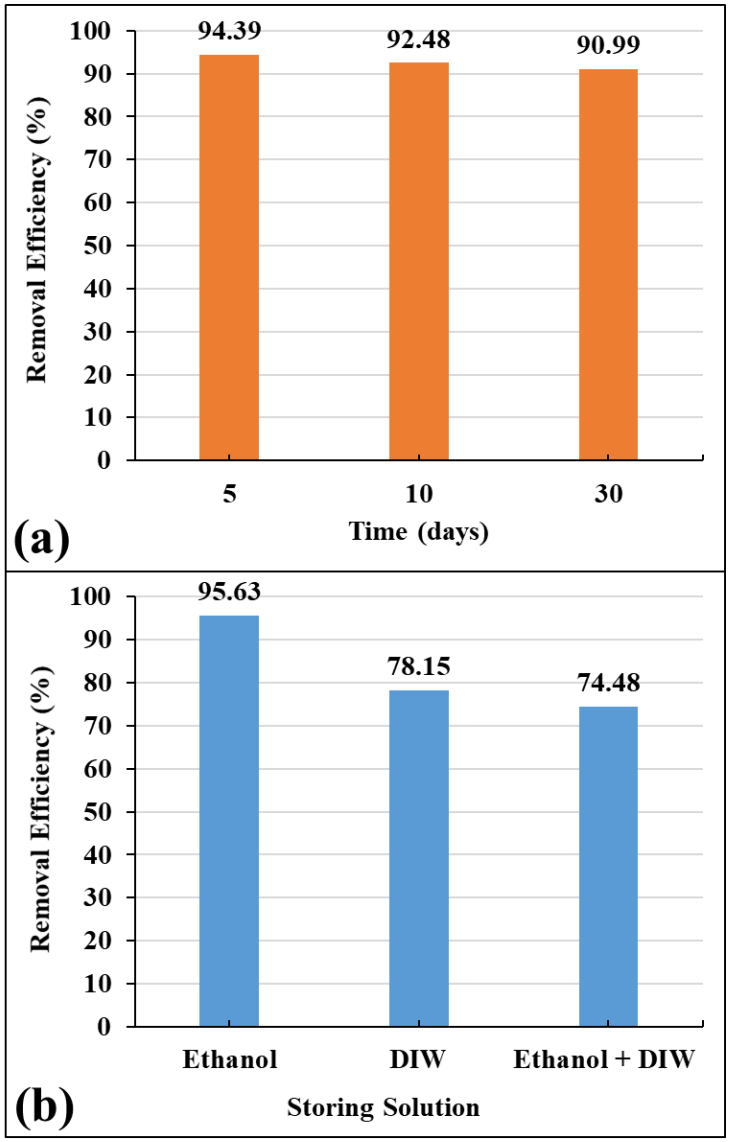

Figure 3.15 Longevity tests for Mg/Fe^0 nanoparticles stored in **(a)** empty bottles, and **(b)** different mediums for 30 days.

Furthermore, Figure 3.15.b shows that storing Mg/Fe^0 nanoparticles in ethanol for 30 days preserved their excellent efficiency towards CIP elimination from water. These results are in good agreement with the results of Ahmed *et al.* as they stored Fe^0 nanoparticles in ethanol for 10 months and used it to remove lead (Pb^{2+}) from water [221]. They revealed that storing Fe^0 nanoparticles particles for a long time in ethanol didn't show any significant changes in the morphology or the crystalline structure of Fe^0 nanoparticles. Furthermore, they reported that the efficiency of Fe^0 nanoparticles towards removing lead from the water wasn't affected by the storing condition. However, Figure 3.15.b indicates that 17.48% and 21.15% of Mg/Fe^0 nanoparticle's efficiency were sacrificed when the nanoparticles were stocked for 30 days in deionized water (DIW) and the mixture of deionized water and ethanol, respectively. These results manifest that a 5%

coating ratio of [$Mg(OH)_2/Fe^0$] wasn't sufficient to protect the core of Fe^0 nanoparticles from the aggressive aqueous corrosion. Hence, Mg/Fe^0 nanoparticles can be easily transported from the production facility to the contaminated locations by storing them in well-closed containers with no liquid mediums. However, if it is intended to utilize Mg/Fe^0 nanoparticles after a long time, it is preferred to store them in ethanol to achieve better performance.

3.11. Comparison between the performance of Mg/Fe^0 nanoparticles and other reported iron-based nanomaterials

The superiority of Mg/Fe^0 nanoparticles in removing CIP from the water was highlighted by making a reliable comparison between the performance of Mg/Fe^0 nanoparticles and some of the reported iron-based nanomaterials in the literature, as summarized in Table 3.5. It is evident from Table 3.5 that Mg/Fe^0 nanoparticles exhibit remarkable removal efficiencies compared with most of the reported iron-based nanomaterials under similar treatment conditions. In addition, Mg/Fe^0 nanoparticles promote the exceptional uptake of CIP from water without the need for external magnetic fields that may increase the cost of the treatment process or hinder their application in real contaminated sites [106,125].

Table 3.5 Reliable comparison between the efficiency of Mg/Fe^0 nanoparticles and previously reported iron-based nanomaterials in remediating CIP-polluted water.

Applied iron-based nanomaterials or systems	Experimental conditions	Removal efficiency (%)	The removal efficiency of CIP by Mg/Fe^0 under comparable conditions	Ref.
Zero-valent iron (ZVI)	[ZVI] = 2.5 g L^{-1}, [CIP] = 65µM, pH = 6.5, and contact time = 120 min.	85%	92.83%	[114]
Activation of persulfate by zero-valent metal (ZVI)	[Persulfate] = 2.25 mM, [ZVI] = 126 mg L^{-1}, [CIP] = 30 µM, pH = 3, and contact time = 60 min.	84.5%	92.83%	[115]
Activation of persulfate by nano zero-valent iron (nZVI)	[Persulfate] = 1200 mg L^{-1}, [nZVI] = 120 mg L^{-1}, [CIP] = 50 mg L^{-1}, pH = 4.5, and contact time = 60 min.	57%	92.83%	[123]

Table 3.5 Reliable comparison between the efficiency of Mg/Fe^0 nanoparticles and previously reported iron-based nanomaterials in remediating CIP-polluted water (cont.).

Applied iron-based nanomaterials or systems	Experimental conditions	Removal efficiency (%)	The removal efficiency of CIP by Mg/Fe^0 under comparable conditions	Ref.
Activation of Persulfate by sulfide-modified nanoscale iron supported by biochar (S-nZVI/BC)	[Persulfate] = 1 mM, S-[nZVI/BC] = 0.4 g L^{-1}, S/Fe molar ratio = 0.25, [CIP] = 50 mg L^{-1}, pH = 5, and contact time = 60 min.	89.78%	92.83%	[120]
Activation of persulfate by a granular adsorbent-supported Fe/Ni nanoparticle	[Persulfate] = 10mM, [Ni@PGA] = 0.1g, [CIP] = 100 mg L^{-1}, pH = 3.0, temperature = 30°C, and contact time =12 h.	93.24%	95.04%	[121]
Activation of H_2O_2 by biochar-supported nanoscale zerovalent iron (BC-nZVI)	[H_2O_2] = 20 mM, BC:nZVI = 1:1, [BC-nZVI] = 0.4 g L^{-1}, [CIP] = 100 mg L^{-1}, pH = 3~4, temperature = 25°C, and contact time = 60 min.	70%	95.04%	[119]
Ultrasonic enhanced zero-valent iron (nZVI)-based Fenton reaction	[H_2O_2] = 3 mM, [nZVI] = 117 mg L^{-1}, [CIP] = 100 mg L^{-1}, pH = 7, aeration = 1.61 L min^{-1}, and contact time = 60 min.	94%	95.04%	[122]
Polyvinylpyrrolidone stabilized NZVI/Cu bimetallic particles (PVP-NZVI/Cu)	[nZVI] = 0.5 g L^{-1}, nZVI/Cu = 1:0.04, [CIP] = 100 mg L^{-1}, pH = 6, weak magnetic field = 2 mT, temperature = 35°C, and contact time = 120 min.	98.4%	95.04%	[106]
Green synthesized bimetallic GT-nZVI/Cu composites	[GT-nZVI/Cu] = 0.5 g L^{-1}, GT-nZVI/Cu = 1/0.08, [CIP] = 30 µM, pH = 6, weak magnetic field = 5mT, temperature = 35°C, and contact time = 90 min.	100%	92.83%	[125]

3.12. Economic Evaluation of Mg/Fe^0 nanoparticles for environmental remediation

One of the challenges of nanomaterials in water and wastewater treatment applications is the high cost of nanomaterial synthesis. Therefore, it is essential to ensure that the treatment cost of CIP-polluted water by Mg/Fe^0 nanoparticles is more cost-effective than that of Fe^0 nanoparticles. This section compares the treatment cost of 100 mg L^{-1} of CIP-polluted water by Fe^0 and Mg/Fe^0 nanoparticles by taking into consideration only the cost of the nanomaterial synthesis. At the same time, the other parameters (e.g., energy, labor, transportation, etc.) are assumed to be constant. According to Figure 4.7.a, 0.7 g L^{-1} of Fe^0 nanoparticles was necessary to treat 100 mg L^{-1} of CIP-polluted water with 96.10% removal efficiency. On the other hand, Figure 3.5.b illustrates that 0.4 g L^{-1} of Mg/Fe^0 nanoparticles was enough to remediate 95.35% of 100 mg L^{-1} of CIP-polluted water. Table 3.6 shows the estimation cost for treating 1 L of 100 mg L^{-1} of CIP by Fe^0 and Mg/Fe^0 nanoparticles. The cost of employing Fe^0 nanoparticles to remediate CIP-polluted water is around 65.72¥/L. In contrast, as demonstrated in Table 3.6, the utilization of Mg/Fe^0 nanoparticles increases the treatment cost of CIP-polluted water to nearly 88.51¥/L. This increase (i.e., 34.68%) is associated with the use of ethanol in preparing Mg^{2+} and NaOH stock solutions, as the cost of 1L of ethanol is approximately 2395.56¥. Therefore, to decrease the cost of producing Mg/Fe^0 nanoparticles and the overall treatment process, it is recommended to examine the utilization of deionized water or distilled water instead of ethanol. However, it is essential to highlight that Mg/Fe^0 nanoparticles were reused for at least five treatment cycles with a trivial drop in performance (Figure 3.13) which would significantly decrease the overall treatment cost of CIP-polluted water. Conversely, Fe^0 nanoparticles couldn't be recycled for several treatment processes, and it is required to produce new Fe^0 nanoparticles for each treatment process. Finally, according to the previous discussion, it can be said that the utilization of Mg/Fe^0 nanoparticles to clean up CIP-polluted water is more cost-efficient than that of Fe^0 nanoparticles.

Table 3.6 Estimation cost for treating CIP-polluted water by iron-based nanomaterials.

Cost of chemicals	
Chemical name	***Price***
$FeCl_3$ (¥/g)	5.4
$NaBH_4$ (¥/g)	30.4
$MgCl_2$ (¥/g)	3.2
NaOH (¥/g)	1.8
Ethanol (¥/L)	2395.56
Preparation of 2 g L^{-1} of Mg^{2+} solution	
Required item	***Quantity***
Volume of ethanol (L)	1
Required mass of Mg^{2+} (g)	2
Required mass of $MgCl_2$ (g)	16.73
Preparation cost of 2 g L^{-1} of Mg^{2+} = ***2449.09 ¥/L***	
Preparation of 6 g L^{-1} of NaOH solution	
Required item	***Quantity***
Volume of ethanol (L)	1
Required mass of NaOH (g)	6
Preparation cost of 6 g L^{-1} of NaOH = ***2406.36 ¥/L***	
Preparation of 1 g of Fe^0 nanoparticles	
Required item	***Quantity***
Required mass of $FeCl_3$ (g)	5
Required mass of $NaBH_4$ (g)	2.2
Preparation cost of Fe^0 nanoparticles = ***93.88 ¥/g***	
Preparation of 1 g of Mg/Fe^0 nanoparticles	
Required item	***Quantity***
Required volume of Mg^{2+} solution (mL)	25
Required volume of NaOH (mL)	27.5
Preparation cost of Mg/Fe^0 nanoparticles = **221.28 ¥/g**	

Table 3.6 Estimation cost for treating CIP-polluted water by iron-based nanomaterials (cont.).

Estimation cost of remediating 1 L of 100 mg L^{-1} of CIP-polluted water by iron-based nanoparticles	
Nanomaterial	***Cost (¥/L)***
Fe^0 nanoparticles	65.72
Mg/Fe^0 nanoparticles	88.51

Chapter 4

Promotion of ciprofloxacin adsorption from contaminated solutions by oxalate-modified nanoscale zerovalent iron particles

Graphical Abstract:

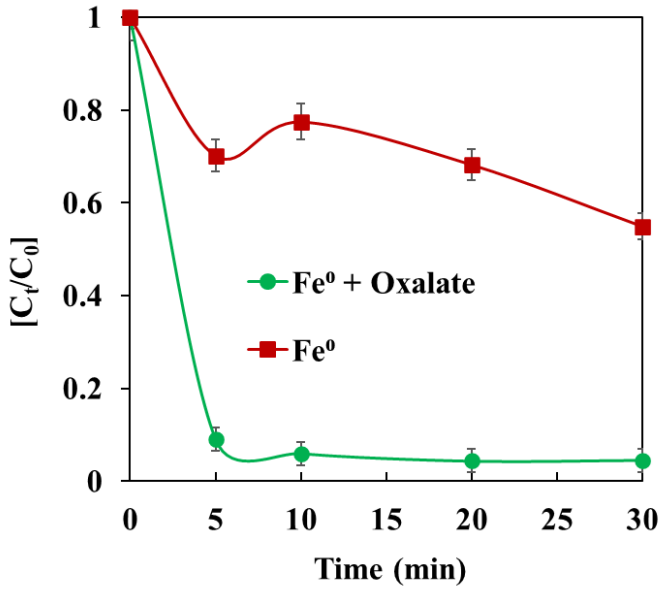

Advantages of oxalate addition to Fe^0

CIP removal improved from 45.04% to 95.74%.

55.68% reduction in treatment cost.

Reduction of generated sludge by 57%.

Fast removal kinetics (5 min).

4.1. Characterization of Fe^0 nanoparticles with and without oxalate

4.1.1. Scanning electron microscopy-energy dispersive X-ray spectrum (SEM-EDS)

Figure 4.1 shows the SEM images for Fe^0 nanoparticles before and after the reaction with oxalate in water. Figure 4.1.a and Figure 4.1.b display that the fresh Fe^0 nanoparticles had a spherical shape and tended to agglomerate and form a chain-like structure due to the magnetic attraction between Fe^0 nanoparticles [222]. The chain-like structure and agglomeration deteriorate the performance of Fe^0 nanoparticles because they decrease the surface area of Fe^0 nanoparticles and the number of reactive sites on the surface of Fe^0 nanoparticles [223].

On the other hand , Figure 4.1.c reveals that besides the spherical particles of Fe^0, some particles with a flake-like structure or a needle-like structure were observed in the SEM of Fe^0 nanoparticles after reacting with 0.3 mM of oxalate in water [224]. The development of flake-like structure particles is attributed to the formation of iron oxide and hydroxide particles which results from the facilitated corrosion of Fe^0 nanoparticles by oxalate [224]. Fe^0 nanoparticles were furtherly oxidized, and the flake-like structure particles became more dominant and pronounced than the spherical particles after increasing the oxalate concentration from 0.3 mM to 0.5 mM (Figure 4.1.d), 1 mM (Figure 4.1.e**)**, or 4 mM (Figure 4.1.f**)**.

Furthermore, energy-dispersive X-ray spectroscopy was employed to determine the elemental composition of Fe^0 nanoparticles before and after the reaction with different oxalate concentrations in water. Figure 4.2 manifests that the surface of fresh Fe^0 nanoparticles composed of 86.04% iron and 13.96% oxygen. Whereas the percentage of iron on the surface of Fe^0 nanoparticles gradually decreased from 86.04% to 66.77%. In comparison, the oxygen ratio progressively increased from 13.96% to 33.23% after rising oxalate concentration in water from 0 to 4 mM. This proves that the addition of oxalate to Fe^0 nanoparticles in aqueous solution promoted the oxidation of Fe^0 nanoparticles to iron oxides and hydroxides.

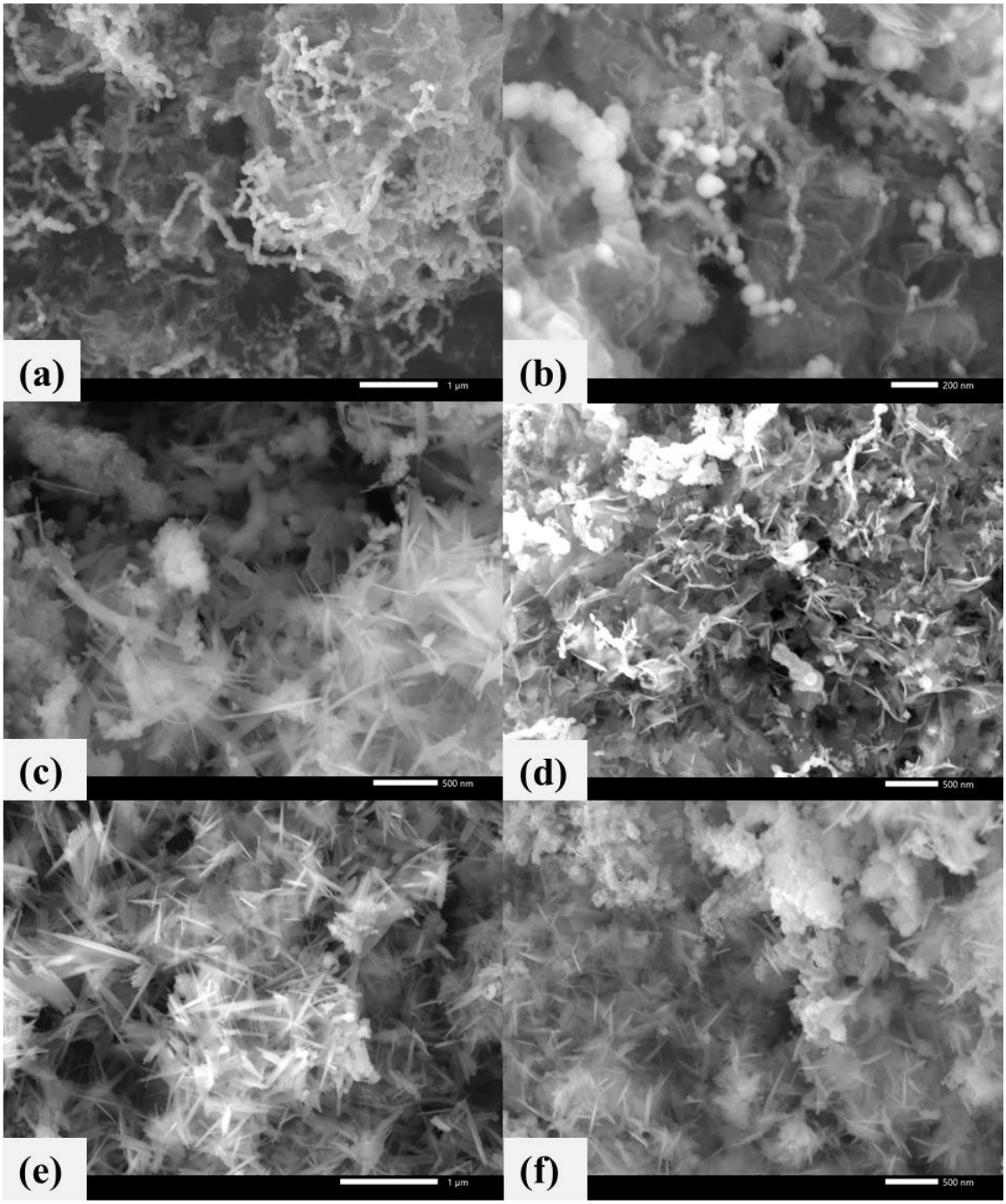

Figure 4.1 SEM pictures for fresh Fe^0 nanoparticles at different scales: **(a)** 1µm and **(b)** 500 nm. Also, SEM images for reacted Fe^0 nanoparticles with various oxalate concentrations in water: **(c)** 0.3 mM, **(d)** 0.5 mM, **(e)** 1 mM, and **(f)** 4 mM. Reaction parameters were as follows: $[Fe^0]$ = 0.3 g L^{-1}, volume of water = 200 mL, pH of water = 7, temperature = 25 °C, stirring speed = 500 rpm, and reaction time = 30 min.

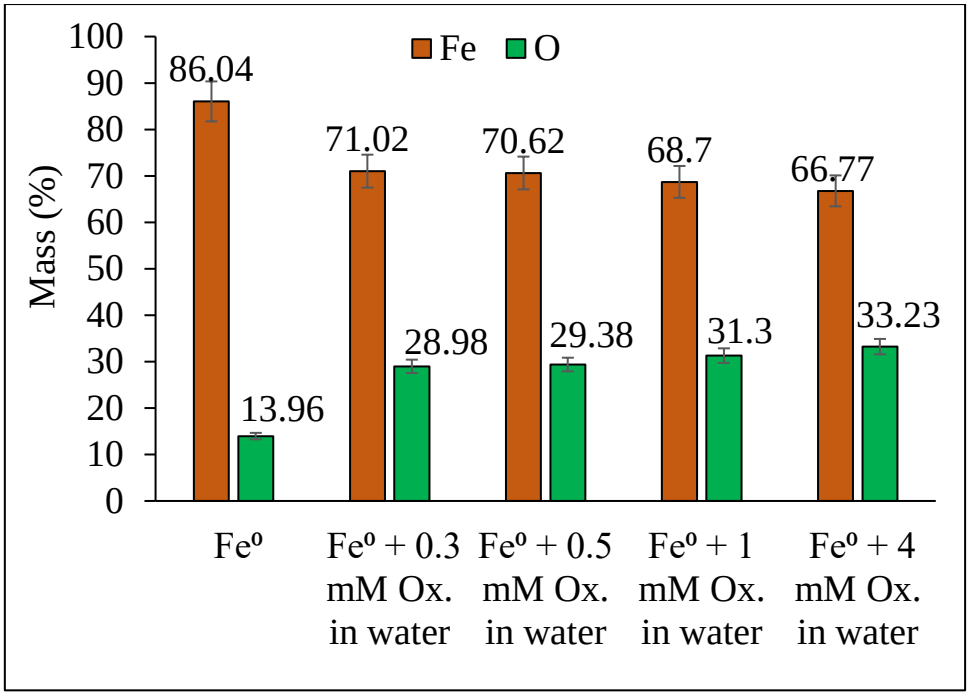

Figure 4.2 EDS analysis for fresh and reacted Fe^0 nanoparticles with different concentrations of oxalate in water. Reaction parameters were as follows: [Fe^0] = 0.3 g L^{-1}, [oxalate] = 0.3, 0.5, 1, and 4 mM, volume of water = 200 ml, pH = 7, temperature = 25 °C, stirring speed = 500 rpm, and reaction time = 30 min.

4.1.2. X-ray diffraction (XRD)

The crystalline structure of Fe^0 nanoparticles before and after the interaction with different concentrations of oxalate in water was acquired by XRD analysis [225,226]. Figure 4.3 demonstrates that the two characteristic peaks of Fe^0 were observed in the XRD pattern of fresh Fe^0 nanoparticles at 2θ = 44.7° and 82.6° which confirms the successful synthesis of Fe^0 nanoparticles [227,228]. Moreover, based on Scherrer's equation, the synthesized Fe^0 nanoparticles had a crystalline size of 3.64 nm.

The XRD patterns of the reacted Fe^0 nanoparticles illustrated that the strength of the distinctive peaks of Fe^0 considerably weakened after the reaction with 0.3 and 0.5 mM of oxalate, and they completely vanished after rising the oxalate concentration in water to 1 and 4 mM (Figure 4.3). Furthermore, the presence of 0.3, 0.5, and 1 mM of oxalate in water mainly promoted the oxidation of Fe^0 nanoparticles to magnetite (Fe_3O_4) as several peaks corresponding to magnetite appeared in XRD patterns at 2θ = 30.29°, 35.75°, 43.46°, 57.47°, and 62.96° [229]. Notably, the strength of magnetite peaks increased when the oxalate concentration in water increased from 0.3 to 1 mM (Figure 4.3).

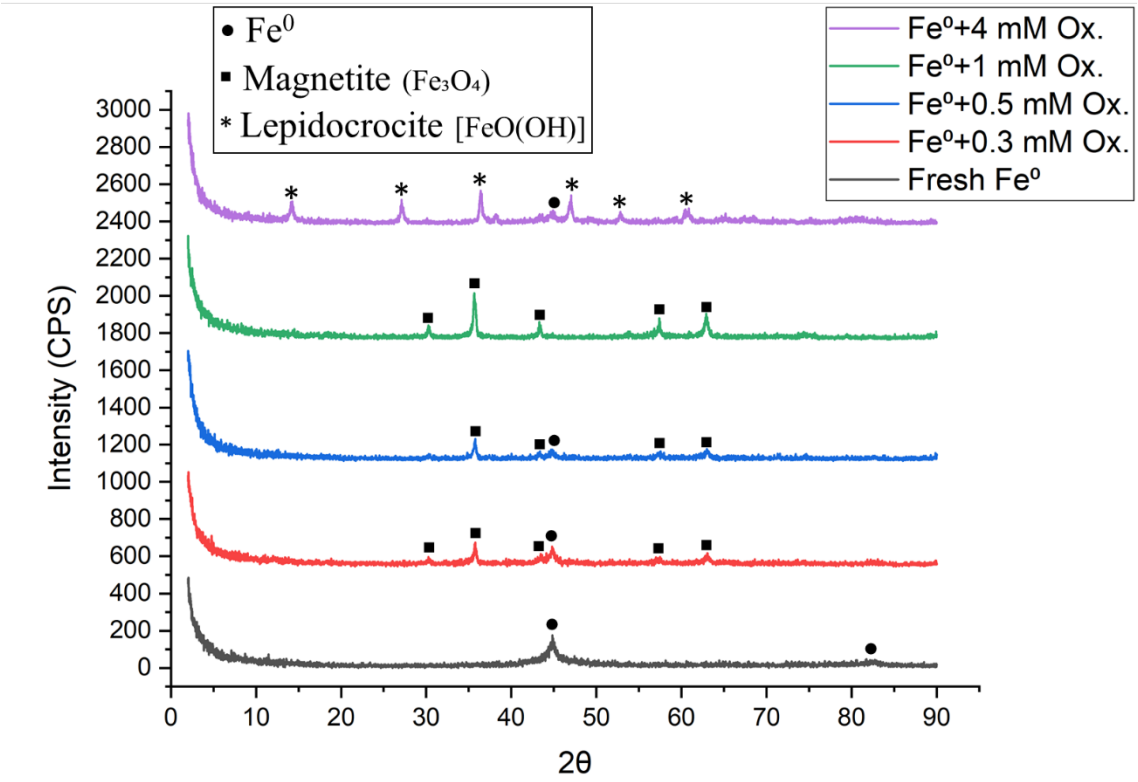

Figure 4.3 XRD analysis for Fe^0 nanoparticles before and after the reaction with different oxalate concentrations water. Reaction parameters were as follows: [Fe^0] = 0.3 g L^{-1}, [oxalate] = 0.3, 0.5, 1, and 4 mM, volume of water = 200 mL, pH of water = 7, temperature = 25 °C, stirring speed = 500 rpm, and reaction time = 30 min.

On the other hand, Figure 4.3 exhibits that 4 mM of oxalate favored the corrosion of Fe^0 nanoparticles to lepidocrocite [FeO(OH)] as many lepidocrocite peaks were detected in the XRD pattern of [Fe^0 + 4 mM oxalate] at 2θ = 14.16°, 27.13°, 36.40°, 38.16°, 47.03°, 52.77°, 60.56°, and 80.36° [230,231]. The results of SEM-EDS, and XRD confirmed that the existence of oxalate in water progressively oxidized Fe^0 nanoparticles, and these outcomes are in good agreement with the findings of Wang *et al.* [224].

4.1.3. Fourier Transform Infrared (FTIR)

The chemistry of Fe^0 nanoparticle's surface was investigated using FTIR analysis within a wavenumber ranging from 500 to 3000 cm^{-1}. Figure 4.4 presents the FTIR spectrum for Fe^0 nanoparticles before and after the reaction with various oxalate concentrations in water. Two stretching vibrations around 548 cm^{-1} and 621 cm^{-1} were observed in the FTIR spectrum of fresh Fe^0 nanoparticles, which correspond to the bands of magnetite (Fe_3O_4) and maghemite (Fe_2O_3) [232]. The intensity of these bands noticeably evolved after Fe^0 nanoparticles reacted with different concentrations of oxalate in water.

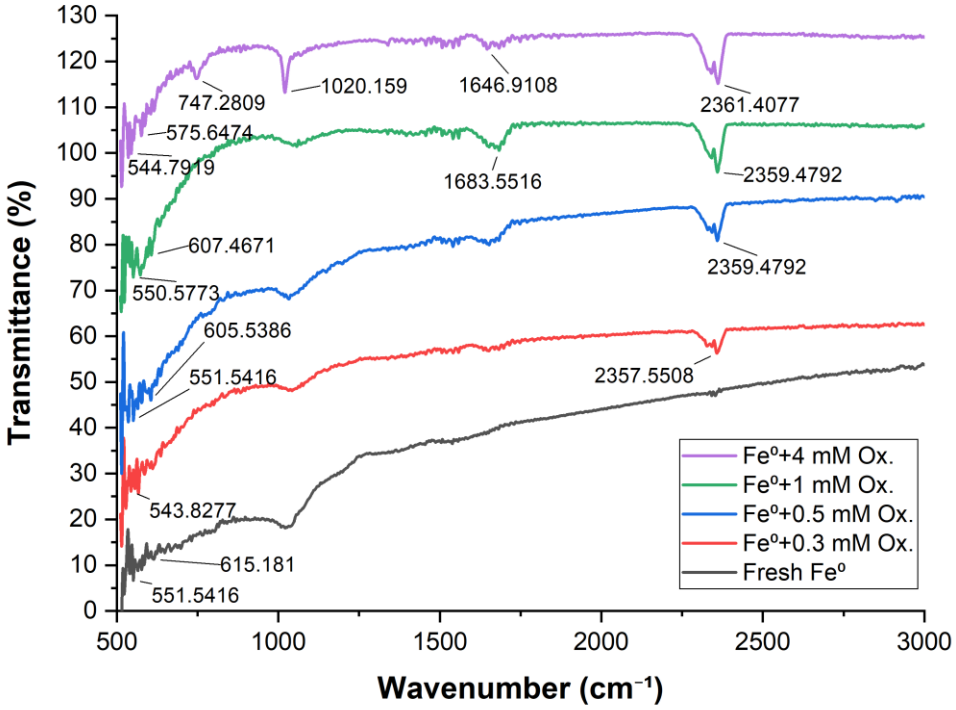

Figure 4.4 FTIR analysis for Fe^0 nanoparticles before and after the reaction with different oxalate concentrations in water. Reaction parameters were as follows: [Fe^0] = 0.3 g L^{-1}, [oxalate] = 0.3, 0.5, 1, and 4 mM, volume of water = 200 mL, pH of water = 7, temperature = 25 °C, stirring speed = 500 rpm, and reaction time = 30 min.

This may result from the formulation of iron-oxalate complexation on the surface of Fe^0 nanoparticles [224]. Also, Figure 4.4 displays that the saturation band of carbon dioxide (CO_2) was developed around 2359 cm^{-1} after the reaction of Fe^0 nanoparticles with oxalate [232]. However, the distinctive C=O band of oxalate around 1630 cm^{-1} wasn't detectable in the FTIR spectrum of Fe^0 nanoparticles after the interaction with low concentrations of oxalate, e.g., 0.3 and 0.5 mM [137]. On the contrary, when the concentration of oxalate was increased to 1 and 4 mM, the absorption band of C=O in oxalate appeared in the FTIR spectrum, as exhibited in Figure 4.4.

4.1.4. Particle size, specific surface area, and point of zero charge of Fe^0 nanoparticles

The particle size distribution (PSD) of fresh Fe^0 nanoparticles was obtained by laser diffraction particle size analyzer. Figure 4.5 illustrates the PSD of Fe^0 nanoparticles, where the average diameter of Fe^0 nanoparticles was 45.90 nm. Furthermore, the PSD analysis emphasized that 25%, 50%, and 75% of Fe^0 nanoparticles had a particle size of less than 32.52 nm, 45.86 nm, and 64.78 nm, respectively. Moreover, the specific surface area analysis manifested that the SSA_{BET} of Fe^0 nanoparticles was 57.51 m^2 g^{-1}, consistent

with the previous studies [233]. Also, Figure 4.6 shows that the $pH_{(PZC)}$ of Fe^0 and (Fe^0/oxalate) nanoparticles were 8.22 and 8, respectively. Hence, it can be anticipated that the surface of Fe^0 and (Fe^0/oxalate) nanoparticles were positively charged in the aqueous solution when the pH was less than ~8. In contrast, the surface of Fe^0 and (Fe^0/oxalate) nanoparticles were negatively charged when the pH of the solution was higher than ~8 [234].

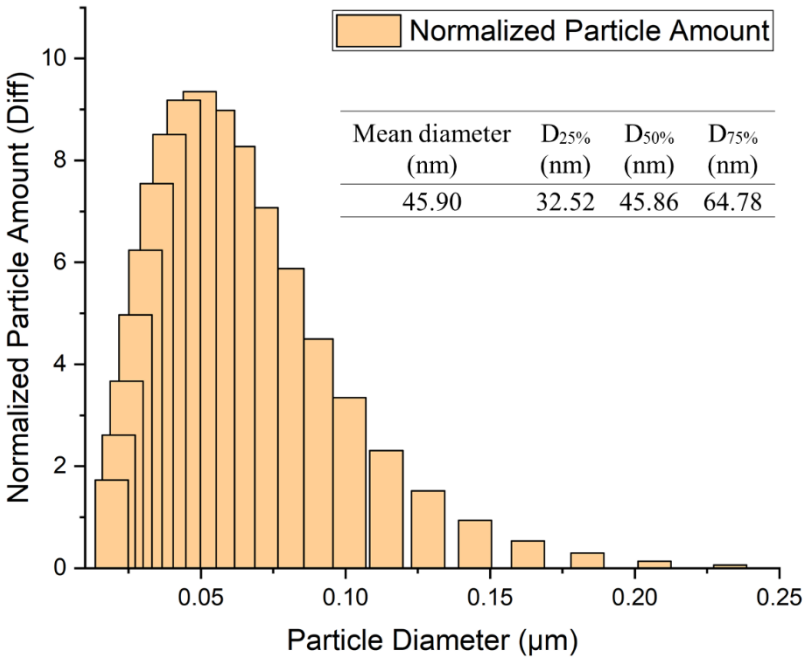

Figure 4.5 Analysis of particle size distribution of Fe^0 nanoparticles.

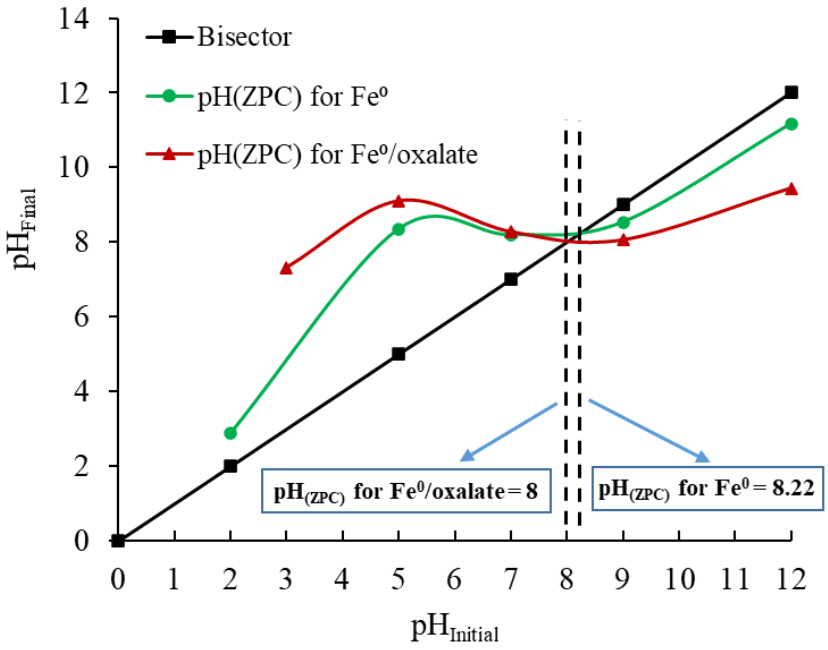

Figure 4.6 Measurements of zero point of charge [pH(ZPC)] of Fe^0 and (Fe^0/oxalate) nanoparticles.

4.2. Comparison between Fe^0 and (Fe^0/oxalate) nanoparticles

The effectiveness of Fe^0 nanoparticles alone (Fe^0 system) in remediating CIP-polluted water was initially evaluated by varying Fe^0 dosage from 0.1 to 1.1 g L^{-1} (Table 2.3). Figure 4.7 shows that 0.1 g L^{-1} of Fe^0 nanoparticles removed less than 32% of 100 mg L^{-1} of CIP from aqueous solutions after 30 min of reaction.

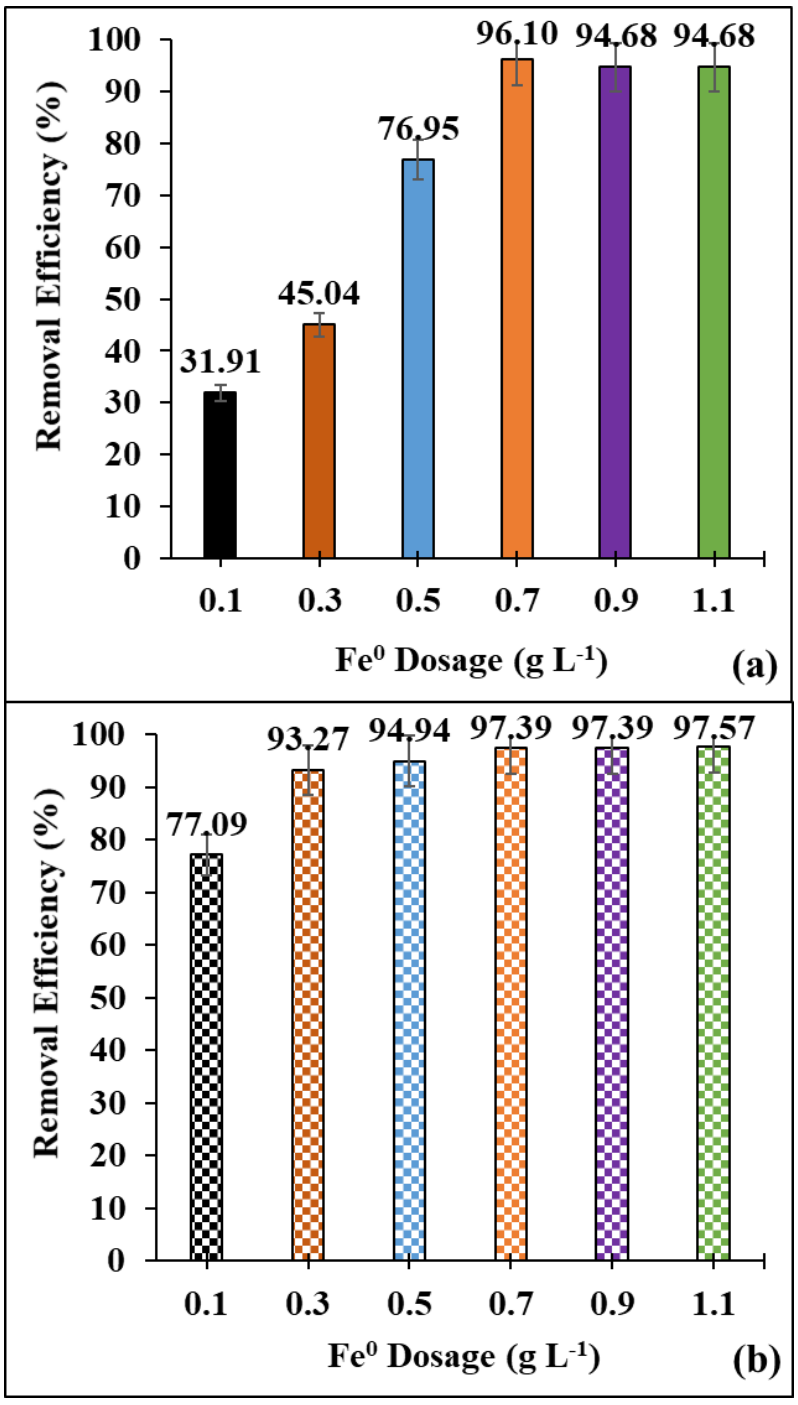

Figure 4.7 CIP removal by **(a)** Fe^0 and **(b)** [Fe^0/oxalate]. Reaction parameters were as follows: [CIP] = 100 mg L^{-1}, [Fe^0] = 0.5 g L^{-1}, [Oxalate] = 0.5 mM, pH = 7, temperature = 25 ºC, stirring speed = 500 rpm, and reaction time = 30 min.

This percentage was gradually enhanced to 45.04% and 76.95% by increasing the dosage of Fe^0 nanoparticles to 0.3g L^{-1} and 0.5 g L^{-1}. However, it is important to mention that the unstable performance of Fe^0 nanoparticles at these concentrations (i.e., 0.1, 0.3, and 0.5 g L^{-1}) led to significant desorption of CIP after extending the reaction time to 120 min (Data not shown). On the other hand, increasing the Fe^0 dosage to 0.7 g L^{-1} remarkably improved and strengthened the competence of Fe^0 nanoparticles as more than 96% of CIP was eliminated within 30 min **(**Figure 4.7.a**)**. It is also evident that the excessive addition of Fe^0 nanoparticles, for example, 0.9 and 1.1 g L^{-1}, slightly declined the removal efficiency of CIP to 94.68% **(**Figure 4.7.a**)**. This unexpected performance could result from the high aggregation of Fe^0 nanoparticles at high concentrations, which in turn decreases the surface area and the available reactive sites of Fe^0 nanoparticles. Hence, according to Figure 4.7, the optimum dosage for Fe^0 nanoparticles is 0.7 g L^{-1}. On the other hand, Figure 4.7.b confirms that adding 0.5 mM of oxalate boosted the performance of 0.5 g L^{-1} of Fe^0 nanoparticles in remediating CIP-polluted waters. For instance, after the addition of 0.5 mM of oxalate, the removal efficiency of CIP by 0.1, 0.3, and 0.5 g L^{-1} was improved from 31.91% to 77.09%, 45.05% to 93.27%, and 76.95% to 94.94%, respectively **(**Figure 4.7.b**)**. Furthermore, slight improvements in the removal efficiency of CIP were noticed after adding 0.5 mM of oxalate to 0.7, 0.9, and 1.1 g L^{-1} of Fe^0. Therefore, Figure 4.7 proved that the addition of oxalate positively reduced the optimum Fe^0 dosage from 0.7 g L^{-1} (Fe^0 nanoparticles) to 0.3 g L^{-1} [(Fe^0/oxalate) nanoparticles].

As previously mentioned in Figure 4.7, the removal efficiency of CIP by Fe^0 nanoparticles and (Fe^0/oxalate) nanoparticles was likewise enhanced by increasing the dosage of Fe^0 nanoparticles. This can be explained by two hypotheses as follows: *(1)* if the adsorption of CIP occurs, the addition of more Fe^0 in the treatment system will provide additional reactive sites to uptake CIP from the aqueous solution, and *(2)* if the oxidation of CIP occurs, higher concentrations of Fe^0 will generate more Fe^{2+} and H_2O_2, consequently, produce more ROS in the system.

Adding oxalate to Fe^0 nanoparticles will form complexes with iron ions (Fe-oxalate complex). The formation of Fe-oxalate complexes will promote the generation of ROS through various mechanisms [96,146]. These mechanisms are summarized as follows:

1. The reaction rate of Fe^{2+}-oxalate complexes with H_2O_2 is 3 times faster than the reaction of bare Fe^{2+} with H_2O_2. This means that the presence of oxalate will

prefer the consumption of H_2O_2 by Fe^{2+} to produce more ROS [Equation (1.5)] rather than transferring H_2O_2 to water by Fe^0 [Equation (1.2)].

2. The formation of Fe^{2+}-oxalate complexes boots the oxidation of Fe^{2+} by oxygen [Equation (1.3)] under acidic pH.
3. Oxalate will form Fe^{3+}-oxalate complexes, which will increase the solubility of Fe^{3+} ions and prevent the passivation of Fe^0 nanoparticles. The formation of iron oxides and hydroxides on the surface of Fe^0 nanoparticles after the reaction with oxalate in water indicates that the addition of oxalate neither enhanced the solubility of Fe^{3+} nor prevented the passivation of Fe^0 nanoparticles (Figure 4.1 and Figure 4.2). Thus, this mechanism was not responsible for improving the elimination of CIP by (Fe^0/oxalate) system.
4. The formation of Fe-oxalate complexes can change the nature of the produced ROS. The responsible enhancement mechanism will be clarified in detail in section 4.11.

4.3. Influence of oxalate concentration

The concentration of oxalate was varied from 0.1 to 0.9 mM at three different Fe^0 dosages (e.g., 0.1, 0.3, and 0.5 g L^{-1}) to identify the optimum combination between Fe^0 and oxalate that provides the best performance in remediating CIP-polluted water (Table 2.3). At the three dosages of Fe^0 nanoparticles, increasing oxalate concentration from 0 to 0.3 mM improved the removal efficiency of CIP, as illustrated in Figure 4.8. For example, the addition of 0.3 mM of oxalate to 0.1, 0.3, and 0.5 g L^{-1} of Fe^0 promoted the removal efficiency of CIP from 31.91% to 65.15%, 45.04% to 95.74%, and 76.95% to 96.80%, respectively. Nevertheless, it was found that adding oxalate with concentrations more than 0.3 mM moderately decreased the competence of (Fe^0/oxalate) nanoparticles. For instance, the removal efficiency of CIP by 0.3 g L^{-1} of Fe^0 declined from 95.74% to 90.90% after rising oxalate concentration from 0.3 to 0.9 mM (Figure 4.8.b). The excessive existence of oxalate in water could compete with CIP on either the adsorption sites of Fe^0 nanoparticles or the generated ROS [235]. Therefore, based on Figure 4.8, the optimum removal efficiency of CIP was 95.74%, and this percentage was achieved by adding 0.3 mM of oxalate to 0.3 g L^{-1} of Fe^0 nanoparticles. This combination of Fe^0 and oxalate (i.e., 0.3 g L^{-1} and 0.3 mM) was applied in the following experiments.

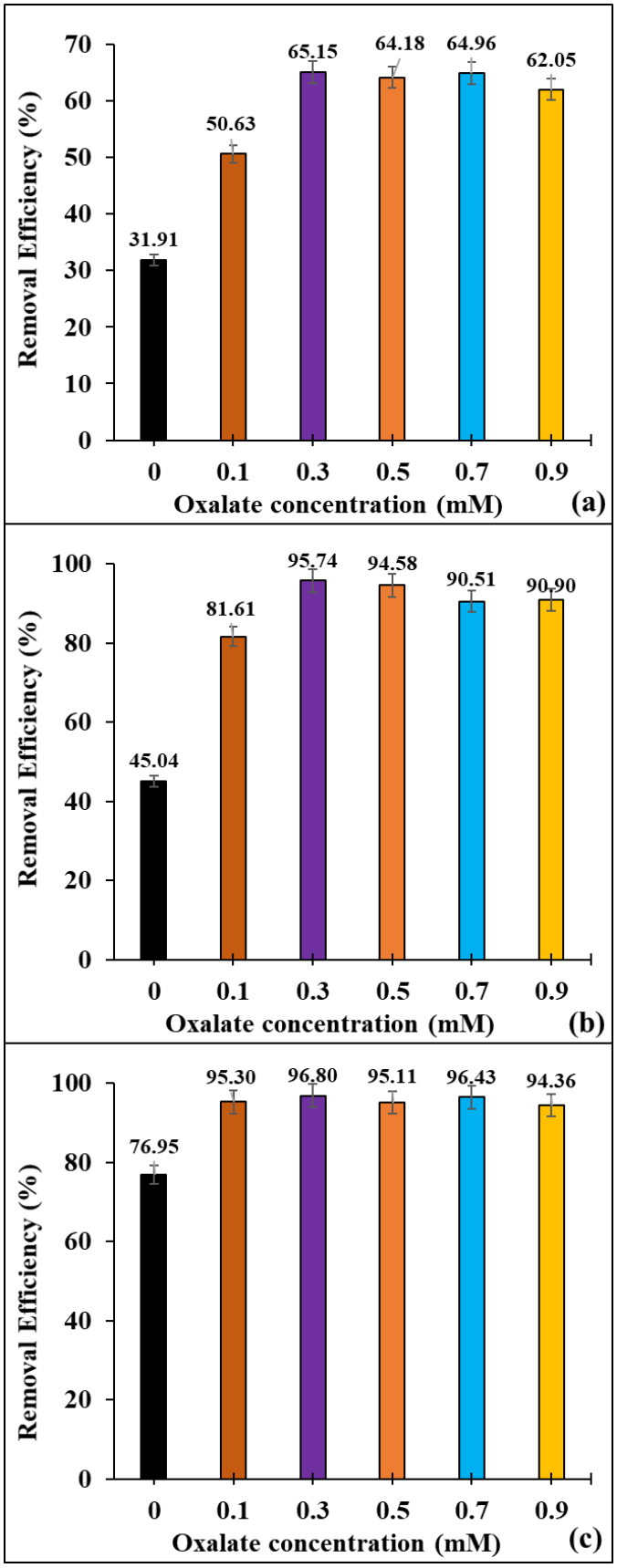

Figure 4.8 Influence of oxalate concentration at different dosages of Fe^0 nanoparticles: **(a)** 0.1 g L^{-1}, **(b)** 0.3 g L^{-1}, and **(c)** 0.5 g L^{-1}. Other reaction parameters were as follows: [CIP] = 100 mg L^{-1}, pH = 7, temperature = 25 ºC, stirring speed = 500 rpm, and reaction time = 30 min.

4.4. Effect of dissolved oxygen concentration

The effect of dissolved oxygen on the removal of CIP by (Fe^0/oxalate) nanoparticles was examined by carrying out three separate batch experiments with three different aeration conditions as follows: the first flask was open to the atmosphere; meanwhile, the second flask was continuously supplied with air using an air pump, and the last flask was purged with pure nitrogen gas (N_2) during the entire experiment. Air and nitrogen gas were supplied at a flow rate of 30 ml min^{-1}. Figure 4.9 exhibits that more than 95% of 100 mg L^{-1} of CIP was effectively removed by (Fe^0/oxalate) nanoparticles when the flask was open to the atmosphere. Furthermore, the competence of (Fe^0/oxalate) nanoparticles was trivially improved to approximately 97.69% when a constant supply of N_2 was provided during the treatment process. Conversely, the presence of excessive dissolved oxygen in the aqueous solution during the removal of CIP diminished the performance of (Fe^0/oxalate) nanoparticles to 67.47%. Peng *et al.* reported similar results where they observed that the degradation of nitrobenzene by (Fe^0/oxalate) under various aeration conditions was in the following order: 100% (N_2) > 95% (without aeration) > 85% (O_2) [96]. In addition to Peng *et al.*, Yin et al. demonstrated that the anoxic condition (N_2) was more preferable for nitrobenzene reduction by zerovalent iron than the oxic conditions (e.g., air or O_2) [236].

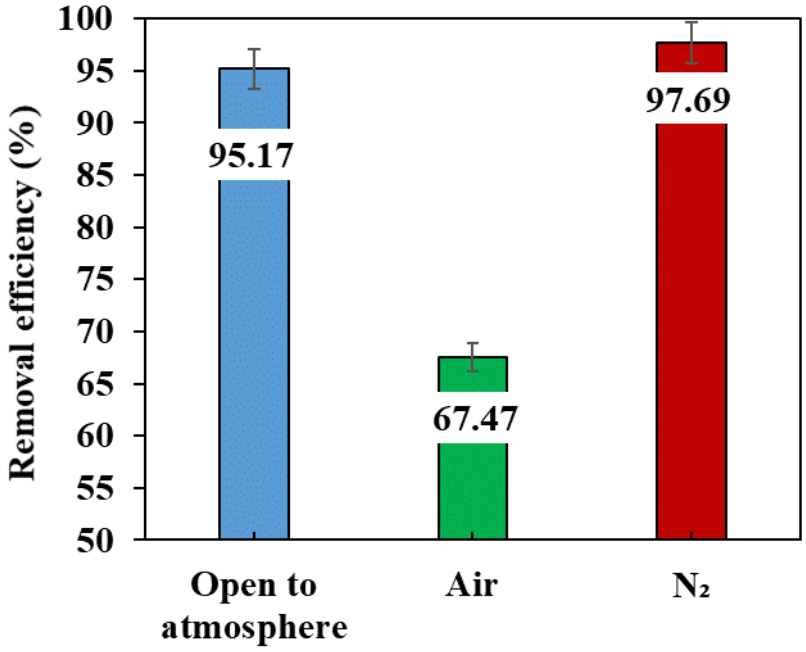

Figure 4.9 Effect of dissolved oxygen content on the effectiveness of (Fe^0/oxalate) nanoparticles in treating CIP-polluted solutions. Reaction parameters were as follows: [Fe^0] = 0.3 g L^{-1}, , [CIP] = 100 mg L^{-1}, [oxalate] = 0.3 mM pH = 7, temperature = 25 ºC, stirring speed = 500 rpm, and reaction time = 30 min.

Based on the responsible removal mechanism, there are two possible explanations for the performance of (Fe^0/oxalate) nanoparticles under different aeration conditions. If the oxidation of CIP is dominant, the existence of an excellent electron acceptor such as dissolved oxygen in the polluted water will strongly compete with CIP for the released electrons from the core of Fe^0 nanoparticles during the treatment [236]. However, if adsorption is the main removal mechanism, providing excessive molecules of oxygen will promptly oxidize Fe^0 nanoparticles and severely decrease the adsorption power of Fe^0 nanoparticles. Since there were no significant differences between purging N_2 or opening to the atmosphere, the flasks were open to the atmosphere in the rest of the batch experiments.

4.5. Influence of initial pH

The pH of the solution manipulates the surface charge of Fe^0 nanoparticles as shown in the determination of $pH_{(PZC)}$ (Figure 4.6) [234]. Moreover, changing the pH of the solution will change the dominant species of CIP in the aqueous solution [237]. For example, at acidic pH ($pH < pK_{a1} = 6.1$), most of CIP molecules will be cationic (CIP^+). On the other hand, at neutral pH ($pK_{a1} = 6.1 < pH < pK_{a2} = 8.4$) and alkaline pH ($pH > pK_{a2} = 8.4$), the majority of CIP molecules will be zwitterionic ($CIP^{\pm}$) and anionic (CIP^-), respectively. In other words, the pH of the solution will affect the interaction between CIP and (Fe^0/oxalate) nanoparticles. In addition, the generation of ROS by Fe^0 nanoparticles is highly dependent on the pH of the solution [238]. Therefore, it was necessary to study the impact of the initial pH of water on the elimination of CIP by (Fe^0/oxalate) nanoparticles. The initial pH of the polluted solution was increased from 3 to 11, as exhibited in Table 2.3 and Figure 4.10. The addition of 0.3 mM of oxalate completely dissolved Fe^0 nanoparticles at pH 3; thus, the elimination of CIP from a strongly acidic solution by (Fe^0/oxalate) nanoparticles was unsuccessful (Figure 4.10). However, the removal efficiency of CIP by (Fe^0/oxalate) nanoparticles was notably enhanced to 88.67% after increasing the initial pH of the solution to 5 (Figure 4.10). Surprisingly, Figure 4.10 confirms that 95.43% of 100 mg L^{-1} of CIP was eliminated within 10 min at neutral pH (e.g., pH 7). In contrast, the moderate and strong alkaline pH (i.e., pH 9 and pH 11) reduced the remediation of CIP-polluted water to 88.48% and 17%, respectively (Figure 4.10). The addition of low concentration of oxalate (0.3 mM) and the poor performance of (Fe^0/oxalate) nanoparticles under acidic pH (i.e., pH 3) could initially indicate that the oxidation of CIP by (Fe^0/oxalate) nanoparticles didn't occur.

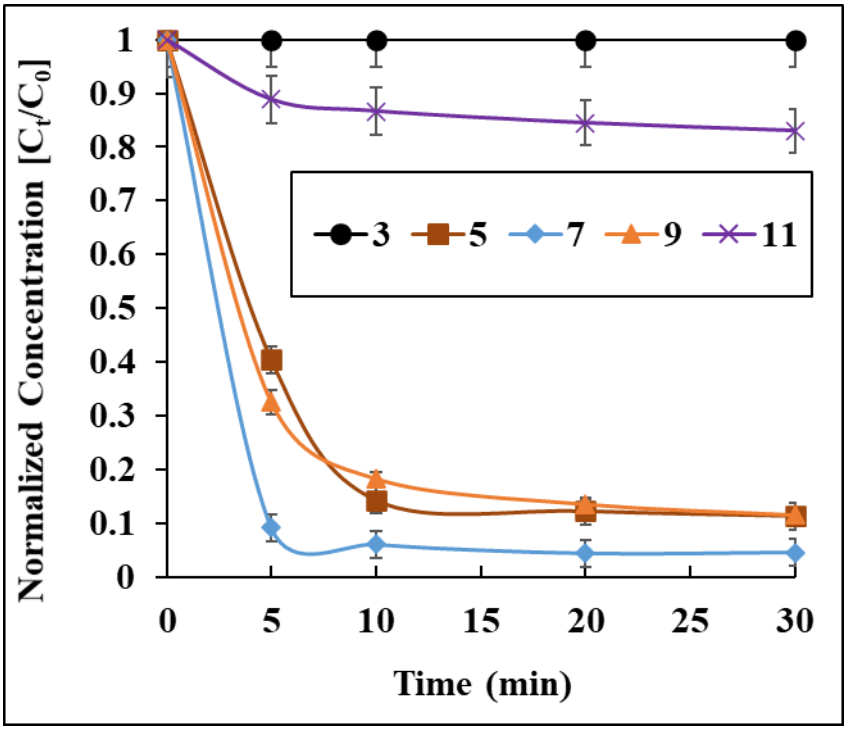

Figure 4.10 Effect of initial pH on the competence of (Fe^0/oxalate) nanoparticles. Reaction conditions were as follows: [Fe^0] = 0.3 g L^{-1}, [CIP] = 100 mg L^{-1}, [oxalate] = 0.3 mM, pH = 3-11, temperature = 25 ºC, mixing speed = 500 rpm, and reaction time = 30 min.

The findings of previous researchers can support this hypothesis. Most of the previous articles indicated that the optimum pH for oxidizing organic pollutants by (Fe^0/oxalate) nanoparticles was acidic [239]. For instance, Peng *et al.* manifested that pH 3 was the optimum pH for nitrobenzene oxidation by (Fe^0/oxalate) nanoparticles [96]. Also, Kong *et al.* showed that pH 3 boosted the oxidation of phenol by sulfidated zerovalent iron (SnZVI) with the existence of oxalate and tripolyphosphate [146]. In addition, most of the articles demonstrated that adding considerable amounts of oxalate is essential to stimulate the oxidation of organic contaminants [96]. For example, Keenan and Sedlak illustrated that 10 mM of oxalate was needed to promote the oxidation of organic pollutants by (Fe^0/O_2) nanoparticles [135]. Moreover, Kong *et al.* reported that 15 mM of oxalate was required to accelerate the degradation of phenol by SnZVI [146].

4.6. Desorption experiments

Desorption experiments were performed after the elimination of CIP at initial pH = 5, 7, and 9 to define the contribution of adsorption and oxidation from the total removal efficiency of CIP by (Fe^0/oxalate) nanoparticles. Deionized water with different pH, such as pH = 3, 5, and 12, was utilized in the desorption experiments, as manifested in section 2.5.3.2 and Figure 4.11.

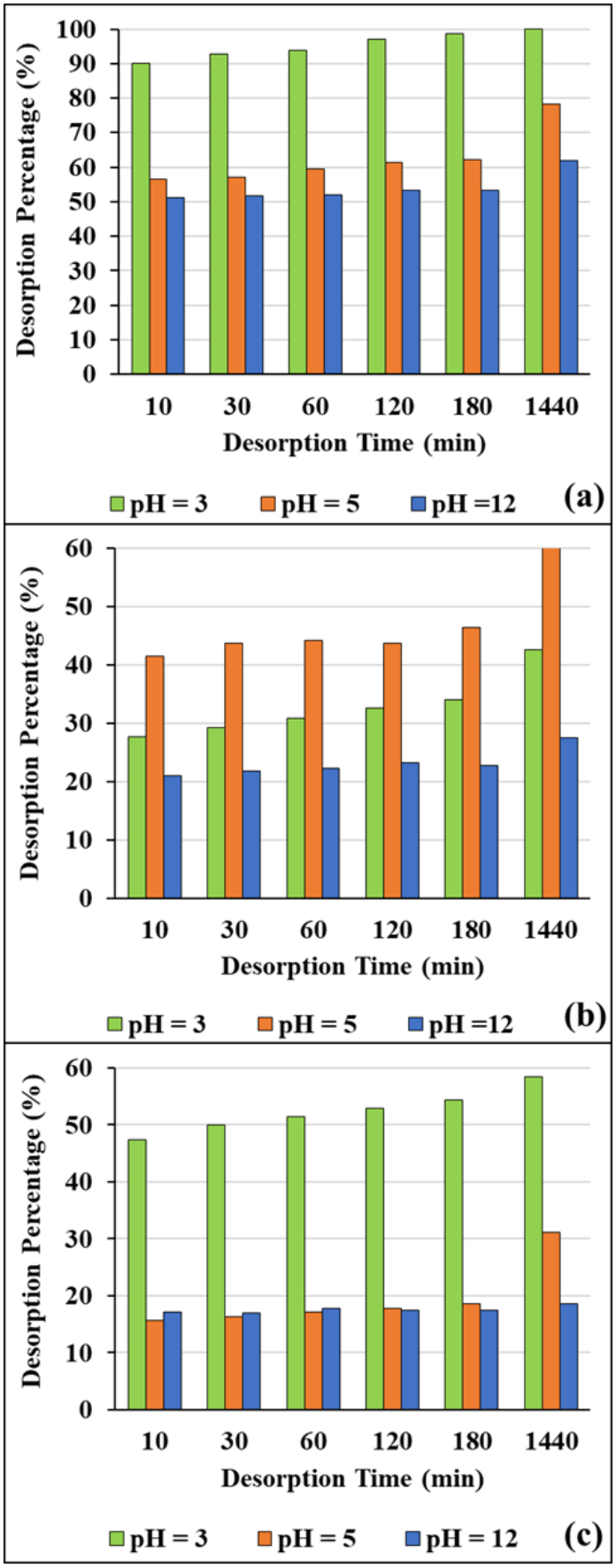

Figure 4.11 Desorption of CIP molecules after adsorption by (Fe^0/oxalate) nanoparticles at initial pH of: **(a)** 5, **(b)** 7, and **(c)** 9, using three desorption solutions with different pH such as pH = 3, pH = 5, and pH =12.

After removing CIP at initial pH of 5, 100% of the eliminated CIP molecules were desorbed back into the acidic deionized water (pH = 3) after 24h (Figure 4.11.a). However, approximately 80% and 60% of the removed CIP were desorbed back into deionized water with pH = 5 and pH =12, respectively (Figure 4.11.a). On the other hand, after the elimination of CIP at initial pH of 7, 42.67%, 61.13%, and 27.51% of the total removed CIP were desorbed back into the deionized water with pH = 3, 5, and 12, respectively (Figure 4.11.b). Whilst after the removal of CIP at initial pH of 9, 58.40%, 31.09%, and 18.59% of the total removed CIP were desorbed into the deionized water with pH = 3, 5, and 12, respectively (Figure 4.11.c). Since the complete desorption wasn't achieved within 24 h for initial pH 7 and 9, as displayed in (Figure 4.11.b) and (Figure 4.11.c), the desorption experiments were extended for 48 h. As anticipated, the complete desorption of CIP molecules for initial pH of 7 and 9 was achieved in the deionized water with pH = 5 and pH = 3, respectively (Data is not shown). These results confirm that the addition of 0.3 mM of oxalate to 0.3 g L^{-1} of Fe^0 improved the adsorption of CIP rather than oxidation.

At pH 5, both CIP and (Fe^0/oxalate) nanoparticles will be positively charged; however, at pH 9, CIP and (Fe^0/oxalate) nanoparticles will be negatively charged (Figure 4.6) [212]. Therefore, the reduction in the removal efficiency of CIP at initial pH = 5 and pH = 9 could result from the electrostatic repulsion between the same charges of CIP and (Fe^0/oxalate) nanoparticles. On the contrary, the emergence of a passivation layer and the electrostatic repulsion between the negatively charged CIP and Fe^0 could be responsible for the severe reduction in the removal efficiency of CIP at pH 11. In conclusion, Figure 4.10 elucidates that the optimum pH for removing CIP by (Fe^0/oxalate) nanoparticles is pH 7. This value was generalized in all experiments.

4.7. Monitoring of the release of iron species

The concentration of total dissolved iron, ferric, and ferrous was monitored during the remediation of CIP-polluted water at various initial pH (e.g., 5, 7, 9, and 11) to evaluate the chelating effect of oxalate. Figure 4.12 and Figure 4.13 present the concentration of the released iron species throughout the removal of CIP by (Fe^0/oxalate) and Fe^0 nanoparticles, respectively. Figure 4.12 and Figure 4.13 proved that the addition 0.3 mM of oxalate didn't improve the release of iron species during the removal of CIP at different initial pH. These outcomes are in good agreement with the previous reports [96].

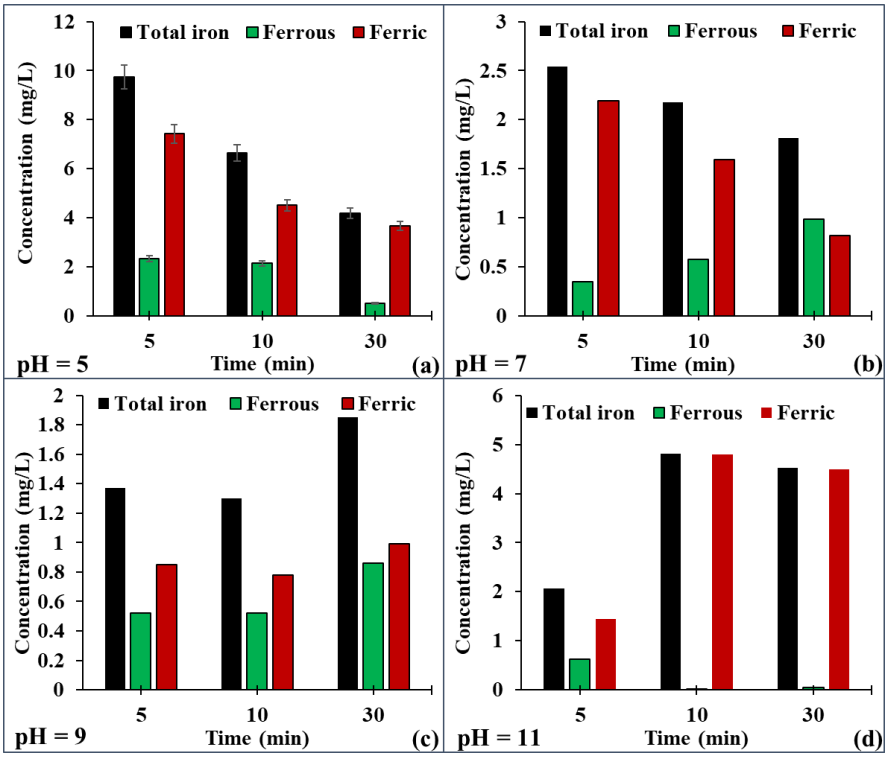

Figure 4.12 Concentrations of released iron species during the reaction of (Fe^0/oxalate) nanoparticles with CIP at different initial pH: **(a)** pH 5, **(b)** pH 7, **(c)** pH 9, **(d)** pH 11. Other reaction parameters were as follows: [Fe^0] = 0.3 g L^{-1}, [CIP] = 100 mg L^{-1}, [oxalate] = 0.3 mM, temperature = 25 ºC, stirring speed = 500 rpm, and reaction time = 30 min.

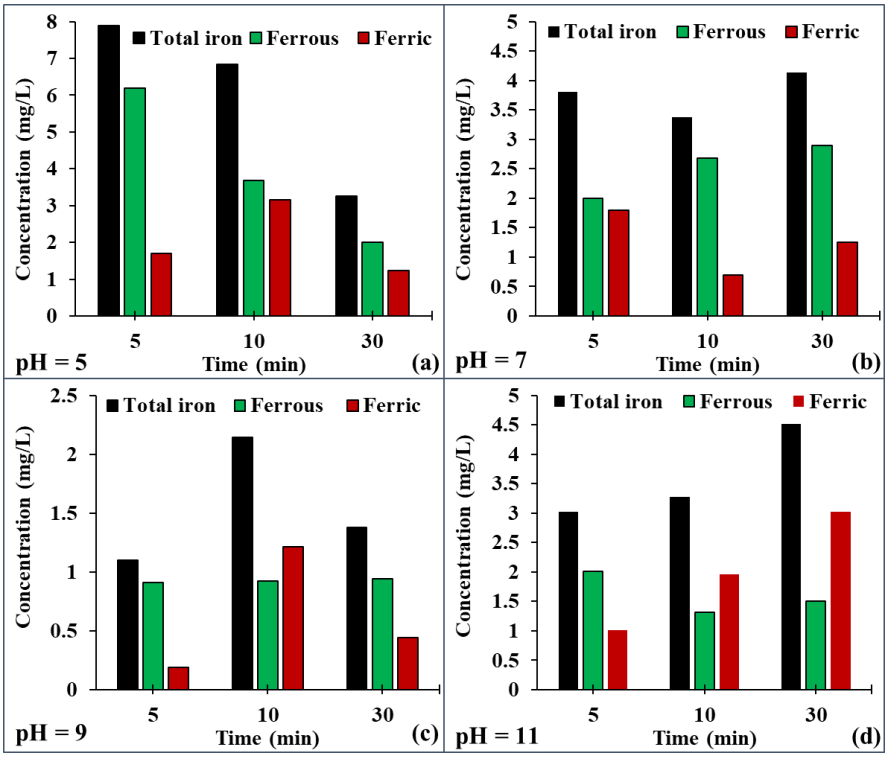

Figure 4.13 Concentrations of released iron species during the reaction of Fe^0 nanoparticles with CIP at different initial pH: **(a)** pH 5, **(b)** pH 7, **(c)** pH 9, **(d)** pH 11. Other reaction parameters were as follows: [Fe^0] = 0.3 g L^{-1}, [CIP] = 100 mg L^{-1}, temperature = 25 ºC, stirring speed = 500 rpm, and reaction time = 30 min.

4.8. Influence of initial ciprofloxacin concentration and isotherm analysis

The effect of CIP initial concentration on the efficacy of (Fe^0/oxalate) nanoparticles was assessed by increasing CIP initial concentration from 10 to 100 mg L^{-1} as presented in Table 2.3. Surprisingly, Figure 4.14 illustrates that only 65.28% of 10 mg L^{-1} of CIP was treated by (Fe^0/oxalate) nanoparticles. However, the performance of (Fe^0/oxalate) nanoparticles was greatly enhanced to 95.75% after increasing CIP's initial concentration to 100 mg L^{-1}. The unsatisfied competence of (Fe^0/oxalate) system in treating low concentrations of CIP (i.e., 10, 30, and 50 mg L^{-1}) can be explained by the fact that the less availability of CIP molecules in the aquatic solution will negatively impact the mass transfer rate of CIP from the solution to the surface of Fe^0 nanoparticles and decrease the removal efficiency [240,241]. Banat *et al.* also found that the elimination of phenol by bentonite improved as the phenol concentration increased [240]. The dosage of Fe^0 nanoparticles in (Fe^0/oxalate) was increased from 0.3 to 0.5 and 0.7 g L^{-1} to determine the optimum Fe^0 dosages for remediating specific ranges of CIP initial concentration. It should be noted that while changing the dosage of Fe^0, the oxalate concentration was fixed (i.e., 0.3 mM) because Figure 4.8 emphasized that increasing oxalate concentration to more than 0.3 mM wasn't beneficial. Figure 4.14.b and Figure 4.14.c confirmed that increasing the dosage of Fe^0 to 0.5 and 0.7 g L^{-1} enhanced the removal of different CIP concentrations by (Fe^0/oxalate) nanoparticles. This enhancement was noticeable in treating low concentrations of CIP. For instance, the removal efficiency of 10 mg L^{-1} of CIP was enhanced from 65.28% to 71.83% and 73.96% after rising Fe^0 dosage from 0.3 to 0.5 and 0.7 g L^{-1}, respectively. These findings suggest that the optimum Fe^0 in the (Fe^0/oxalate) should be modified according to CIP initial concentration [CIP] as follows: 0.7 g L^{-1} is the optimum Fe^0 dosage when [CIP] < 50 mg L^{-1}, whereas 0.5 and 0.3 g L^{-1} are the optimum Fe^0 dosages when 50 mg L^{-1} ≤ [CIP] <100 mg L^{-1} and [CIP] ≥ 100 mg L^{-1}, respectively.

Isotherm analysis was conducted to predict the nature of CIP adsorption by (Fe^0/oxalate) nanoparticles. During the isotherm analysis, it was noted that the trend of removing [CIP] ≥ 100 mg L^{-1} is different from removing [CIP] ≤ 70 mg L^{-1}. This difference could be due to the occurrence of different adsorption mechanisms depending on the initial CIP concentration. Therefore, it was decided to perform the isotherm modeling for [CIP] ≥ 100 mg L^{-1} and [CIP] ≤ 70 mg L^{-1} separately.

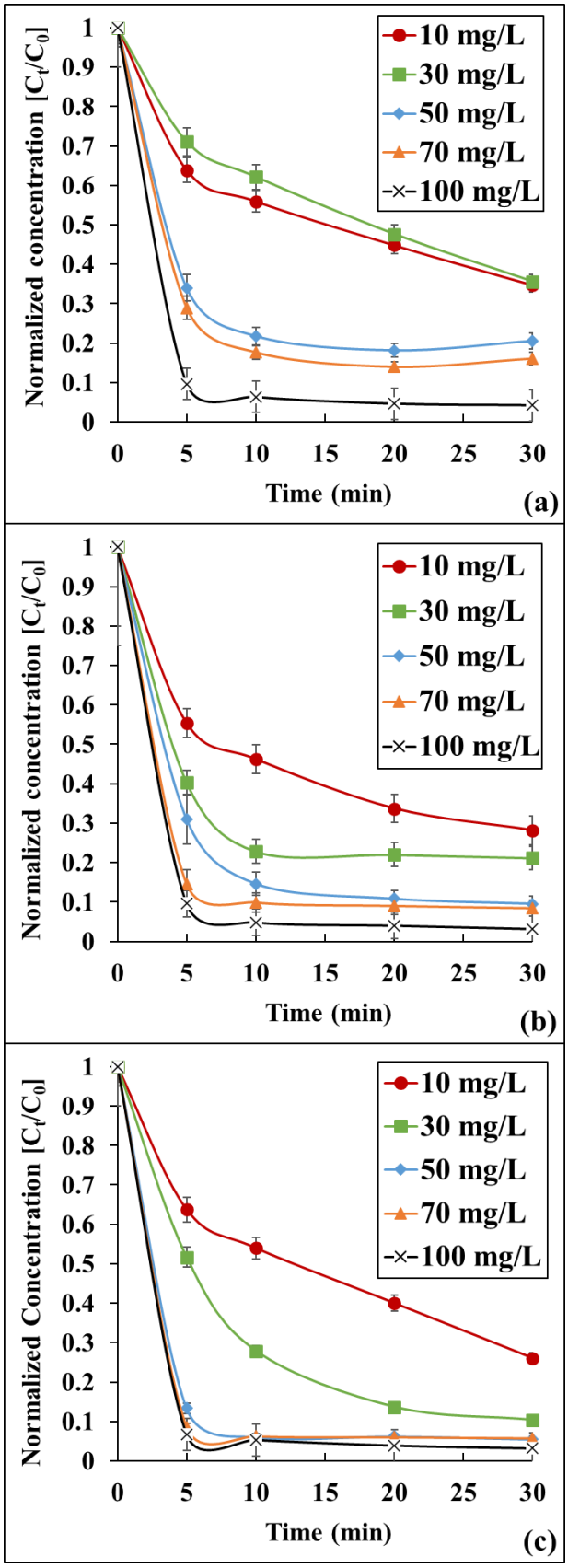

Figure 4.14 Influence of CIP concentration on the competence of (Fe^0/oxalate) nanoparticles. (a) [Fe^0] = 0.3 g L^{-1}, (b) [Fe^0] = 0.5 g L^{-1}, and (c) [Fe^0] = 0.7 g L^{-1}. Other reaction parameters were as follows: [CIP] = 100 mg L^{-1}, [oxalate] = 0.3 mM, pH = 7, temperature = 25 ºC, stirring speed = 500 rpm, and reaction time = 30 min.

It can be observed from Figure 4.15 and Table 4.1 that the equilibrium data for the removal of [CIP] ≤ 70 mg L^{-1} is well represented by Sips isotherm model as it owns the lowest AIC value (e.g., 51.68) and the highest coefficient of determination (R^2 = 0.994) among the five used isotherm models. Also, Table 4.2 shows that the calculated adsorption capacities from sips isotherm model is almost identical to the experimental adsorption capacities except the adsorption capacity of removing 10 mg L^{-1} of CIP. Thus, the multilayer adsorption of low CIP concentrations ([CIP] ≤ 70 mg L^{-1}) is predicted to occur on the heterogenous surface of (Fe^0/oxalate) nanoparticles [242]. It worth mentioning that a cooperative adsorption process could also be expected as the inverse of the adsorption intensity (1/n = 4.023) of Freundlich isotherm model is higher than 1 (Table 4.1). Furthermore, Table 4.3 articulates that the adsorption of CIP by (Fe^0/oxalate) nanoparticles is favorable as the separation factor ($R_{L)}$ of Langmuir isotherm at all initial CIP concentrations is less than 1 [243,244]. In addition, Table 4.1 demonstrates that the mean adsorption energy of Dubinin-Radushkevich isotherm (E) is 116.186 J mol^{-1} (E < 8 kJ mol^{-1}) which suggests that the adsorption of CIP by (Fe^0/oxalate) nanoparticles is govern by physisorption [189].

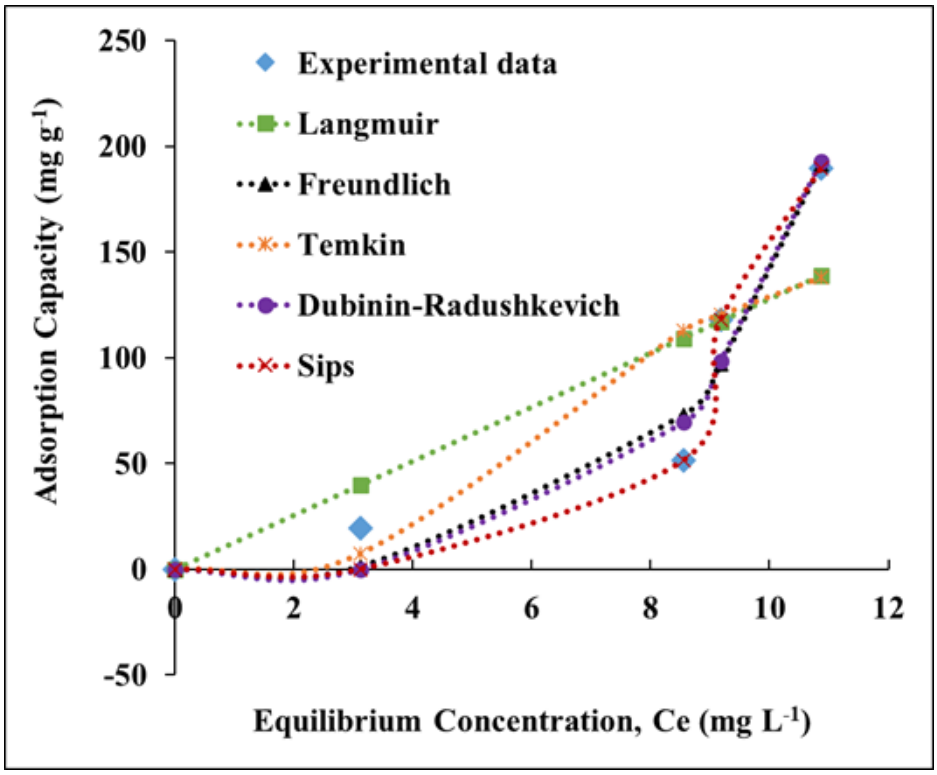

Figure 4.15 Isotherm analysis for the treatment of low CIP concentrations. Reaction parameters were as follows: [Fe^0] = 0.3 g L^{-1}, [CIP] = 10-70 mg L^{-1}, [oxalate] = 0.3 mM, pH = 7, temperature = 25 ºC, stirring speed = 500 rpm, and reaction time = 30 min.

Table 4.1 Isotherm parameters for removing low concentrations of CIP (10-70 mg L^{-1}).

Langmuir Isotherm				
Maximum adsorption capacity, q_e (mg g^{-1})	Langmuir constant (K_{ads}) (L mg $^{-1}$)	R^2	AIC	
2065.66	6.462E-03	0.749	65.911	
Freundlich Isotherm				
Freundlich isotherm constant, K_f $[(mg/g)(mg/L)^{1/n}]$	Adsorption intensity (n)	(1/n)	R^2	AIC
0.013	0.249	4.023	0.953	57.576
Temkin Isotherm				
Temkin isotherm equilibrium binding constant, A_T (L g^{-1})	Temkin isotherm constant, b_T	R^2	AIC	
0.344	23.724	0.728	65.911	
Dubinin-Radushkevich Isotherm				
Theoretical isotherm saturation capacity, q_s (mg g^{-1})	Dubinin–Radushkevich isotherm constant, K_{ad} (mol^2 J^{-2})	Mean adsorption energy, E (J mol^{-1})	R^2	AIC
1123.725	3.704E-05	116.186	0.960	56.954
Sips Isotherm				
Theoretical isotherm saturation capacity, q_s (mg g^{-1})	Sips equilibrium constant, K_S (L mg^{-1})	Sips constant, (n_S) (Dimensionless)	R^2	AIC
193.101	0.111	20.765	0.990	51.680

Table 4.2 Comparison between experimental data and isotherm model data.

Adsorption capacity (mg g^{-1})	Langmuir adsorption capacity (mg g^{-1})	Freundlich adsorption capacity (mg g^{-1})	Temkin adsorption capacity (mg g^{-1})	Dubinin-Radushkevich adsorption capacity (mg g^{-1})	Sips adsorption capacity (mg g^{-1})
19.54[(1)]	39.87	1.26	7.45	2.55E-05	5.59E-08
51.51[(2)]	109.25	73.03	112.88	69.60	51.51
117.92[(3)]	117.21	96.94	120.23	98.53	117.92
189.51[(4)]	138.79	191.55	137.92	192.88	189.51

CIP initial concentration = [(1)] 10, [(2)] 30, [(3)] 50, and [(4)] 70 mg L^{-1}

Table 4.3 Separation factor of Langmuir isotherm for low CIP concentrations (10-70 mg L^{-1}).

Initial concentration of CIP (mg/L)	Separation factor (R_L)
10	0.9984
30	0.9954
50	0.9923
70	0.9892

For the adsorption of high CIP concentrations (i.e., [CIP] ≥ 100 mg L^{-1}), the Freundlich isotherm model was found to be the best model to describe the experimental data as exhibited in Figure 4.16, Table 4.4 as well as Table 4.5. The reciprocal of adsorption intensity (1/n = 2.559) is larger than unity which suggests that cooperative adsorption is responsible for the multilayer adsorption of high concentrations of CIP on the heterogeneous surface of (Fe^0/oxalate) nanoparticles [245]. Furthermore, Table 4.6 illustrates that the R_L of Langmuir isotherm at all initial CIP concentrations is less than 1, suggesting the adsorption of high CIP concentrations by (Fe^0/oxalate) system is favorable.

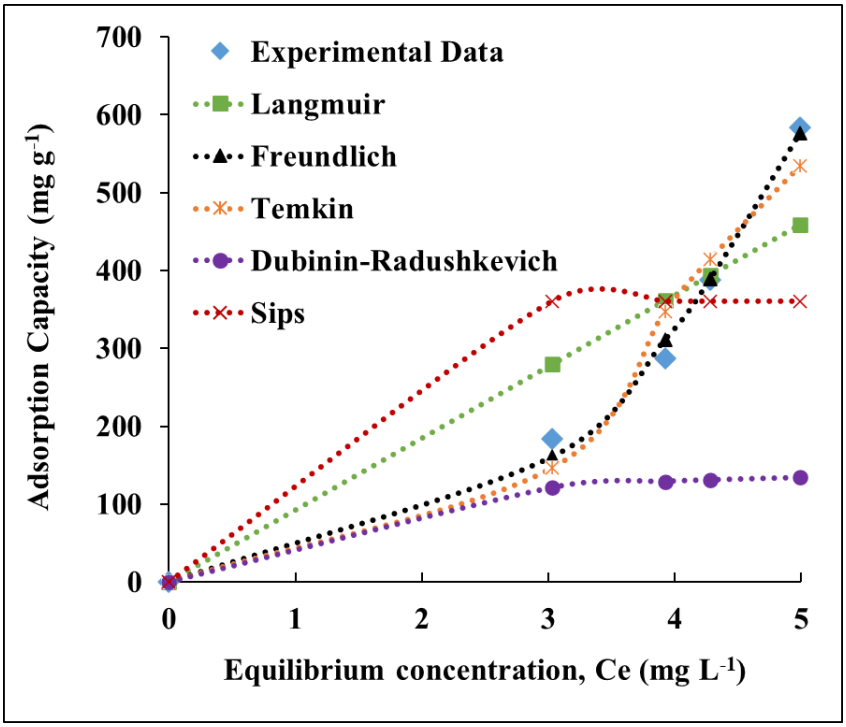

Figure 4.16 Isotherm analysis for treating high concentrations of CIP. Reaction parameters were as follows: Fe^0 dosage = 0.3 g L^{-1}, [CIP] = 100-300 mg L^{-1}, [oxalate] = 0.3 mM, pH = 7, temperature = 25 ºC, stirring speed = 500 rpm, and reaction time = 30 min.

Table 4.4 Isotherm parameters for removing high CIP concentrations (100-300 mg L^{-1}).

Langmuir Isotherm				
Maximum adsorption capacity, q_e (mg g^{-1})	Langmuir constant (K_{ads}) (L mg^{-1})	R^2	AIC	
59754.270	1.551E-03	0.856	73.546	
Freundlich Isotherm				
Freundlich isotherm constant, K_f $[(mg/g)(mg/L)^{1/n}]$	Adsorption intensity (n)	(1/n)	R^2	AIC
9.428	0.391	2.559	0.994	57.127
Temkin Isotherm				
Temkin isotherm equilibrium binding constant, A_T (L g^{-1})	Temkin isotherm constant, b_T	R^2	AIC	
0.398	3.186	0.958	66.922	

Table 4.4 Isotherm analysis for removing high CIP concentrations (100-300 mg L^{-1}) (cont.).

Dubinin-Radushkevich Isotherm				
Theoretical isotherm saturation capacity, q_s (mg g^{-1})	Dubinin–Radushkevich isotherm constant, K_{ad} (mol^2 J^{-2})	Mean adsorption energy, E (J mol^{-1})	R^2	AIC
143.862	3.444E-07	1204.972	0.618	84.970
Sips Isotherm				
Theoretical isotherm saturation capacity, q_s (mg g^{-1})	Sips equilibrium constant, K_S (L mg^{-1})	Sips constant, (n_S) (Dimensionless)	R^2	AIC
721.073	0.142	2.565E-05	0.544	78.840

Table 4.5 Comparison between experimental data and isotherm model data.

Adsorption capacity (mg g^{-1})	Langmuir adsorption capacity (mg g^{-1})	Freundlich adsorption capacity (mg g^{-1})	Temkin adsorption capacity (mg g^{-1})	Dubinin-Radushkevich adsorption capacity (mg g^{-1})	Sips adsorption capacity (mg g^{-1})
183.57[(1)]	279.56	160.89	146.52	121.11	360.53
287.29[(2)]	361.28	311.25	347.12	128.98	360.53
388.52[(3)]	393.91	388.89	414.83	131.03	360.53
583.85[(4)]	459.05	576.99	534.76	134.06	360.53

CIP initial concentration = [(1)] 100, [(2)] 150, [(3)] 200, and [(4)] 300 mg L^{-1}

Table 4.6 Separation factor of Langmuir isotherm for removing high CIP concentrations (100-300 mg L^{-1}).

Initial concentration of CIP (mg/L)	Separation factor (R_L)
100	0.8657
150	0.8112
200	0.7632
300	0.6824

4.9. Influence of contact time and kinetics analysis

The effect of contact time was investigated by increasing the reaction time from 0 to 30 min, as shown in Figure 4.14. Figure 4.14.a displays that the (Fe^0/oxalate) nanoparticles at Fe^0 dosage of 0.3 g L^{-1} quickly attained the equilibrium state after 10 min of starting the reaction when treating high concentrations of CIP (e.g., 50, 70, and 100 mg L^{-1}). The presence of excessive molecules of CIP in the aqueous solution facilitated the mass transfer of CIP to the solid phase, where the adsorption locations of (Fe^0/oxalate) nanoparticles were rapidly occupied within a short time (i.e., 10 min). This reflects the excellent competence of (Fe^0/oxalate) nanoparticles in treating high concentrations of CIP. In contrast, eliminating low concentrations of CIP, such as 10 and 30 mg L^{-1} of CIP, need more than 30 min to reach the equilibrium stage because of the slow mass transfer of low CIP molecules to the surface of (Fe^0/oxalate) nanoparticles. It can be seen from Figure 4.14.b and Figure 4.14.c that increasing the concentration of Fe^0 nanoparticles, in the (Fe^0/oxalate) nanoparticles, to 0.5 and 0.7 g L^{-1} provided more reactive sites to target 30 mg L^{-1} within 10-20 min effectively. On the contrary, at all studied concentrations of Fe^0 (i.e., 0.3, 0.5, and 0.7 g L^{-1}), more than 30 min are needed to efficiently treat 10 mg L^{-1} of CIP or less. Since 100 mg L^{-1} of CIP was chosen to study the effect of all other parameters, 30 min was selected as an equilibrium time for all experiments.

Kinetics analysis for the treatment of CIP-polluted waters by (Fe^0/oxalate) nanoparticles was carried out as dementated in Figure 4.17 to predict the controlling removal mechanism [246,247]. Pseudo-first-order, Pseudo-second-order, intraparticle diffusion, and Elovich were applied to describe the kinetics of CIP removal by (Fe^0/oxalate) nanoparticles. Table 4.7 as well as Figure 4.17 elucidate that there is no single kinetic model to represent the removal of various CIP concentrations. For example, the kinetics of removing 10 mg L^{-1} by (Fe^0/oxalate) nanoparticles is well described by the Elovich model because it owns the lowest AIC value and the highest coefficient of determination (R^2). However, the kinetics of removing 30, 50, and 70 mg L^{-1} of CIP are well fitted by the Pseudo-first-order model. Whilst Pseudo second-order model is the best model to represent the kinetics of eliminating 100 mg L^{-1} of CIP. These results confirms that the effect of CIP initial concentration on the performance of (Fe^0/oxalate) nanoparticles is significant as it not only affects the competence of (Fe^0/oxalate) nanoparticles but might also change the controlling removal mechanism. For instance, it can be expected that adsorption of 10 and 100 mg L^{-1} of CIP by (Fe^0/oxalate) nanoparticles is chemisorption

as their kinetics data are well fitted by Elovich and Pseudo second-order, respectively [176,248]. On the other hand, the uptake of 30, 50, and 70 mg L^{-1} of CIP by (Fe^0/oxalate) nanoparticles could be controlled by physisorption (i.e., electrostatic attraction, Van der Waals forces, co-precipitation, etc.) since their kinetics data are best represented by Pseudo first-order model [249].

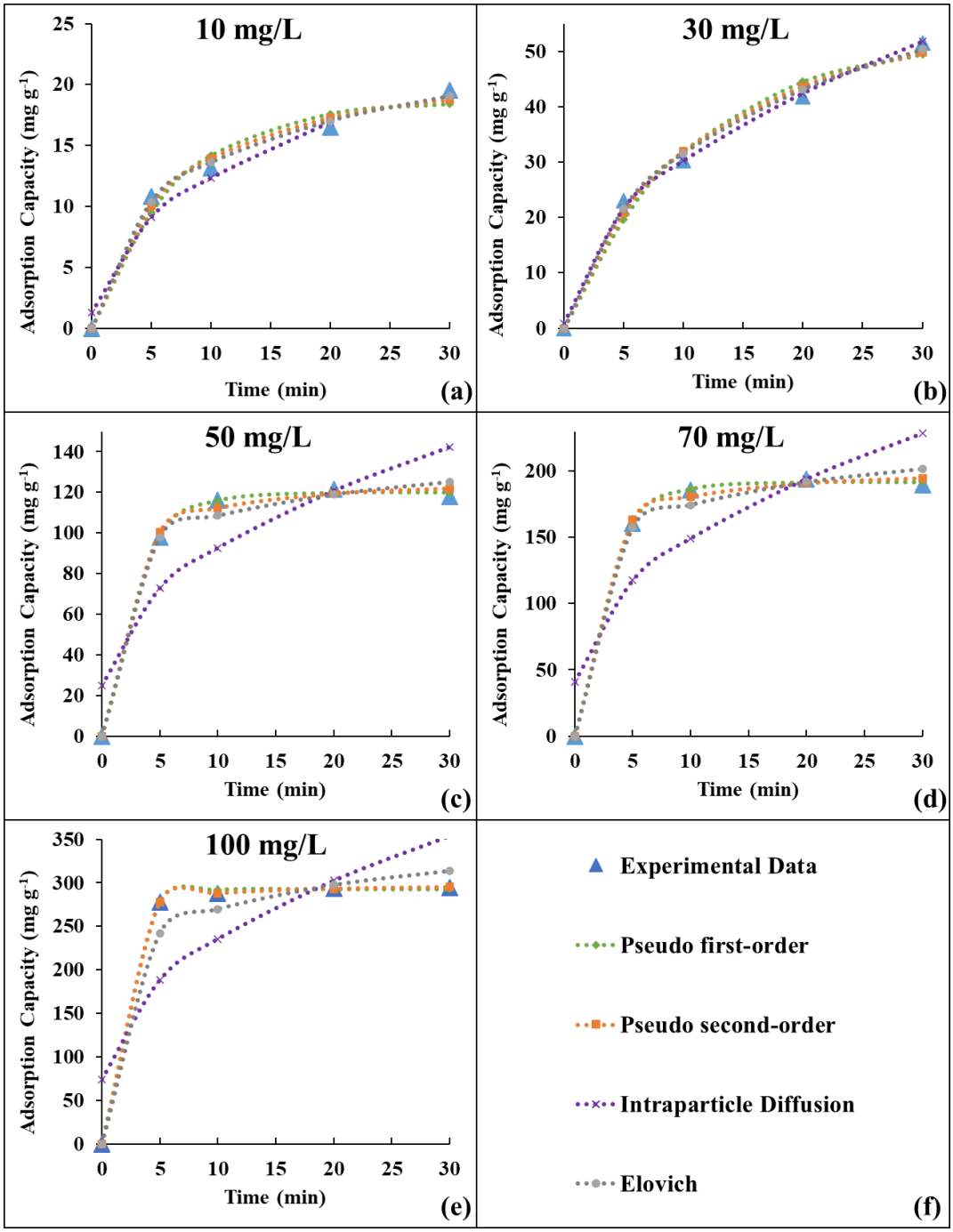

Figure 4.17 Kinetic analysis for the removal of different CIP concentrations by (Fe^0/oxalate) nanoparticles: **(a)** [CIP] = 10 mg L^{-1}, **(b)** [CIP] = 30 mg L^{-1}, **(c)** [CIP] = 50 mg L^{-1}, **(d)** [CIP] = 70 mg L^{-1}, **(e)** [CIP] = 100 mg L^{-1}, and **(f)** legend. Other reaction parameters are as follows: [Fe^0] = 0.3 g L^{-1}, [oxalate] = 0.3 mM, pH = 7, temperature = 25 ºC, and stirring speed = 500 rpm.

Table 4.7 Kinetics parameters for CIP removal by (Fe^0/oxalate) using 0.3 g L^{-1} of Fe^0.

Pseudo-first-order model					**Pseudo-second-order model**			
[CIP] (mg L^{-1})	K_1 (min^{-1})	q_e (mg g^{-1})	R^2	AIC	K_2 (g mg^{-1} min^{-1})	q_e (mg g^{-1})	R^2	AIC
10	0.1425	18.67	0.978	30.11	6.998E-03	22.68	0.990	26.13
30	0.0934	52.65	0.984	38.23	1.235E-03	69.25	0.991	35.28
50	0.3419	119.83	0.999	31.60	5.838E-03	127.30	0.996	40.51
70	0.3613	191.72	1	34.56	4.097E-03	202.65	0.997 4	43.36
100	0.5969	292.45	1	36.64	9.093E-03	298.60	1	13.91
Intraparticle diffusion model					**Elovich Model**			
[CIP] (mg L^{-1})	K_{intra} (mg g^{-1} $min^{1/2}$)	C_{intra} (mg g^{-1})	R^2	AIC	A (mg g^{-1} min^{-1})	β (mg g^{-1})	R^2	AIC
10	3.49	1.30	0.972	31.11	6.67	0.1934	0.996	21.19
30	9.30	0.82	0.998	27.85	7.91	0.0512	0.996	31.65
50	21.43	24.93	0.774	60.87	1950	0.0660	0.989	45.75
70	34.23	40.96	0.767	65.76	2900	0.0405	0.990	50.35
100	51.21	73.68	0.702	71.44	3400	0.0250	0.973	59.96

The conclusions of the kinetics analysis suggest that physisorption and chemisorption were collaboratively responsible for the adsorption of CIP by (Fe^0/oxalate) nanoparticles. This suggestion is consistent with the results of the desorption experiments (Figure 4.11) and the isotherm analysis.

4.10. Influence of temperature and thermodynamic analysis

The effect of temperature on the removal of CIP by (Fe^0/oxalate) nanoparticles was investigated by rising the temperature from 25 to 65 ℃. It is evident from Figure 4.18 that the removal of CIP by (Fe^0/oxalate) nanoparticles prefers the low temperatures. For example, the efficacy of (Fe^0/oxalate) nanoparticles at 25 ℃ was remarkable as 95.50% of 100 mg L^{-1} of CIP was eliminated within 5 min (Figure 4.18**)**. However, a sign of deterioration in the performance of (Fe^0/oxalate) nanoparticles was noted after elevating the reaction temperature to 35 and 45 ℃ where the removal efficiency insignificantly

dropped from 95.50% to 93.58% and 90.28%, respectively (Figure 4.18). In addition, the removal efficiency of CIP considerably decreased to 75.78% and 63.12% because of rising the reaction temperature to 55 and 65 ℃ (Figure 4.18). It can be inferred from Figure 4.18 that the high reaction temperature provides the required energy to break the formed adsorption bonds between CIP and the adsorptive sites on the surface of Fe^0 nanoparticles, as it can be observed that at 65 ℃ the concentration of CIP in the aqueous solution started to increase after 10 min. These results confirm the exothermic nature of CIP adsorption by (Fe^0/oxalate) nanoparticles. The parameters of thermodynamics, namely ΔH^0, ΔS^0, and ΔG^0 were determined by applying Van't Hoff equation [Equation (2.28)] and the 3rd principle in thermodynamics [Equation (2.27)] as manifested in section 2.8.5. Table 4.8 and Figure 4.19 summarize the outcomes of thermodynamic analysis. Moreover, Table 2.7 and Table 2.8 epitomize the interoperation of both the sign and the magnitude of thermodynamics parameters. The obtained ΔG^0 is negative at all reaction temperatures which indicates that the adsorption of CIP by (Fe^0/oxalate) nanoparticles was favorable and spontaneous (Table 4.8) [198]. Also, the negative sign of ΔH^0 suggests that the adsorption of CIP was exothermic, which is in good agreement with the experimental results [213,247].

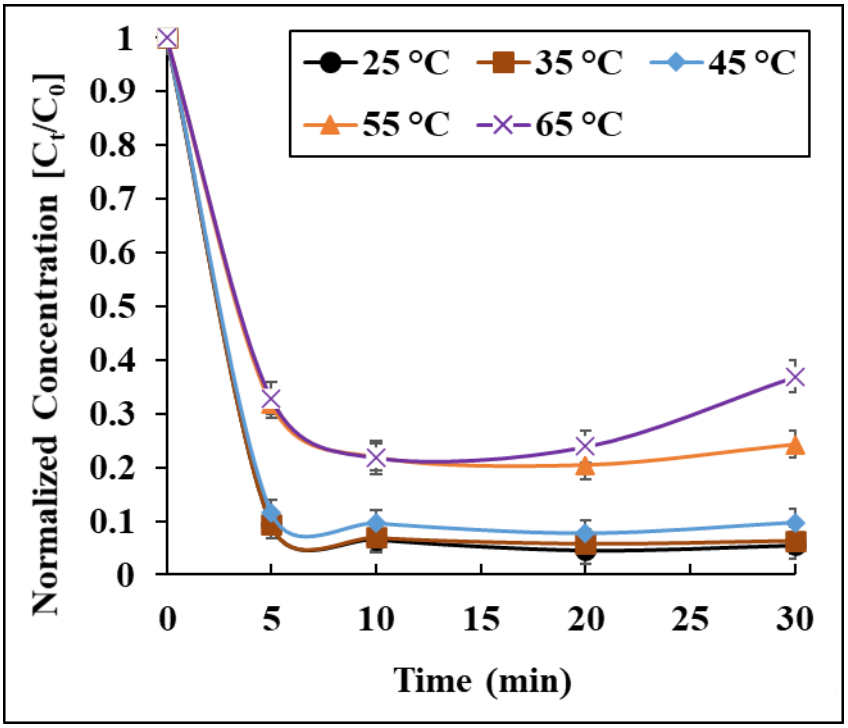

Figure 4.18 Effect of temperature on the competence of (Fe^0/oxalate) nanoparticles. Reaction parameters were as follows: [Fe^0] = 0.3 g L^{-1}, [CIP] = 100 mg L^{-1}, [oxalate] = 0.3 mM, pH = 7, and 11, temperature = 25, 35, 45, 55, and 65 ºC, stirring speed = 500 rpm, and reaction time = 30 min.

Table 4.8 Parameters of thermodynamic analysis for treating CIP-polluted solutions by (Fe^0/oxalate) nanoparticles.

Temperature (K)	Gibbs free energy change (ΔG^o) (kJ mol^{-1})	Entropy change (ΔS^o) (kJ mol^{-1} K^{-1})	Enthalpy change (ΔH^o) (kJ mol^{-1})	Activation Energy (kJ mol^{-1})
298.15	-10.776			
308.15	-9.423			
318.15	-8.071	-1.35E-01	-51.1	15.20
328.15	-6.719			
338.15	-5.366			

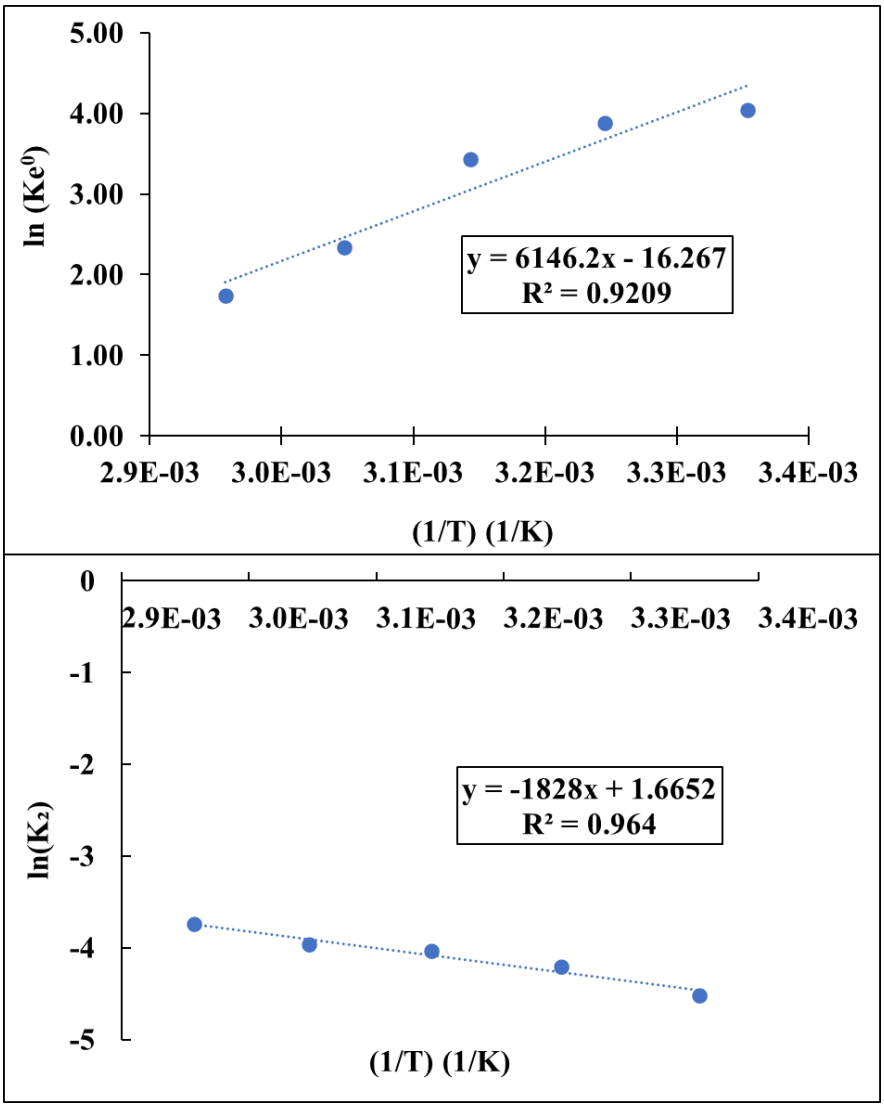

Figure 4.19 Thermodynamic analysis of CIP removal by (Fe^0/oxalate) nanoparticles. **(a)** Determination of thermodynamic parameters by Van't Hoff equation and **(b)** calculation of activation energy by Arrhenius equation.

Furthermore, the negative value of ΔS^0 indicates that the freedom of CIP molecules and the randomness at the surface of (Fe^0/oxalate) decreased during the adsorption of CIP [250]. In addition to the sign, the absolute value ΔG^0 and ΔH^0 can emphasize the type of CIP adsorption by (Fe^0/oxalate) nanoparticles (Table 2.7). The absolute value of ΔG^0 at all temperatures is less than 20 kJ mol^{-1} (2 kJ/mol $<\Delta G^0<$ 20 kJ/mol). Consequently, the adsorption of CIP by (Fe^0/oxalate) nanoparticles could be physisorption [63]. However, the absolute magnitude of ΔH^0 is 51.1kJ mol^{-1} (20 kJ mol^{-1} $<\Delta H^0<$ 80 kJ mol^{-1}) which implies that both physisorption and chemisorption occurred during the adsorption of CIP [251]. These results are consistent with the findings of Zhang *et al.* as they confirmed that physisorption and chemisorption both contributed to the adsorption of CIP by sulfate-reducing bacteria sludge because of the absolute value of ΔH^0 was 49.51 kJ mol^{-1}, although, the absolute value of ΔG^0 ranged from 8.05 to 12.09 kJ mol^{-1} [213]. The activation energy (E_a) of CIP adsorption was obtained by the Arrhenius equation (Figure 4.19.b) to distinguish between the physisorption and chemisorption processes. Table 4.8 exhibits that the calculated E_a is 15.20 kJ mol^{-1}, suggesting that the adsorption of CIP might be controlled by physical adsorption since E_a lies between 5 and 50 kJ mol^{-1} [197,252]. In conclusion, the results of the thermodynamic analysis are consistent with the results of isotherm and kinetics analysis.

4.11. Removal mechanism of ciprofloxacin by (Fe^0/oxalate)

Figure 4.11 proved that the oxidation of CIP didn't occur, and the treatment of CIP by (Fe^0/oxalate) nanoparticles was entirely governed by adsorption. It is important to mention that there are two types of adsorptions, namely physisorption and chemisorption. Physisorption occurs when CIP forms weak bonds with the surface of (Fe^0/oxalate) such as van der Waals forces, hydrogen bonding, electrostatic attraction, etc. [253]. On the contrary, chemisorption of CIP by (Fe^0/oxalate) nanoparticles occurs when strong bonds are formed [253]. It is also clear from Figure 4.11 that physisorption was more dominant at initial pH 5 because it was desorbed with a little bit of resistance. While chemisorption was more predominant at initial pH = 7 and pH = 9 since a long time was needed to achieve the complete desorption (i.e., 48h). Based on the strength of CIP desorption (Figure 4.11), it can be concluded that physisorption and chemisorption simultaneously occurred during the adsorption of CIP by (Fe^0/oxalate) nanoparticles. These findings are consistent with the outcomes of kinetics, isotherm, and thermodynamics analysis.

To further clarify the nature of CIP adsorption by (Fe^0/oxalate) nanoparticles, SEM-EDS, XRD, and FTIR analysis for the spend (Fe^0/oxalate) nanoparticles after the adsorption of CIP at different initial pH (e.g., 5, 7, 9, and 11) were conducted. Figure 4.20 shows that the spherical particles of Fe^0 were partially deformed after the reaction with CIP at different initial pH with the existence of oxalate. Also, needle-shaped particles of iron oxides were also observed in the SEM images of spent (Fe^0/oxalate) nanoparticles. The development of needle-shaped iron oxides was confirmed by the identification of several peaks for magnetite (Fe_3O_4) and lepidocrocite [FeO(OH)] in the XRD patterns of the reacted (Fe^0/oxalate) nanoparticles at different initial pH (Figure 4.21). Gu and Karthikeyan stated that CIP was efficiently removed by hydrous oxides of iron (HOF) [212]. Thus, the presence of needle-shaped particles of iron oxides could favor the exceptional adsorption of CIP by (Fe^0/oxalate) nanoparticles.

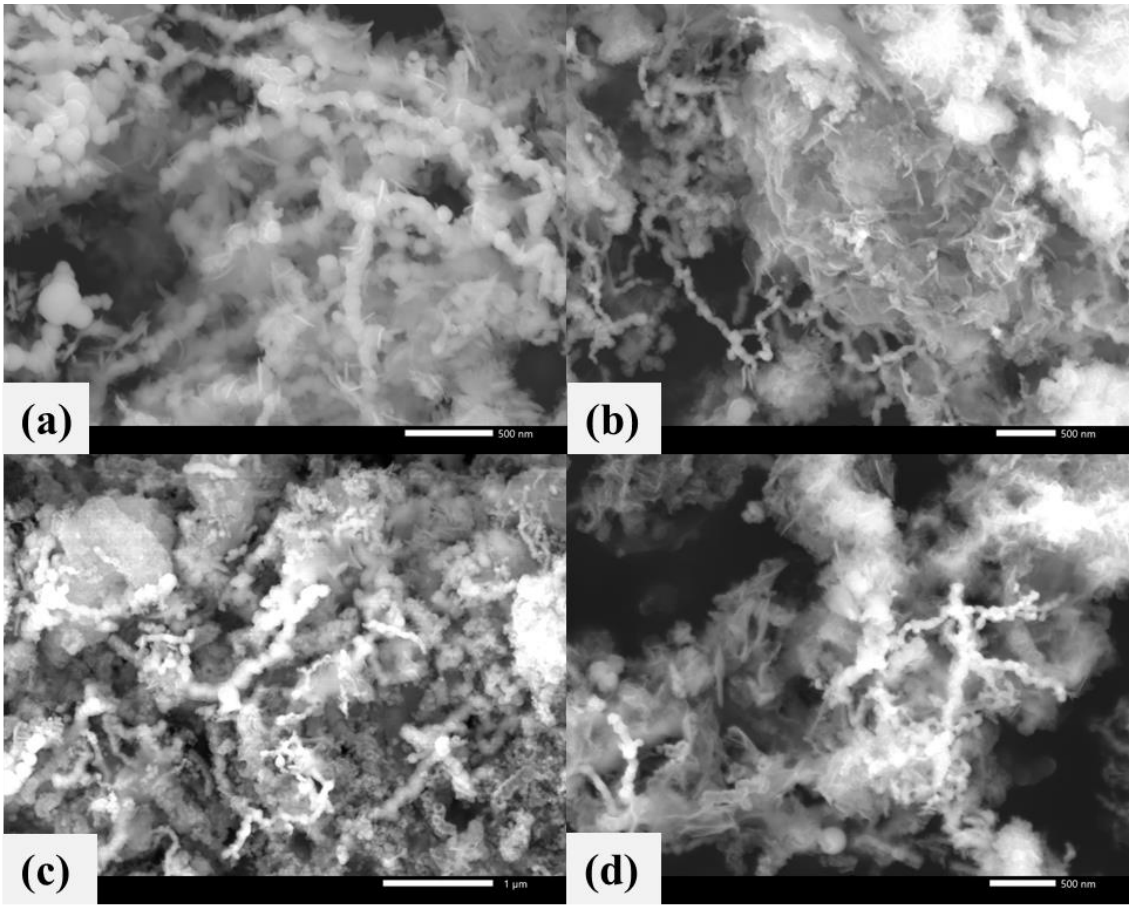

Figure 4.20 SEM pictures for reacted (Fe^0/oxalate) nanoparticles with CIP solution at different initial pH: **(a)** pH 5, **(b)** pH 7, **(c)** pH 9, and **(d)** pH 11. Other reaction parameters were as follows: [CIP] = 100 mg L^{-1}, [Fe^0] = 0.3 g L^{-1}, [oxalate] = 0.3 mM, temperature = 25 °C, stirring speed = 500 rpm, and reaction time = 30 min.

Moreover, Figure 4.22 demonstrates a clear deterioration in the intensity of the characteristic peak of Fe^0 at $2\theta = 44.7°$ as well as noticeable evolution of a new peak at $2\theta = 5°$ after the reaction of (Fe^0/oxalate) nanoparticles with high CIP concentrations such as 200 and 400 mg L^{-1}. These changes in the XRD pattern of (Fe^0/oxalate) nanoparticles after the reaction with elevated CIP concentrations are additional signs of CIP adsorption. Jiang *et al.* reported similar interpretations after the adsorption of CIP by birnessite [41]. Figure 4.23 presents the FTIR spectrums of (Fe^0/oxalate) nanoparticles after the reaction with 100 mg L^{-1} of CIP at different initial pH (e.g., 5, 7, 9, and 11). The FTIR spectrum of CIP powder is complicated, as shown in Figure 4.23.a, because of the huge number of functional groups in the structure of CIP molecule [254].

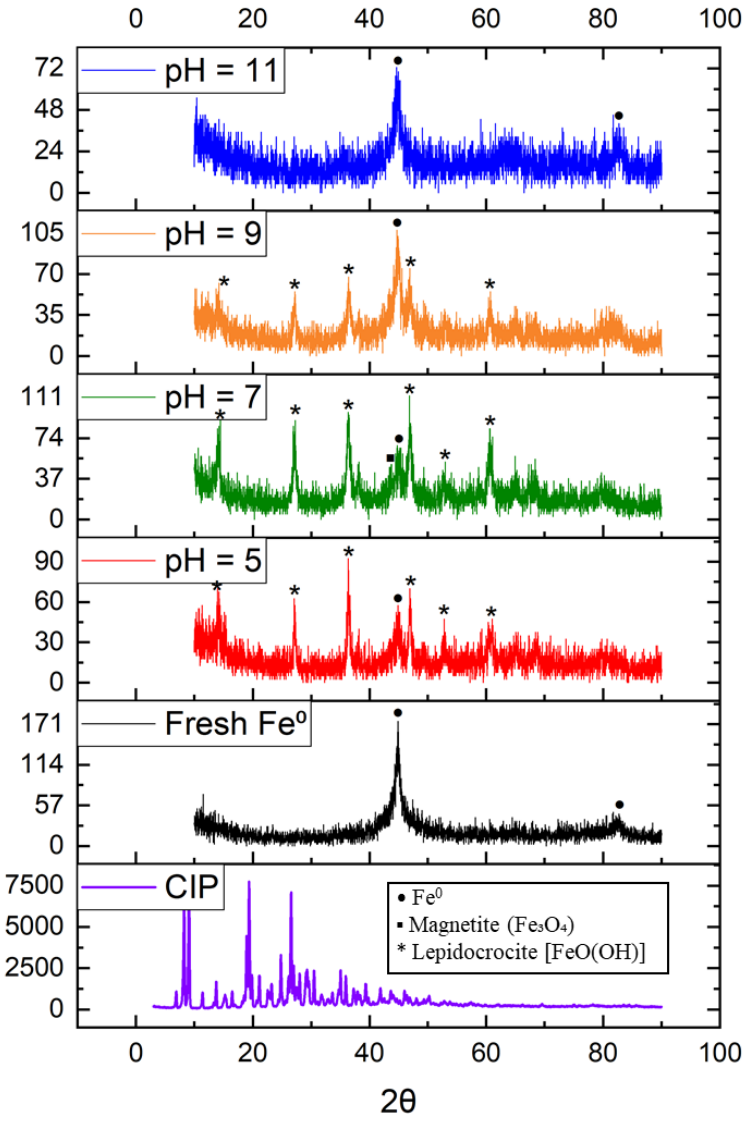

Figure 4.21 XRD analysis for reacted (Fe^0/oxalate) nanoparticles with CIP under the effect of different initial pH. Reaction parameters were as follows: [CIP] = 100 mg L^{-1}, [Fe^0] = 0.3 g L^{-1}, [oxalate] = 0.3 mM, temperature = 25 °C, stirring speed = 500 rpm, and reaction time = 30 min.

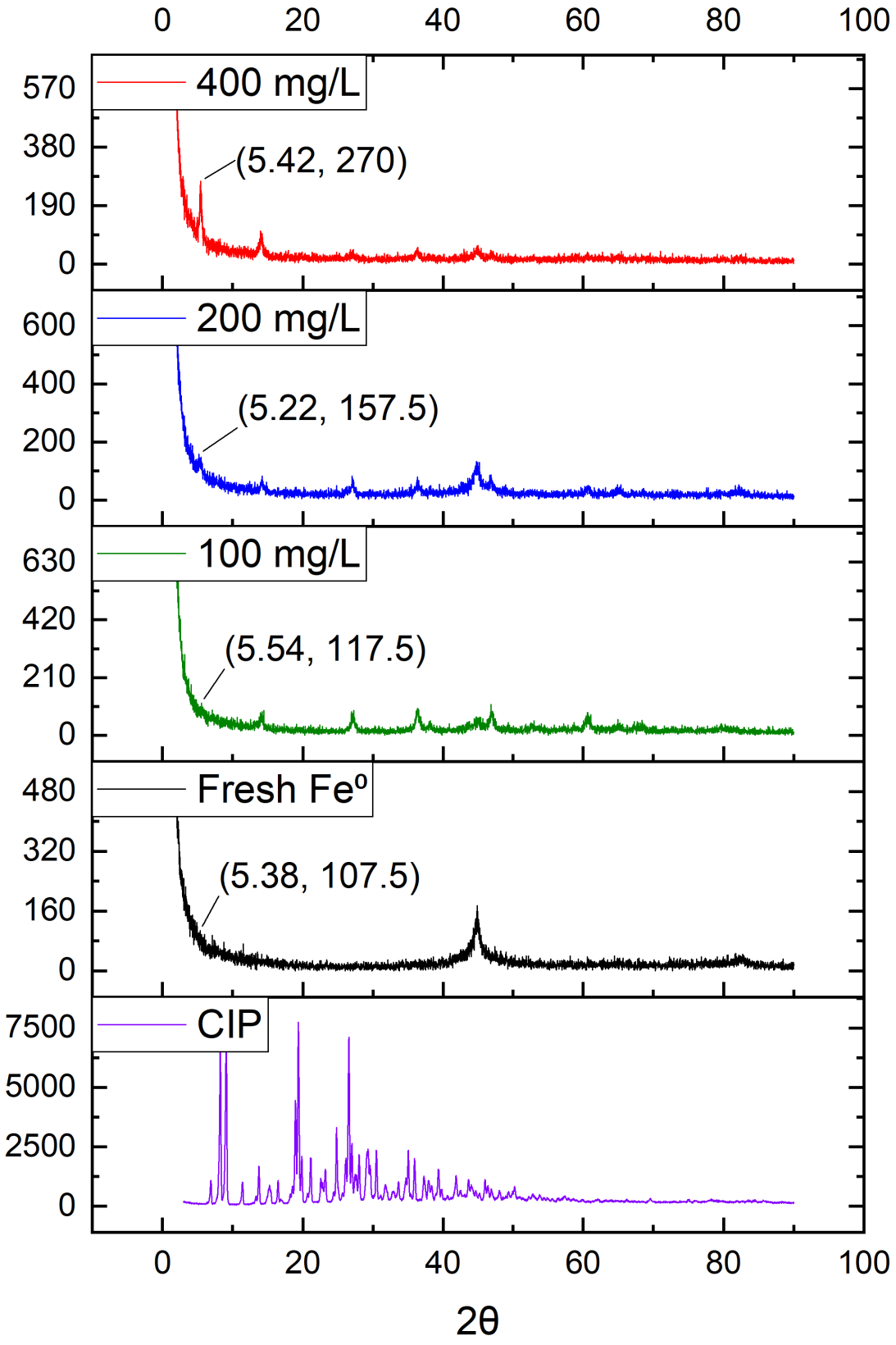

Figure 4.22 XRD analysis for reacted (Fe^0/oxalate) nanoparticles with different CIP concentrations. Reaction parameters were as follows: [Fe^0] = 0.3 g L^{-1}, [oxalate] = 0.3 mM, pH = 7, temperature = 25 °C, stirring speed = 500 rpm, and reaction time = 30 min.

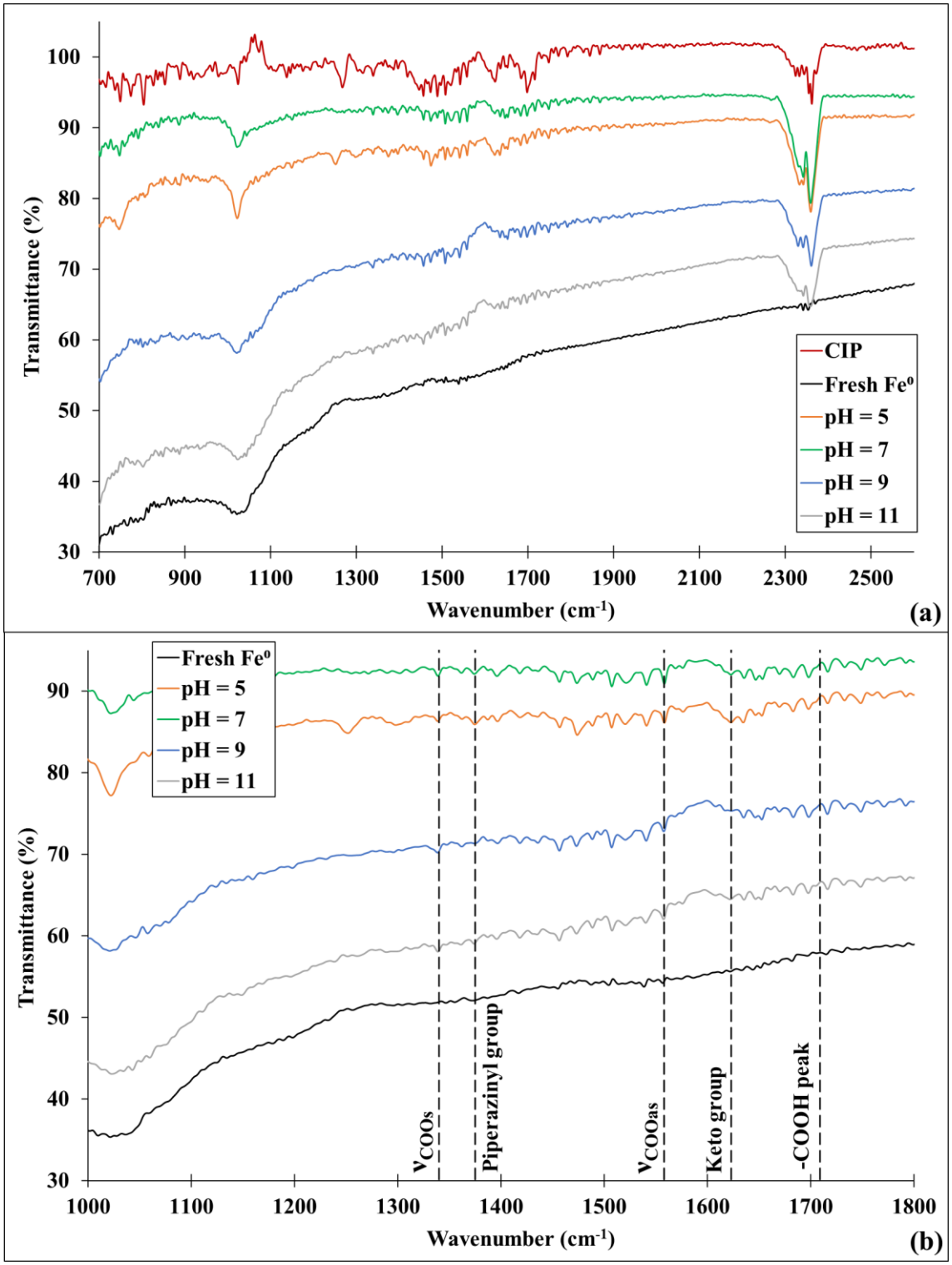

Figure 4.23 Spectrums of FTIR analysis for the reacted (Fe^0/oxalate) nanoparticles with CIP under the effect of different initial pH. **(a)** Full spectrum and **(b)** focused spectrum between 1000 and 1800 cm^{-1}. Reaction parameters were as follows: [CIP] = 100 mg L^{-1}, [Fe^0] = 0.3 g L^{-1}, [oxalate] = 0.3 mM, pH = 5, 7, 9, and 11, temperature = 25 °C, stirring speed = 500 rpm, and reaction time = 30 min.

However, it can be easily recognized in Figure 4.23.a that the distinctive bands of CIP identically appeared in the FTIR spectrum of the reacted (Fe^0/oxalate) nanoparticles at different initial pH. This evidence the successful adsorption of CIP by (Fe^0/oxalate) nanoparticles. The main functional groups in CIP molecule, such as carboxylic, COO^-, ketone, and piperazinyl groups, are located within a wavenumber between 1200 and 1800 cm^{-1} [254]. Hence, Figure 4.23.b displays the same FTIR spectrums as Figure 4.23.a but with a narrow range of wavenumber (1000 cm^{-1}-1800 cm^{-1}) to discuss the contribution of the main functional groups of CIP in the adsorption of CIP by (Fe^0/oxalate) nanoparticles. The absorption peak of -COOH group ($\nu_{C=Ocarboxyl}$) at 1709 cm^{-1} disappeared from the FTIR spectrum of (Fe^0/oxalate) nanoparticles due to the deprotonation of the carboxylic group at pH > pK_{a1} as well as the surface complexation between the carboxylic group and (Fe^0/oxalate) nanoparticles (Figure 4.23.b) [212]. Moreover, COO^- group has two distinctive bands: asymmetric band (ν_{COOas}) at 1580 cm^{-1} and symmetric band (ν_{COOs}) at 1380 cm^{-1}. The difference between these two bands ($\Delta\nu_{aqueous} = \nu_{COOas} - \nu_{COOs}$) in the FTIR spectrum of CIP in the aqueous solution is 200. However, the adsorption of CIP by an adsorbent will alert the value of $\Delta\nu_{aqueous}$ by changing the distance between ν_{COOas} and ν_{COOs} [255]. The value of $\Delta\nu_{adsorption}$ after CIP adsorption can help to predict the nature of the surface complexation between the carboxylic group and (Fe^0/oxalate) nanoparticles. In detail, if $\Delta\nu_{adsorption} > \Delta\nu_{aqueous}$, monodentate surface complexation is expected where the carboxylic group tends to form a bond with a metal center via a single oxygen atom. In contrast, if $\Delta\nu_{adsorption} < \Delta\nu_{aqueous}$, mononuclear complexation is suggested where the carboxylic group connects to the metal center through two oxygen atoms. On the other hand, bridging or binuclear bidentate complexation with the carboxylic group through two metal centers is predicted to occur if $\Delta\nu_{adsorption}$ is comparable to $\Delta\nu_{aqueous}$. Figure 4.23.b demonstrates that the $\Delta\nu_{adsorption}$ (1558-1340) is approximately 218, which is very close to $\Delta\nu_{aqueous}$. Therefore, it is expected that the carboxylic group will form binuclear bidentate or bridging complexation with (Fe^0/oxalate) nanoparticles. The band of the ketone group around 1628 cm^{-1} was barely identified in the FTIR spectrum of the reacted (Fe^0/oxalate) nanoparticles after the adsorption of 100 mg L^{-1} of CIP (Figure 4.23.b). However, Figure 4.23.b illustrated that the peak of the ketone group, at 1628 cm^{-1}, after the adsorption of 400 mg L^{-1} of CIP was split into two adjacent peaks at 1616 cm^{-1} and 1632 $cm^{-1,}$ which confirms the involvement of the ketone group in the adsorption of CIP by (Fe^0/oxalate) nanoparticles [255]. The band of the piperazinyl group at 1389 cm^{-1} was slightly shifted to lower wavenumber (i.e., 1375 cm^{-1}) after the adsorption of 100, 200,

and 400 mg L^{-1} as demonstrated in Figure 4.23.b and Figure 4.24.b [212]. It seems that the addition of a low concentration of oxalate boosted and strengthened the surface complexation between Fe^0 nanoparticles and the main functional groups of CIP instead of promoting the oxidation of CIP by increasing the generation of ROS.

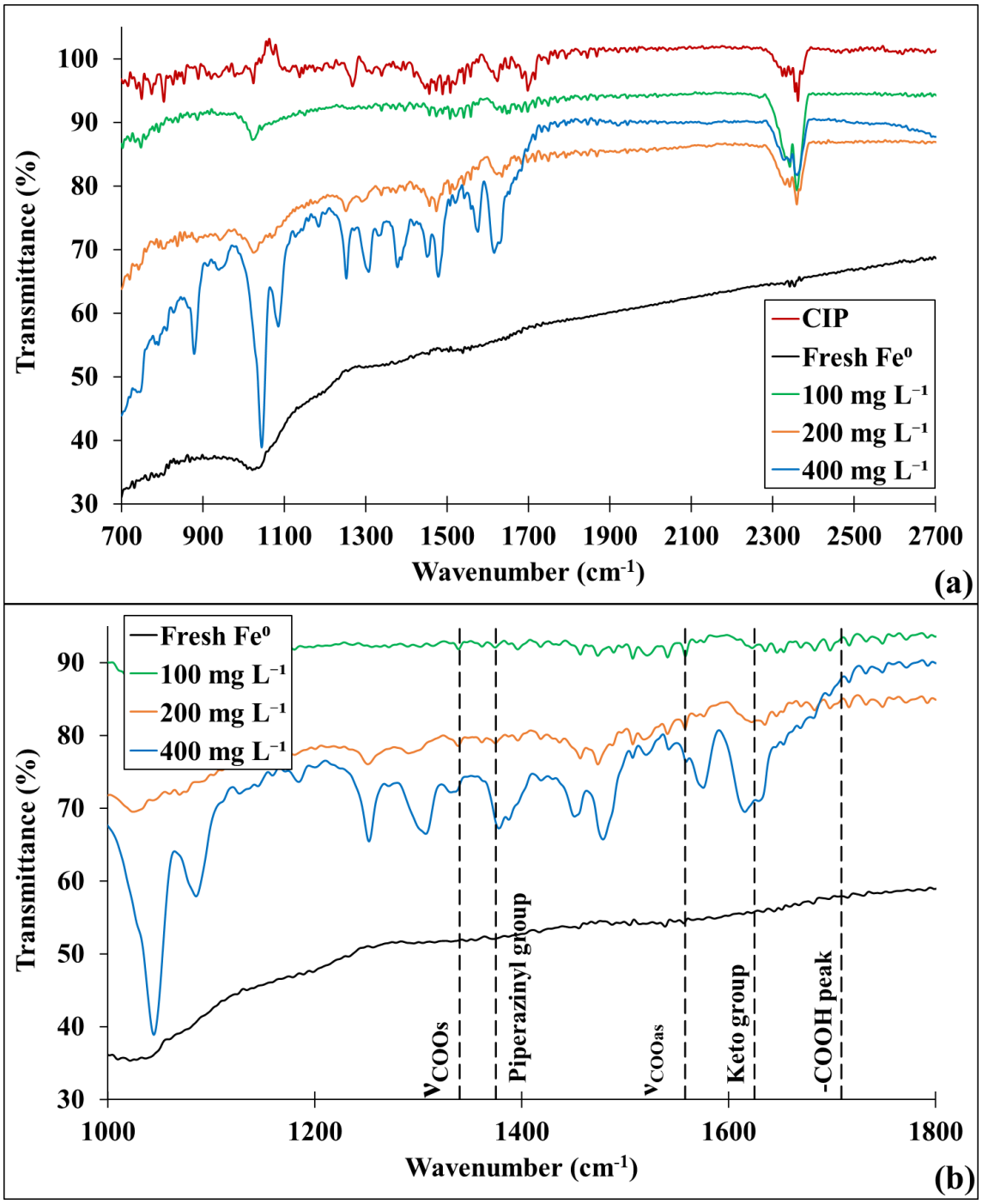

Figure 4.24 Spectrums of FTIR analysis for reacted (Fe^0/oxalate) nanoparticles with different CIP concentrations. reaction parameters were as follows: [Fe^0] = 0.3 g L^{-1}, [oxalate] = 0.3 mM, pH = 7, temperature = 25 °C, stirring speed = 500 rpm, and reaction time = 30 min.

4.12. Influence of water matrix

The impact of water components such as ionic strength (IS), natural organic matters (NOM), and coexisting ions on the elimination of CIP by (Fe^0/oxalate) nanoparticles was elucidated in this section to assure the applicability of utilizing (Fe^0/oxalate) nanoparticles in field-scale applications.

4.12.1. Effect of ionic strength of the polluted water

Industrial and pharmaceutical wastewater are complex and usually contain high concentrations of salts, which could hinder the removal of CIP by (Fe^0/oxalate) nanoparticles [170]. Thus, the influence of the ionic strength (IS) of the polluted solution on the performance of (Fe^0/oxalate) nanoparticles was investigated by increasing the concentrations of sodium chloride (NaCl) from 2.5 to 100 mM, as shown in Table 2.4**.** Figure 4.25 indicates that the removal efficiency of CIP by (Fe^0/oxalate) nanoparticles trivially deteriorated from 95.43% to 92.76% due to the increase of IS from 0 to 50 mM. However, the effect of IS on the performance of (Fe^0/oxalate) nanoparticles was more severe when the concentrations of NaCl were increased to 100 mM as the removal efficiency of CIP diminished by approximately 10% (Figure 4.25). At the beginning of the reaction (i.e., 0-20 min), the presence of 100 mM of NaCl moderately affected the removal of CIP, as displayed in Figure 4.25.

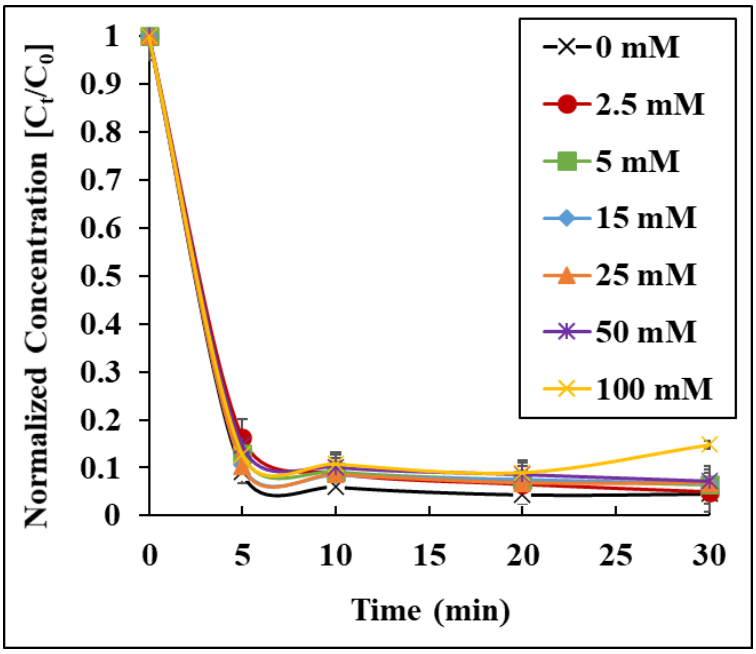

Figure 4.25 : Influence of the ionic strength on the competence of (Fe^0/oxalate) nanoparticles. Reaction parameters were as follows: [Fe^0] = 0.3 g L^{-1}, [oxalate] = 0.3 mM, [CIP] = 100 mg L^{-1}, pH = 7, temperature = 25 ºC, stirring speed = 500 rpm, and reaction time = 30 min.

However, eventually, the excessive concentrations of NaCl competed with CIP on the adsorption sites of Fe^0 nanoparticles, occupied some of them, and expelled the molecules of CIP from the surface of Fe^0 nanoparticles [173]. Consequently, significant desorption of CIP after 20 min of starting the reaction was observed in Figure 4.25, and the final removal efficiency of CIP declined to 85.23% (Figure 4.25). It can be predicted from Figure 4.25 that the electrostatic attraction might not be the main adsorption mechanism since the ionic strength of the solution had limited influence on the performance of (Fe^0/oxalate) nanoparticles to remove CIP from industrial and pharmaceutical wastewater [42].

4.12.2. Effect of natural organic matters

Besides the inorganic salts, the industrial and pharmaceutical wastewater and the natural water include natural organic matters such as humic acid, fulvic acid, and so on. [171]. Humic acid, as a representative of natural organic matter, has serval functional groups, for instance, phenolic, carboxyl, and hydroxyl groups [256]. These groups can interact with Fe^0 nanoparticles and obstruct the removal of CIP from water by (Fe^0/oxalate) nanoparticles [172]. Hence, humic acid was added with different concentrations (e.g., 5, 10, 20, and 40 mg L^{-1}) as demonstrated in Table 2.4 to assess its effect on the elimination of CIP by (Fe^0/oxalate) nanoparticles.

Figure 4.26 deduced that the presence of humic acid in CIP-polluted water didn't adversely impact the removal of CIP by (Fe^0/oxalate) nanoparticles. In other words, humic didn't compete with CIP on the reactive sites of (Fe^0/oxalate) nanoparticles, so the removal efficiency of CIP barely decreased from 95.43% to 94.42% after adding 40 mg L^{-1} of humic acid **(**Figure 4.26**)**. Therefore, these results confirm the remarkable and promising capabilities of (Fe^0/oxalate) nanoparticles in treating actual CIP-polluted waters. Likewise, Ji *et al.* noted that the presence of 10 mg L^{-1} of humic acid didn't affect the adsorption of CIP by titanate nanotubes [172]. On the other hand, Luo *et al.* reported that the presence of humic acid inhibited the adsorption of CIP by sludge-derived biochar [257].

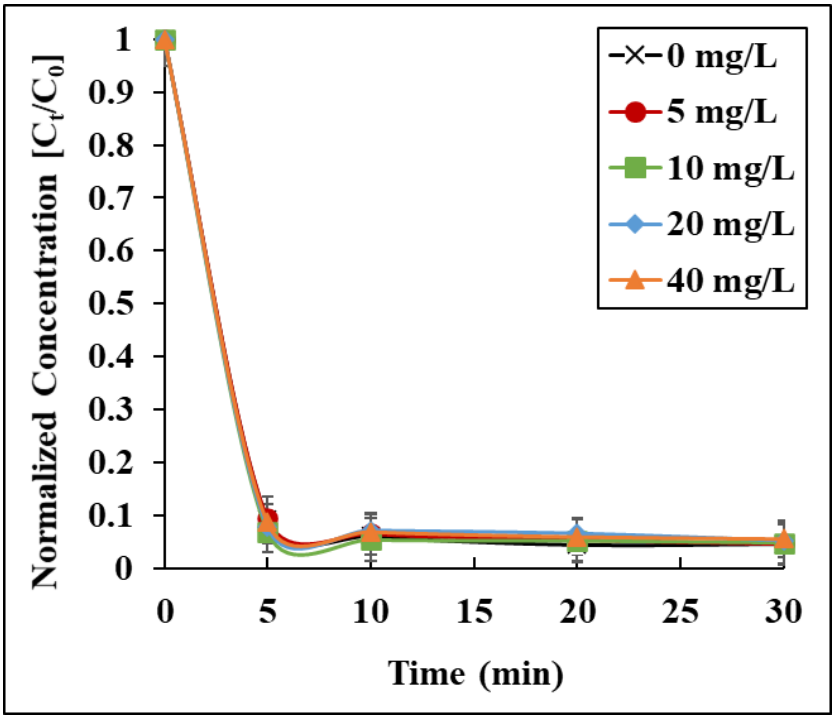

Figure 4.26 Influence of humic acid on the competence of (Fe^0/oxalate) nanoparticles. Reaction parameters were as follows: [Fe^0] = 0.3 g L^{-1}, [oxalate] = 0.3 mM, [CIP] = 100 mg L^{-1}, pH = 7, temperature = 25 ºC, stirring speed = 500 rpm, and reaction time = 30 min.

4.12.3. Effect of coexisting ions

The complex pharmaceutical and industrial wastewater don't only include NaCl as a foreign ion, but they also contain many coexisting ions. Hence, it is important to understand the influence of coexisting ions, for example, potassium (K^+), calcium (Ca^{2+}), magnesium (Mg^{2+}), carbonate (CO_3^{2-}), sulfate (SO_4^{2-}), and nitrate (NO_3^-) on the elimination of CIP by (Fe^0/oxalate) to accurately design a treatment unit based on (Fe^0/oxalate) that could be used as a tool to mitigate CIP contamination in water. Each ion's concentration was modified according to its inhibitory strength, as shown in Table 2.4. Figure 4.27.a illustrates that the presence of K^+ with concentrations ranging from 0 to 50 mM slightly decreased the removal efficiency of CIP by 3.61%. On the other hand, Figure 4.27.c, Figure 4.27.e points out that the inhibitory effect of the divalent cations, namely Ca^{2+} and Mg^{2+} was more robust than the inhibitory effect of K^+. In detail, increasing the concentration of Ca^{2+} from 0 to 30 mM diminished the removal efficiency of CIP by 38.12% (Figure 4.27.c), while rising Mg^{2+} concentration from 0 to 10 mM significantly deteriorated the removal efficiency of CIP by 57.54% (Figure 4.27.e). If 10 mM concentration was selected to make a comparison, the negative influence of cations on the removal of CIP by (Fe^0/oxalate) nanoparticles could be ranked as follows: K^+ <

$Ca^{2+} < Mg^{2+}$. The divalent cations, with higher valance numbers, tend to interact with the surface of (Fe^0/oxalate) nanoparticles stronger than the monovalent cations by occupying more reactive sites [39,255].

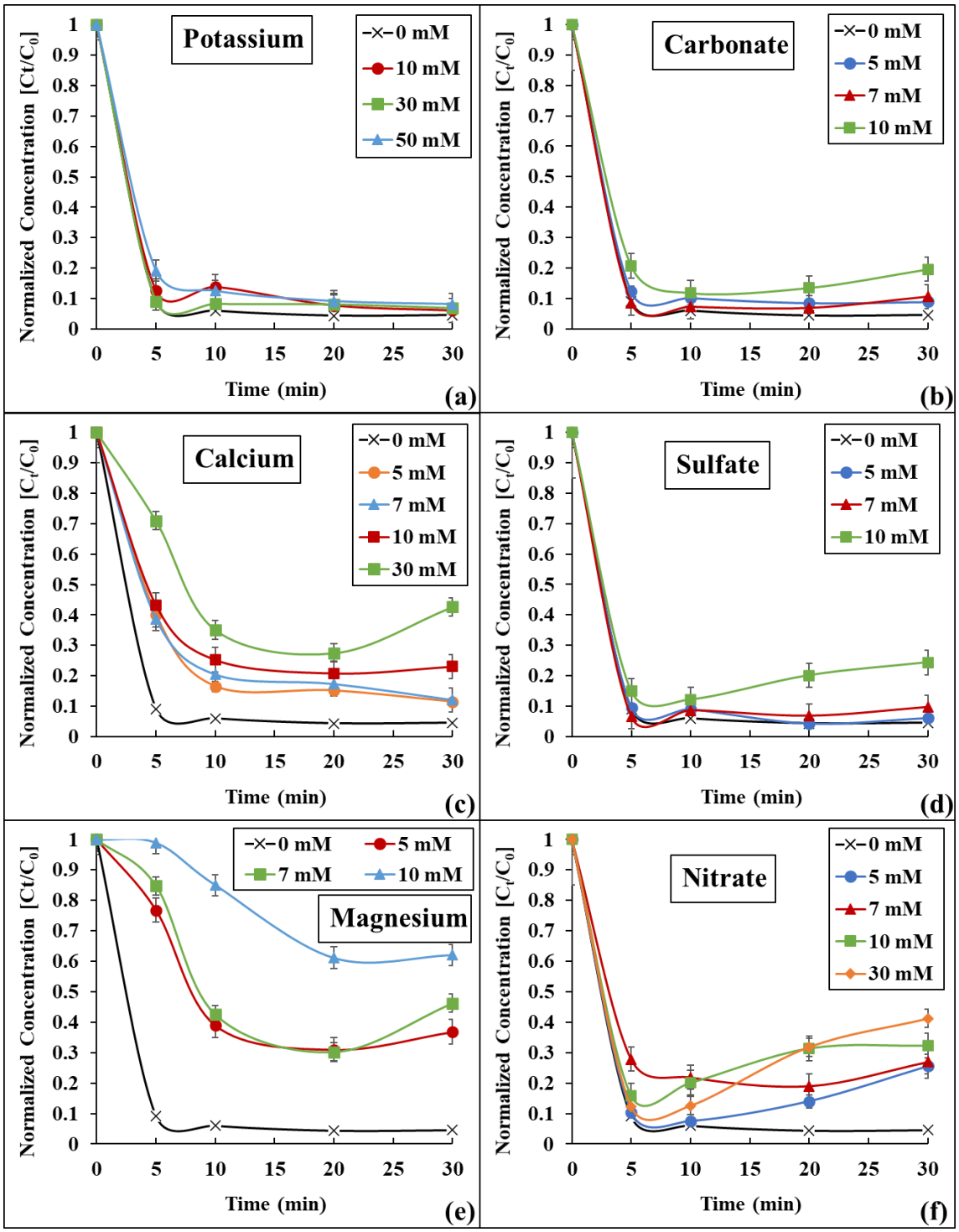

Figure 4.27 Influence of coexisting ions on the competence of (Fe^0/oxalate) nanoparticles. **(a)** Potassium, **(b)** carbonate, **(c)** calcium, **(d)** sulfate, **(e)** magnesium, and **(f)** nitrate. Reaction parameters are as follows: [Fe^0] = 0.3 g L^{-1}, [oxalate] = 0.3 mM, [CIP] = 100 mg L^{-1}, pH = 7, temperature = 25 ºC, stirring speed = 500 rpm, and reaction time = 30 min.

Consequently, the divalent cations will robustly compete with CIP on the adsorption locations of (Fe^0/oxalate) nanoparticles, promote the desorption of CIP as exhibited in Figure 4.27.c and Figure 4.27.e, and significantly decrease CIP removal by (Fe^0/oxalate) nanoparticles. These results are consistent with the results of Li *et al.* [258] and Zheng *et al.* [42].

Figure 4.27.b demonstrates that the effectiveness of (Fe^0/oxalate) was negatively affected by increasing CO_3^{2-} concentration from 0 to 10 mM because the removal efficiency dropped from 95.43% to 80.41%. Whilst Figure 4.27.d and Figure 4.27.f displays that the negative effect of 10 mM of SO_4^{2-} and NO_3^- on the removal efficiency of CIP was more severe than CO_3^{2-} as the competence of (Fe^0/oxalate) nanoparticles deteriorated from 95.43% to 75.60% and 58.81%, respectively. Similar to cations, based on the effect of the presence of 10 mM of anions, their negative effect can be ranked as follows: CO_3^{2-} < SO_4^{2-} < NO_3^- (Figure 4.27.b, Figure 4.27.d, and Figure 4.27.f). Both CO_3^{2-} and SO_4^{2-} can compete with CIP on the adsorption sites by creating complexes with the iron oxides on the surface of Fe^0 nanoparticles [259]. Yang *et al.* also indicated that the exitance of SO_4^{2-} restrained the removal of metronidazole by PAA/PVDF–NZVI hybrids [259–261]. On the other hand, it is well documented in the literature that the presence of NO_3^- will force the core of Fe^0 nanoparticles to release electrons to reduce it to nitrite, ammonia, and N_2 [149,262]. Thus, donating electrons from the core of Fe^0 nanoparticles will weaken the adsorption capacity of Fe^0 nanoparticles and desorb the molecules of CIP to the aqueous solution, as exhibited in Figure 4.27.f.

Overall, based on Figure 4.27, the inhibitory effect of coexisting ions on the elimination of CIP by (Fe^0/oxalate) nanoparticles can be ordered as follows: Mg^{2+} > NO_3^- > SO_4^{2-} > Ca^{2+} > CO_3^{2-} > K^+.

4.13. Regeneration and recycling of (Fe^0/oxalate) nanoparticles

(Fe^0/oxalate) nanoparticles were regenerated and reutilized for four adsorption processes to investigate the recyclability of (Fe^0/oxalate) nanoparticles. According to Figure 4.28, the removal efficiency of CIP by (Fe^0/oxalate) nanoparticles slightly decreased from 95.17% to 83.59% after the first cycle. Afterwards, the performance of (Fe^0/oxalate) nanoparticles sharply deteriorated as the number of cycles increased. At the end of the fourth cycle, the removal efficiency of CIP by (Fe^0/oxalate) nanoparticles remarkably declined from 83.59% to 5.66%. The massive loss in the efficiency of (Fe^0/oxalate) nanoparticles during the recycling process was due to the considerable drop in the mass

of (Fe^0/oxalate) nanoparticles after each adsorption cycle, as well as the excessive corrosion of (Fe^0/oxalate) nanoparticles during the successive treatment processes.

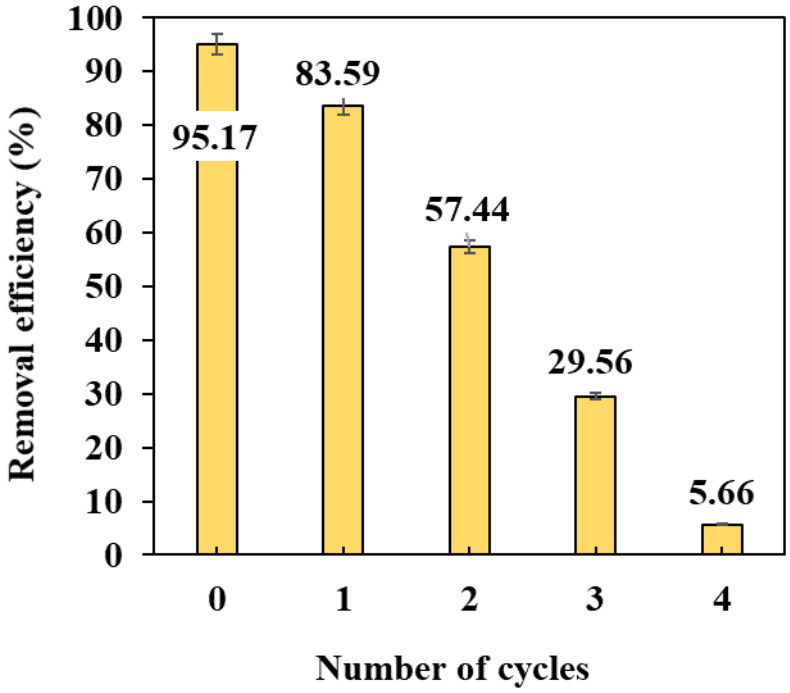

Figure 4.28 Regeneration and reuse of (Fe^0/oxalate) nanoparticles.

4.14. Cost analysis of the treatment process by Fe^0 and (Fe^0/oxalate)

A cost analysis for remediating CIP-polluted water by Fe^0 and (Fe^0/oxalate) nanoparticles was conducted to reflect the economic benefits of adding oxalate to Fe^0 nanoparticles in wastewater treatment. The cost analysis was performed based on the cost of the synthesis materials of Fe^0 nanoparticles, such as ferric chloride ($FeCl_3$) and sodium borohydride ($NaBH_4$), and the cost of the added sodium oxalate. While the cost of other parameters, for instance, electricity, water, etc., was considered as a constant. Table 4.9 summarizes the analysis of the treatment cost.

Table 4.9 Cost analysis for treating CIP-polluted waters by Fe^0 and (Fe^0/oxalate) nanoparticles.

Price of $FeCl_3$	Price of $NaBH_4$	Price of sodium oxalate	Cost of 1 g Fe^0 nanoparticles	Treatment cost by Fe^0	Treatment cost by (Fe^0/oxalate)
(¥2700/500g) or (¥5.4/1g)	(¥15200/500g) or (¥30.4/1g)	(¥2400/100g) or (¥24/1g)	¥93.88	¥65.716/L	¥29.124/L

As stated in section 2.2, 5 g of $FeCl_3$ and 2.2 g of $NaBH_4$ are required to synthesize 1 g of Fe^0 nanoparticles. Therefore, according to Table 4.9, the cost of producing 1 g of Fe^0 nanoparticles can be estimated to be ¥93.88 [(5×5.4) + (2.2×30.4)]. If it is decided to treat 1 L of 100 mg L^{-1} of CIP-polluted water, 0.7 and 0.3 g L^{-1} of Fe^0 nanoparticles were needed for the treatment process by Fe^0 and (Fe^0/oxalate) nanoparticles, respectively, as illustrated in Figure 4.7 and Figure 4.8. Furthermore, Figure 4.8 proved that the optimum concentration of oxalate is 0.3 mM (40 mg L^{-1}). It is evident from Table 4.9 that the addition of oxalate to Fe^0 remarkably reduced the treatment cost of 1 L of 100 mg L^{-1} from ¥65.716 [0.7×93.88] to ¥29.124 [(0.3×93.88) + (40×24/1000)]. Moreover, the addition of oxalate to Fe^0 significantly lowered the volume of the generated sludge after the treatment process by nearly 57% due to the reduction of Fe^0 dosage from 0.7 to 0.3 g L^{-1}. Hence, the addition of oxalate to Fe^0 nanoparticles is an efficient, economical, and environmentally friendly approach for exceptional adsorption of CIP from water.

4.15. Comparison between the efficacy of (Fe^0/oxalate) nanoparticles and previously reported Fe^0-based nanomaterials

Many approaches were previously employed to enhance the competence of Fe^0 nanoparticles in removing CIP from water, such as doping noble metals [i.e., copper (Cu), nickel (Ni), etc.] [125], addition of oxidants [e.g., hydrogen peroxide (H_2O_2), persulfate, etc.] [119], dispersion of Fe^0 nanoparticles on supporting materials (i.e., biochar, wheat straw, etc.) [116], solidification of Fe^0 nanoparticles [120], stabilization of Fe^0 nanoparticles (e.g., surfactants, polymers, etc.) [106], application of weak magnetic field (WMF) [124], etc. On the contrary, the removal of CIP by (Fe^0/oxalate) nanoparticles is reported for the first time in the literature; thus, a comparison between (Fe^0/oxalate) nanoparticles and other reported Fe^0-based treatment systems was made to highlight the effectiveness, simplicity, and applicability of (Fe^0/oxalate) nanoparticles over the other reported Fe^0-based treatment systems. Table 4.10 shows that the efficiency of (Fe^0/oxalate) nanoparticles is better than most of the reported Fe^0-based nanomaterials or systems. For example, the maximum removal capacity of (Fe^0/oxalate) nanoparticles (294.66 mg g^{-1}) is approximately 3 times higher than that of wheat straw-supported nanoscale zero-valent iron (WS-nZVI) (104.693 mg g^{-1}) [116]. In addition to the extraordinary performance, Table 4.10 demonstrates that (Fe^0/oxalate) nanoparticles is simple, environmentally friendly, inexpensive, and more applicable than most of the

proposed Fe^0-based system as it doesn't require complex synthesis procedures, addition of toxic substances (e.g., H_2O_2, persulfate, etc.) or an external magnetic field.

Table 4.10 Comparison between (Fe^0/oxalate) nanoparticles and previously reported Fe^0-based treatment systems.

Treatment system	Removal conditions	Maximum removal capacity (mg g^{-1})	Ref.	This study: maximum removal capacity (mg g^{-1})
Wheat straw-supported nanoscale zero-valent iron (WS-nZVI)	[CIP] = 100 mg L^{-1}, WS-nZVI dosage = 0.75 g L^{-1}, pH = NA, temperature = 25 °C, and reaction time = 240 min.	104.693	[116]	294.66 [CIP =100 mg L^{-1}]
Polyvinylpyrrolidone stabilized nZVI/Cu bimetallic particles (PVP-nZVI/Cu)	[CIP] = 100 mg L^{-1}, PVP-nZVI/Cu dosage = 0.5 g L^{-1}, nZVI/Cu = 1:0.04, initial pH = 6, temperature = 35 °C, weak magnetic field = 2 mT, and reaction time = 120 min.	196.8	[106]	294.66 [CIP =100 mg L^{-1}]
Green synthesized bimetallic GT-nZVI/Cu composites	[CIP] = 50 mg L^{-1}, pH = 6, GT-nZVI/Cu dosage = 0.5 g L^{-1}, GT-nZVI/Cu = 1/0.08, weak magnetic field = 2 mT, temperature = 35°C, and contact time = 90 min.	100	[125]	117.92 [CIP =50 mg L^{-1}]
Activation of H_2O_2 by biochar-supported nanoscale zero-valent iron (BC-nZVI)	[CIP] = 100 mg L^{-1}, BC:nZVI = 1:1, BC-nZVI dosage = 0.4 g L^{-1}, pH = 3~4, [H_2O_2] = 20 mM, temperature = 25 °C, and reaction time = 60 min.	175	[119]	294.66 [CIP =100 mg L^{-1}]
Activation of persulfate sulfide-modified nanoscale iron supported by biochar (S-nZVI/BC)	[CIP] = 50 mg L^{-1}, S/Fe molar ratio = 0.25, S-nZVI/BC dosage = 0.4 g L^{-1}, pH = NA, [Persulfate] = 1 mM, temperature = NA, and reaction time = 125 min.	112.23	[120]	117.92 [CIP =50 mg L^{-1}]
Activation of H_2O_2 by nZVI with the presence of weak magnetic field (WMF) and aeration	[CIP] = 100 mg L^{-1}, nZVI dosage = 0.6 g L^{-1}, initial pH = 7, [H_2O_2] = 14.2 mM, weak magnetic field = 40 mT, temperature = NA, and reaction time = 10 min.	161.67	[124]	294.66 [CIP =100 mg L^{-1}]

Chapter 5

Conclusions & Recommendations

5.1. Major findings and conclusions

Ciprofloxacin (CIP) is a contaminant of emerging concern (CEC). Its persisting detection and other antibiotics in various aquatic environments is a global threat and causes chronic and lethal diseases to humans and animals, in addition to adversely affecting multiple ecosystems in the environment. This research has proposed an environmentally friendly, efficient, and innovative treatment technology based on nanotechnology to combat the ubiquitous occurrence of ciprofloxacin in our limited water resources.

The present research has adopted iron nanoparticles (Fe^0) as a reactive and base nanomaterial to develop novel iron-based nanomaterials; namely, $Mg(OH)_2$-encapsulated iron nanoparticles (Mg/Fe^0) and oxalate-modified iron nanoparticles (Fe^0/oxalate), for superior and remarkable removal of ciprofloxacin from polluted waters. Accordingly, the doctoral research work was divided into two major research projects: **(I)** remediation of ciprofloxacin-polluted water by Mg/Fe^0 nanoparticles and **(II)** effective removal of ciprofloxacin from polluted water by (Fe^0/oxalate) nanoparticles. This section will summarize each research project's outcomes and conclusions separately.

The key findings and conclusions of the first research project are as follows:

1. The characterization techniques, e.g., TEM and XRD, proved that the external morphology and crystalline structure of Mg/Fe^0 nanoparticles didn't change after the encapsulation by a shell of $Mg(OH)_2$, compared with Fe^0 nanoparticles, except the presence of a shell of $Mg(OH)_2$ surrounding Fe^0 nanoparticles and the emergence of small peaks for brucite in the XRD patterns of Mg/Fe^0 nanoparticles.

2. Encapsulation of iron nanoparticles by $Mg(OH)_2$ layer with a [$Mg(OH)_2/Fe^0$] mass ratio of 5 % remarkably enhanced the elimination rate of CIP from 41.76% to 96.31%.

3. The optimization of the treatment conditions demonstrated that 100 mg L^{-1} of CIP can be optimally remediated with more than 90% removal efficiency by 0.5 g L^{-1} over a broad range of initial pH (i.e., 3-11) at 25 ℃.

4. The kinetics analysis for eliminating CIP by Mg/Fe^0 nanoparticles showed that the adsorption data was well represented by both Pseudo first-order and Pseudo-second-order models.

5. The isotherm analysis declared that Freundlich isotherm model was the best isotherm model to describe the equilibrium data of CIP adsorption by Mg/Fe^0 nanoparticles.

6. The thermodynamic modeling concludes that the adsorption of CIP by Mg/Fe^0 nanoparticles from polluted waters was exothermic, spontaneous, and governed by chemisorption.

7. Mg/Fe^0 nanoparticles were regenerated and reutilized for five treatment processes with removal efficiencies higher than 95%.

8. The prototype lab-scale treatment system successfully treated 10 liters of 100 mg L^{-1} of CIP-polluted water with 100% overall removal efficiency.

9. The longevity experiment manifested that the coating process extended and preserved the excellent effectiveness of Mg/Fe^0 nanoparticles for 30 days. However, storing Mg/Fe^0 nanoparticles in ethanol is recommended to preserve them for more than a month.

The key findings and conclusions of the second research project are as follows:

1. The preliminary experiments elucidated that the remediation of CIP-polluted water by Fe^0 nanoparticles was greatly improved from 45.05% to nearly 95.74% after adding low concentrations of the organic ligand oxalate (0.3 mM) to Fe^0 nanoparticles.

2. The optimization process of the treatment conditions revealed that the optimal treatment parameters of 100 mg L^{-1} of CIP-polluted water by (Fe^0/oxalate) nanoparticles were as follows: [Fe^0] = 0.3 g L^{-1}, [oxalate] = 0.3 mM, initial pH = 7, and reaction temperature = 25 ℃.

3. The desorption experiments confirmed that the oxidation of CIP by (Fe^0/oxalate) nanoparticles didn't occur. Conversely, physical and chemical adsorption were cooperatively responsible for eliminating CIP from aqueous solutions.

4. SEM-EDS, XRD, and FTIR analysis for (Fe^0/oxalate) nanoparticles before and after the reaction with CIP indicated that the addition of 0.3 mM of oxalate boosted the oxidation of 0.3 g L^{-1} of Fe^0 nanoparticles to needle-shaped particles of iron oxides and strengthened the surface complexation between Fe^0 and the major functional groups of CIP; namely, carboxylic (i.e., bridging complexation), ketone, and piperazinyl groups (i.e., electrostatic attraction).

5. The outcomes of kinetics, isotherm, and thermodynamic analysis suggest that the multilayer adsorption of CIP on the heterogeneous surface of (Fe^0/oxalate) nanoparticles was favorable, exothermic, and spontaneous.

6. The effectiveness of (Fe^0/oxalate) nanoparticles to remediate 100 mg L^{-1} of CIP slightly deteriorated from 95.43% to 85.23% as a result of increasing the ionic strength of the background solution from 0 to 100 mM.

7. The effect of humic acid on the competence of (Fe^0/oxalate) nanoparticles to treat CIP-polluted water was minimal as the removal efficiency slightly dropped from 95.43% to 95.42% due to the increase of humic acid concentrations from 0 to 40 mg L^{-1} in the background solution.

8. The inhibitory effect of coexisting ions on the treatment of CIP-polluted water by (Fe^0 oxalate) nanoparticles was observed in the following order: $Mg^{2+} > NO_3^- > SO_4^{2-} > Ca^{2+} > CO_3^{2-} > K^+$.

9. The oxalate addition is a cost-effective and environmentally friendly method to improve the performance of Fe^0 nanoparticles towards CIP, as the cost of remediating 1 liter of 100 mg L^{-1} of CIP-polluted water notably declined from ¥65.716 (Fe^0 alone) to ¥29.124 (Fe^0/oxalate) and the volume of the generated sludge considerably decreased by 57%.

5.2. Recommendations

Based on the aforementioned major findings, the following are recommendations and suggestions for prospective researchers:

- The synthesis cost of Mg/Fe^0 nanoparticles is still higher than that of Fe^0 nanoparticles due to the use of ethanol as a dispersion solution. Therefore, it is recommended to investigate the possibility of substituting ethanol with deionized water throughout the synthesis procedures to decrease the treatment cost of CIP-polluted water by Mg/Fe^0 nanoparticles.
- The proposed lab-scale treatment system successfully treated continuous streams of CIP-polluted water with 100% overall removal efficiency. The promising performance of this system is reported for the first time in this study, and it is vital to ensure the possibility of applying such as system in real contamination sites. Thus, it is recommended to scale the system up and use it either as an additional unit in wastewater treatment plants or as a separate treatment unit for treating real CIP-polluted waters.
- The suggested iron-nanomaterials were employed to remove CIP alone from aqueous solutions. However, the real polluted water, such as hospital wastewater, contains a mixture of pharmaceuticals and other organic pollutants that might interfere with the treatment process. Hence, it is essential to examine the competence of these nanomaterials to remove CIP while being mixed with other pharmaceuticals to ensure the feasibility of these nanomaterials in field-scale applications.
- This study proved the possibility of storing Mg/Fe^0 nanomaterials for 30 days with no signs of deterioration in their efficiency in remediating CIP-polluted waters. However, on some occasions, we might need to transport Mg/Fe^0 nanoparticles overseas for commercial purposes, which may take more than one month. Therefore, it is recommended to investigate the potential of storing Mg/Fe^0 nanoparticles for longer periods (e.g., 6 – 12 months).
- In this study, Fe^0 nanoparticles were synthesized using sodium borohydride as a reducing agent. However, sodium borohydride is a toxic substance, and it can cause secondary pollution. Hence, it is recommended to utilize environmentally friendly reducing agents to produce Fe^0 nanoparticles for environmental applications. Some of the eco-friendly reducing chemicals could be plant extracts (e.g., Rosa, etc.) [263], green tea extracts [125,264], pomegranate peel extracts [265,266], and so forth.

5.3. Future work

The future research work will focus on tackling the pollution of water by another class of organic chemicals called poly- and per-fluoroalkyl substances (PFAS). This section will give a brief introduction about PFAS-water pollution and the proposed innovative treatment technology.

5.3.1. Research background

Poly- and per-fluoroalkyl substances (PFAS) are unique organic compounds belong to the perfluorinated compounds [267]. They are known for their unique organic structure that composes of fully or partially fluorinated carbon chains [267]. These chains (e.g., C-F bonds) are hydrophobic and characterized by high bond dissociation energy (i.e., 544 kJ mol^{-1}) compared with carbon-hydrogen bonds (i.e., 389 kJ mol^{-1}) [267]. In addition to the hydrophobic C-F chains, PFAS are decorated with amphiphilic functional groups [267]. Due to this distinctive structure, PFAS possesses excellent tensioactive properties and remarkable chemical and thermal stability. PFAS are broadly utilized in various industries such as paint production, food packaging, firefighting foam, non-stick cookware, medicine, agriculture, and so forth (Figure 5.1) [267,268].

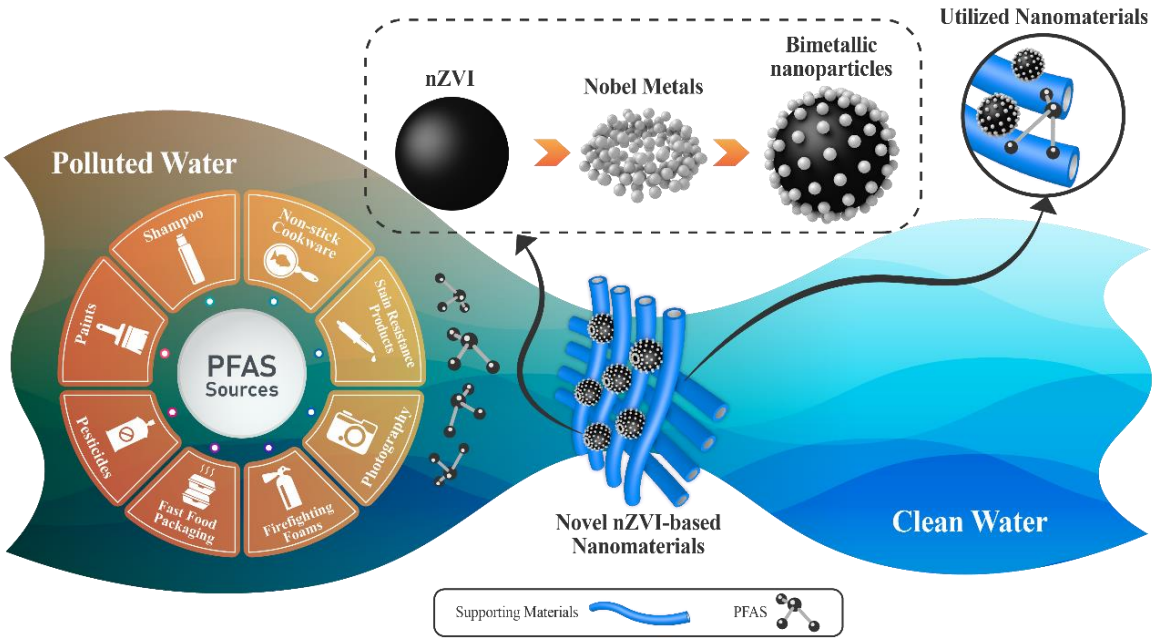

Figure 5.1 Problem statement of PFAS and proposed treatment technology.

5.3.2. Problem identification:

With the uncontrollable use in many aspects of life and poor disposable procedures, PFAS are persisting and bioaccumulating in the environment [267]. Consequently, PFAS are frequently detected in different water bodies (e.g., groundwater, surface water, drinking water, etc.) across the universe (Figure 5.1). For example, PFAS were identified in Europe, China, the United States, Japan, Australia, etc. [267]. Besides the ubiquitous occurrence in several water systems, PFAS were also detected in vegetables (i.e., potato, cucumber, etc.), poultry (e.g., chicken), livestock (e.g., pig), milk products, fish, and so on [269]. Human exposure to PFAS through contaminated water and food has severe health consequences as PFAS are suspected of causing cancer, thyroid hormone disruption, development delays, and so on [268,270]. Hence, an innovative remediation technology is urgently needed to treat PFAS-contaminated water to protect the public and provide safe drinking water.

5.3.3. Proposed treatment technology

Nanoscale Zero-Valent Iron particles (nZVI) are one of the most promising nanomaterials for environmental remediation because of their potential to overcome the limitations of conventional treatment technologies (Figure 5.1) [46]. They are featured by their small size, high surface area, high reducing potentials, nontoxicity, cost-effectiveness, and so forth. nZVI is widely applied to remove a broad range of contaminants and pollutants from various types of water (e.g., groundwater, surface water, etc.) and wastewater (e.g., domestic, industrial, hospital, etc.) [102,153,262]. However, the utilization of nZVI to treat PFAS-contaminated water is poorly explored in the literature.

5.3.4. Aim of the proposed research

By considering the advantages of nZVI and the research gaps in the previous studies, this research aims to employ nZVI as a base nanomaterial to fabricate novel nZVI-based nanomaterials to remove PFAS from contaminated water bodies (Figure 5.1).

5.3.5. Research methodology:

5.3.5.1. Literature review and experimental preparation:

An intensive literature review has been done to identify the critical research gaps, and additional information related to the research subject will be collected to build a solid

scientific background. Moreover, the experimental bench, the required chemicals and instruments, and the experimental plan will be prepared for the research project at this stage.

5.3.5.2. Synthesis of nZVI-based nanomaterial

nZVI will be synthesized in the laboratory via the chemical reduction method. Also, nZVI-based nanomaterials will be fabricated following the same technique. However, they will be modified with several improvement technologies, as illustrated in Figure 5.1, to overcome the defects of nZVI in water treatment, such as fast surface oxidation, particle aggregation, etc. [270]. Many modification methods will be employed to produce novel nZVI-based nanomaterials [46]:

a) **Doping Nobel metals:** deposition of Nobel metals (e.g., Cu, Ni, Ag, or Pd) on the surface of nZVI will remarkably enhance its reactivity. Thus, the first step is to identify the best noble metal to synthesize highly efficient bimetallic nanoparticles (Figure 5.1).
b) **Excellent supporting materials:** the second step is to identify the ideal supporting material, for instance, graphene oxide, titanium oxide nanowires, biochar, etc., to support the nominated bimetallic nanoparticles and decrease the particle aggregation (Figure 5.1).

5.3.5.3. Characterization of nZVI-based nanomaterial

After the synthesis of nZVI and nZVI-based nanomaterials, multiple techniques will be used to prove the successful synthesis procedures of the nanomaterials, such as transmission electron microscopy (TEM) for morphological investigation, X-ray diffraction analysis (XRD) for crystallinity examination, BET surface measurements, laser particle size analyzer, and zeta potential analyzer for measurement of point of zero charge of the nanomaterials.

5.3.5.4. Laboratory batch experiments

The performance of the nominated nZVI-based nanomaterial in removing PFAS from the water will be evaluated via batch mood. Several batch experiments will be implemented under various removal conditions (e.g., nanomaterial dosage, initial pH, temperature, initial PFAS concentration) to define the optimal removal conditions of PFAS by the proposed nZVI-based nanomaterial. Also, a regeneration and recycling protocol will be

developed to ensure the reusability of the nanomaterials for several treatment cycles. Furthermore, it is vital to ensure the competence of the selected nZVI-based nanomaterial in field-scale applications. Hence, the nZVI-based nanomaterial will be employed to remediate real contaminated water and wastewater.

5.3.6. Research timetable

The following table demonstrates the proposed schedule for the research activities over two years:

Activity description	Period
Literature review and experimental preparation	3 months
Synthesis and characterization of nanomaterials	5months
Laboratory batch experiments	6 months
Design, construct and operate the treatment system	6 months
Writing and publications	4 months

5.3.7. Expected results and impacts

1. Synthesis and fabrication of a novel, efficient, and superior nZVI-based nanomaterial for effective removal of PFAS from water.
2. Remarkable treatment efficiency of PFAS-contaminated water by the selected nZVI-based nanomaterial under optimal treatment conditions.
3. An effective regeneration and recycling protocol to successfully reuse the nZVI-based nanomaterial for multiple treatment cycles.
4. The outcomes of this proposal are expected to provide a pioneered and environmentally friendly treatment technology for PFAS contamination which can be easily used at a reasonable cost to provide clean and safe water.

Bibliography

[1] P.K. Goel, Water pollution: causes, effects and control, New Age International, 2006.

[2] J.N. Halder, M.N. Islam, Water pollution and its impact on the human health, J. Environ. Hum. 2 (2015) 36–46.

[3] A.K. Dwivedi, Researches in water pollution: A review, Int. Res. J. Nat. Appl. Sci. 4 (2017) 118–142.

[4] P. Dugan, Biochemical ecology of water pollution, Springer Science & Business Media, 2012.

[5] A. Azizullah, M.N.K. Khattak, P. Richter, D.-P. Häder, Water pollution in Pakistan and its impact on public health — A review, Environ. Int. 37 (2011) 479–497. https://doi.org/https://doi.org/10.1016/j.envint.2010.10.007.

[6] I.A. Shiklomanov, Appraisal and assessment of world water resources, Water Int. 25 (2000) 11–32.

[7] T. Oki, S. Kanae, Global hydrological cycles and world water resources, Science (80-.). 313 (2006) 1068–1072.

[8] J.F. Schyns, A.Y. Hoekstra, M.J. Booij, R.J. Hogeboom, M.M. Mekonnen, Limits to the world's green water resources for food, feed, fiber, timber, and bioenergy, Proc. Natl. Acad. Sci. 116 (2019) 4893–4898.

[9] M. Haseena, M.F. Malik, A. Javed, S. Arshad, N. Asif, S. Zulfiqar, J. Hanif, Water pollution and human health, Environ. Risk Assess. Remediat. 1 (2017).

[10] R.P. Schwarzenbach, T. Egli, T.B. Hofstetter, U. Von Gunten, B. Wehrli, Global water pollution and human health, Annu. Rev. Environ. Resour. 35 (2010) 109–136.

[11] Y. Jiang, China's water scarcity, J. Environ. Manage. 90 (2009) 3185–3196. https://doi.org/https://doi.org/10.1016/j.jenvman.2009.04.016.

[12] H. Wang, X. Mi, Y. Li, S. Zhan, 3D graphene-based macrostructures for water treatment, Adv. Mater. 32 (2020) 1806843.

[13] F.D. Owa, Water pollution: sources, effects, control and management, Mediterr. J. Soc. Sci. 4 (2013) 65.

[14] Q. Wang, Z. Yang, Industrial water pollution, water environment treatment, and

health risks in China, Environ. Pollut. 218 (2016) 358–365. https://doi.org/https://doi.org/10.1016/j.envpol.2016.07.011.

[15] F.N. Chaudhry, M.F. Malik, Factors affecting water pollution: a review, J Ecosyst Ecography. 7 (2017) 1–3.

[16] Unicef, Progress on drinking water, sanitation and hygiene, (2017).

[17] L.J. Puckett, Identifying the major sources of nutrient water pollution, Environ. Sci. Technol. 29 (1995) 408A-414A.

[18] M.-K. Kim, K.-D. Zoh, Occurrence and removals of micropollutants in water environment, Environ. Eng. Res. 21 (2016) 319–332.

[19] J. Virkutyte, R. Varma, Treatment of micropollutants in water and wastewater, IWA Publishing, 2010.

[20] W. Yang, H. Zhou, N. Cicek, Treatment of organic micropollutants in water and wastewater by UV-based processes: a literature review, Crit. Rev. Environ. Sci. Technol. 44 (2014) 1443–1476.

[21] M. Verma, I. Lee, S. Sharma, R. Kumar, V. Kumar, H. Kim, Simultaneous Removal of Heavy Metals and Ciprofloxacin Micropollutants from Wastewater Using Ethylenediaminetetraacetic Acid-Functionalized β-Cyclodextrin-Chitosan Adsorbent, ACS Omega. 6 (2021) 34624–34634.

[22] H.A. Afan, A. El-shafie, W.H.M.W. Mohtar, Z.M. Yaseen, Past, present and prospect of an Artificial Intelligence (AI) based model for sediment transport prediction, J. Hydrol. 541 (2016) 902–913. https://doi.org/https://doi.org/10.1016/j.jhydrol.2016.07.048.

[23] R. Passino, Water pollution: Causes, effects and control measures, Agric. e Dif. Dell'ambiente Ed. Riveduta Ed Ampliata. (1974).

[24] D.H. Kumar Reddy, S.M. Lee, Water pollution and treatment technologies, J Env. Anal Toxicol. 2 (2012) e103.

[25] Y. Wu, J. Chen, Investigating the effects of point source and nonpoint source pollution on the water quality of the East River (Dongjiang) in South China, Ecol. Indic. 32 (2013) 294–304. https://doi.org/https://doi.org/10.1016/j.ecolind.2013.04.002.

[26] Z. Shen, Q. Liao, Q. Hong, Y. Gong, An overview of research on agricultural non-point source pollution modelling in China, Sep. Purif. Technol. 84 (2012) 104–111. https://doi.org/https://doi.org/10.1016/j.seppur.2011.01.018.

[27] E.D. Ongley, Z. Xiaolan, Y. Tao, Current status of agricultural and rural non-point

source Pollution assessment in China, Environ. Pollut. 158 (2010) 1159–1168. https://doi.org/https://doi.org/10.1016/j.envpol.2009.10.047.

[28] L. Cizmas, V.K. Sharma, C.M. Gray, T.J. McDonald, Pharmaceuticals and personal care products in waters: occurrence, toxicity, and risk, Environ. Chem. Lett. 13 (2015) 381–394. https://doi.org/10.1007/s10311-015-0524-4.

[29] J.-L. Liu, M.-H. Wong, Pharmaceuticals and personal care products (PPCPs): a review on environmental contamination in China, Environ. Int. 59 (2013) 208–224.

[30] J. Wang, S. Wang, Removal of pharmaceuticals and personal care products (PPCPs) from wastewater: A review, J. Environ. Manage. 182 (2016) 620–640. https://doi.org/https://doi.org/10.1016/j.jenvman.2016.07.049.

[31] M.B. Ahmed, J.L. Zhou, H.H. Ngo, W. Guo, Adsorptive removal of antibiotics from water and wastewater: Progress and challenges, Sci. Total Environ. 532 (2015) 112–126. https://doi.org/https://doi.org/10.1016/j.scitotenv.2015.05.130.

[32] H.Q. Anh, T.P.Q. Le, N. Da Le, X.X. Lu, T.T. Duong, J. Garnier, E. Rochelle-Newall, S. Zhang, N.-H. Oh, C. Oeurng, C. Ekkawatpanit, T.D. Nguyen, Q.T. Nguyen, T.D. Nguyen, T.N. Nguyen, T.L. Tran, T. Kunisue, R. Tanoue, S. Takahashi, T.B. Minh, H.T. Le, T.N.M. Pham, T.A.H. Nguyen, Antibiotics in surface water of East and Southeast Asian countries: A focused review on contamination status, pollution sources, potential risks, and future perspectives, Sci. Total Environ. 764 (2021) 142865. https://doi.org/https://doi.org/10.1016/j.scitotenv.2020.142865.

[33] Y. Cai, Z. Yan, Y. Ou, B. Peng, L. Zhang, J. Shao, Y. Lin, J. Zhang, Effects of different carbon sources on the removal of ciprofloxacin and pollutants by activated sludge: Mechanism and biodegradation, J. Environ. Sci. 111 (2022) 240–248. https://doi.org/https://doi.org/10.1016/j.jes.2021.03.037.

[34] R. Gothwal, T. Shashidhar, Antibiotic pollution in the environment: a review, Clean–Soil, Air, Water. 43 (2015) 479–489.

[35] A. Jia, Y. Wan, Y. Xiao, J. Hu, Occurrence and fate of quinolone and fluoroquinolone antibiotics in a municipal sewage treatment plant, Water Res. 46 (2012) 387–394. https://doi.org/https://doi.org/10.1016/j.watres.2011.10.055.

[36] O.A. Arikan, C. Rice, E. Codling, Occurrence of antibiotics and hormones in a major agricultural watershed, Desalination. 226 (2008) 121–133. https://doi.org/https://doi.org/10.1016/j.desal.2007.01.238.

[37] P. Sukul, M. Spiteller, Fluoroquinolone antibiotics in the environment, Rev. Environ. Contam. Toxicol. (2007) 131–162.

[38] D. Mazel, J. Davies, Antibiotic resistance in microbes, Cell. Mol. Life Sci. C. 56 (1999) 742–754.

[39] A.A. Robinson, J.B. Belden, M.J. Lydy, Toxicity of fluoroquinolone antibiotics to aquatic organisms, Environ. Toxicol. Chem. An Int. J. 24 (2005) 423–430.

[40] C. Wang, H. Rong, H. Liu, X. Wang, Y. Gao, R. Deng, R. Liu, Y. Liu, D. Zhang, Detoxification mechanisms, defense responses, and toxicity threshold in the earthworm Eisenia foetida exposed to ciprofloxacin-polluted soils, Sci. Total Environ. 612 (2018) 442–449. https://doi.org/https://doi.org/10.1016/j.scitotenv.2017.08.120.

[41] W.-T. Jiang, P.-H. Chang, Y.-S. Wang, Y. Tsai, J.-S. Jean, Z. Li, K. Krukowski, Removal of ciprofloxacin from water by birnessite, J. Hazard. Mater. 250–251 (2013) 362–369. https://doi.org/https://doi.org/10.1016/j.jhazmat.2013.02.015.

[42] C. Zheng, H. Zheng, C. Hu, Y. Wang, Y. Wang, C. Zhao, W. Ding, Q. Sun, Structural design of magnetic biosorbents for the removal of ciprofloxacin from water, Bioresour. Technol. 296 (2020) 122288. https://doi.org/https://doi.org/10.1016/j.biortech.2019.122288.

[43] B. De Witte, J. Dewulf, K. Demeestere, H. Van Langenhove, Ozonation and advanced oxidation by the peroxone process of ciprofloxacin in water, J. Hazard. Mater. 161 (2009) 701–708. https://doi.org/https://doi.org/10.1016/j.jhazmat.2008.04.021.

[44] C. Girardi, J. Greve, M. Lamshöft, I. Fetzer, A. Miltner, A. Schäffer, M. Kästner, Biodegradation of ciprofloxacin in water and soil and its effects on the microbial communities, J. Hazard. Mater. 198 (2011) 22–30. https://doi.org/https://doi.org/10.1016/j.jhazmat.2011.10.004.

[45] T. Thai, P.M. Zito, Ciprofloxacin, (2019). http://europepmc.org/books/NBK535454.

[46] O. Falyouna, M. Faizul Idham, I. Maamoun, K. Bensaida, U.P.M. Ashik, Y. Sugihara, O. Eljamal, Promotion of ciprofloxacin adsorption from contaminated solutions by oxalate modified nanoscale zerovalent iron particles, J. Mol. Liq. 359 (2022) 119323. https://doi.org/https://doi.org/10.1016/j.molliq.2022.119323.

[47] Y. Zhang, Y. Shao, N. Gao, Y. Gao, W. Chu, S. Li, Y. Wang, S. Xu, Kinetics and by-products formation of chloramphenicol (CAP) using chlorination and

photocatalytic oxidation, Chem. Eng. J. 333 (2018) 85–91.

[48] C. Yan, Y. Yang, J. Zhou, M. Liu, M. Nie, H. Shi, L. Gu, Antibiotics in the surface water of the Yangtze Estuary: occurrence, distribution and risk assessment, Environ. Pollut. 175 (2013) 22–29.

[49] A. Prieto, M. Möder, R. Rodil, L. Adrian, E. Marco-Urrea, Degradation of the antibiotics norfloxacin and ciprofloxacin by a white-rot fungus and identification of degradation products, Bioresour. Technol. 102 (2011) 10987–10995. https://doi.org/https://doi.org/10.1016/j.biortech.2011.08.055.

[50] Y. Picó, V. Andreu, Fluoroquinolones in soil—risks and challenges, Anal. Bioanal. Chem. 387 (2007) 1287–1299.

[51] S.J. Rooklidge, Environmental antimicrobial contamination from terraccumulation and diffuse pollution pathways, Sci. Total Environ. 325 (2004) 1–13. https://doi.org/https://doi.org/10.1016/j.scitotenv.2003.11.007.

[52] L. Tahrani, J. Van Loco, H. Ben Mansour, T. Reyns, Occurrence of antibiotics in pharmaceutical industrial wastewater, wastewater treatment plant and sea waters in Tunisia, J. Water Health. 14 (2016) 208–213.

[53] R. Wei, F. Ge, M. Chen, R. Wang, Occurrence of ciprofloxacin, enrofloxacin, and florfenicol in animal wastewater and water resources, J. Environ. Qual. 41 (2012) 1481–1486.

[54] M.C. Dodd, A.D. Shah, U. von Gunten, C.-H. Huang, Interactions of fluoroquinolone antibacterial agents with aqueous chlorine: reaction kinetics, mechanisms, and transformation pathways, Environ. Sci. Technol. 39 (2005) 7065–7076.

[55] E.-S.I. El-Shafey, H. Al-Lawati, A.S. Al-Sumri, Ciprofloxacin adsorption from aqueous solution onto chemically prepared carbon from date palm leaflets, J. Environ. Sci. 24 (2012) 1579–1586.

[56] S. Ahmadzadeh, A. Asadipour, M. Pournamdari, B. Behnam, H.R. Rahimi, M. Dolatabadi, Removal of ciprofloxacin from hospital wastewater using electrocoagulation technique by aluminum electrode: Optimization and modelling through response surface methodology, Process Saf. Environ. Prot. 109 (2017) 538–547. https://doi.org/https://doi.org/10.1016/j.psep.2017.04.026.

[57] K. Sun, Y. Shi, X. Wang, J. Rasmussen, Z. Li, J. Zhu, Organokaolin for the uptake of pharmaceuticals diclofenac and chloramphenicol from water, Chem. Eng. J. 330 (2017) 1128–1136. https://doi.org/https://doi.org/10.1016/j.cej.2017.08.057.

[58] L. Serwecińska, Antimicrobials and antibiotic-resistant bacteria: a risk to the environment and to public health, Water. 12 (2020) 3313.

[59] A. Karcı, I.A. Balcıoğlu, Investigation of the tetracycline, sulfonamide, and fluoroquinolone antimicrobial compounds in animal manure and agricultural soils in Turkey, Sci. Total Environ. 407 (2009) 4652–4664.

[60] W.W.-P. Lai, Y.-C. Lin, Y.-H. Wang, Y.L. Guo, A.Y.-C. Lin, Occurrence of emerging contaminants in aquaculture waters: cross-contamination between aquaculture systems and surrounding waters, Water, Air, Soil Pollut. 229 (2018) 1–12.

[61] G. Huys, K. Bartie, M. Cnockaert, D.T.H. Oanh, N.T. Phuong, T. Somsiri, S. Chinabut, F.M. Yusoff, M. Shariff, M. Giacomini, Biodiversity of chloramphenicol-resistant mesophilic heterotrophs from Southeast Asian aquaculture environments, Res. Microbiol. 158 (2007) 228–235.

[62] A. Hossain, M. Habibullah-Al-Mamun, I. Nagano, S. Masunaga, D. Kitazawa, H. Matsuda, Antibiotics, antibiotic-resistant bacteria, and resistance genes in aquaculture: risks, current concern, and future thinking, Environ. Sci. Pollut. Res. (2022) 1–22.

[63] O. Falyouna, I. Maamoun, K. Bensaida, A. Tahara, Y. Sugihara, O. Eljamal, Encapsulation of iron nanoparticles with magnesium hydroxide shell for remarkable removal of ciprofloxacin from contaminated water, J. Colloid Interface Sci. 605 (2022) 813–827. https://doi.org/https://doi.org/10.1016/j.jcis.2021.07.154.

[64] T. Kivits, H.P. Broers, H. Beeltje, M. van Vliet, J. Griffioen, Presence and fate of veterinary antibiotics in age-dated groundwater in areas with intensive livestock farming, Environ. Pollut. 241 (2018) 988–998. https://doi.org/https://doi.org/10.1016/j.envpol.2018.05.085.

[65] C.S.S.S. Collaborators, Ciprofloxacin resistance in Campylobacter jejuni: case–case analysis as a tool for elucidating risks at home and abroad, J. Antimicrob. Chemother. 50 (2002) 561–568.

[66] Jim O'Neill, Antimicrobial resistance: tackling a crisis for the health and wealth of nations, Review on Antimicrobial Resistance, 2014.

[67] A. O'Rourke, S. Beyhan, Y. Choi, P. Morales, A.P. Chan, J.L. Espinoza, C.L. Dupont, K.J. Meyer, A. Spoering, K. Lewis, Mechanism-of-action classification of antibiotics by global transcriptome profiling, Antimicrob. Agents Chemother.

64 (2020) e01207-19.

[68] S. Ganesan, M. Amirthalingam, P. Arivalagan, S. Govindan, S. Palanisamy, A.P. Lingassamy, V.K. Ponnusamy, Absolute removal of ciprofloxacin and its degraded byproducts in aqueous solution using an efficient electrochemical oxidation process coupled with adsorption treatment technique, J. Environ. Manage. 245 (2019) 409–417.

[69] O. Falyouna, I. Maamoun, K. Bensaida, Y. Sugihara, O. Eljamal, Removal of Ciprofloxacin from Aqueous Solutions by Nanoscale Zerovalent Iron-Based Materials: A Mini Review, in: Proc. Int. Exch. Innov. Conf. Eng. Sci., School of Engineering Sciences, Kyushu University, 2020: pp. 179–185. https://doi.org/10.5109/4102485.

[70] A.K. Al-Buriahi, M.M. Al-shaibani, R.M.S.R. Mohamed, A.A. Al-Gheethi, A. Sharma, N. Ismail, Ciprofloxacin removal from non-clinical environment: A critical review of current methods and future trend prospects, J. Water Process Eng. 47 (2022) 102725. https://doi.org/https://doi.org/10.1016/j.jwpe.2022.102725.

[71] C.A. Igwegbe, S.N. Oba, C.O. Aniagor, A.G. Adeniyi, J.O. Ighalo, Adsorption of ciprofloxacin from water: A comprehensive review, J. Ind. Eng. Chem. 93 (2021) 57–77. https://doi.org/https://doi.org/10.1016/j.jiec.2020.09.023.

[72] N.-X. Feng, J. Yu, L. Xiang, L.-Y. Yu, H.-M. Zhao, C.-H. Mo, Y.-W. Li, Q.-Y. Cai, M.-H. Wong, Q.X. Li, Co-metabolic degradation of the antibiotic ciprofloxacin by the enriched bacterial consortium XG and its bacterial community composition, Sci. Total Environ. 665 (2019) 41–51. https://doi.org/https://doi.org/10.1016/j.scitotenv.2019.01.322.

[73] F. Polesel, H.R. Andersen, S. Trapp, B.G. Plósz, Removal of Antibiotics in Biological Wastewater Treatment Systems□ A Critical Assessment Using the Activated Sludge Modeling Framework for Xenobiotics (ASM-X), Environ. Sci. Technol. 50 (2016) 10316–10334.

[74] L. Pan, J. Li, C. Li, X. Tang, G. Yu, Y. Wang, Study of ciprofloxacin biodegradation by a Thermus sp. isolated from pharmaceutical sludge, J. Hazard. Mater. 343 (2018) 59–67. https://doi.org/https://doi.org/10.1016/j.jhazmat.2017.09.009.

[75] N.F.F. Moreira, J.M. Sousa, G. Macedo, A.R. Ribeiro, L. Barreiros, M. Pedrosa, J.L. Faria, M.F.R. Pereira, S. Castro-Silva, M.A. Segundo, C.M. Manaia, O.C. Nunes, A.M.T. Silva, Photocatalytic ozonation of urban wastewater and surface

water using immobilized TiO2 with LEDs: Micropollutants, antibiotic resistance genes and estrogenic activity, Water Res. 94 (2016) 10–22. https://doi.org/https://doi.org/10.1016/j.watres.2016.02.003.

[76] C. Liu, V. Nanaboina, G. V Korshin, W. Jiang, Spectroscopic study of degradation products of ciprofloxacin, norfloxacin and lomefloxacin formed in ozonated wastewater, Water Res. 46 (2012) 5235–5246.

[77] H. Wang, W. Shi, D. Ma, Y. Shang, Y. Wang, B. Gao, Formation of DBPs during chlorination of antibiotics and control with permanganate/bisulfite pretreatment, Chem. Eng. J. 392 (2020) 123701. https://doi.org/https://doi.org/10.1016/j.cej.2019.123701.

[78] Z.-H. Diao, X.-R. Xu, D. Jiang, G. Li, J.-J. Liu, L.-J. Kong, L.-Z. Zuo, Enhanced catalytic degradation of ciprofloxacin with FeS2/SiO2 microspheres as heterogeneous Fenton catalyst: kinetics, reaction pathways and mechanism, J. Hazard. Mater. 327 (2017) 108–115.

[79] S.K. Mondal, A.K. Saha, A. Sinha, Removal of ciprofloxacin using modified advanced oxidation processes: Kinetics, pathways and process optimization, J. Clean. Prod. 171 (2018) 1203–1214. https://doi.org/https://doi.org/10.1016/j.jclepro.2017.10.091.

[80] T. An, H. Yang, G. Li, W. Song, W.J. Cooper, X. Nie, Kinetics and mechanism of advanced oxidation processes (AOPs) in degradation of ciprofloxacin in water, Appl. Catal. B Environ. 94 (2010) 288–294.

[81] H. Ou, J. Ye, S. Ma, C. Wei, N. Gao, J. He, Degradation of ciprofloxacin by UV and UV/H2O2 via multiple-wavelength ultraviolet light-emitting diodes: effectiveness, intermediates and antibacterial activity, Chem. Eng. J. 289 (2016) 391–401.

[82] F. Biancullo, N.F.F. Moreira, A.R. Ribeiro, C.M. Manaia, J.L. Faria, O.C. Nunes, S.M. Castro-Silva, A.M.T. Silva, Heterogeneous photocatalysis using UVA-LEDs for the removal of antibiotics and antibiotic resistant bacteria from urban wastewater treatment plant effluents, Chem. Eng. J. 367 (2019) 304–313.

[83] S. Barışçı, O. Turkay, Optimization and modelling using the response surface methodology (RSM) for ciprofloxacin removal by electrocoagulation, Water Sci. Technol. 73 (2016) 1673–1679.

[84] J.J.S. Alonso, N. El Kori, N. Melián-Martel, B. Del Río-Gamero, Removal of ciprofloxacin from seawater by reverse osmosis, J. Environ. Manage. 217 (2018)

337–345. https://doi.org/https://doi.org/10.1016/j.jenvman.2018.03.108.

[85] D.A. Palacio, B.L. Rivas, B.F. Urbano, Ultrafiltration membranes with three water-soluble polyelectrolyte copolymers to remove ciprofloxacin from aqueous systems, Chem. Eng. J. 351 (2018) 85–93. https://doi.org/https://doi.org/10.1016/j.cej.2018.06.099.

[86] S.P. Sun, T.A. Hatton, T.-S. Chung, Hyperbranched polyethyleneimine induced cross-linking of polyamide− imide nanofiltration hollow fiber membranes for effective removal of ciprofloxacin, Environ. Sci. Technol. 45 (2011) 4003–4009.

[87] S.K. Bajpai, M. Bhowmik, Poly (acrylamide-co-itaconic acid) as a potential ion-exchange sorbent for effective removal of antibiotic drug-ciprofloxacin from aqueous solution, J. Macromol. Sci. Part A. 48 (2010) 108–118.

[88] A.S. Adeleye, J.R. Conway, K. Garner, Y. Huang, Y. Su, A.A. Keller, Engineered nanomaterials for water treatment and remediation: Costs, benefits, and applicability, Chem. Eng. J. 286 (2016) 640–662.

[89] D.E. Helbling, Bioremediation of pesticide-contaminated water resources: the challenge of low concentrations, Curr. Opin. Biotechnol. 33 (2015) 142–148. https://doi.org/https://doi.org/10.1016/j.copbio.2015.02.012.

[90] X. Luo, F. Deng, Nanomaterials for the removal of pollutants and resource reutilization, Elsevier, 2018.

[91] Q. Li, Z. Chen, H. Wang, H. Yang, T. Wen, S. Wang, B. Hu, X. Wang, Removal of organic compounds by nanoscale zero-valent iron and its composites, Sci. Total Environ. 792 (2021) 148546. https://doi.org/https://doi.org/10.1016/j.scitotenv.2021.148546.

[92] D. Lv, X. Zhou, J. Zhou, Y. Liu, Y. Li, K. Yang, Z. Lou, S.A. Baig, D. Wu, X. Xu, Design and characterization of sulfide-modified nanoscale zerovalent iron for cadmium(II) removal from aqueous solutions, Appl. Surf. Sci. 442 (2018) 114–123. https://doi.org/https://doi.org/10.1016/j.apsusc.2018.02.085.

[93] Y. Zou, X. Wang, A. Khan, P. Wang, Y. Liu, A. Alsaedi, T. Hayat, X. Wang, Environmental Remediation and Application of Nanoscale Zero-Valent Iron and Its Composites for the Removal of Heavy Metal Ions: A Review, Environ. Sci. Technol. 50 (2016) 7290–7304. https://doi.org/10.1021/acs.est.6b01897.

[94] W. Yan, A.A. Herzing, C.J. Kiely, W. Zhang, Nanoscale zero-valent iron (nZVI): Aspects of the core-shell structure and reactions with inorganic species in water, J. Contam. Hydrol. 118 (2010) 96–104.

https://doi.org/https://doi.org/10.1016/j.jconhyd.2010.09.003.

[95] Y. Song, Y. Zeng, J. Liao, J. Chen, Q. Du, Efficient removal of sulfamethoxazole by resin-supported zero-valent iron composites with tunable structure: Performance, mechanisms, and degradation pathways, Chemosphere. 269 (2021) 128684. https://doi.org/https://doi.org/10.1016/j.chemosphere.2020.128684.

[96] R. Peng, J. Shao, Y. Xie, A. Chen, L. Peng, Q. Zeng, S. Luo, Oxalate-enhanced reactivity of nanoscale zero-valent iron under different conditions of O2, N2 or without aeration, Chem. Eng. J. 330 (2017) 398–406. https://doi.org/https://doi.org/10.1016/j.cej.2017.07.154.

[97] C.R. Keenan, D.L. Sedlak, Factors affecting the yield of oxidants from the reaction of nanoparticulate zero-valent iron and oxygen, Environ. Sci. Technol. 42 (2008) 1262–1267.

[98] H. Yoon, M. Pangging, M.-H. Jang, Y.S. Hwang, Y.-S. Chang, Impact of surface modification on the toxicity of zerovalent iron nanoparticles in aquatic and terrestrial organisms, Ecotoxicol. Environ. Saf. 163 (2018) 436–443. https://doi.org/https://doi.org/10.1016/j.ecoenv.2018.07.099.

[99] I. Maamoun, O. Eljamal, I. Thompson, R. Eljamal, O. Falyouna, Y. Sugihara, Effect of Nano Zero Valent Iron Delivery Method into Porous Media on Phosphorus Removal from Groundwater, in: Proc. Int. Exch. Innov. Conf. Eng. Sci., 2019: pp. 9–11.

[100] T.W.M. Amen, O. Eljamal, A.M.E. Khalil, Y. Sugihara, N. Matsunaga, Methane yield enhancement by the addition of new novel of iron and copper-iron bimetallic nanoparticles, Chem. Eng. Process. - Process Intensif. 130 (2018) 253–261. https://doi.org/https://doi.org/10.1016/j.cep.2018.06.020.

[101] K. Bensaida, R. Eljamal, kareman Eljamal, Y. Sughihara, O. Eljamal, The impact of iron bimetallic nanoparticles on bulk microbial growth in wastewater, J. Water Process Eng. 40 (2021) 101825. https://doi.org/https://doi.org/10.1016/j.jwpe.2020.101825.

[102] I. Maamoun, O. Falyouna, R. Eljamal, K. Bensaida, O. Eljamal, Optimization modeling of nFe0/Cu-PRB design for Cr (VI) removal from groundwater, Int J Env. Sci Dev. 12 (2021) 131–138.

[103] O. Falyouna, I. Maamoun, K. Bensaida, A. Tahara, Y. Sugihara, O. Eljamal, Chemical deposition of iron nanoparticles (Fe0) on titanium nanowires for efficient adsorption of ciprofloxacin from water, Water Pract. Technol. (2021).

[104] Y. Yang, L. Xu, J. Wang, An enhancement of singlet oxygen generation from dissolved oxygen activated by three-dimensional graphene wrapped nZVI-doped amorphous Al species for chloramphenicol removal in the Fenton-like system, Chem. Eng. J. 425 (2021) 131497. https://doi.org/https://doi.org/10.1016/j.cej.2021.131497.

[105] Y. Wu, Q. Yue, Z. Ren, B. Gao, Immobilization of nanoscale zero-valent iron particles (nZVI) with synthesized activated carbon for the adsorption and degradation of Chloramphenicol (CAP), J. Mol. Liq. 262 (2018) 19–28. https://doi.org/https://doi.org/10.1016/j.molliq.2018.04.032.

[106] L. Chen, T. Yuan, R. Ni, Q. Yue, B. Gao, Multivariate optimization of ciprofloxacin removal by polyvinylpyrrolidone stabilized NZVI/Cu bimetallic particles, Chem. Eng. J. 365 (2019) 183–192. https://doi.org/https://doi.org/10.1016/j.cej.2019.02.051.

[107] W. Wang, S. Li, H. Lei, B. Pan, W. Zhang, Enhanced separation of nanoscale zero-valent iron (nZVI) using polyacrylamide: Performance, characterization and implication, Chem. Eng. J. 260 (2015) 616–622. https://doi.org/https://doi.org/10.1016/j.cej.2014.09.042.

[108] W. Xu, Z. Li, S. Shi, J. Qi, S. Cai, Y. Yu, D.M. O'Carroll, F. He, Carboxymethyl cellulose stabilized and sulfidated nanoscale zero-valent iron: Characterization and trichloroethene dechlorination, Appl. Catal. B Environ. 262 (2020) 118303.

[109] I. Maamoun, O. Eljamal, O. Falyouna, R. ELJAMAL, Y. Sugihara, Stimulating effect of magnesium hydroxide on aqueous characteristics of iron nanocomposites, Water Sci. Technol. 80 (2020) 1996–2002. https://doi.org/10.2166/wst.2020.027.

[110] G. Wu, W. Kong, Y. Gao, Y. Kong, Z. Dai, H. Dan, Y. Shang, S. Wang, F. Yin, Q. Yue, B. Gao, Removal of chloramphenicol by sulfide-modified nanoscale zero-valent iron activated persulfate: Performance, salt resistance, and reaction mechanisms, Chemosphere. 286 (2022) 131876. https://doi.org/https://doi.org/10.1016/j.chemosphere.2021.131876.

[111] M. Nie, C. Yan, M. Li, X. Wang, W. Bi, W. Dong, Degradation of chloramphenicol by persulfate activated by Fe2+ and zerovalent iron, Chem. Eng. J. 279 (2015) 507–515. https://doi.org/https://doi.org/10.1016/j.cej.2015.05.055.

[112] C. Tan, Y. Dong, D. Fu, N. Gao, J. Ma, X. Liu, Chloramphenicol removal by zero valent iron activated peroxymonosulfate system: Kinetics and mechanism of radical generation, Chem. Eng. J. 334 (2018) 1006–1015.

https://doi.org/https://doi.org/10.1016/j.cej.2017.10.020.

[113] Z.-H. Diao, W. Chu, FeS2 assisted degradation of atrazine by bentonite-supported nZVI coupling with hydrogen peroxide process in water: Performance and mechanism, Sci. Total Environ. 754 (2021) 142155. https://doi.org/https://doi.org/10.1016/j.scitotenv.2020.142155.

[114] J.A. de Lima Perini, B.F. Silva, R.F.P. Nogueira, Zero-valent iron mediated degradation of ciprofloxacin – Assessment of adsorption, operational parameters and degradation products, Chemosphere. 117 (2014) 345–352. https://doi.org/https://doi.org/10.1016/j.chemosphere.2014.07.071.

[115] N.T. Hoa, H. Nguyen, L. Nguyen, K.N. Do, L.D. Vu, Efficient removal of ciprofloxacin in aqueous solutions by zero-valent metal-activated persulfate oxidation: A comparative study, J. Water Process Eng. 35 (2020) 101199. https://doi.org/https://doi.org/10.1016/j.jwpe.2020.101199.

[116] Y. Shao, P. Zhao, Q. Yue, Y. Wu, B. Gao, W. Kong, Preparation of wheat straw-supported Nanoscale Zero-Valent Iron and its removal performance on ciprofloxacin, Ecotoxicol. Environ. Saf. 158 (2018) 100–107. https://doi.org/https://doi.org/10.1016/j.ecoenv.2018.04.020.

[117] M. Pirsaheb, S. Moradi, M. Shahlaei, X. Wang, N. Farhadian, A new composite of nano zero-valent iron encapsulated in carbon dots for oxidative removal of bio-refractory antibiotics from water, J. Clean. Prod. 209 (2019) 1523–1532.

[118] W. Zhang, H. Gao, J. He, P. Yang, D. Wang, T. Ma, H. Xia, X. Xu, Removal of norfloxacin using coupled synthesized nanoscale zero-valent iron (nZVI) with H2O2 system: Optimization of operating conditions and degradation pathway, Sep. Purif. Technol. 172 (2017) 158–167. https://doi.org/https://doi.org/10.1016/j.seppur.2016.08.008.

[119] Q. Mao, Y. Zhou, Y. Yang, J. Zhang, L. Liang, H. Wang, S. Luo, L. Luo, P. Jeyakumar, Y.S. Ok, M. Rizwan, Experimental and theoretical aspects of biochar-supported nanoscale zero-valent iron activating H2O2 for ciprofloxacin removal from aqueous solution, J. Hazard. Mater. 380 (2019) 120848. https://doi.org/https://doi.org/10.1016/j.jhazmat.2019.120848.

[120] J. Gao, D. Han, Y. Xu, Y. Liu, J. Shang, Persulfate activation by sulfide-modified nanoscale iron supported by biochar (S-nZVI/BC) for degradation of ciprofloxacin, Sep. Purif. Technol. 235 (2020) 116202. https://doi.org/https://doi.org/10.1016/j.seppur.2019.116202.

[121] J. Liu, Y. Du, W. Sun, Q. Chang, C. Peng, A granular adsorbent-supported Fe/Ni nanoparticles activating persulfate system for simultaneous adsorption and degradation of ciprofloxacin, Chinese J. Chem. Eng. 28 (2020) 1077–1084. https://doi.org/https://doi.org/10.1016/j.cjche.2019.12.019.

[122] M. Pirsaheb, S. Moradi, M. Shahlaei, X. Wang, N. Farhadian, Ultrasonic Enhanced Zero-Valent Iron-Based Fenton Reaction for Ciprofloxacin Removal under Aerobic Condition, Environ. Process. 7 (2020) 227–241. https://doi.org/10.1007/s40710-019-00415-5.

[123] A.R. Rahmani, H. Almasi, S. Bajalan, H. Rezaei Vahidian, A. Zarei, A. Shabanloo, Optimization of Ciprofloxacin Antibiotic Sonochemical Degradation with Persulfate Activated by Nano Zero-Valent Iron by Central Composite Design Method TT - بهینه سازی تجزیه سونوشیمیایی آنتی بیوتیک سیپروفلوکساسین با پرسولفات فعال شده توسط نانو ذرات آهن ص, Arumshealth. 8 (2017) 231–245. http://healthjournal.arums.ac.ir/article-1-1238-en.html.

[124] M. Pirsaheb, S. Moradi, M. Shahlaei, X. Wang, N. Farhadian, Simultaneously implement of both weak magnetic field and aeration for ciprofloxacin removal by Fenton-like reaction, J. Environ. Manage. 246 (2019) 776–784.

[125] L. Chen, R. Ni, T. Yuan, Y. Gao, W. Kong, P. Zhang, Q. Yue, B. Gao, Effects of green synthesis, magnetization, and regeneration on ciprofloxacin removal by bimetallic nZVI/Cu composites and insights of degradation mechanism, J. Hazard. Mater. 382 (2020) 121008. https://doi.org/https://doi.org/10.1016/j.jhazmat.2019.121008.

[126] R. Giorgi, C. Bozzi, L. Dei, C. Gabbiani, B.W. Ninham, P. Baglioni, Nanoparticles of Mg(OH)2: Synthesis and Application to Paper Conservation, Langmuir. 21 (2005) 8495–8501. https://doi.org/10.1021/la050564m.

[127] X. Zheng, Y. Mao, J. Wen, X. Fu, X. Liu, CuInS2/Mg (OH) 2 nanosheets for the enhanced visible-light photocatalytic degradation of tetracycline, Nanomaterials. 9 (2019) 1567.

[128] A. Pandiarajan, R. Kamaraj, S. Vasudevan, Enhanced removal of cephalosporin based antibiotics (CBA) from water by one-pot electrosynthesized Mg (OH) 2: a combined theoretical and experimental study to pilot scale, New J. Chem. 41 (2017) 4518–4530.

[129] C. Chen, X. Zhang, T. Jiang, M. Li, Y. Peng, X. Liu, J. Ye, Y. Hua, Removal of uranium(VI) from aqueous solution by Mg(OH)2-coated nanoscale zero-valent

iron: Reactivity and mechanism, J. Environ. Chem. Eng. 9 (2021) 104706. https://doi.org/https://doi.org/10.1016/j.jece.2020.104706.

[130] J.R. Lee, J.Y. Bae, W. Jang, J.-H. Lee, W. San Choi, H.Y. Koo, Magnesium hydroxide nanoplate/graphene oxide composites as efficient adsorbents for organic dyes, RSC Adv. 5 (2015) 83668–83673.

[131] W. Liu, F. Huang, Y. Wang, T. Zou, J. Zheng, Z. Lin, Recycling Mg(OH)2 Nanoadsorbent during Treating the Low Concentration of CrVI, Environ. Sci. Technol. 45 (2011) 1955–1961. https://doi.org/10.1021/es1035199.

[132] C. Dong, D. Song, J. Cairney, O.L. Maddan, G. He, Y. Deng, Antibacterial study of Mg(OH)2 nanoplatelets, Mater. Res. Bull. 46 (2011) 576–582. https://doi.org/https://doi.org/10.1016/j.materresbull.2010.12.023.

[133] I. Maamoun, O. Falyouna, R. Eljamal, K. Bensaida, K. Tanaka, T. Tosco, Y. Sugihara, O. Eljamal, Multi-functional magnesium hydroxide coating for iron nanoparticles towards prolonged reactivity in Cr(VI) removal from aqueous solutions, J. Environ. Chem. Eng. 10 (2022) 107431. https://doi.org/https://doi.org/10.1016/j.jece.2022.107431.

[134] M. Liu, Y. Wang, L. Chen, Y. Zhang, Z. Lin, Mg(OH)2 Supported Nanoscale Zero Valent Iron Enhancing the Removal of Pb(II) from Aqueous Solution, ACS Appl. Mater. Interfaces. 7 (2015) 7961–7969. https://doi.org/10.1021/am509184e.

[135] C.R. Keenan, D.L. Sedlak, Ligand-Enhanced Reactive Oxidant Generation by Nanoparticulate Zero-Valent Iron and Oxygen, Environ. Sci. Technol. 42 (2008) 6936–6941. https://doi.org/10.1021/es801438f.

[136] Y. Su, D. Jassby, S. Song, X. Zhou, H. Zhao, J. Filip, E. Petala, Y. Zhang, Enhanced oxidative and adsorptive removal of diclofenac in heterogeneous Fenton-like reaction with sulfide modified nanoscale zerovalent iron, Environ. Sci. Technol. 52 (2018) 6466–6475.

[137] Y. Pan, M. Zhou, Q. Wang, J. Cai, Y. Tian, Y. Zhang, EDTA, oxalate, and phosphate ions enhanced reactive oxygen species generation and sulfamethazine removal by zero-valent iron, J. Hazard. Mater. 391 (2020) 122210. https://doi.org/https://doi.org/10.1016/j.jhazmat.2020.122210.

[138] K. Luo, Q. Yang, Y. Pang, D. Wang, X. Li, M. Lei, Q. Huang, Unveiling the mechanism of biochar-activated hydrogen peroxide on the degradation of ciprofloxacin, Chem. Eng. J. 374 (2019) 520–530. https://doi.org/https://doi.org/10.1016/j.cej.2019.05.204.

[139] P. Du, W. Liu, H. Cao, H. Zhao, C.-H. Huang, Oxidation of amino acids by peracetic acid: Reaction kinetics, pathways and theoretical calculations, Water Res. X. 1 (2018) 100002. https://doi.org/https://doi.org/10.1016/j.wroa.2018.09.002.

[140] M. Deborde, U. von Gunten, Reactions of chlorine with inorganic and organic compounds during water treatment—Kinetics and mechanisms: A critical review, Water Res. 42 (2008) 13–51. https://doi.org/https://doi.org/10.1016/j.watres.2007.07.025.

[141] K. Xiao, K. Pei, H. Wang, W. Yu, S. Liang, J. Hu, H. Hou, B. Liu, J. Yang, Citric acid assisted Fenton-like process for enhanced dewaterability of waste activated sludge with in-situ generation of hydrogen peroxide, Water Res. 140 (2018) 232–242. https://doi.org/https://doi.org/10.1016/j.watres.2018.04.051.

[142] Y. Zong, H. Zhang, Y. Shao, W. Ji, Y. Zeng, L. Xu, D. Wu, Surface-mediated periodate activation by nano zero-valent iron for the enhanced abatement of organic contaminants, J. Hazard. Mater. 423 (2022) 126991.

[143] M. Liao, X. Wang, S. Cao, M. Li, X. Peng, L. Zhang, Oxalate Modification Dramatically Promoted Cr(VI) Removal with Zero-Valent Iron, ACS ES&T Water. 1 (2021) 2109–2118. https://doi.org/10.1021/acsestwater.1c00183.

[144] Q. Tao, J. Zhao, J. Li, Y. Liu, J. Luo, S. Yuan, B. Li, Q. Li, Q. Xu, X. Yu, H. Huang, T. Li, C. Wang, Unique root exudate tartaric acid enhanced cadmium mobilization and uptake in Cd-hyperaccumulator Sedum alfredii, J. Hazard. Mater. 383 (2020) 121177. https://doi.org/https://doi.org/10.1016/j.jhazmat.2019.121177.

[145] J. Fan, H. Wang, L. Ma, Oxalate-assisted oxidative degradation of 4-chlorophenol in a bimetallic, zero-valent iron–aluminum/air/water system, Environ. Sci. Pollut. Res. 23 (2016) 16686–16698.

[146] X. Kong, C. Zhang, J. Zhang, L. Xuan, C. Qin, Oxidative degradation of phenol by sulfidated zero valent iron under aerobic conditions: The effect of oxalate and tripolyphosphate ligands, J. Environ. Sci. 100 (2021) 82–89. https://doi.org/https://doi.org/10.1016/j.jes.2020.07.018.

[147] O. Falyouna, O. Eljamal, I. Maamoun, A. Tahara, Y. Sugihara, Magnetic zeolite synthesis for efficient removal of cesium in a lab-scale continuous treatment system, J. Colloid Interface Sci. 571 (2020). https://doi.org/10.1016/j.jcis.2020.03.028.

[148] O. Eljamal, T. Shubair, A. Tahara, Y. Sugihara, N. Matsunaga, Iron based

nanoparticles-zeolite composites for the removal of cesium from aqueous solutions, J. Mol. Liq. 277 (2019) 613–623. https://doi.org/10.1016/j.molliq.2018.12.115.

[149] I. Maamoun, O. Eljamal, R. Eljamal, O. Falyouna, Y. Sugihara, Promoting aqueous and transport characteristics of highly reactive nanoscale zero valent iron via different layered hydroxide coatings, Appl. Surf. Sci. 506 (2020). https://doi.org/10.1016/j.apsusc.2019.145018.

[150] K.A. Abd-Elsalam, R. Periakaruppan, S. Rajeshkumar, Agri-Waste and Microbes for Production of Sustainable Nanomaterials, Elsevier, 2021.

[151] Y. Feng, S.R. Kilker, Y. Lee, Characterization of Nanoencapsulated Food Ingredients, (2020).

[152] J.E. Martin, A.A. Herzing, W. Yan, X. Li, B.E. Koel, C.J. Kiely, W. Zhang, Determination of the oxide layer thickness in core− shell zerovalent iron nanoparticles, Langmuir. 24 (2008) 4329–4334.

[153] O. Falyouna, K. Bensaida, I. Maamoun, U.P.M. Ashik, A. Tahara, K. Tanaka, N. Aoyagi, Y. Sugihara, O. Eljamal, Synthesis of hybrid magnesium hydroxide/magnesium oxide nanorods [Mg(OH)2/MgO] for prompt and efficient adsorption of ciprofloxacin from aqueous solutions, J. Clean. Prod. 342 (2022) 130949. https://doi.org/https://doi.org/10.1016/j.jclepro.2022.130949.

[154] S. Rončević, I. Nemet, T.Z. Ferri, D. Matković-Čalogović, Characterization of nZVI nanoparticles functionalized by EDTA and dipicolinic acid: a comparative study of metal ion removal from aqueous solutions, RSC Adv. 9 (2019) 31043–31051. https://doi.org/10.1039/C9RA04831F.

[155] M. Bodik, C. Walker, M. Demydenko, T. Michlmayr, T. Bähler, U. Ramsperger, A.-K. Thamm, S. Tear, A. Pratt, M. El-Gomati, The effect of work function during electron spectroscopy measurements in Scanning Field-Emission Microscopy, Ultramicroscopy. (2022) 113547.

[156] T. Phenrat, N. Saleh, K. Sirk, H.-J. Kim, R.D. Tilton, G. V Lowry, Stabilization of aqueous nanoscale zerovalent iron dispersions by anionic polyelectrolytes: adsorbed anionic polyelectrolyte layer properties and their effect on aggregation and sedimentation, J. Nanoparticle Res. 10 (2008) 795–814. https://doi.org/10.1007/s11051-007-9315-6.

[157] S.M. Kurtz, UHMWPE biomaterials handbook: ultra high molecular weight polyethylene in total joint replacement and medical devices, Academic Press,

2009.

[158] S. Ebnesajjad, C. Ebnesajjad, Surface treatment of materials for adhesive bonding, William Andrew, 2013.

[159] I. Dincer, Comprehensive energy systems, Elsevier, 2018.

[160] K. Torres-Rivero, J. Bastos-Arrieta, N. Fiol, A. Florido, Chapter Ten - Metal and metal oxide nanoparticles: An integrated perspective of the green synthesis methods by natural products and waste valorization: applications and challenges, in: S.K. Verma, A.K.B.T.-C.A.C. Das (Eds.), Biosynthesized Nanomater., Elsevier, 2021: pp. 433–469. https://doi.org/https://doi.org/10.1016/bs.coac.2020.12.001.

[161] M. Nasrollahzadeh, M. Atarod, M. Sajjadi, S.M. Sajadi, Z. Issaabadi, Chapter 6 - Plant-Mediated Green Synthesis of Nanostructures: Mechanisms, Characterization, and Applications, in: M. Nasrollahzadeh, S.M. Sajadi, M. Sajjadi, Z. Issaabadi, M.B.T.-I.S. and T. Atarod (Eds.), An Introd. to Green Nanotechnol., Elsevier, 2019: pp. 199–322. https://doi.org/https://doi.org/10.1016/B978-0-12-813586-0.00006-7.

[162] N. Raval, R. Maheshwari, D. Kalyane, S.R. Youngren-Ortiz, M.B. Chougule, R.K. Tekade, Importance of physicochemical characterization of nanoparticles in pharmaceutical product development, in: Basic Fundam. Drug Deliv., Elsevier, 2019: pp. 369–400.

[163] A. Monshi, M.R. Foroughi, M.R. Monshi, Modified Scherrer equation to estimate more accurately nano-crystallite size using XRD, World J. Nano Sci. Eng. 2 (2012) 154–160.

[164] R. Sindhu, P. Binod, A. Pandey, Chapter 17 - Microbial Poly-3-Hydroxybutyrate and Related Copolymers, in: A. Pandey, R. Höfer, M. Taherzadeh, K.M. Nampoothiri, C.B.T.-I.B.& W.B. Larroche (Eds.), Elsevier, Amsterdam, 2015: pp. 575–605. https://doi.org/https://doi.org/10.1016/B978-0-444-63453-5.00019-7.

[165] V. Chevali, E. Kandare, 13 - Rigid biofoam composites as eco-efficient construction materials, in: F. Pacheco-Torgal, V. Ivanov, N. Karak, H.B.T.-B. and B.A. for E.-E.C.M. Jonkers (Eds.), Woodhead Publishing, 2016: pp. 275–304. https://doi.org/https://doi.org/10.1016/B978-0-08-100214-8.00013-0.

[166] S. Brunauer, P.H. Emmett, E. Teller, Adsorption of gases in multimolecular layers, J. Am. Chem. Soc. 60 (1938) 309–319.

[167] S.U. Rawal, M.M. Patel, Chapter 2 - Lipid nanoparticulate systems: Modern

versatile drug carriers, in: A.M.B.T.-L.N. for D.T. Grumezescu (Ed.), William Andrew Publishing, 2018: pp. 49–138. https://doi.org/https://doi.org/10.1016/B978-0-12-813687-4.00002-5.

[168] T. Saeed, A. Naeem, T. Mahmood, Z. Ahmad, M. Farooq, Farida, I.U. Din, I.W. Khan, Comparative study for removal of cationic dye from aqueous solutions by manganese oxide and manganese oxide composite, Int. J. Environ. Sci. Technol. 18 (2021) 659–672. https://doi.org/10.1007/s13762-020-02844-4.

[169] F. khan, N. A, I.U. Din, T. Saeed, M.A. Alotaibi, A.I. Alharthi, A. Habib, T. Malik, Synthesis, characterization and adsorption studies of h-BN crystal for efficient removal of Cd2+ from aqueous solution, Ceram. Int. 47 (2021) 4749–4757. https://doi.org/https://doi.org/10.1016/j.ceramint.2020.10.044.

[170] M. Li, Y. Liu, S. Liu, G. Zeng, X. Hu, X. Tan, L. Jiang, N. Liu, J. Wen, X. Liu, Performance of magnetic graphene oxide/diethylenetriaminepentaacetic acid nanocomposite for the tetracycline and ciprofloxacin adsorption in single and binary systems, J. Colloid Interface Sci. 521 (2018) 150–159. https://doi.org/https://doi.org/10.1016/j.jcis.2018.03.003.

[171] Z. Zhao, J. Zhao, C. Yang, Efficient removal of ciprofloxacin by peroxymonosulfate/Mn3O4-MnO2 catalytic oxidation system, Chem. Eng. J. 327 (2017) 481–489. https://doi.org/https://doi.org/10.1016/j.cej.2017.06.064.

[172] H. Ji, T. Wang, T. Huang, B. Lai, W. Liu, Adsorptive removal of ciprofloxacin with different dissociated species onto titanate nanotubes, J. Clean. Prod. 278 (2021) 123924. https://doi.org/https://doi.org/10.1016/j.jclepro.2020.123924.

[173] X. Xu, J. He, Y. Li, Z. Fang, S. Xu, Adsorption and transport of ciprofloxacin in quartz sand at different pH and ionic strength, Open J. Soil Sci. 4 (2014) 407.

[174] O. Eljamal, A.M.E. Khalil, Y. Sugihara, N. Matsunaga, Phosphorus removal from aqueous solution by nanoscale zero valent iron in the presence of copper chloride, Chem. Eng. J. 293 (2016) 225–231. https://doi.org/https://doi.org/10.1016/j.cej.2016.02.052.

[175] A.M.E. Khalil, F.A. Memon, T.A. Tabish, D. Salmon, S. Zhang, D. Butler, Nanostructured porous graphene for efficient removal of emerging contaminants (pharmaceuticals) from water, Chem. Eng. J. 398 (2020) 125440. https://doi.org/https://doi.org/10.1016/j.cej.2020.125440.

[176] I. Maamoun, R. Eljamal, O. Falyouna, K. Bensaida, Y. Sugihara, O. Eljamal, Insights into kinetics, isotherms and thermodynamics of phosphorus sorption onto

nanoscale zero-valent Iron, J. Mol. Liq. 328 (2021) 115402. https://doi.org/https://doi.org/10.1016/j.molliq.2021.115402.

[177] S. Sen Gupta, K.G. Bhattacharyya, Kinetics of adsorption of metal ions on inorganic materials: A review, Adv. Colloid Interface Sci. 162 (2011) 39–58. https://doi.org/https://doi.org/10.1016/j.cis.2010.12.004.

[178] S.K. Lagergren, About the theory of so-called adsorption of soluble substances, Sven. Vetenskapsakad. Handingarl. (1898).

[179] W. Plazinski, W. Rudzinski, A. Plazinska, Theoretical models of sorption kinetics including a surface reaction mechanism: A review, Adv. Colloid Interface Sci. 152 (2009) 2–13. https://doi.org/https://doi.org/10.1016/j.cis.2009.07.009.

[180] G. Blanchard, M. Maunaye, G. Martin, Removal of heavy metals from waters by means of natural zeolites, Water Res. 18 (1984) 1501–1507. https://doi.org/https://doi.org/10.1016/0043-1354(84)90124-6.

[181] J. Lin, L. Wang, Comparison between linear and non-linear forms of pseudo-first-order and pseudo-second-order adsorption kinetic models for the removal of methylene blue by activated carbon, Front. Environ. Sci. Eng. China. 3 (2009) 320–324. https://doi.org/10.1007/s11783-009-0030-7.

[182] H. Qiu, L. Lv, B. Pan, Q. Zhang, W. Zhang, Q. Zhang, Critical review in adsorption kinetic models, J. Zhejiang Univ. A. 10 (2009) 716–724. https://doi.org/10.1631/jzus.A0820524.

[183] F.-C. Wu, R.-L. Tseng, R.-S. Juang, Initial behavior of intraparticle diffusion model used in the description of adsorption kinetics, Chem. Eng. J. 153 (2009) 1–8. https://doi.org/https://doi.org/10.1016/j.cej.2009.04.042.

[184] K.Y. Foo, B.H. Hameed, Insights into the modeling of adsorption isotherm systems, Chem. Eng. J. 156 (2010) 2–10. https://doi.org/https://doi.org/10.1016/j.cej.2009.09.013.

[185] M.A. Al-Ghouti, D.A. Da'ana, Guidelines for the use and interpretation of adsorption isotherm models: A review, J. Hazard. Mater. 393 (2020) 122383. https://doi.org/https://doi.org/10.1016/j.jhazmat.2020.122383.

[186] T.W. Weber, R.K. Chakravorti, Pore and solid diffusion models for fixed-bed adsorbers, AIChE J. (1974). https://doi.org/10.1002/aic.690200204.

[187] D. A.O, Langmuir, Freundlich, Temkin and Dubinin–Radushkevich Isotherms Studies of Equilibrium Sorption of Zn 2+ Unto Phosphoric Acid Modified Rice Husk, IOSR J. Appl. Chem. (2012). https://doi.org/10.9790/5736-0313845.

[188] M.A. Fawzy, Biosorption of copper ions from aqueous solution by Codium vermilara: Optimization, kinetic, isotherm and thermodynamic studies, Adv. Powder Technol. 31 (2020) 3724–3735. https://doi.org/https://doi.org/10.1016/j.apt.2020.07.014.

[189] S. Chowdhury, R. Mishra, P. Saha, P. Kushwaha, Adsorption thermodynamics, kinetics and isosteric heat of adsorption of malachite green onto chemically modified rice husk, Desalination. 265 (2011) 159–168. https://doi.org/https://doi.org/10.1016/j.desal.2010.07.047.

[190] A. Günay, E. Arslankaya, I. Tosun, Lead removal from aqueous solution by natural and pretreated clinoptilolite: adsorption equilibrium and kinetics, J. Hazard. Mater. 146 (2007) 362–371.

[191] A.B. Pérez-Marín, V.M. Zapata, J.F. Ortuno, M. Aguilar, J. Sáez, M. Lloréns, Removal of cadmium from aqueous solutions by adsorption onto orange waste, J. Hazard. Mater. 139 (2007) 122–131.

[192] K.V. Kumar, K. Porkodi, Relation between some two- and three-parameter isotherm models for the sorption of methylene blue onto lemon peel, J. Hazard. Mater. 138 (2006) 633–635. https://doi.org/https://doi.org/10.1016/j.jhazmat.2006.06.078.

[193] Y.S. Ho, J.F. Porter, G. McKay, Equilibrium isotherm studies for the sorption of divalent metal ions onto peat: copper, nickel and lead single component systems, Water. Air. Soil Pollut. 141 (2002) 1–33.

[194] S. Çoruh, F. Geyikci, Adsorption of copper (II) ions on montmorillonite and sepiolite clays: equilibrium and kinetic studies, Desalin. Water Treat. 45 (2012) 351–360.

[195] H.N. Tran, S.-J. You, H.-P. Chao, Thermodynamic parameters of cadmium adsorption onto orange peel calculated from various methods: a comparison study, J. Environ. Chem. Eng. 4 (2016) 2671–2682.

[196] P.S. Ghosal, A.K. Gupta, An insight into thermodynamics of adsorptive removal of fluoride by calcined Ca–Al–(NO 3) layered double hydroxide, RSC Adv. 5 (2015) 105889–105900.

[197] M. Doğan, H. Abak, M. Alkan, Adsorption of methylene blue onto hazelnut shell: Kinetics, mechanism and activation parameters, J. Hazard. Mater. 164 (2009) 172–181. https://doi.org/https://doi.org/10.1016/j.jhazmat.2008.07.155.

[198] S. Hussain, M. Kamran, S.A. Khan, K. Shaheen, Z. Shah, H. Suo, Q. Khan, A.B.

Shah, W.U. Rehman, Y.O. Al-Ghamdi, U. Ghani, Adsorption, kinetics and thermodynamics studies of methyl orange dye sequestration through chitosan composites films, Int. J. Biol. Macromol. 168 (2021) 383–394. https://doi.org/https://doi.org/10.1016/j.ijbiomac.2020.12.054.

[199] Y. Wang, J. Lin, Y. Wang, Z. Liu, J. Lian, M. Liu, Highly efficient and selective removal of low-concentration antibiotics from aqueous solution by regenerable Mg(OH)2, J. Environ. Sci. 87 (2020) 228–237. https://doi.org/https://doi.org/10.1016/j.jes.2019.06.017.

[200] Y. Hu, M. Zhang, X. Li, Improved longevity of nanoscale zero-valent iron with a magnesium hydroxide coating shell for the removal of Cr(VI) in sand columns, Environ. Int. 133 (2019) 105249. https://doi.org/https://doi.org/10.1016/j.envint.2019.105249.

[201] M.E. Mahmoud, S.R. Saad, A.M. El-Ghanam, R.H.A. Mohamed, Developed magnetic Fe3O4–MoO3-AC nanocomposite for effective removal of ciprofloxacin from water, Mater. Chem. Phys. 257 (2021) 123454. https://doi.org/https://doi.org/10.1016/j.matchemphys.2020.123454.

[202] X. Li, D.W. Elliott, W. Zhang, Zero-valent iron nanoparticles for abatement of environmental pollutants: materials and engineering aspects, Crit. Rev. Solid State Mater. Sci. 31 (2006) 111–122.

[203] X. Liu, Z. Cao, Z. Yuan, J. Zhang, X. Guo, Y. Yang, F. He, Y. Zhao, J. Xu, Insight into the kinetics and mechanism of removal of aqueous chlorinated nitroaromatic antibiotic chloramphenicol by nanoscale zero-valent iron, Chem. Eng. J. 334 (2018) 508–518. https://doi.org/https://doi.org/10.1016/j.cej.2017.10.060.

[204] Y. Liu, S.A. Majetich, R.D. Tilton, D.S. Sholl, G. V Lowry, TCE dechlorination rates, pathways, and efficiency of nanoscale iron particles with different properties, Environ. Sci. Technol. 39 (2005) 1338–1345.

[205] K. Bensaida, R. Eljamal, kareman Eljamal, Y. Sughihara, O. Eljamal, The impact of iron bimetallic nanoparticles on bulk microbial growth in wastewater, J. Water Process Eng. 40 (2020) 101825. https://doi.org/https://doi.org/10.1016/j.jwpe.2020.101825.

[206] R. Mokete, O. Eljamal, Y. Sugihara, Exploration of the reactivity of nanoscale zero-valent iron (NZVI) associated nanoparticles in diverse experimental conditions, Chem. Eng. Process. - Process Intensif. 150 (2020) 107879. https://doi.org/https://doi.org/10.1016/j.cep.2020.107879.

[207] C.-C. Lin, Y.-H. Chen, Feasibility of using nanoscale zero-valent iron and persulfate to degrade sulfamethazine in aqueous solutions, Sep. Purif. Technol. 194 (2018) 388–395. https://doi.org/https://doi.org/10.1016/j.seppur.2017.10.073.

[208] J. Xu, Z. Cao, Y. Wang, Y. Zhang, X. Gao, M.B. Ahmed, J. Zhang, Y. Yang, J.L. Zhou, G. V Lowry, Distributing sulfidized nanoscale zerovalent iron onto phosphorus-functionalized biochar for enhanced removal of antibiotic florfenicol, Chem. Eng. J. 359 (2019) 713–722.

[209] D.A. Demirezen, Y.Ş. Yıldız, D.D. Yılmaz, Amoxicillin degradation using green synthesized iron oxide nanoparticles: Kinetics and mechanism analysis, Environ. Nanotechnology, Monit. Manag. 11 (2019) 100219.

[210] A.H. Berger, A.S. Bhown, Comparing physisorption and chemisorption solid sorbents for use separating CO2 from flue gas using temperature swing adsorption, Energy Procedia. 4 (2011) 562–567. https://doi.org/https://doi.org/10.1016/j.egypro.2011.01.089.

[211] M. Schmidt, A. Masson, H.-P. Cheng, C. Bréchignac, Physisorption and Chemisorption on Silver Clusters, ChemPhysChem. 16 (2015) 855–865. https://doi.org/https://doi.org/10.1002/cphc.201402726.

[212] C. Gu, K.G. Karthikeyan, Sorption of the Antimicrobial Ciprofloxacin To Aluminum and Iron Hydrous Oxides, Environ. Sci. Technol. 39 (2005) 9166–9173. https://doi.org/10.1021/es051109f.

[213] H. Zhang, S.K. Khanal, Y. Jia, S. Song, H. Lu, Fundamental insights into ciprofloxacin adsorption by sulfate-reducing bacteria sludge: Mechanisms and thermodynamics, Chem. Eng. J. 378 (2019) 122103. https://doi.org/https://doi.org/10.1016/j.cej.2019.122103.

[214] J.A. de Lima Perini, B.F. Silva, R.F.P. Nogueira, J.A. de L. Perini, B.F. Silva, R.F.P. Nogueira, Zero-valent iron mediated degradation of ciprofloxacin – Assessment of adsorption, operational parameters and degradation products, Chemosphere. 117 (2014) 345–352. https://doi.org/https://doi.org/10.1016/j.chemosphere.2014.07.071.

[215] G. Bayramoglu, B. Altintas, M.Y. Arica, Adsorption kinetics and thermodynamic parameters of cationic dyes from aqueous solutions by using a new strong cation-exchange resin, Chem. Eng. J. 152 (2009) 339–346. https://doi.org/https://doi.org/10.1016/j.cej.2009.04.051.

[216] D. Zide, O. Fatoki, O. Oputu, B. Opeolu, S. Nelana, O. Olatunji, Zeolite

‘adsorption’ capacities in aqueous acidic media; The role of acid choice and quantification method on ciprofloxacin removal, Microporous Mesoporous Mater. 255 (2018) 226–241. https://doi.org/https://doi.org/10.1016/j.micromeso.2017.07.033.

[217] N. Genç, E.C. Dogan, Adsorption kinetics of the antibiotic ciprofloxacin on bentonite, activated carbon, zeolite, and pumice, Desalin. Water Treat. 53 (2015) 785–793. https://doi.org/10.1080/19443994.2013.842504.

[218] J. Xu, X. Liu, Z. Cao, W. Bai, Q. Shi, Y. Yang, Fast degradation, large capacity, and high electron efficiency of chloramphenicol removal by different carbon-supported nanoscale zerovalent iron, J. Hazard. Mater. 384 (2020) 121253. https://doi.org/https://doi.org/10.1016/j.jhazmat.2019.121253.

[219] J. Fan, Y. Hu, X. Li, Nanoscale Zero-Valent Iron Coated with Magnesium Hydroxide for Effective Removal of Cyanobacteria from Water, ACS Sustain. Chem. Eng. 6 (2018) 15135–15142. https://doi.org/10.1021/acssuschemeng.8b03593.

[220] Y. Hu, M. Zhang, R. Qiu, X. Li, Encapsulating nanoscale zero-valent iron with a soluble Mg(OH)2 shell for improved mobility and controlled reactivity release, J. Mater. Chem. A. 6 (2018) 2517–2526. https://doi.org/10.1039/C7TA08605A.

[221] M.A. Ahmed, S.T. Bishay, F.M. Ahmed, S.I. El-Dek, Effective Pb2+ removal from water using nanozerovalent iron stored 10 months, Appl. Nanosci. 7 (2017) 407–416. https://doi.org/10.1007/s13204-017-0581-z.

[222] S. Ahmad, X. Liu, J. Tang, S. Zhang, Biochar-supported nanosized zero-valent iron (nZVI/BC) composites for removal of nitro and chlorinated contaminants, Chem. Eng. J. (2021) 133187. https://doi.org/https://doi.org/10.1016/j.cej.2021.133187.

[223] W. Xu, T. Yang, S. Liu, L. Du, Q. Chen, X. Li, J. Dong, Z. Zhang, S. Lu, Y. Gong, L. Zhou, Y. Liu, X. Tan, Insights into the Synthesis, types and application of iron Nanoparticles: The overlooked significance of environmental effects, Environ. Int. 158 (2022) 106980. https://doi.org/https://doi.org/10.1016/j.envint.2021.106980.

[224] F. Wang, Y. Wu, Y. Gao, H. Li, Z. Chen, Effect of humic acid, oxalate and phosphate on Fenton-like oxidation of microcystin-LR by nanoscale zero-valent iron, Sep. Purif. Technol. 170 (2016) 337–343. https://doi.org/https://doi.org/10.1016/j.seppur.2016.06.046.

[225] M. Elkady, H. Shokry, H. Hamad, Microwave-assisted synthesis of magnetic

hydroxyapatite for removal of heavy metals from groundwater, Chem. Eng. Technol. 41 (2018) 553–562.

[226] M. Eltarahony, M. Abu-Serie, H. Hamad, S. Zaki, D. Abd-El-Haleem, Unveiling the role of novel biogenic functionalized CuFe hybrid nanocomposites in boosting anticancer, antimicrobial and biosorption activities, Sci. Rep. 11 (2021) 1–22.

[227] Y. Zhou, X. Li, Green synthesis of modified polyethylene packing supported tea polyphenols-NZVI for nitrate removal from wastewater: Characterization and mechanisms, Sci. Total Environ. 806 (2022) 150596. https://doi.org/https://doi.org/10.1016/j.scitotenv.2021.150596.

[228] M. Elkady, H. Shokry, A. El-Sharkawy, G. El-Subruiti, H. Hamad, New insights into the activity of green supported nanoscale zero-valent iron composites for enhanced acid blue-25 dye synergistic decolorization from aqueous medium, J. Mol. Liq. 294 (2019) 111628. https://doi.org/https://doi.org/10.1016/j.molliq.2019.111628.

[229] Y. Sun, M. Ma, Y. Zhang, N. Gu, Synthesis of nanometer-size maghemite particles from magnetite, Colloids Surfaces A Physicochem. Eng. Asp. 245 (2004) 15–19. https://doi.org/https://doi.org/10.1016/j.colsurfa.2004.05.009.

[230] A. Liu, J. Liu, B. Pan, W. Zhang, Formation of lepidocrocite (γ-FeOOH) from oxidation of nanoscale zero-valent iron (nZVI) in oxygenated water, Rsc Adv. 4 (2014) 57377–57382.

[231] A. Liu, J. Liu, W. Zhang, Transformation and composition evolution of nanoscale zero valent iron (nZVI) synthesized by borohydride reduction in static water, Chemosphere. 119 (2015) 1068–1074. https://doi.org/https://doi.org/10.1016/j.chemosphere.2014.09.026.

[232] H. Dong, F. Zhao, Q. He, Y. Xie, Y. Zeng, L. Zhang, L. Tang, G. Zeng, Physicochemical transformation of carboxymethyl cellulose-coated zero-valent iron nanoparticles (nZVI) in simulated groundwater under anaerobic conditions, Sep. Purif. Technol. 175 (2017) 376–383. https://doi.org/https://doi.org/10.1016/j.seppur.2016.11.053.

[233] A.M.E. Khalil, O. Eljamal, S. Jribi, N. Matsunaga, Promoting nitrate reduction kinetics by nanoscale zero valent iron in water via copper salt addition, Chem. Eng. J. 287 (2016) 367–380. https://doi.org/https://doi.org/10.1016/j.cej.2015.11.038.

[234] A.B.M. Giasuddin, S.R. Kanel, H. Choi, Adsorption of humic acid onto nanoscale zerovalent iron and its effect on arsenic removal, Environ. Sci. Technol. 41 (2007)

2022–2027.

[235] Y. Ou, C.-Y. Wei, Y. Shih, Short-chain organic acids increase the reactivity of zerovalent iron nanoparticles toward polychlorinated aromatic pollutants, Chem. Eng. J. 284 (2016) 372–379. https://doi.org/https://doi.org/10.1016/j.cej.2015.08.138.

[236] W. Yin, J. Wu, P. Li, X. Wang, N. Zhu, P. Wu, B. Yang, Experimental study of zero-valent iron induced nitrobenzene reduction in groundwater: the effects of pH, iron dosage, oxygen and common dissolved anions, Chem. Eng. J. 184 (2012) 198–204.

[237] Y. Hu, N. Habibul, Y.-Y. Hu, F.-L. Meng, G.-P. Sheng, Chemical speciation of ciprofloxacin in aqueous solution regulates its phytotoxicity and uptake by rice (Oryza sativa L.), Sci. Total Environ. 771 (2021) 144787. https://doi.org/https://doi.org/10.1016/j.scitotenv.2020.144787.

[238] G.-D. Fang, D.-M. Zhou, D.D. Dionysiou, Superoxide mediated production of hydroxyl radicals by magnetite nanoparticles: Demonstration in the degradation of 2-chlorobiphenyl, J. Hazard. Mater. 250–251 (2013) 68–75. https://doi.org/https://doi.org/10.1016/j.jhazmat.2013.01.054.

[239] A. Correia de Velosa, R.F. Pupo Nogueira, 2,4-Dichlorophenoxyacetic acid (2,4-D) degradation promoted by nanoparticulate zerovalent iron (nZVI) in aerobic suspensions, J. Environ. Manage. 121 (2013) 72–79. https://doi.org/https://doi.org/10.1016/j.jenvman.2013.02.031.

[240] F.A. Banat, B. Al-Bashir, S. Al-Asheh, O. Hayajneh, Adsorption of phenol by bentonite, Environ. Pollut. 107 (2000) 391–398. https://doi.org/https://doi.org/10.1016/S0269-7491(99)00173-6.

[241] O. Eljamal, K. Jinno, T. Hosokawa, Modeling of solute transport and biological sulfate reduction using low cost electron donor, Environ. Geol. 56 (2009) 1605–1613.

[242] M.J. Ahmed, S.K. Dhedan, Equilibrium isotherms and kinetics modeling of methylene blue adsorption on agricultural wastes-based activated carbons, Fluid Phase Equilib. 317 (2012) 9–14. https://doi.org/https://doi.org/10.1016/j.fluid.2011.12.026.

[243] A.N. Fernandes, C.A.P. Almeida, N.A. Debacher, M.M. de S. Sierra, Isotherm and thermodynamic data of adsorption of methylene blue from aqueous solution onto peat, J. Mol. Struct. 982 (2010) 62–65.

https://doi.org/https://doi.org/10.1016/j.molstruc.2010.08.006.

[244] D. Bassyouni, M. Mohamed, E.-S. El-Ashtoukhy, M. Abd El-Latif, A. Zaatout, H. Hamad, Fabrication and characterization of electrospun Fe3O4/o-MWCNTs/polyamide 6 hybrid nanofibrous membrane composite as an efficient and recoverable adsorbent for removal of Pb (II), Microchem. J. 149 (2019) 103998.

[245] A.B.D. Nandiyanto, G.C.S. Girsang, R. Maryanti, R. Ragadhita, S. Anggraeni, F.M. Fauzi, P. Sakinah, A.P. Astuti, D. Usdiyana, M. Fiandini, Isotherm adsorption characteristics of carbon microparticles prepared from pineapple peel waste, Commun. Sci. Technol. 5 (2020) 31–39.

[246] A.A. Hamad, M.S. Hassouna, T.I. Shalaby, M.F. Elkady, M.A. Abd Elkawi, H.A. Hamad, Electrospun cellulose acetate nanofiber incorporated with hydroxyapatite for removal of heavy metals, Int. J. Biol. Macromol. 151 (2020) 1299–1313. https://doi.org/https://doi.org/10.1016/j.ijbiomac.2019.10.176.

[247] S. Zulfiqar, U. Rafique, M.J. Akhtar, H. Hamad, On the Behavior of Newly Synthesized Functionalized Imidazolium-Based Ionic Liquids for Highly Efficient Extraction and Separation of Pirimicarb from Orchard Real Wastewater, Adsorpt. Sci. Technol. 2022 (2022).

[248] A. Hamadi, N. Yeddou-Mezenner, A. Lounis, R.M. Ali, H. Hamad, Upgrading of agro-industrial green biomass residues from chocolate industry for adsorption process: diffusion and mechanistic insights, J. Food Sci. Technol. 58 (2021) 1081–1092.

[249] R. Davarnejad, S. Afshar, P. Etehadfar, Activated carbon blended with grape stalks powder: Properties modification and its application in a dye adsorption, Arab. J. Chem. 13 (2020) 5463–5473. https://doi.org/https://doi.org/10.1016/j.arabjc.2020.03.025.

[250] Z. Movasaghi, B. Yan, C. Niu, Adsorption of ciprofloxacin from water by pretreated oat hulls: Equilibrium, kinetic, and thermodynamic studies, Ind. Crops Prod. 127 (2019) 237–250. https://doi.org/https://doi.org/10.1016/j.indcrop.2018.10.051.

[251] Y. Ma, M. Li, P. Li, L. Yang, L. Wu, F. Gao, X. Qi, Z. Zhang, Hydrothermal synthesis of magnetic sludge biochar for tetracycline and ciprofloxacin adsorptive removal, Bioresour. Technol. 319 (2021) 124199. https://doi.org/https://doi.org/10.1016/j.biortech.2020.124199.

[252] E.M. El-Sayed, H.A. Hamad, R.M. Ali, Journey from ceramic waste to highly efficient toxic dye adsorption from aqueous solutions via one-pot synthesis of CaSO4 rod-shape with silica, J. Mater. Res. Technol. 9 (2020) 16051–16063. https://doi.org/https://doi.org/10.1016/j.jmrt.2020.11.037.

[253] B.S. Rathi, P.S. Kumar, Application of adsorption process for effective removal of emerging contaminants from water and wastewater, Environ. Pollut. 280 (2021) 116995. https://doi.org/https://doi.org/10.1016/j.envpol.2021.116995.

[254] Q. Wu, Z. Li, H. Hong, K. Yin, L. Tie, Adsorption and intercalation of ciprofloxacin on montmorillonite, Appl. Clay Sci. 50 (2010) 204–211.

[255] S. Rakshit, D. Sarkar, E.J. Elzinga, P. Punamiya, R. Datta, Mechanisms of ciprofloxacin removal by nano-sized magnetite, J. Hazard. Mater. 246–247 (2013) 221–226. https://doi.org/https://doi.org/10.1016/j.jhazmat.2012.12.032.

[256] K. Yonebayashi, T. Hattori, Chemical and biological studies on environmental humic acids: I. Composition of elemental and functional groups of humic acids, Soil Sci. Plant Nutr. 34 (1988) 571–584.

[257] K. Luo, Y. Pang, Q. Yang, D. Wang, X. Li, L. Wang, M. Lei, J. Liu, Enhanced ciprofloxacin removal by sludge-derived biochar: Effect of humic acid, Chemosphere. 231 (2019) 495–501. https://doi.org/https://doi.org/10.1016/j.chemosphere.2019.05.151.

[258] M. Li, Y. Liu, S. Liu, D. Shu, G. Zeng, X. Hu, X. Tan, L. Jiang, Z. Yan, X. Cai, Cu(II)-influenced adsorption of ciprofloxacin from aqueous solutions by magnetic graphene oxide/nitrilotriacetic acid nanocomposite: Competition and enhancement mechanisms, Chem. Eng. J. 319 (2017) 219–228. https://doi.org/https://doi.org/10.1016/j.cej.2017.03.016.

[259] J. Yang, X. Wang, M. Zhu, H. Liu, J. Ma, Investigation of PAA/PVDF–NZVI hybrids for metronidazole removal: Synthesis, characterization, and reactivity characteristics, J. Hazard. Mater. 264 (2014) 269–277. https://doi.org/https://doi.org/10.1016/j.jhazmat.2013.11.037.

[260] Z. Wen, Y. Zhang, C. Dai, Removal of phosphate from aqueous solution using nanoscale zerovalent iron (nZVI), Colloids Surfaces A Physicochem. Eng. Asp. 457 (2014) 433–440. https://doi.org/https://doi.org/10.1016/j.colsurfa.2014.06.017.

[261] B. Hao, F. Wang, H. Huang, Y. Wu, S. Jia, Y. Liao, H. Mao, Tannin foam immobilized with ferric ions for efficient removal of ciprofloxacin at low

concentrations, J. Hazard. Mater. 414 (2021) 125567. https://doi.org/https://doi.org/10.1016/j.jhazmat.2021.125567.

[262] O. Eljamal, R. Eljamal, I. Maamoun, A.M.E. Khalil, T. Shubair, O. Falyouna, Y. Sugihara, Efficient treatment of ammonia-nitrogen contaminated waters by nano zero-valent iron/zeolite composite, Chemosphere. 287 (2022) 131990. https://doi.org/https://doi.org/10.1016/j.chemosphere.2021.131990.

[263] M. Fazlzadeh, K. Rahmani, A. Zarei, H. Abdoallahzadeh, F. Nasiri, R. Khosravi, A novel green synthesis of zero valent iron nanoparticles (NZVI) using three plant extracts and their efficient application for removal of Cr(VI) from aqueous solutions, Adv. Powder Technol. 28 (2017) 122–130. https://doi.org/https://doi.org/10.1016/j.apt.2016.09.003.

[264] J. Qu, Y. Liu, L. Cheng, Z. Jiang, G. Zhang, F. Deng, L. Wang, W. Han, Y. Zhang, Green synthesis of hydrophilic activated carbon supported sulfide nZVI for enhanced Pb(II) scavenging from water: Characterization, kinetics, isotherms and mechanisms, J. Hazard. Mater. 403 (2021) 123607. https://doi.org/https://doi.org/10.1016/j.jhazmat.2020.123607.

[265] Y. Rashtbari, S. Hazrati, A. Azari, S. Afshin, M. Fazlzadeh, M. Vosoughi, A novel, eco-friendly and green synthesis of PPAC-ZnO and PPAC-nZVI nanocomposite using pomegranate peel: Cephalexin adsorption experiments, mechanisms, isotherms and kinetics, Adv. Powder Technol. 31 (2020) 1612–1623. https://doi.org/https://doi.org/10.1016/j.apt.2020.02.001.

[266] G. Gopal, H. Sankar, C. Natarajan, A. Mukherjee, Tetracycline removal using green synthesized bimetallic nZVI-Cu and bentonite supported green nZVI-Cu nanocomposite: A comparative study, J. Environ. Manage. 254 (2020) 109812. https://doi.org/https://doi.org/10.1016/j.jenvman.2019.109812.

[267] J.L. Domingo, M. Nadal, Human exposure to per- and polyfluoroalkyl substances (PFAS) through drinking water: A review of the recent scientific literature, Environ. Res. 177 (2019) 108648. https://doi.org/https://doi.org/10.1016/j.envres.2019.108648.

[268] N. Bolan, B. Sarkar, M. Vithanage, G. Singh, D.C.W. Tsang, R. Mukhopadhyay, K. Ramadass, A. Vinu, Y. Sun, S. Ramanayaka, S.A. Hoang, Y. Yan, Y. Li, J. Rinklebe, H. Li, M.B. Kirkham, Distribution, behaviour, bioavailability and remediation of poly- and per-fluoroalkyl substances (PFAS) in solid biowastes and biowaste-treated soil, Environ. Int. 155 (2021) 106600.

https://doi.org/https://doi.org/10.1016/j.envint.2021.106600.

[269] B. Ji, P. Kang, T. Wei, Y. Zhao, Challenges of aqueous per- and polyfluoroalkyl substances (PFASs) and their foreseeable removal strategies, Chemosphere. 250 (2020) 126316. https://doi.org/https://doi.org/10.1016/j.chemosphere.2020.126316.

[270] A. Masud, M.G.E. Guardian, S.C. Travis, N.G. Chavez Soria, M. Jarin, D.S. Aga, N. Aich, Redox-active rGO-nZVI nanohybrid-catalyzed chain shortening of perfluorooctanoic acid (PFOA) and perfluorooctane sulfonic acid (PFOS), J. Hazard. Mater. Lett. 2 (2021) 100007. https://doi.org/https://doi.org/10.1016/j.hazl.2020.100007.